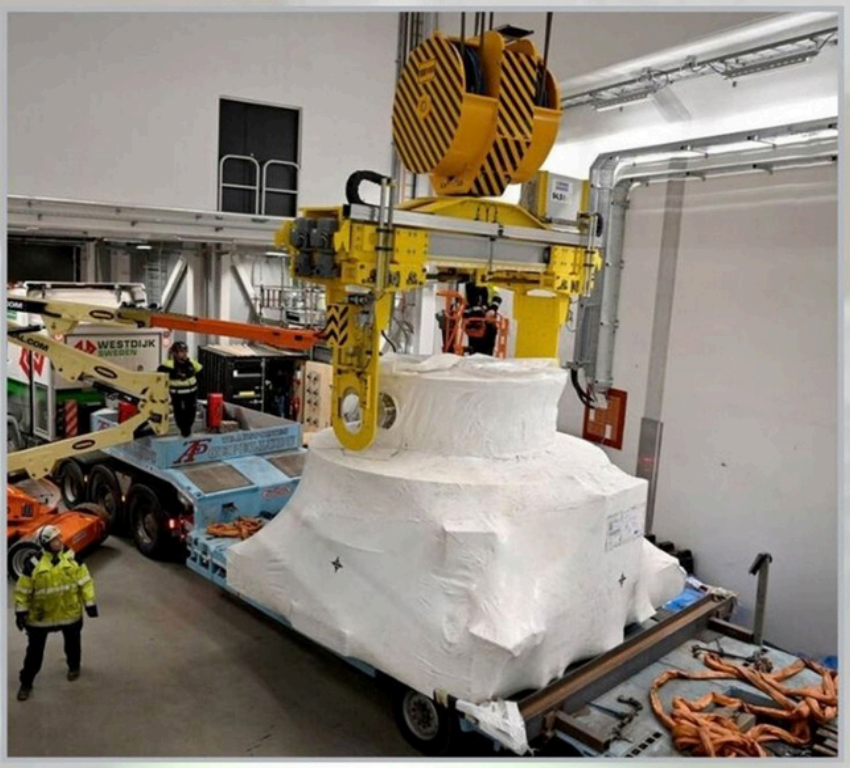
HUN REN

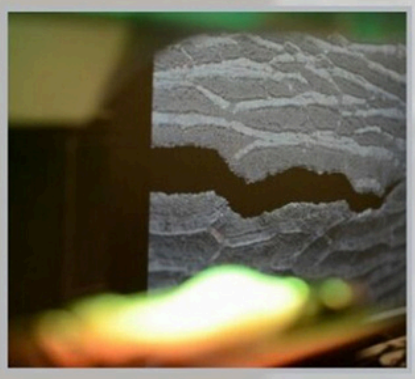
Centre for Energy Research











Progress Report on Research Activities 2025

HUN-REN CENTRE FOR ENERGY RESEARCH

29-33 KONKOLY-THEGE MIKLÓS ÚT

1121 BUDAPEST, HUNGARY

PROGRESS REPORT ON RESEARCH ACTIVITIES IN 2025

DEAR READER

In the life of a research institution, each year is both a milestone and part of a continuing process. It is a milestone because, year after year, our scientific community contributes new discoveries, research results and technological developments; and it is a process because these achievements form part of a long-term scientific endeavour whose full significance often becomes visible only over many years.

The year 2025 at the **HUN-REN Centre for Energy Research** reflects this diverse and continuously evolving research activity. Our researchers achieved new results in nuclear energy and technology, materials science and nanoscience, photonics, micro- and nanosystems, sensing technologies, as well as medical technology and biological applications. Behind this diversity of research fields, however, there is a common ambition: **to generate and share knowledge that can contribute to the development of safe, sustainable and innovative technologies for the future.**

I consider it particularly important that fundamental research, technology development and practical application are becoming increasingly closely connected across our research activities. Research on two-dimensional materials and nanostructures, for example, combines fundamental advances in materials science with perspectives for future energy technologies. Our work on catalysts for hydrogen evolution, together with investigations into new approaches to solar-driven hydrogen production, illustrates how fundamental scientific discoveries can open pathways towards future technologies.

In the field of nuclear research, we further strengthened the knowledge base required for the safe application of both current and future reactor technologies. Our work on reactor physics and thermal-hydraulic modelling included participation in international benchmarks, further development of our own computational methods, and investigations related to small modular reactors, energy storage and hydrogen production.

At the same time, the research profile of our Centre extends well beyond the traditional boundaries of energy research. The development of advanced materials and thin films, photonic and sensing technologies, microfluidic systems and medical applications brings together physics, chemistry, engineering, biology and information science, creating opportunities for these fields to reinforce one another.

Looking towards the technologies of the future, our research is also increasingly embracing emerging fields such as quantum electronics, neuromorphic systems and intelligent sensing. While many of these activities are still situated at the frontiers of fundamental research, it is precisely in such fields that the knowledge and methods shaping the next generations of technology may emerge.

None of this would be possible without our research infrastructure, our network of national and international collaborations, and, above all, the expertise and dedication of the people working at the Centre. The achievements of 2025 are therefore not the accomplishments of individual laboratories or research groups alone, but **the result of a shared endeavour**. They reflect a community that combines scientific curiosity with responsibility, established expertise with innovative thinking, and international cooperation with a strong commitment to Hungarian science.

The yearbook presented here offers a snapshot of this work. Behind the results featured in its pages lie countless experiments, calculations, measurements, discussions and moments of shared scientific thinking. They reflect the perseverance of our researchers, the expertise of our engineers and technical staff, the energy of our younger colleagues, and the knowledge and experience accumulated by generations of scientists at the Centre.

I would like to express my sincere appreciation to everyone whose work contributed to the achievements of the HUN-REN Centre for Energy Research in 2025. I am confident that in the years ahead we will continue to preserve the intellectual openness and scientific excellence that enable us to ask new questions, seek new answers and contribute, through our knowledge and expertise, to the future of Hungary and the international scientific community.

Ákos Horváth
Director General
horvath.akos@ek.hun-ren.hu

CONTENTS

Dear Reader 2
Contents 4
Mission Statement of the HUN-REN Centre for Energy Research 8
Organisation Structure of the HUN-REN Centre for Energy Research (2025) 9
Quality Management 10
Budapest Research Reactor 14
Environmental Protection Service 16

I. RESEARCH ACTIVITIES SUPPORTED BY DOMESTIC AND INTERNATIONAL PUBLIC AGENCIES 17

OECD NEA Thermal Hydraulic Code Validation Benchmark Activity for High Temperature Gas-Cooled Reactors 18
Current Status of the TREASURE Project 19
Research on Material Ageing and Structural Integrity of Research Reactors 20
OECD NEA Working Group on Fuel Safety Water Cooled Small Modular Reactor Fuel Design and Safety Evaluation 21
Development of the Combined Effect of Pre-treatment and Radiation on Mechanical Properties of Cladding Materials Proposal for FIDES-II 22
Pre-test and Post-test Simulations of RIA and LOCA Experiments in the HERA and LOC-HBu Projects 23
Optimisation of Engineered Barrier Systems for Radioactive Waste Storage 24
Simulation of Pellet-cladding Mechanical Interaction with Accident Tolerant Fuel Claddings 27
Fusion Research and Development in the Eurofusion Program 28
Support Laboratory for the ITER Disruption Mitigation System 30
Development of a Propellant Valve Prototype for the ITER Disruption Mitigation System 32
Development of a Remote In-Bore Brazing Tool for DEMO Breeding Blankets 33
Fusion Material Science Research: Material Development, Irradiation and Radiation Damage Testing 35
Education and Training Activities in Radiation Protection and Nuclear Safety 36

II. RESEARCH AND DEVELOPMENT RELATED TO NUCLEAR POWER PLANTS 37

Activities of HUN-REN EK as the Main Consultant of Paks Nuclear Power Plant 38
SURET – Modelling Two-Phase Flow in Subchannels with a Graphical User Interface 40
Investigation of the CERES Facility Coolability Limit 42
Turbine Emulator Development for the Turbine Control System of Paks NPP 43
Validation of the KARATE Code System Against Operational Data and Startup Measurements with Modified Group Constant Libraries 45
Neutron Irradiation Loading and Heat Generation Assessment of Components Between the Core and Reactor Pressure Vessel for Subsequent Long-Term Operation Extension of the Paks Nuclear Power Plant 46
Integral Testing of Accident Tolerant Fuel Design under Air Ingress Conditions 48
Acoustic Emission Laboratory Accreditation Project 50
Effect of Steam Pre-oxidation on the Air Oxidation of SLIM Cladding 52
Parameterised Cross-section Library Generation with the SERPENT 2 Code and Testing in VVER-1200 Core Geometry with the KIKO3DMG Nodal Simplified Spherical Harmonics (SPN) Code 53
Benchmarking and Improving Computational Tools for SMR Analysis 55
Support for the Preparation of Small Modular Reactors in Hungary 57
Optimised Manoeuvring of Nuclear Power Plants: The Actual Constraints and Consequences 58

Finite Element Analysis of the Necking of Tensile Tests....59
A New Concept for the Methodology of Structural Integrity Computations....61
III. NUCLEAR SECURITY, DOSIMETRY AND SPACE RESEARCH....65
Development and Implementation of Cultural Heritage Preservation using Ionising Radiation Technology....66
Developments in Personal Dosimetry: Part 3....70
Improvements in Personal Dosimetry....71
Organisation of an International Comparison on the Determination of Internal Exposure (ICIDOSE#2) – Part 2....72
Examination of the Potential Applications of Big Data Analysis for Radiation Protection Purposes....74
Revision of Environmental Radiological Consequence Assessments and Development of an Uncertainty Analysis Framework....75
Dose-rate Assessments for Design Basis Accidents within the Paks Nuclear Power Plant....76
Environmental Impact Assessment Procedure for the Subsequent Service Life Extension of the Paks Nuclear Power Plant....77
Development Directions for Space Weather and Space Dosimetry Detector Systems....78
Investigation of Methodological Development Directions for the Joint Evaluation of TRITEL and RADTEL Measurements Performed in Parallel on Board Multiple Spacecraft....79
Development of a Plasma Thruster for Pocket Sats....80
Wireless Gamma Radiation Detector System for Environmental Monitoring, Dose Rate Mapping and Search for Radioactive Sources....81
Dose Distribution Inside the International Space Station-3D / DOSIS 3D....83
RadMag Space Weather Instrument Development....84
The Internal Dosimetry Array for Gateway, the Space Station of the Artemis Program....85
Development and Qualification Testing of a Complex Space Dosimetry System for Interplanetary Missions....86
IV. ENERGY SECURITY AND ENVIRONMENTAL STUDIES....88
Energy Strategy and Network Research for Future Low-Carbon Energy Systems....89
Improvement of Energy Security by the Utilisation of Low-temperature Heat Sources and by Energy Storage....91
Synchronisation Modelling and Development of Power Grids....93
Particulate Matter Load and Lung Deposition of Aerosol Particles During the Use of Different Gym Equipment....96
Selective Binding of Rare Earth Elements with Silica Adsorbents: Environmental Protection and Metal Recovery....101
Characterisation and Lung Deposition of Harmful Aerosol Particles....106
V. NUCLEAR ANALYSIS AND CHEMISTRY....109
Energy Carrier and Raw Material Production via Chemical (Catalytic) Methods and Energy-Efficient Water Purification....110
Real-time Monitoring of Cell Response/Cell Death due to Ionising Radiation Dose Effect by Tracking Cell Nanomotion....113
Application of Electron Beam Irradiation in Ground Tire Rubber Recycling....119
Magnetic Characterisation of Radioactive Materials....125
Comparative Petrological, Petrophysical and Geochemical Investigations of Polished Stone Artefacts and Potential Source Rocks from the Point of Prehistoric Raw Material Selection Strategy....131
Granum Remodelling During Drought and Recovery in Ctenanthe Setosa....133
VI. RESEARCH AND DEVELOPMENT IN INSTITUTE OF TECHNICAL PHYSICS AND MATERIAL SCIENCES....134
Impact of Ambient Molecular Contamination on Scanning Tunnelling Microscopy Measurements of Van der Waals Materials....135
Stabilisation of Ultra-small Magic Angle Graphene Superlattices by Molecular Intercalation....137
Directional Reflection Asymmetry in Hexagonal and Rhombohedral Graphite Nanoribbons....139
Bias-free Generation of Solar Hydrogen and High-value Glycerol Oxidation Products by Low-bandgap Perovskite Photoelectrodes....141

Strain-induced Modulation of the Local Conductance in MoS_2 Layers on Gold Nanoparticles 143
Bioinspired Semiconductor Nanoarchitectures for Environmentally Friendly Photocatalysis 145
Validity of Young-Dupré Equation for Advancing and Receding Situations by the Capillary Bridge Probe Method 147
A novel, Photoassisted Synthetic Route to Transform Cu_2O Nanooctahedra to Cu_2S Quantum-dot Superstructures 149
Spatial Modulation of Cu_2O Shell Growth on Gold Nanoprisms 152
Electrochemical Methods and Ellipsometric Characterisation of Gold Nanoparticle-Based Sensors 154
Investigation of In- and Out-diffusion of Li-ions in Electrochromic Tungsten-molybdenum Combinatorial Oxide Films by Spectroscopic Ellipsometry 156
Effects of Global Curvature and Illumination Conditions on Magic-mirror Imaging 158
Composition-dependent Structural and Optical Properties of Combinatorially Deposited, RF-sputtered Gallium Oxynitride Layers 160
The Common Sublattice Method Quantifies Local Deformations in Epilayers 162
Evaluation Methods for XPS Depth Profiling: A Review 165
Effect of Non-spherical Shape of Dry Powder Aerosol Drugs on their Airway Deposition Distribution 166
Microcombinatorial Preparation and Characterisation of Multicomponent Thin Films 167
Combinatorially Optimised Sensorics of Sputtered Gradient Gold Nanoparticle Layers 169
Dramatic Interaction Between the Au TEM Grid and Sample as well as Supported MoNi/MgO Catalysts 171
Structural Study of (001) Rutile-type GeO_2 Semiconductor on Rutile (TiO_2) 172
Effect of Nitrogen Content on Microstructure and Mechanical Properties of DC Magnetron Sputtered CrMnMoSiY(N) High Entropy Coatings 173
Biomineralisation at the Nanoscale 175
Preparation and Investigation of Biopolymer Composite Materials Containing Calcium Phosphate Doped with Mg and Zn Components 177
Synthesis and Characterisation of Hydroxyapatite from Eggshells 179
Hungarian Chips Competence Centre (HCHiP) 180
Neutron Absorption in Thin Boron Carbide Layers 181
Controlled Nucleation of Metal Sulphide Layers via Sulphur-Based Surface Functionalisation: Enhanced Initial Growth of GaS_x Thin Films 183
Ultrafast Oscillators Made of Nanoscale VO_2 Memristors for Neuromorphic Electronics 185
Progress Toward Kitaev Transmon Generation 188
Biomechanical Investigation of Soft Tissue Transection using MEMS Force Sensing 190
Wearable Gas Sensors for Emergency and Extreme Conditions 191
3D MEMS Force Sensor for Tissue Recognition 193
Characterisation of Materials for BioMEMS Applications 195
Microfluidic Methods for Particle and Cell Manipulation and Analysis 197
Small-scale Production and Development of Near-Infrared LEDs 200
Cell Culture Media Analysis in Organ-on-Chip Applications 201
Solid-state Nanopores for Extremely Sensitive Nanosensors 203
Kinetic Monitoring of Molecular Interactions during Surfactant-driven Self-propelled Droplet Motion by High Spatial Resolution Waveguide Sensing 204
Temporal pH Waveforms Generated in an Enzymatic Reaction Network in Batch and Cell-Sized Microcompartments 205
Robotic Manipulations of Single Cells using a Large-volume Piezoelectric Micropipette with Nanolitre Precision 206
Kinetic Analysis of SARS-CoV-2 S1–integrin Binding Using Live-cell, Label-free Optical Biosensing 207
In Situ Monitoring of Cell Adhesion Kinetics using Label-Free Optical Biosensors: Evaluating Anticancer Potential and Selectivity of Natural Compounds 208
Inter-role Reciprocity in Evolutionary Trust Game on Square Lattices 209

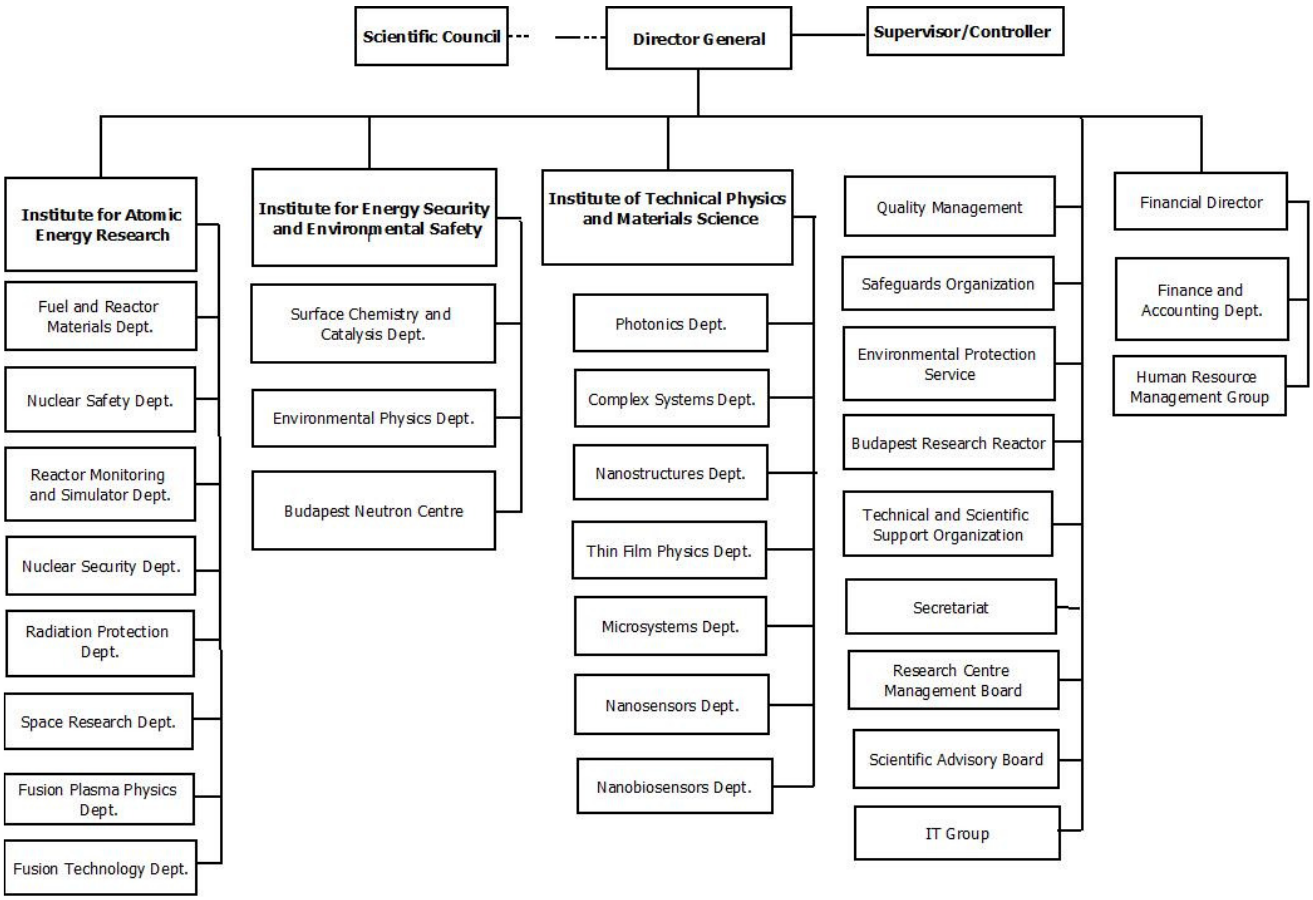
Quantitative Comparison of Power Grid Reinforcements 211
Scale-free Behaviour of Weight Distributions of Connectomes 212
Derivation of Potential for Group Interactions in Evolutionary Games 213

ABBREVIATIONS 214
IMPRINT 220

MISSION STATEMENT OF THE HUN-REN CENTRE FOR ENERGY RESEARCH

- Research and development in the field of nuclear science and technology for facilitating the adoption and the safe use of nuclear technology in Hungary.
- To participate in international research effort aiming at the establishing a new generation of nuclear power plants and closing the fuel cycle.
- Maintaining and improving competence in nuclear science and technology, especially in the field of nuclear safety, security, health physics, nuclear and isotope chemistry.
- To guarantee the safe operation of Budapest Research Reactor (BRR), and to ensure the open access to the research facilities around the reactor operated by the Budapest Neutron Centre.
- Research activities to improve nuclear analytical and imaging methods and their applications for energy and materials science.
- Perform studies in the field of environmental physics related to energy generation, renewable energies, energy storage and their impact on public health, and on environmental safety.
- Research and development in the field of low-carbon energy technologies and of energy saving in industrial technologies.
- Development of nuclear energy production processes based on nuclear fusion, research and development of related technological and physical issues.
- Development of manned mission space dosimetry and space weather measurement systems, furthermore, improvement of devices for space-biological, -chemical and -material science experiments.
- Interdisciplinary research on complex functional materials and nanometer-scale structures, exploration of their physical, chemical, and biological principles, exploitation their operations in integrated micro- and nanosystems, and in the development of characterization techniques.
- Dissemination of the results in international programs, education and industrial research.

ORGANISATION STRUCTURE OF THE HUN-REN CENTRE FOR ENERGY RESEARCH (2025)



QUALITY MANAGEMENT

In order to achieve the highest quality of research, development, design, condition monitoring and valuation, engineering, contracting and managing in design, production, implementation and inspection, the Research Centre's quality management system has continuously been upgraded by the recommendations of the ISO 9001 standard since 1994. Reviewing our QM system by integral audits and management reviews, evaluating improvement opportunities, maintaining project documentation, infrastructure, supporting communication, and ensuring the competence of workers the management improves the Centre's QM system. For the new organisational structure, our Quality Policy has been renewed. Many new employees induced a need to upgrade our QM tuition practice. We organised the work and fire safety educations. Our QM system has been certified by the Hungarian Standards Institution, IQNet and MVM Paks NPP.



NAH-4-0044/2023
IRÁNYÍTÁSI RENDSZEREKET TANÚSÍTÓ SZERVEZET

MSZT 1921

MEMBER OF IQNET

MAGYAR SZABVÁNYÜGYI TESTÜLET
HUNGARIAN STANDARDS INSTITUTION
H-1082 Budapest, Horváth Mihály tér 1.

TANÚSÍTÁSI OKIRAT
CERTIFICATE

Tanúsítjuk, hogy a
We certify that the Management System of

Energiatudományi Kutatóközpont
(kivéve az MFA és a Reaktorüzem)

H-1121 Budapest, Konkoly-Thege Miklós út 29-33.
Tanúsított székhely: H-1121 Budapest, Konkoly-Thege Miklós út 29-33.

irányítási rendszere megfelel a szabvány követelményeinek a következő alkalmazási területen:
kutatás, fejlesztés, tervezés, állapotfelmérés és szakvéleményezés, mérnökszolgálat, fővállalkozási tevékenység tervezési, gyártási, kivitelezési és vizsgálati munkák irányítására, atomenergia alkalmazása körében eljáró független műszaki szakértői tevékenység

meets the requirements of the standard for the following activities:
research, development, design, condition monitoring and valuation, engineering, contracting and managing in design, production, implementation and inspection, independent technological expert activity in the field of application of nuclear energy

MSZ EN ISO 9001:2015 (ISO 9001:2015)

A tanúsítási okirat érvényes / The certificate is valid: **2023. 06. 23. – 2026. 06. 22.**
Ez a tanúsítvány az MSZT által évente kiadott fenntartási határozattal együtt érvényes.
This certificate is valid together with the maintenance decision annually issued by MSZT.
A tanúsítási okirat száma / Reg. number: **503/0309(8)**
Budapest, **2023. június 23.**
Az első tanúsítás dátuma / Date of the first certification: **1999. 06. 22.**

Pónyai György
ügyvezető igazgató

MSZT CERT

IQNET

Building trust together.

Certificate

MSZT has issued an IQNET recognized certificate that the organization:

Centre for Energy Research (except Institute of Technical Physics and Materials Science (MFA) and Reactor Department (Reaktorüzem))

Certified headquarters: Konkoly-Thege Miklós út 29-33.
HU-1121 Budapest Hungary

has implemented and maintains a

Quality Management System

for the following scope:

research, development, design, condition monitoring and valuation, engineering, contracting and managing in design, production, implementation and inspection, independent technological expert activity in the field of application of nuclear energy

which fulfils the requirements of the following Standard:

ISO 9001:2015

Issued on: **2023-06-23**
First issued on: **1999-06-22**
Expires on: **2026-06-22**

Registration Number: **HU-MSZT-503/0309(8)-097(8)**

Alex Stoichitoiu
President of IQNet

György Pónyai
general director

This attestation is directly linked to the IQNET Member's original certificate and shall not be used as a stand-alone document.

IQNET Members*:
AENOR Spain **AFNOR Certification** France **APCER** Portugal **CCC** Cyprus **CISQ** Italy **CQC** China **CQM** China **CQS** Czech Republic **Cro Cert** Croatia **DQS Holding GmbH** Germany **EAGLE Certification Group** USA **FCAV** Brazil **FONDONORMA** Venezuela **ICONTEC** Colombia **ICS** Bosnia and Herzegovina **Inspecta Sertifiointi Oy** Finland **INTECO** Costa Rica **IRAM** Argentina **JQA** Japan **KFQ** Korea **LSQA** Uruguay **MIRTEC** Greece **MSZT** Hungary **Nemko AS** Norway **NSAI** Ireland **NYCE-SIGE** México **PCBC** Poland **Quality Austria** Austria **SII** Israel **SIQ** Slovenia **SIRIM QAS International** Malaysia **SQS** Switzerland **SRAC** Romania **TSE** Türkiye **YUQS** Serbia

* The list of IQNET Members is valid at the time of issue of this certificate. Updated information is available under www.iqnet-certification.com

IQNET

Building trust together.

Annex 1 to IQNET Certificate Number

HU-MSZT-503/0309(8)-097(8)

Centre for Energy Research (except Institute of Technical Physics and Materials Science (MFA) and Reactor Department (Reaktorüzem))

Certified headquarters: Konkoly-Thege Miklós út 29-33.
HU-1121 Budapest

Scope
kutatás, fejlesztés, tervezés, állapotfelmérés és szakvéleményezés, mérnökszolgálat, fővállalkozási tevékenység tervezési, gyártási, kivitelezési és vizsgálati munkák irányítására, atomenergia alkalmazása körében eljáró független műszaki szakértői tevékenység

This annex is only valid in connection with the original certificate number mentioned above.

IQNET Members*:
AENOR Spain **AFNOR Certification** France **APCER** Portugal **CCC** Cyprus **CISQ** Italy **CQC** China **CQM** China **CQS** Czech Republic **Cro Cert** Croatia **DQS Holding GmbH** Germany **EAGLE Certification Group** USA **FCAV** Brazil **FONDONORMA** Venezuela **ICONTEC** Colombia **ICS** Bosnia and Herzegovina **Inspecta Sertifiointi Oy** Finland **INTECO** Costa Rica **IRAM** Argentina **JQA** Japan **KFQ** Korea **LSQA** Uruguay **MIRTEC** Greece **MSZT** Hungary **Nemko AS** Norway **NSAI** Ireland **NYCE-SIGE** México **PCBC** Poland **Quality Austria** Austria **SII** Israel **SIQ** Slovenia **SIRIM QAS International** Malaysia **SQS** Switzerland **SRAC** Romania **TSE** Turkey **YUQS** Serbia

* The list of IQNET Members is valid at the time of issue of this certificate. Updated information is available under www.iqnet-certification.com



AZ MVM PAKSI ATOMERŐMŰ ZRT. IGAZOLJA, HOGY
KÖVETELMÉNYEINEK AZ

ENERGIATUDOMÁNYI KUTATÓKÖZPONT

MINŐSÉGIRÁNYÍTÁSI RENDSZERE

M E G F E L E L.

MINŐSÍTETT TERÜLET:

ABOS 1, 2, 3 biztonsági osztályokba sorolt technológiai rendszerek és rendszerelemek átalakításával, javításával, karbantartásával és üzemeltetésével összefüggően főkonzulensi, tervezői, szakértői, valamint független műszaki szakértői tevékenységek végzése.

A MINŐSÍTÉS ÉRVÉNYESSÉGI IDEJE: 2026.08.31.

A MINŐSÍTÉS SZÁMA: KM 55/2023

EZEN MINŐSÍTŐ LAP A MELLÉKLETTEL EGYÜTT ÉRVÉNYES.

Paks, **2023. augusztus 18.**

PUSKÁS LÁSZLÓ
főosztályvezető

REPOVSZKI GÁBOR
osztályvezető

MVM Paksi Atomerőmű

Certifications by Hungarian Standards Institution, IQNet and MVM Paks NPP

Centre for Energy Research has complied with the requirements of the Hungarian Academy of Sciences, which follow international standards. In 2019, the Hungarian Academy of Sciences thereby authorised the Centre for Energy Research to use the label MTA Centre of Excellence. This certificate was extended annually in 2020, 2021, 2022, 2023 and 2024.

BUDAPEST RESEARCH REACTOR

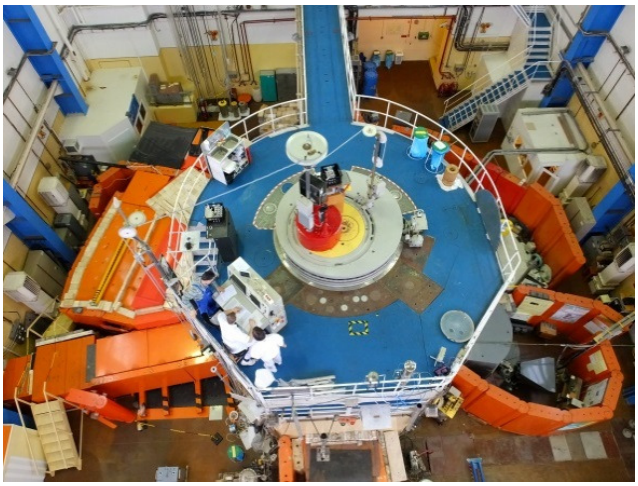
One of Hungary's most important strategic large-scale research facilities is the Budapest Research Reactor (BRR). It serves the needs of an extensive and diverse scientific community by supporting R&D opportunities, helping innovation and providing a strong foundation for training and education.



Renovated building of the Budapest Research Reactor

BRR is a VVR-type reactor that uses light water as moderator and cooling fluid. The power of the reactor is 10 MW provided from low enrichment uranium fuel, and its main purposes – as established during the feasibility/functionality study – are radioisotope production, production of thermal and cold neutron beams for research and applications in many areas of development of material sciences and nuclear physics.

The core is designed to have about 120 reactor days per year, having a time span of 4 days a week. We are committed to long-term safety and responsible operations, taking care of the wastes from the spent fuel coming from the reactor. Besides the temporary spent fuel storage pool, we also operate a long-term spent fuel storage building for the physical and environmental separation between the reactor and the spent fuel storage.



Top view of the research reactor



Layout of the BRR's facilities

The reactor hosts three kinds of activities: research activities utilizing neutron beams, production of radioisotopes for industrial, medical and research purposes, and providing national and international training. We are proud of our innovative flagship research topics, which are carried out by a network of neutron beam stations, including beam lines of thermal neutrons, experiments on powder and residual stress diffractometry, TOF neutron spectroscopy, radiography, biological irradiations, and beam lines of cold neutrons for experiments on small angle neutron scattering, reflectometry, prompt gamma activation analysis and nuclear data measurements. In accordance with recent worldwide trends, we are open to establishing new industrial relations and supporting innovation. The BRR's experimental facilities are open to science based on excellence for researchers from all around the world. We aim to increase our competence on special topics, implement new technologies and develop new materials, to promote and exploit our R&D capacity at the national, regional, as well as international levels. During the past years, BRR hosted several international schools on various technical and research topics, special trainings in the field of reactor physics, reactor operation, nuclear measurement techniques, and safety and environmental issues. Typical research fields are physics, chemistry, material sciences, engineering, life sciences and biotech.

BRR is used by groups of different scientific communities from medical, environmental, material, archaeological, nuclear sciences, and industry, as well as several Hungarian Universities. Neutron beams are uniquely suited to study the structure and dynamics of materials at the atomic level. The Budapest Neutron Centre (BNC) coordinates the scientific utilisation of the research reactor. Some of the main research topics currently are as follows.

- Neutron scattering is used to examine changes in sample properties under different conditions, such as variations in vacuum or pressure, high and low temperature and magnetic field, modelling real-world conditions.
- Using prompt and delayed neutron activation analysis makes it possible to measure the concentration of elements in ppm and ppb levels even for small samples. They decay by gamma-rays characteristic for each element that can be detected by suitable detectors.
- Neutron activation to produce different radioisotopes is widely used in industry and medicine production. For example, Y-90 microspheres to treat liver cancer are produced by bombarding Y-89 with neutrons, which capture them. Radioisotopes are produced for different applications such as medicine, sterilisation and industrial use.
- Testing reactor materials are subjected to intense neutron irradiation, which causes radiation damage to their crystalline structure. For instance, some steels become brittle. Thus, the so-called high-entropy alloys resisting embrittlement are to be used in nuclear reactors instead.
- Applied research using neutron beams produces images of the material interior. Examples are the visualisation of porosities in materials or changes of density inside the sample. Dynamic neutron radiography is capable of visualising motion in materials. Examples are the viewing bubble forming in the cooling system of a refrigerator or the visualisation of fuel burn in the engine system of a car.

BNC provides researchers with 15 neutron instruments; 13 of them are installed directly on the horizontal beam ports of the reactor or on the thermal and cold neutron guides, while the other 2 are placed at the vertical irradiation channels. The instruments are supported by a variety of sample environments, data acquisition hardware, analysis software, and visualisation tools.

BNC provides access to the international neutron user community through a peer-review system. Local scientists assist researchers and industrial users in identifying the most suitable neutron techniques that meet their specific research needs. The various neutron scattering instruments in BNC cater to many users from Europe and have grown in strength over the years. Since the COVID-19 pandemic, BNC also accepts so-called remote users, which means that samples are sent by mail and measurements are performed by instrument scientists without the user's presence. The results are then forwarded to the users via electronic means.

BNC is a member of the League of advanced European Neutron Sources (LENS) and CERIC-ERIC, and a partner in recent EU Framework Programme projects (ReMade@ARI, EVEREST, SECURE, and NEPHEWS).

BNC is strongly committed to the training of professionals from inland and all over the world through the International Atomic Energy Agency. We cooperate with several Hungarian universities (Budapest University of Technology and Economics (BME), Eötvös Loránd University (ELTE), Pannon University, Óbuda University, Moholy-Nagy University of Art and Design, and University of Pécs). BNC accommodates students for laboratory practice for studying nuclear-based techniques. A specialised course was developed for geology students of ELTE to introduce nuclear analytical techniques into their education. BNC organises the Central European Training School on Neutron Scattering biannually. The school provides insight into neutron scattering, element analysis and imaging techniques and their applications to study the structure and dynamics of condensed matter.

Two semesters of lectures and practical sessions were delivered as part of the ELTE Faculty of Science (TTK) PhD program in Earth Sciences under the title *"Nuclear Element Analytical Methods and their Applications in Earth Science and Archaeometry Research I & II,"* in collaboration with the BME Doctoral School of Physics. Additionally, the course *"Advanced Neutron Techniques of Material Characterisation"* was offered at ELTE's Doctoral School of Physics by experts from the Budapest Neutron Centre (BNC). BNC staff also contributed to the *"Advanced Neutron Techniques of Material Characterisation, Historical and Modern Materials Science III, Historical and Contemporary Building Materials III"* course at the Breuer Marcell Doctoral School, University of Pécs. Beyond academic instruction, the Budapest Research Reactor (BRR) actively engages with the public, welcoming local community members, high school students, and university students for regular visits that showcase the exciting possibilities of nuclear science and the cutting-edge research conducted at BRR.

ENVIRONMENTAL PROTECTION SERVICE

Main tasks of the Environmental Protection Service of the Centre for Energy Research (EK) are the radiological environmental and emission monitoring of the KFKI campus, the personal dosimetry, assistance to the radiation protection of workplaces and to maintain the emergency preparedness at the KFKI-campus.



Environmental monitoring station and the two priority installations of the KFKI campus: level "A" isotope laboratories and the Budapest Research Reactor

Our environmental monitoring and radiation protection related activities are conducted according to national legislation, international standards, recommendations of professional organisations and quality management procedures. The emission and environmental monitoring systems cover the radiological facilities' emission points and typical irradiation routes, especially the two priority installations. This concept is practically realised via monitoring of airborne and liquid emissions, environmental dose rates, air activity-concentrations and atmospheric fallout. The environmental samples are analysed by sensitive radioanalytical methods as beta counting, liquid scintillation spectrometry and gamma-spectrometry. Individual dose monitoring is conducted with thermoluminescent gamma- and neutron dosimeters for external doses, while whole body counting is applied for internal monitoring. The environmental and individual dose monitoring systems are continuously improved and developed to fulfil the requirements of international standards, to keep the state-of-the-art and improve reliability.

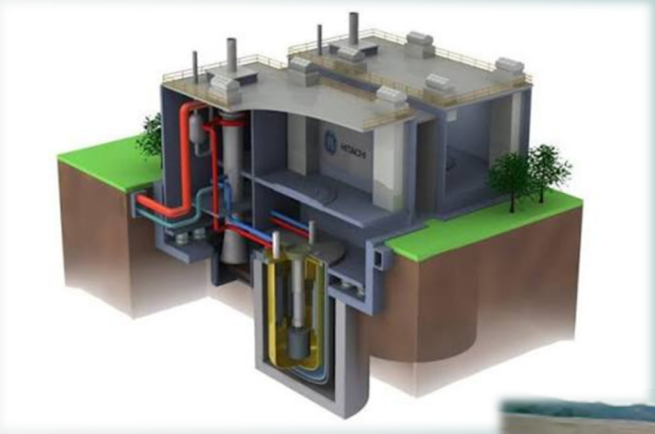




Our whole body counter

The results of emission and environmental monitoring and radiation dose monitoring are reported to the supervising authorities (Hungarian Atomic Energy Authority, National Centre for Public Health and Pharmacy, National Directorate General for Disaster Management) and to the local government of XII. district of Budapest. Annual reports of the Environmental Protection Service is published at the webpage of the institute, while environmental dose rates are accessible on-line. More information is available on the website of the institute.

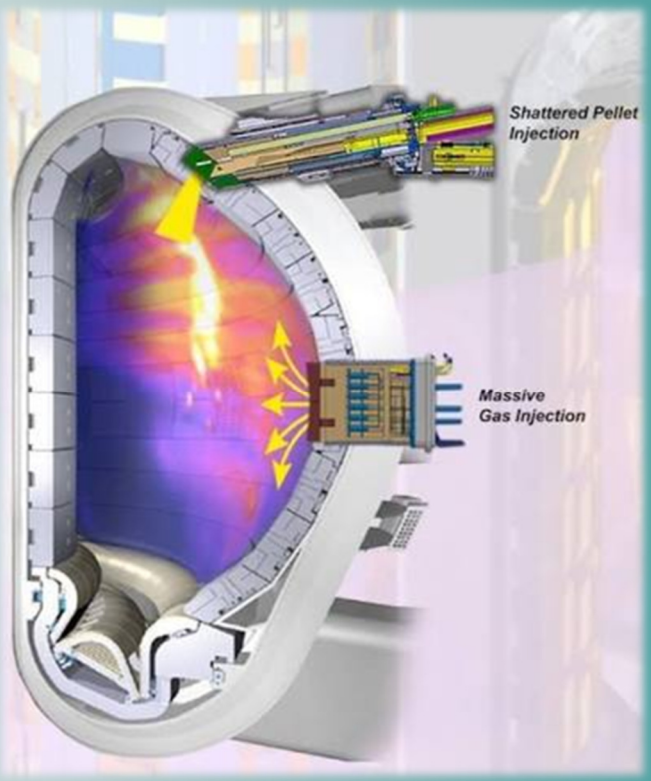
András Kocsonya
Acting Head of Environmental Protection Service
kocsonya.andras@ek.hun-ren.hu





I. RESEARCH ACTIVITIES SUPPORTED BY DOMESTIC AND INTERNATIONAL PUBLIC AGENCIES





OECD NEA THERMAL HYDRAULIC CODE VALIDATION BENCHMARK ACTIVITY FOR HIGH TEMPERATURE GAS-COOLED REACTORS

Gusztáv Mayer, Zsombor Bali

Objective

Accurate modelling of radial heat transfer in a gas-cooled nuclear reactor is an important topic, especially when it is simulated using a one-dimensional thermal hydraulics code. To gain knowledge in this field, HUN-REN EK decided to participate in the Thermal Hydraulic Code Validation for High Temperature Gas-Cooled Reactors (HTGR T/H) benchmark, which is based on measurements conducted on the helium-cooled High Temperature Test Facility (HTTF) built at Oregon State University (OSU). Although the HTTF is a demonstrator of the Modular High Temperature Gas-cooled Reactor (MHTGR) with a relatively low power density in which the heat is mostly transferred via conduction, we believe that the knowledge gained here can be used in Gas-cooled Fast Reactor (GFR) development, such as helium-cooled fast reactor ALLEGRO, where the core power density is more than one order of magnitude higher. Here, we briefly present the benchmark activity of HUN-REN EK in the OECD NEA HTGR T/H benchmark using the CATHARE thermal hydraulics code.

Methods

In this work, a new input deck was developed from scratch to model the dominant heat transfer phenomena in the HTTF core. As part of the OECD benchmark, the simulation results are compared with other codes and measurements.

We used the French CATHARE thermal hydraulics system code for the calculations. The CATHARE 3 v2.1 thermal-hydraulic system code and its graphical user interface GUITHARE were developed by C.E.A., E.D.F., FRAMATOME, and IRSN (cathare-maintenance@cea.fr). The code itself is applicable to a wide variety of nuclear reactors, including Pressurised Water Reactors (PWRs), Boiling Water Reactors (BWRs), and GEN IV reactors (fast reactors), such as sodium- or gas-cooled thermal-hydraulics calculations.

For the gas-cooled calculations in this study, the HIGHXNC fluid and the MONOPHASE directive were selected to model the helium flow in the pipes. In the case of the HTTF benchmark activity, we started the input development from scratch. Since complex, three-dimensional heat transport processes can occur in the ceramic core of the HTTF, our main goal was to capture these three-dimensional phenomena. To do so, we modelled the core with great resolution - 67 hydraulic elements and thermal structures – and established thermal connections between them to capture both the radial and the azimuthal heat transport.

Results

The results [1, 2] showed that when the model is sufficiently detailed, the corresponding temperature profiles are adequately described by the CATHARE code. The model was tested against other participants' models and a measurement, which showed that the current modelling depth is able to give back the temperature distributions within the ceramic test section.

Remaining work

This OECD project finished in 2025. We plan to present our results in a peer-reviewed journal as soon as possible.

Related publications

[1] R. F. Kile, A. S. Epiney, T. Hua, L. Zou, L. Sung Nam, G. Waddington, X. Huang, T. Jafri, F. Pangukir, M. Stempniewicz, F. Roelofs, G. Mayer, & Z. Bali: *Code Benchmark of a Depressurized Conduction Cooldown Transient in the High Temperature Test Facility,* Advances in Thermal Hydraulics - ATH2024. (2024)

[2] T. Hua, L. Zou, R. Kile, A. Epiney, S. N. Lee, T. Jafri, X. Huang, G., Waddington, F. Pangukir, M. Stempniewicz, F. Roelofs, G. Mayer, & Z. Bali: *Benchmarking Low-Power Pressurized Conduction Cooldown Transient in the High Temperature Test Facility* - NURETH21. (2025)

CURRENT STATUS OF THE TREASURE PROJECT

Gusztáv Mayer, Zsombor Bali, Attila Guba, Zalán Csekei, István Panka, Petra Pónya, István Pataki, Dániel Sebestyén, Zoltán István Böröczki, Emese Slonszki, Zoltán Hózer

Objective

Gas-cooled Fast Reactor (GFR) is considered one of the six most promising advanced nuclear reactor technologies. It combines very high core outlet temperatures and the possibility to close the fuel cycle, allowing for very efficient and sustainable electricity and industrial heat production, replacing the burning of fossil fuels. The EC-Euratom-founded TREASURE project presents a Research and Innovation Action aiming at connecting European developers of the GFR demonstrator ALLEGRO (V4G4 Centre of Excellence) with expert organisations having experience in GFR. The project contains several work packages in which HUN-REN EK actively participates. The current goals are: 1. developing a new optimised refractory core, 2. describing the S-ALLEGRO pretest calculations carried out by the CATHARE input deck of HUN-REN EK, 3. developing a strategy for the coupling of the in-house KIKO3DMG neutronics and the French CATHARE3 thermal hydraulics system codes.

Methods

For the optimised refractory core, an updated genetic algorithm was used. For the S-ALLEGRO facility pretest calculations, a previously developed CATHARE input deck of HUN-REN EK was updated, and the simulation results were compared with measured values. A preliminary coupling methodology was proposed for the KIKO3DMG and the CATHARE3 codes using engineering judgement and an AI tool.

Results

A new REFRACTORY_V5 core layout (Figure 1) was proposed and documented in a new TREASURE deliverable. This core serves as a basis for further calculations in the project. The comparison of the natural circulation measurements of S-ALLEGRO and the CATHARE thermal hydraulics calculations showed that there is a significant bypass through the flanges in the real measurements. For this reason, further measures were taken to decrease the leakage in the test facility. Concerning the KIKO3DMG and CATHARE3 coupling, a new promising methodology was proposed.

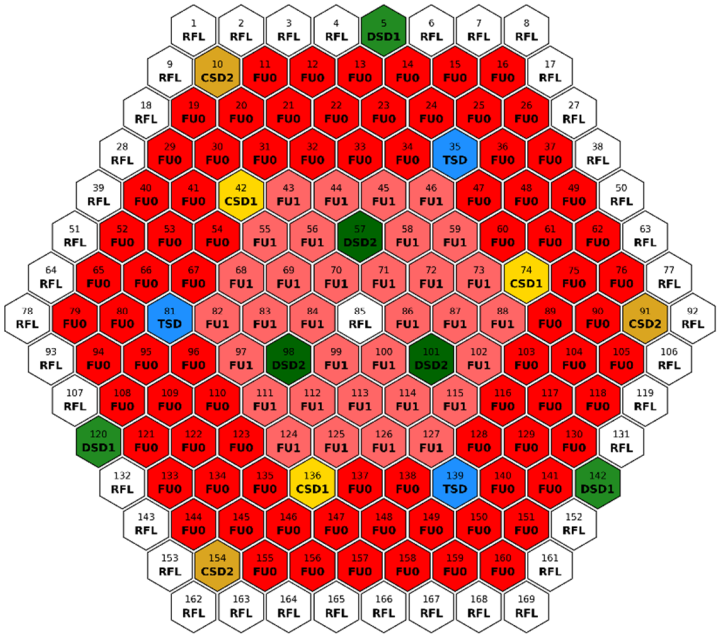


Figure 1: The REFRACTORY_V5 core layout. RFL – Reflector, CSD1 – Control and Shutdown Device 1, CSD2 – Control and Shutdown Device 2, FU0 – Fuel assembly, FU1 – Fuel assembly with 90% PU content of FU0, DSD1 – Diverse Shutdown Device 1, DSD2 – Diverse Shutdown Device 2. TSD – Third Shutdown Device.

Remaining work

This project continues in the following years, and it finishes in 2028. In parallel with the above-mentioned topics, new tasks have to be elaborated, for instance, building a new CATHARE input for the new ALLEGRO with thermal coupling.

RESEARCH ON MATERIAL AGEING AND STRUCTURAL INTEGRITY OF RESEARCH REACTORS

Ildikó Szenthe, Dávid Cinger, Ferenc Gillemot

Objective

Many of the existing Research Reactors in Europe are very old, having been operated for more than 60 years. Only a few initiatives have been taken to partially replace this capacity. Continued operation of these Research Reactors is mandatory to maintain European excellence in the development and qualification of nuclear materials for advanced reactor concepts and to maintain the supply of medical isotopes. License extensions require ageing management review and time-limited ageing analysis of critical structures and components. However, there is limited understanding of damage mechanisms and a lack of materials data on Research Reactors' materials at relevant operating conditions for Long-Term Operation (LTO). In addition, there is a shortage of surveillance specimens for extending the operational life. Lastly, sharing of knowledge and operational experience is crucial in this relatively small research reactors' community.

Methods

The Magic-RR project (2024-2028) is a four-year Euratom initiative that unites 11 expert partners from across the world. The project addresses the aforementioned issues by leveraging available archive materials and data from the existing research reactors, e.g. from surveillance programs and shut-down reactors, operational experience of research reactor operators and advanced characterisation and modelling techniques at universities and nuclear research centres. To achieve this goal, Magic-RR focuses on the following topics in order to support the safe long-term operation of European Research Reactors:

- Improved understanding of irradiation-induced damage in RR materials at high fluence conditions,
- Investigation of corrosion mechanisms and their prevention/mitigation,
- Assessment of sub-size testing for surveillance programs,
- Sharing knowledge on reactor operation and providing guidelines on best practices,
- Structural integrity assessment of critical components of RRs to support safe LTO.

HUN-REN EK leads the whole project as coordinator, performs supervision of deliverables and milestones, risk analysis and management plan, and continuous monitoring of the partner's scientific achievements.

Results

HUN-REN EK developed the test matrix for the mechanical tests of the project. It harvested materials from the shut-down Budapest reactor operated from 1957 to 1986. A list of the irradiated materials and an overview of their service history have been prepared. Samples for mechanical tests were machined, and tests have been started. HUN-REN EK has installed a lathe machine for the manufacturing of round specimens in the hot cell. As experimental validation of sub-size specimens for surveillance programs, HUN-REN EK developed a pre-cracking procedure for compact tension specimens in an unirradiated 5052 aluminium alloy and performed the first tests with these specimens. In parallel, the methodology to determine fracture properties using notched tensile specimens is also being developed.

HUN-REN EK leads the work package of „Ageing Management and Structural Integrity of Research Reactors". In support of enhancing the ageing management of existing research reactors to aid their continued safe operation, a questionnaire was developed by HUN-REN EK to gather information from research reactor operators regarding current practices in ageing management and structural integrity. The questions covered the topics of the periodic safety inspection, periodic safety review, and their frequency, consideration of the ageing effects of thermal and fast neutrons' fatigue and corrosion, especially the irradiation-assisted stress corrosion, embrittlement of welds, applied mitigation methods, ageing management, and corrective actions. The questionnaire findings indicate that although ageing management strategies vary based on reactor power and design, there is a universal move toward systematic Periodic Safety Reviews and the integration of international safety standards. Furthermore, the report highlights "good practices" in transitioning from monitoring to active design improvements, ensuring the continued safe and sustainable operation of research reactors within the global nuclear community.

Remaining work

The work will be continued in the next years as it is described in the Grant Agreement.

Related publications

[1] F. Gillemot, M. Kolluri, I. Szenthe, F. Naziris, L Berzy: *Review of Radiation Embrittlement of Aluminum Alloys used in Research Reactors,* Materials **18:(22),** 5236 (2025) https://doi.org/10.3390/ma18225236

OECD NEA WORKING GROUP ON FUEL SAFETY WATER COOLED SMALL MODULAR REACTOR FUEL DESIGN AND SAFETY EVALUATION

Márton Király

Objective

The OECD/NEA Working Group on Fuel Safety (WGFS) launched a dedicated activity to assess the design and safety evaluation of fuels for Water-Cooled Small Modular Reactors (WC-SMRs). Building on the 2023 NEA Technical Opinion Paper that identified SMR fuel safety as a cross-cutting priority, the initiative seeks to provide a coherent, technically grounded overview of WC-SMR fuel concepts and their safety implications. Its central goal is to review how existing Light-Water-Reactor (LWR) fuel design criteria and analytical methods apply to SMRs expected to reach licensing and operation before 2030. The project analyses selected high-TRL (Technology Readiness Level) designs—such as NuScale VOYGR, BWRX-300, Rolls-Royce SMR, NUWARD, SMART, and SMR-160—examining expected fuel performance (cycle length, burnup, boron-free or load-following operation) and the safety-relevant phenomena that could emerge under normal and accident conditions. By comparing these features with the established LWR knowledge base, the activity aims to determine whether current safety criteria, evaluation codes, and validation approaches are sufficient for modular reactors or require adaptation.

Methods

The work proceeds through a structured review process coordinated by Tractebel (ENGIE) under NEA/WGFS supervision and supported by nineteen organisations from eleven countries. The methodology combines literature review, expert assessment, and data collection through an international questionnaire distributed in 2025 to task group members, regulators, and selected SMR designers and vendors. The questionnaire, organised into four parts, gathers information on organisational roles, fuel design and operation, accident scenarios and fuel phenomena, and applies analytical tools and methods. It also asks respondents to identify critical safety criteria, validation needs for the model, and open technical issues. Initial responses, though limited by confidentiality constraints, provided insight into a subset of designs—mainly NuScale, BWRX-300, Rolls-Royce SMR, SMART, iSMR, LDR-50, and CAL-30. Analysis of these inputs and other open-source data confirmed that WC-SMRs generally rely on proven LWR-type fuels but may encounter distinct challenges linked to modularity, passive systems, boron-free control, and flexible operation. The task group, therefore, focuses on understanding whether these features alter established failure mechanisms such as pellet-cladding interaction, corrosion-induced embrittlement, or high-temperature deformation, and how existing fuel performance codes capture these effects. The findings to date suggest that while LWR experience provides a strong foundation, verification and validation gaps remain for SMR-specific transients such as long-term natural-circulation cooling or repeated power-cycling operations.

Remaining work

Given the partial response to the data request and the proprietary nature of detailed design information, the WGFS task group decided to adjust its scope. Instead of a full NEA status report, it may produce a Committee on the Safety of Nuclear Installations (CSNI) Technical Opinion Paper or two focused working papers concentrating on the applicability of current fuel design and safety criteria to WC-SMRs, and on good practices and gaps in safety evaluation. The questionnaire will be reissued with a narrower focus on high-TRL designs and cooperating vendors, with an extended deadline into late 2025. Subsequent meetings will refine the structure of the final report, validate findings, and prepare coordinated recommendations. The project's milestones foresee draft reports in 2026 and final deliverables for CSNI approval by the end of 2027. Through this process, the WGFS aims to strengthen the scientific basis for SMR fuel safety, support regulatory harmonisation, and provide clear guidance for future joint research and benchmarking on modular reactor fuels.

DEVELOPMENT OF THE COMBINED EFFECT OF PRE-TREATMENT AND RADIATION ON MECHANICAL PROPERTIES OF CLADDING MATERIALS PROPOSAL FOR FIDES-II

Ildikó Szenthe, Ferenc Gillemot, Márta Horváth, Dávid Cinger, Erzsébet Perez-Feró, Tamás Novotny, András Ványi, Zoltán Hózer

Objective

The current activities within the OECD NEA Second Framework for Irradiation Experiments (FIDES-II) will be completed by the end of 2026, after which new proposals for irradiation experiments will be reviewed. Considering the capabilities of the Budapest Research Reactor, HUN-REN EK, concerning the irradiation of pre-treated zirconium cladding samples developed a proposal.

Methods

The development of the CEPROMAC (Combined Effect of Pre-treatment and Radiation on Mechanical Properties of Cladding Materials) proposal was based on the previous irradiation experience of HUN-REN EK experts gained in several research programmes involving Zr cladding materials.

Results

The formal CEPROMAC proposal was submitted to the FIDES-II Technical Advisory Group, and detailed presentations were given during its two meetings. The feedback from the meetings was incorporated into the updated proposal. The main Empty cladding tube samples will be pre-treated in high-temperature furnaces under well-defined conditions to produce a wide range of material states with respect to oxidation, hydrogen uptake, and thermal treatment.

A set of pre-treated rings from various manufacturers will be irradiated in the BAGIRA loop of the Budapest Research Reactor up to 0.7 dpa (displacements per atom). Currently, two sets of irradiated and reference traditional and sponge-based E110 cladding samples are available; these will be used first for mechanical testing and Post-Irradiation Examination (PIE). The selection of further materials will be discussed with FIDES-II partners.

Mechanical testing and material structure investigations will be performed on all samples. A comprehensive database will be created from the measurement results, enabling further development and validation of numerical models for predicting power-plant processes. This will support more accurate descriptions of the phenomena occurring in the reactor and in storage facilities.

A database will be compiled from measurement results to support the further development and validation of numerical models for predicting power-plant processes and to facilitate a more accurate representation of the phenomena occurring in the reactor and in storage facilities.

Remaining work

If the proposal is accepted, the pre-treatments, irradiation and post-test examination program must be carried out.

Related publication

[1] I. Szenthe: *Combined Effect of Pre-treatment and Radiation on Mechanical Properties of Cladding Materials*, FIDES-II/CEPROMAC JEEP Proposal, September 2025.

PRE-TEST AND POST-TEST SIMULATIONS OF RIA AND LOCA EXPERIMENTS IN THE HERA AND LOC-HBU PROJECTS

András SzabolcsVányi, Dorina Szili, Bence Várszegi

Objective

The OECD NEA Second Framework for Irradiation Experiments (FIDES-II) is an international consortium of nuclear research institutes, fuel vendors and utilities. The project was established in 2019 to address the lack of irradiation facilities after the closure of the Halden Reactor. In FIDES-II, several Joint Experimental Projects (JEEPs) run in parallel, and they usually also include Modelling and Simulation (M&S) activities that support and leverage the experimental work performed. HUN-REN EK is part of the FIDES-II framework since its establishment and is closely involved in the M&S activities of the HERA (High Burnup Experiment in Reactivity Initiated Accident) and LOC-HBu (Loss-of-Coolant High Burnup) JEEPs. In HERA, pre-test and post-test benchmark calculations have already been carried out for pre-hydrided rodlets. This year, the post-test calculations were repeated with more detailed experimental descriptions available and pre-test calculations for high-burnup rodlets were performed based on the limited data available. The M&S exercise of LOC-HBu was based on the LOC-C-4 fresh fuel commissioning test and included five exclusively fuel performance cases (Cases 2-5) and one exercise (Case 1), in which thermal-hydraulics codes were utilised to compute the boundary conditions for the fuel calculations.

Methods

The simulations in both projects were carried out using the FRAPTRAN-2.0 transient fuel behaviour code (Pacific Northwest National Laboratory, USA).

Results

The post-test simulation of the four pre-hydrided High Burnup Experiment in Reactivity Initiated Accident (HERA RIA) cases was repeatedly simulated using the new data available and was compared to the measurements and to the calculation results of the other partners as well. The overall results were consistent with the measurements and were among the best-performing calculations in the group (Fig. 1). The high-burnup RIA calculations yielded reasonable results; however, no comparison could be made due to the lack of experimental data and calculation results of other partners. Similar to the pre-hydrided RIA cases, the LOC-HBu calculation results were consistent with the measurements and yielded similar results to the better-performing simulations of the benchmark group (see Fig. 1).

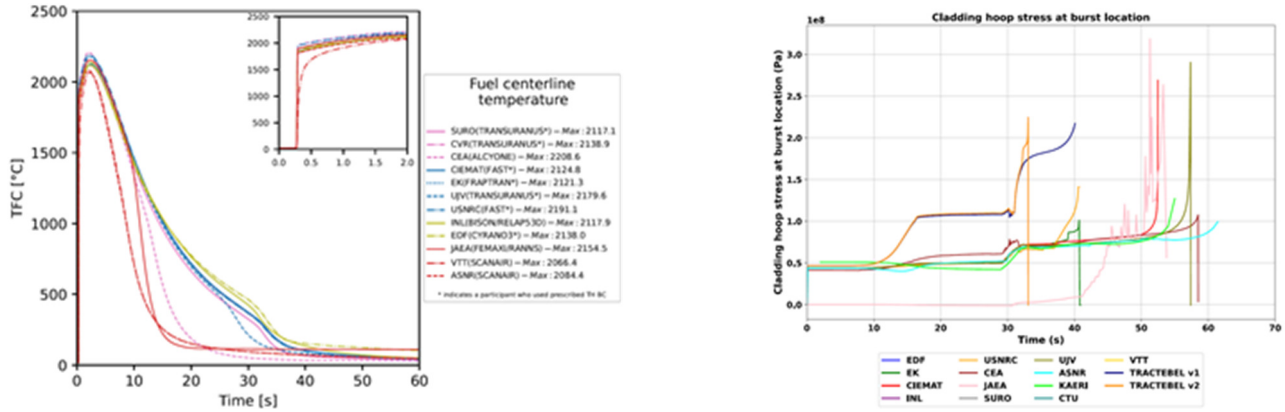


Figure 1: Calculated centreline fuel temperatures for the first pre-hydrided HERA sample (left) and simulated cladding hoop stress results for Case 5 of the LOC-HBu M&S exercise (right)

Remaining work

The high-burnup RIA simulations will be repeated when a more detailed description and the corresponding data become available.

Related publications

[1] A. Sz. Ványi: *Post-test calculations of RIA experiments on pre-hydrided rodlets*, Research on Westinghouse fuel elements by participation in the FIDES HERA M&S activities, EK-FRL-2024-705-01-02-M1, in Hungarian (2025)

[2] D. Szili, B. Várszegi, A. Sz. Ványi: *Pre-test calculations of RIA experiments on high-burnup rodlets using the FUROM and FRAPTRAN codes*, Research on Westinghouse fuel elements by participation in the FIDES HERA M&S activities, EK-FRL-2025-705-01-01-M0, in Hungarian (2025)

OPTIMISATION OF ENGINEERED BARRIER SYSTEMS FOR RADIOACTIVE WASTE STORAGE

Margit Fábián, János Osán, István Tolnai

Objective

In Europe, the final disposal of high-level radioactive waste is planned in deep geological repositories. Their long-term safety is ensured by natural and engineered barriers that prevent radionuclides from entering the biosphere.

EURAD-2 project implements a joint strategic program of research, development and knowledge management activities at the European level, bringing together and complementing EU Member States programs in order to ensure cutting edge knowledge creation and preservation in view of delivering safe, responsible and publicly acceptable solutions for the management of radioactive waste throughout all program phases (from "cradle to grave") across Europe now and in the future. The main goals are:

- To support Member States in developing and implementing their national R&D programs for the safe long-term management of their full range of different types of radioactive waste through participation in the Radioactive Waste Management (RWM) Joint Programme; Develop and consolidate existing knowledge for the safe start of operation of the first geological disposal facilities for spent fuel, high-level waste, and other long-lived radioactive waste, and support optimisation linked with the stepwise implementation of geological disposal facilities;
- Building on the achievements of EURAD-1, maintain a knowledge management system that enhances the transfer of knowledge between organisations, Member States and generations.

HUN-REN EK Environmental Physics Department participates in three work packages ANCHORS: Hydraulic- mechanical-chemical evolution of bentonite for barrier optimisation, SUDOKU: Near-surface disposal optimisation based on knowledge and understanding and RAMPEC: Radionuclide mobility under perturbed conditions.

In addition, conditioning of radioactive waste using vitrification was studied through structural analysis of a candidate borosilicate glass matrix.

Methods

The SUDOKU work package is dedicated to studying the chemo-mechanical evolution of reinforced and unreinforced cementitious barriers and their effects on the migration of mobile radionuclides. Microstructural, mechanical and chemical characterisation was performed for mortars prepared from two types of cementitious materials (CEM II/B 42.5N and CEM II/B 42.5R). Degradation parameters were calculated as a function of leaching rates. The chemical durability of the system was predicted through leaching tests with ICP-OES and Ion Chromatography (IC) analyses of the liquid phase. Post-mortem characterisation of the solid phase was performed using X-Ray Diffraction (XRD) (D8 Discover, Bruker AXS) operating with a 1 mm x 12 mm Cu Kα X-ray beam. Compressive strength tests were performed before and after leaching (with MQ-water and Synthetic Porewater (SPW)), applying MSZ EN 196-1:2016 protocol.

In the framework of the RAMPEC work package, radionuclide mobility is studied at elevated temperatures and under chemical perturbations such as alkaline conditions or higher sulphate/nitrate concentrations. Sorption isotherms (concentration dependence of sorption at a fixed temperature) for Ni^{2+} and SeO_3^{2-} ions were measured using batch experiments in the concentration range of 10^{-6} M to 3×10^-3 M. Crushed albitic claystone samples (<63 μm) of Boda Claystone Formation (BCF) were suspended in SPW and kept shaken for 10 days at different temperatures (25 °C and 40 °C). The liquid phases were analysed by means of ICP-OES.

Structural characterisation of uranium- and lanthanide-loaded borosilicate glass matrix was performed. This study focuses on the structural integrity and chemical durability of borosilicate glass matrices doped with varying concentrations (30–40 wt%) of uranium and lanthanide oxides (UO_3, CeO_2, Nd_2O_3, Eu_2O_3). Using a multianalytical approach—including X-ray Absorption Spectroscopy (XAS), neutron diffraction with Reverse Monte Carlo (RMC) simulations, and X-ray Photoelectron Spectroscopy (XPS) —the study characterises the local atomic environments critical for High-Level nuclear Waste (HLW) immobilisation.

Results

The compressive strength test results of the cementitious samples before and after leaching (Fig. 1) showed that the sample prepared from CEM 42.5R cement matrix has the highest compressive strength value of 11.4 N/mm² before leaching. The results showed a decrease in compressive strength after leaching in both solutions, but in the case of SPW treatment, the samples are more durable than after MQ treatment.

Mineral phases characteristic of cementitious materials can be identified, such as portlandite, calcite, dolomite and carbonate hydrates, both immediately after curing and in samples after being in contact with the two types of leaching liquids (Table 1). The high quartz content is due to the sand added according to the recipe of the mortar.

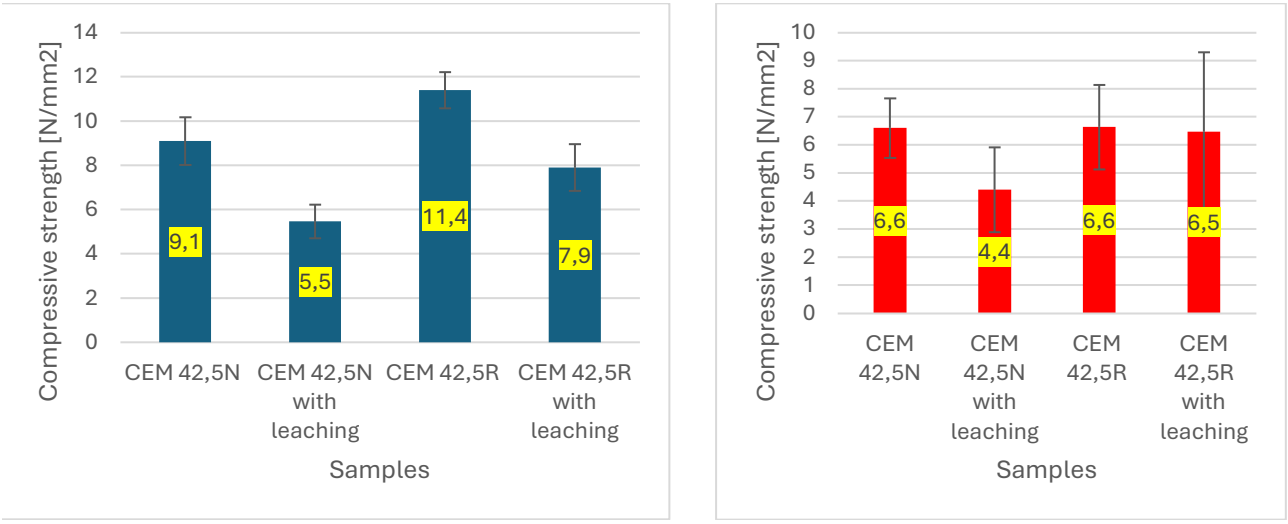


Figure 1: Compressive strength test for CEM II/B 42.5N and CEM II/B 42.5R samples, before and after leaching test, leaching test with MQ-water (left) and with SPW (right)

Table 1: Results of XRD phase analysis of the cementitious materials after curing time and after leaching tests (MQ–water and SPW)

Phase	CEM II/B 42.5N	CEM II/B 42.5N leaching MQ	CEM II/B 42.5N leaching SPW	CEM II/B 42.5R	CEM II/B 42.5R leaching MQ	CEM II/B 42.5R leaching SPW	average
Quartz	**67.4**	**58.9**	**68.2**	**65**	**66.4**	**55.6**	63 ±10
Portlandite	**3.1**	**1.7**	**2.1**	**4.2**	**4.3**	**0.7**	3.5 ±1.5
Clinochlore	2.6	1.6	0	0	2.7	5.4	2.2 ±1
Ettringite	0	9.8	0	6.8	0	9.8	7 ±3
Hatrurite	4.6	0	2.3	1.6	0	2.9	2 ±1
Calcite	**3.9**	**4.1**	**10.5**	**6**	**8.6**	**15.7**	6 ±3
Muscovite	4.4	0	0	0	0	0	2 ±1
CaAlOH Carbonate Hydrate	2.4	0	0	0	1.4	0	2 ±1
Dolomite	**2.9**	**3.9**	**4.1**	**6.2**	**8.2**	**3.5**	5 ±2
Anorthite	**8.7**	**20**	**12.7**	**10.2**	**8.4**	**12.7**	10 ±3

The sorption isotherms for BCF of Ni^{2+} and SeO_3^{2-} recorded at different temperatures are presented in Fig. 2. In general, cations (Ni^{2+}) exhibit an order of magnitude stronger sorption than oxyanions (SeO_3^{2-}). For Ni^{2+}, a significant increase was observed in the sorption with increased temperature, while the sorption of SeO_3^{2-} did not show a clear temperature dependence.

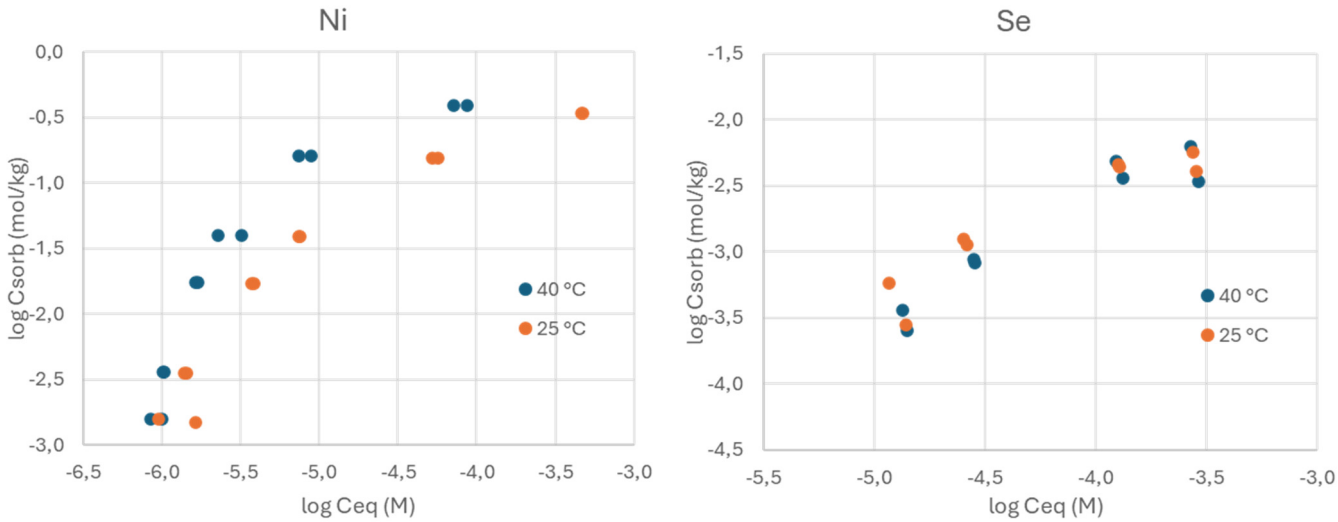


Figure 2: Comparison of sorption isotherms of Ni^{2+} (left) and SeO_3^{2-} (right) for BCF albitic claystone measured at 25 °C and 40 °C. Sorbed amount in the solid phase is plotted against equilibrium concentration of the liquid phases after 7 days contact time.

The glass framework remains robust, primarily composed of SiO_4 tetrahedra and mixed BO_3/BO_4 units. A key finding is the role of dopants as structural modifiers: while uranium acts as an intermediate, decreasing four-coordinated boron, lanthanides promote the isomerisation of BO_3 to BO_4, reducing non-bridging oxygens and stabilising the network. Spectroscopic analysis of the U L_{III}-edge reveals a mixture of U^{VI} (as uranyl units) and U^{V} (octahedral), with no U^{IV} detected. Lanthanides largely maintained stable oxidation states Nd^{III}, Eu^{III}, though cerium exhibited a notable Ce^{IV} fraction (up to 12.3%) in complex mixtures. Durability and leaching tests and product consistency tests in SPW highlighted a correlation between composition and stability. Despite containing the highest waste loading (40 wt%), the glass sample containing U, Ce, Nd, and Eu together (Matrix-UCeNdEu (MUCNE)) demonstrated superior structural stability. In contrast, the glass sample containing U and Nd exhibited the highest dissolution rates of Si, B, and Na, indicating a comparatively weaker matrix. The research confirms that these borosilicate matrices can incorporate high actinide and lanthanide concentrations without significant structural degradation. The synergistic effect of mixed lanthanides in the composition MUCNE suggests that higher waste loading does not inherently compromise durability, supporting its viability for long-term geological disposal.

Remaining work

This is the first year of a five-year project; we continue the well-prepared schedule.

Related publications

[1] I. Tolnai, J. Osan, P. Jovari, F. Pinakidou, A. Sulyok, M. Fabian: *Structural characterization of uranium and lanthanide loaded borosilicate glass matrix*, Scientific Reports **15:** 28352 (2025) https://doi.org/10.1038/s41598-025-13166-1

[2] J. Osán, I. Tolnai, M. Fábián: *Transition metal sorption on bentonite and behaviour of the bentonite/copper/glass barrier system*, FISA-EURADWASTE-2025 Conference, 12-16 May 2025, Warsaw, Poland

[3] J. Osán, B. Börcsök, M. Fábián, I. Tolnai: *TXRF analysis for elemental composition and metal uptake of clays for radioactive waste repository,* TXRF-2025 Conference, 9-12 September 2025, Kielce, Poland

SIMULATION OF PELLET-CLADDING MECHANICAL INTERACTION WITH ACCIDENT TOLERANT FUEL CLADDINGS

Hamidreza Yousefi, Márton Király, Zoltán Hózer, Nóra Vér, Tamás Novotny, Erzsébet Perez-Feró, Márta Horváth, Levente Tatár, Paul Van Uffelen

Objective

Within the OFFERR collaboration, we examined Pellet–Cladding Mechanical Interaction (PCMI) in Accident Tolerant Fuel (ATF) concepts by quantifying the deformation capacity and damage mechanisms of chromium-coated versus uncoated zirconium claddings in segmented mandrel tests, and by assessing how well current simulation tools reproduce the observed response.

Methods

Twenty-five segmented mandrel tests were performed at room temperature and 300 °C. Post-test profilometry, SEM and metallography were used to map deformation and characterise coating cracking and interface integrity. Selected specimens were oxidised in steam at 1000 °C for 1800 s to evaluate how pre-existing cracks influence oxidation. Modelling combined 3D finite-element simulations (Fig. 1) in HEXAGON Marc/Mentat 2022.2 (contact and plasticity) with sequential code coupling to TRANSURANUS using FEM-derived pressure histories. Material inputs were calibrated on uncoated E110G via strain-hardening functions; TRANSURANUS was additionally exercised with an explicit 10 µm Cr coating zone. A complementary gas-expansion model applied strain-based failure criteria to estimate coating fracture thresholds.

Results

Coated and uncoated tubes exhibited a consistent average radial displacement of ≈5% under controlled loading, and all samples remained macroscopically intact to this deformation level (above diameter changes expected in normal operation). Maximum force showed notable scatter, attributed mainly to test uncertainties (e.g., local friction variations and segment misalignment). Coating cracking was, however, widespread: Cr-coated optimised ZIRLO showed sparse, narrow axial cracks; Cr-coated Zr-1%Nb developed wider cracks with limited propagation; and CrN/Cr-based coatings formed dense, branched crack networks with occasional tangential separations and local chipping. Despite cracking, no macroscopic delamination was observed, indicating strong adhesion. Steam oxidation produced localised under-coating attack primarily at crack sites; porous zones formed where ZrN (from CrN intermixing) transformed to ZrO_2, promoting oxygen ingress and α-Zr(O) intrusions, while Cr_2O_3 formation on the coating surface provided a protective barrier consistent with Ellingham-diagram expectations. One specimen (OPZCR-48) failed along an axial crack, showing ductile substrate fracture but brittle, plate-like cracking in the Cr layer, suggesting a grain-boundary-controlled coating failure mode. Profilometry indicated asymmetric deformation consistent with bending effects. Finite Element Method (FEM) captured contact and bulging trends and required revised hardening inputs to match ≈5% tangential plastic strain; TRANSURANUS fuel performance code reproduced azimuthally averaged stress/strain changes but could not capture localised coating fracture, underscoring the need for multidimensional, irradiation-informed material models and improved experimental uncertainty control.

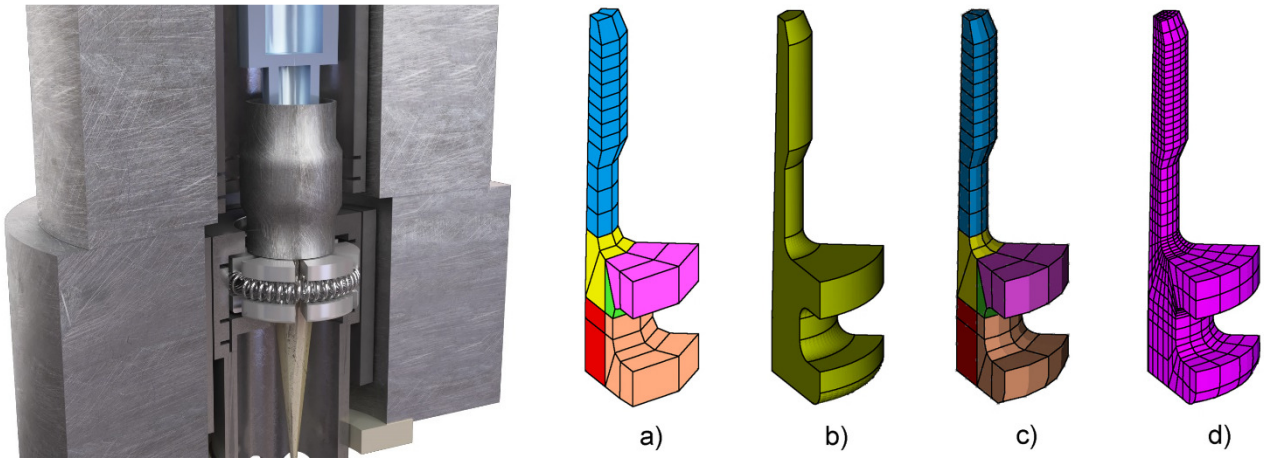


Figure 1: The cross-section of the modelled mandrel test (left) and the 3D mesh of the mandrel segment generated for the FEM (right)

Remaining work

The research revealed interesting phenomena that will be investigated further in the upcoming ACCORD project.

FUSION RESEARCH AND DEVELOPMENT IN THE EUROFUSION PROGRAM

Sándor Zoletnik

Objective

A coordinated research program is being conducted in the European Union for the development of nuclear fusion energy production. It is managed by the Eurofusion consortium, which includes participants from each Member State. From Hungary, the HUN-REN Centre for Energy Research is the member of Eurofusion, and the Budapest University of Technology and Economics participates with some contributions as an "Affiliated Entity". The Eurofusion work program comprises two main elements: plasma physics research on existing magnetic fusion experiments, development of the EU Demonstration Fusion Power Plant (DEMO) conceptual design, and related technology development.

Methods

In 2025, the Fusion Plasma Physics Department (FPL) staff participated in measurements on the Wendelstein 7-X stellarator (Greifswald, Germany) by operating the overview video camera system and the alkali beam diagnostic. On the MAST Upgrade tokamak (Culham, UK), the Beam Emission Spectroscopy (BES) diagnostic was operated for the measurement of plasma turbulence and waves. Synthetic diagnostic development complements the diagnostic and experimental work.

Work continued on the design of the DONES (DEMO Oriented NEutron Source) irradiation facility involving engineers of FPL. The Fusion Technology Department (FTL) contributes to the DEMO design work by studying and testing methods for in-situ joining of cooling pipes. In FPL, the engineering design work for the remote maintenance machine of the European DEMO fusion device has been concluded.

A strong program started in 2024 within the Eurofusion Tritium and Fuelling work package to develop cryogenic pellet technology for magnetic fusion devices. A test cryostat was installed and commissioned in 2025. Pellet-plasma interaction calculations started using the HPI2 code for the COMPASS Upgrade tokamak, which is being built in Prague. This code is now regularly used at FPL and gives the possibility to model injection scenarios for other tokamaks as well. In support of cryogenic pellet technology development, various basic cryogenics experiments were designed and performed: a measurement method for the heat conduction of solid gases, parahydrogen production and hydrogen desublimation studies.

Results

On Wendelstein 7-X, the video diagnostic was specifically used by the FPL team for estimating the plasma size [1]. Both the video and alkali beam system are basic diagnostics on the stellarator for providing plasma shape, edge plasma density profile and turbulence data. These diagnostics provide a service for the Wendelstein 7-X team and are used in many publications by other team members. Due to a vacuum leak, the BES diagnostic on MAST Upgrade had to stop operation during the campaign. The evaluation of the large amount of experimental data is ongoing [2].

In the DONES design project, the Target System and Lithium System designs were completed, and systems engineering design was progressed [3-5]. At the end of the year, this activity was finished in Eurofusion. The detailed design and construction of DONES will be done by a new international legal entity, which Hungary did not join. The pre-conceptual engineering design of the DEMO remote handling concept was finished [6]. The DEMO engineering design is not continued by FPL as the laboratory focuses on other fields.

Deuterium ice extrusion was demonstrated in 2025 in the FPL laboratory. The extrusion speed is currently limited by the available cooling power (1.8 W@5K) of the Sumitomo cryocooler device. Information was collected on a newly developed Chinese cryocooler with 4.4 W@5K cooling power. After discussions with the supplier, it was ordered and has arrived at the laboratory. Additionally to the extruder, a pellet cutter has also been developed and tried. Although pellet cutting was demonstrated, the driver of the device broke after some operation. A higher-power linear motor was ordered for it. Another tritium-compatible pellet cutter built in the previous year was tested in a vacuum up to 15 Hz operation frequency. In the supporting cryogenic experiments, parahydrogen was prepared using a special catalyst. Hydrogen desublimation measurements were compared with room temperature and with increased parahydrogen concentration. The theoretical expectation of faster desublimation was confirmed, which provides an excellent basis for faster cryogenic pellet formation.

The effect of fuelling pellet injection geometry was studied in detail for the COMPASS Upgrade tokamak. An ideal location was found at the top of the machine. This injection line is now in the machine engineering design.

Synthetic diagnostic methods [8] and Machine Learning techniques were developed for fast processing of synthetic diagnostic data for ITER and ASDEX Upgrade. The latter became part of the Integrated Data Evaluation framework.

Eurofusion developed a joint Research Plan [9] with the Institute for Plasma Physics of the Chinese Academy of Sciences for the BEST tokamak, under construction in Hefei, China. The diagnostic section was written by S. Zoletnik from FPL in collaboration with Chinese colleagues. He also chairs the Diagnostics Topical Group of the International Tokamak Physics Activity, an organisation of the international ITER project.

Remaining work

2025 was the last year of the 5-year Euratom work program, and an extension for 2026-27 is being agreed on with the European Commission. This will include a measurement campaign on the Wendelstein 7-X stellarator and the JT-60SA European-Japanese tokamak, where researchers from EK play a significant role. Also, participation in the next MAST-Upgrade campaign is planned after the repair of the vacuum leak.

The cryogenic fuelling pellet experiments will continue with the new cryocooler device. Testing of the tritium-compatible pellet cutter will be demonstrated using deuterium and possibly hydrogen ice. We also plan to assemble a full test cryogenic fuelling pellet injector using the extruder, pellet cutter and a small centrifuge accelerator developed for solid-state pellets a decade ago. Such an experiment will demonstrate the unique capabilities of the research team.

Collaboration on the Chinese BEST device is expected to intensify in 2026, as the first plasma is expected at the end of 2027.

Related publications

This brief list of publications contains only some key journal publications with lead authors from our team. A large number of conference publications and publications where our staff is a co-author were not listed due to the limited space.

[1] A. Buzás, C. Biedermann, G. Cseh, G. Kocsis, M. Krause, T. Szepesi, M. Szűcs, The W7X Team: *Estimating plasma size by visible emission patterns in the Wendelstein 7-X stellarator*, Fusion Engineering and Design **220,** 115304 (2025) https://doi.org/10.1016/j.fusengdes.2025.115304

[2] P. Balazs, O. Asztalos, M. S. Fonyi, S. Thomas, D. Dunai, G. I. Pokol, MAST-U Team: *Assessment of magnetic smearing effects for the MAST-U beam emission spectroscopy system*, Fusion Engineering and Design **216,** 115075 (2025) https://doi.org/10.1016/j.fusengdes.2025.115075

[3] A. Zsákai, M. García, A. Díez, A. Moreno, D. Sánchez-Herranz, A. Ibarra, D. Jiménez: *Leveraging Systems Engineering in IFMIF-DONES*, (invited talk on SOFE 2025, Cambridge, USA)

[4] D. Oravecz, A. Zsákai, R.L. Csiszár, D. Ferenczy, T. Dézsi, F.S. Nitti, J. Maestre, D. Bernardi, A. Ibarra: *Advancements in the IFMIF-DONES target system for fusion materials irradiation,* Fusion Engineering and Design **219,** 115288 (2025) https://doi.org/10.1016/j.fusengdes.2025.115288

[5] D. Ferenczy, A. Zsákai, T. Dézsi, D. Oravecz, F.S. Nitti, J. Maestre, A. Ibarra: *Upgrade design and analysis of the quench tank of the IFMIF-DONES lithium target system,* Fusion Engineering and Design **217,** 115175 (2025) https://doi.org/10.1016/j.fusengdes.2025.115288

[6] L. Poszovecz, B. Longauer, A. Sinha, I. Chiang*: Pre-conceptual design study of remote handling compatible attachment mechanisms for in-vessel components in DEMO tokamak*, Fusion Engineering and Design **215,** 115019 (2025) https://doi.org/10.1016/j.fusengdes.2025.115019

[7] M. Málics, R. Csiszár, G. Z. Kerényi: *The development of a small continuous flow parahydrogen catalyst for cryogenic pellet experiments*, (invited talk on SOFE 2025, Cambridge, USA), Fusion Engineering and Design **216,** 115015 (2025) https://doi.org/10.1016/j.fusengdes.2025.115015

[8] B. Molnár, M. L. Sebestyén, D. I. Réfy, J. Krbec, P. Hacek, S. Zoletnik, COMPASS Team: *A preliminary exploration of edge plasma current profile reconstruction from the atomic beam probe diagnostic*, Fusion Engineering and Design **222,** 115511 (2025) https://doi.org/10.1016/j.fusengdes.2025.115511

[9] BEST Research Plan, https://euro-fusion.org/wp-content/uploads/2025/11/BEST-Research-Plan-v1.1.pdf

SUPPORT LABORATORY FOR THE ITER DISRUPTION MITIGATION SYSTEM

Sándor Zoletnik

Objective

The ITER tokamak will be the first magnetic fusion experiment demonstrating a significantly positive energy balance. In this experiment, an instability called "disruption" can develop on a timescale of a fraction of a second and release several hundred MJ of energy from the hot plasma in the device. An uncontrolled energy release might damage parts of the machine; therefore, some disruption mitigation method is needed. The foreseen technology is Shattered Pellet Injection, when a solid hydrogen or neon pellet is shattered close to the hot plasma. The resulting cryogenic fragment shower injects a large amount of material deep into the plasma, thus cooling it. Although this technology was tested in present-day devices, the large size of ITER requires larger pellets, which have never been used before. To develop the technology, a Disruption Mitigation System (DMS) Support Laboratory was established at the Fusion Plasma Physics Department in 2020, in the framework of an ITER contract. The laboratory aims to develop pellet production and acceleration recipes, measure the fragment distribution and develop components for the DMS.

Methods

During previous years, the necessary pellet formation recipes were developed for hydrogen, neon and neon-hydrogen mixtures using the gas system developed in collaboration with H-Ion Kft. However, this gas system uses high-pressure gases and Mass Flow Controllers (MFC), which are not compatible with safety regulations at ITER and are not radiation-hard. Therefore, ITER created a conceptual design of an alternative gas system, which was implemented in the Support Laboratory. One of the important tasks of 2025 was to demonstrate pellet formation with the ITER-like gas system. Another task was to continue development of the internal structure of the suppressor chamber, where the propellant gas expands and is kept for the time the pellet reaches the shattering head, while assuring a stable pellet trajectory. Several versions of this were designed and built, and the pellet flight and gas expansion were studied.

Results

The pellet formation recipes were successfully adapted to the ITER-like gas system. The major problem to overcome was to be able to control the gas flow rate at the early stage of pellet formation and to control the barrel pressure in the late stage using a simple proportional valve. In the ITER-like gas system, the total gas amount for one pellet is stored in a large volume, in which the pressure changes during pellet formation. The proportional valves are sensitive to pressure changes; therefore, a constant flow rate cannot be achieved with a constant valve setting. The problem was solved by combining the input to the Proportional Integrator Differentiator (PID) controller from the pressure of the feed pipe and the barrel. During the formation, the weighting factors were changed. This modified PID scheme ensured the formation of the same pellets as with the original gas system.

Concerning the suppressor internal structure, the best pellet guidance was achieved by leading the pellet through the suppressor chamber between four guide rails. The propellant gas can expand between the rails, but the pellet trajectory is kept straight. This solution ensured that the pellets arrive at a well-reproducible location to the shattering head, with only a few mm scatter. The pellet rotation is not controlled enough; pellets can arrive at the shattering head by rotating up to 30 degrees. In detailed camera observations, it was found that the pellet diameter is somewhat (~1 mm) smaller than the barrel internal diameter, and therefore, it can move between the rails. The discrepancy in pellet diameter is produced by the amount of material broken from the pellet surface during the launch process. This material is seen as a dust cloud exiting the barrel before the pellet. Besides the pellet observations, this amount was also assessed by capturing this cryogenic dust and measuring its gas production after evaporation. An alternative method was developed to optically measure the density of the dust cloud in the suppressor chamber. These measurements gave a few-tenth mm removed pellet material, which is roughly consistent with the pellet diameter reduction.

Remaining work

The remaining most important question is how to stop pellet rotation during its flight to the shattering head. This is of extreme importance as the prototypes of the ITER SPI injectors should be designed and manufactured in 2026-27 so that they are ready on time for the machine experimental start in 2034. In discussion with ITER, it became clear that some guiding structure cannot be installed, the pellet must cover the approximately 5 m distance between the injector and the shattering head in free flight. As the pellet was seen to have a smaller diameter than the barrel, and it moves between the guide rails, it was a natural idea to gradually reduce the distance between the rails from the barrel to the end. However, it could not be determined what convergence is needed which can stabilise the pellet trajectory and rotation without damaging it. For the experimental investigation, an adjustable converging rail system was designed, and it is under manufacturing. Although adjusting the convergence requires opening the suppressor vacuum chamber, no manufacturing is needed. Experiments in 2026 will be conducted to determine the optimal convergence.

In 2025, discussions started with ITER to build an Alignment Test Facility (ATF) for the final ITER SPI system in our laboratory. Planning is ongoing, the scope and financial envelope of this setup will be determined in early 2026. In any case, the construction of this system will need the refurbishment of a building at the KFKI campus. According to the plan, the present DMS Support Laboratory and the ATF would operate in parallel for some years. In the long term, the ATF supercritical helium cooling infrastructure would remain at the KFKI campus, providing a unique development possibility for various cryogenic systems.

Related publications

[1] G. Kocsis, G. Bartók, A. Buzás, G. Cseh, D. Dunai, G. Gárdonyi, S. Hegedűs, M. Málics, D. Nagy, D. Réfy, T. Szepesi, M. Vavrik, E. Walcz, S. Zoletnik, S. Jachmich, U. Kruezi, M. Lehnen: *Pellet fragmentation studies for the ITER disruption mitigation system*, Fusion Engineering and Design **217,** 115132 (2025) https://doi.org/10.1016/j.fusengdes.2025.115132

[2] R.L. Csiszár, Á. Gyenge, S Hegedűs, U. Kruezi, M. Dibon, S. Jachmich, S. Zoletnik: *Comparison of Propellant Gas Suppressor Configurations for Shattered Pellet Injector*, Fusion Engineering and Design **227,** 115742 (2026) https://doi.org/10.1016/j.fusengdes.2026.115742

[3] Á. Gyenge, R.L. Csiszár, B. Farkas: *Analysis of Propellant Gas Suppression in Shattered Pellet Injector System of the ITER Experiment.* In: M. Grabe, G. Oblapenko, M. Torrilhon, (eds) *Rarefied Gas Dynamics.* RGD 2024. Springer Aerospace Technology (2024)

[4] M.B. Vavrik, D.I. Réfy, G. Cseh, R. Csiszár, S. Hegedűs, G. Kocsis, T. Szepesi, S. Jachmich, U. Kruezi, E. Walcz, and S. Zoletnik: *Gas flow and dust in Shattered Pellet Injection*, Fusion Engineering and Design **229,** 115824 (2026) https://doi.org/10.1016/j.fusengdes.2026.115824

DEVELOPMENT OF A PROPELLANT VALVE PROTOTYPE FOR THE ITER DISRUPTION MITIGATION SYSTEM

Dániel Imre Réfy, Ákos Gyenge, Domonkos Nagy, Zalán Zámbori, Ákos Orosz, Dénes Oravecz, Erik Walcz, Csaba Czuczor, Gergely Bartók, László Richárd Csiszár, András Zsákai, Zsolt Farkas, Balázs Farkas

Objective

ITER will be the first fusion experiment in which the energy stored in the plasma makes active disruption mitigation essential. One of the key protection systems is the Shattered Pellet Injection system, in which cryogenic hydrogen or neon pellets are accelerated by a short gas pulse, fragmented, and injected into the plasma to distribute plasma energy in a controlled manner.

The aim of the project is to develop a prototype propellant gas valve for this injector system. The valve must release a well-controlled amount of gas in less than one millisecond and operate reliably in the demanding ITER environment, including high pressure, radiation and magnetic fields. The work is carried out by the Advanced Valve Technologies consortium, led by the HUN-REN Centre for Energy Research, with CEFusion Ltd. as a consortium partner and modelling support from Budapest University of Technology and Economics.

Methods

Electromagnetic calculations were used to optimise the coil system and moving parts, computational fluid dynamics simulations to investigate gas flow and pellet loading, and finite element analyses to verify the pressure-loaded and cyclically loaded components. In parallel, several metal and polymer-based closing-element concepts were manufactured and tested using leak-rate measurements, repeated actuation cycles and surface preparation trials.

A coupled modelling and design workflow was developed instead of treating the valve as a set of independent components. A numerical design workflow was developed to describe the full process from the discharge of the capacitor bank, through the motion of the eddy-current actuator and closing element, to the gas flow behind the pellet and the resulting pellet acceleration. This made it possible to optimise the valve for pellet arrival time, not only for actuator parameters.

ITER will be equipped with 27 injectors and will be fired simultaneously in the worst-case scenario. The pellets must arrive in the plasma within a 1 millisecond-long window, thus, the target was to minimise the pellet arrival time uncertainty. As a result of the optimisation, the expected value of the time-of-arrival distribution over 10000 shots, which covers ITER's lifetime, will be around 300 μs, taking into account the mechanical, electromagnetic and temperature effects. This extreme reproducibility has been reached by shifting the dominating forces in the valve from flow-induced forces towards inertial forces, e.g. the valve's moving component is a heavy harmonic oscillator.

Results

The Final Design Review confirmed that the propellant valve concept reached a mature prototype design stage. The selected solution uses a robust, axisymmetric eddy-current actuator combined with a mechanically stable spring-mass system. This configuration reduces the sensitivity of the valve dynamics to external magnetic fields, gas-flow variations and small mechanical tolerances. Alternative actuator concepts were also investigated, but they did not offer sufficient advantages for the prototype.

The integrated simulations showed that the valve is expected to meet the required sub-millisecond opening and pellet-timing performance. The dominant uncertainty in pellet arrival time was found to be related to the pellet breakaway process rather than to the valve drive itself, confirming that the valve, pellet and launcher geometry must be treated as one coupled system. Gas-dynamic simulations supported the use of streamlined internal contours and showed that geometry changes needed for connector integration do not compromise the pellet acceleration process.

The mechanical design was consolidated using finite element analyses, with the pressure-loaded parts, material choice and main wall thicknesses selected with manufacturability, cost and fatigue performance in mind. The closing-element test programme led to an important practical design decision: metal-only sealing concepts proved sensitive to wear, surface quality and alignment, while polymer-based solutions showed better reproducibility and sealing behaviour. Based on these tests, a Vespel-based free-floating closing element was selected for the prototype. The manufacturing drawings now contain the consolidated valve geometry, and the Factory Acceptance Test specification defines the required dimensional, pressure, leak-rate and electrical tests before integration.

Remaining work

The next phase is the manufacturing and qualification of the prototype. The selected closing element will be subjected to extended cycling to verify long-term leak-rate stability and wear behaviour. The coil winding, high-voltage connector, cabling and grounding arrangement will also be validated experimentally. After manufacturing, the prototype will undergo the defined Factory Acceptance Tests, followed by an integrated validation campaign covering operation under external magnetic-field conditions and pellet-launching experiments.

DEVELOPMENT OF A REMOTE IN-BORE BRAZING TOOL FOR DEMO BREEDING BLANKETS

József Szőke, Tétény Baross, Péter Figeczki-Mélykuti

Objective

The purpose of DEMO is to validate thermonuclear fusion as an economically viable process for generating power. One crucial aspect of this functionality is the plant having adequate availability to produce power; the plant shall achieve an availability factor of at least 30% and should not require maintenance exceeding 250 days.

This R&D aims to establish maintenance processes for DEMO's In-Shield Magnets and Containment Structures (excluding the Central Solenoid Magnet).

Remote Maintenance will deliver Remote Maintenance Equipment (RME) concept designs for acceptance into the DEMO Technical Baseline by the relevant Configuration Control Board. Candidate RME designs will initially be developed using assumed representative contexts. The documented capabilities of the candidate RME, formatted according to Demo Central Team (DCT) requirements, will constitute the catalogue of RME in the Technical Baseline. This catalogue will serve to inform the design of DEMO in a "bottom-up" sense.

DEMO first wall blanket components will be exposed to high neutron fluence and high levels of thermal energy, the latter being removed by a coolant fluid transmitted out of the reactor via service piping. Due to the thermal and nuclear loading on the first wall, the components will need to be removed and replaced. The installation of new blankets requires the joining of their service pipes. Related to the In-Bore Brazing Heating Trial project - brazing with an in-bore induction heating system is a promising alternative that is considered for joining the service pipes of the DEMO breeding blankets. During the last few years, an induction brazing test rig has been designed in our laboratory, manufactured and assembled to test the feasibility of this technology. This project is part of the Service Joining strand within the Work Package Remote Maintenance (WPRM).

Methods

During the FP9 work period, we are contributing to a generation of this Remote Maintenance Catalogue. With the collection of available technologies/COTS items for each environment and task and identifying the gap between the capabilities of the candidate equipment and the context requirements for them.

Based on the Identified Risks, we could outline the needed number of resources and elaborate on a testing program for the chosen challenges to eliminate them.

Based on the results of the previous years, we continued the development, which branched into 3 directions:

1. Heating the DN200 cooling pipe to 1000 degrees remained a key task. For this purpose, a more efficient inductor was developed using thermal simulations and then manufactured using 3D metal printing. The new inductor and the insulation of the large pipe were performed according to expectations.
2. The project also focused on another pipe size, which involved heating a DN80 lapped pipe connection to 1000 degrees and then brazing it.
3. To select the right brazing filler material and atmosphere as quickly as possible, several small-scale brazing tests were performed in a closed chamber and in air.

Results

The 3D-printed inductor slowly but surely managed to heat the thick-walled DN200 pipe sufficiently and reached 1000 degrees in the pipe wall. The heating process can be seen in Figures 1 and 2.

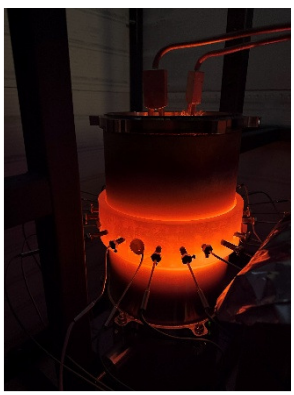


Figure 1: DN200 pipe heating

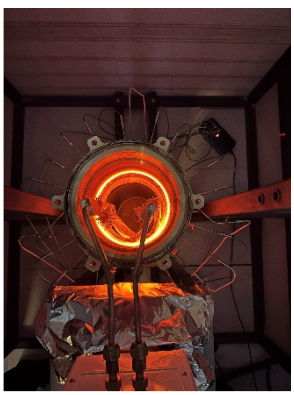


Figure 2: DN200 pipe heating from above

External insulation was placed on the pipe to ensure proper heat dissipation. See Figure 3.



Figure 3: Insulated DN200 pipe heating

Heating the DN80 pipe was less difficult. In this case, a unique In-Bore inductor was also developed based on thermal simulations. The inductor was made entirely in-house using a unique 3D-printed plastic bending tool. The DN80 pipe heating is shown in Figure 4.



Figure 4: DN80 pipe during heating

Following the heating, brazing tests were also carried out with the DN80 pipe.

77 brazing samples were made during the year; these were examined with a tensile machine, and the results obtained were compared. During the tests, the samples brazed in a 99% Argon environment gave the best results. Of the brazing materials Nicrobraz 152 and Nicrobraz 10 were used during the tests; Nicrobraz 152 achieved better results.

Remaining work

This is a long-term, multi-year project with the future goal of developing a standardised brazing procedure that can be easily implemented during the construction of DEMO. Further small-scale and pipe brazing tests with brazing filler materials are needed to select the most suitable brazing filler material for the project.

FUSION MATERIAL SCIENCE RESEARCH: MATERIAL DEVELOPMENT, IRRADIATION AND RADIATION DAMAGE TESTING

Ildikó Szenthe, Dávid Cinger, Balázs Hargitai, Kristóf Andor Csikós, Lajos Berzy

Objective

The development of the new enhanced material for fusion reactors is one of the European Union's highest research priorities. The next step in European fusion research after the ITER reactor is the development of the DEMO fusion reactor. In connection with the DEMO materials science research, HUN-REN EK has participated in the development of new materials suitable for fusion conditions, their testing and the evaluation and summary of the results and has become a member of these peak-level research groups during the past few years.

Methods

One of the main objectives of the WPMAT (Work Package Materials) subproject of EUROfusion is to develop 9Cr Reduced Activation Ferritic Martensitic (RAFM) steels with improved high-temperature mechanical properties in the standard metallurgical condition, as well as steels that would exhibit better mechanical properties (in particular, impact and fracture toughness) following irradiation at low temperature. An important goal will be to select the most promising steels for both high-temperature and low-temperature applications, and to fabricate a larger batch of the materials after final down-selection. In addition, another objective is to evaluate whether full first wall components could be made of Oxide Dispersion-Strengthened (ODS): the goal is to select ODS grades for first wall application and optimise the fabrication route for upscaling to industrial-scale production. Reactor Material Research Group participated in several other subprojects of the WPMAT work package in fusion materials science research in 2025: Mechanical and microstructural investigations of newly developed structural materials, including some steels and CuCrZr alloys, were performed in the frame of the High Heat Flux Material and Steel Development subtask. In the framework of the FP9 project, part of the EUROfusion Reactor Materials Research Group irradiates the material samples in the BAGIRA irradiation probe. To fill the gaps in the database linked to the Tritium Breeder Blanket subtask, the neutron irradiation of the base metal EUROFER97 to achieve 2 dpa (displacements per atom) at 300°C, 1 dpa at 350°C, 2 dpa at 300°C, and 2 dpa at 350°C was continued. HUN-REN EK performed an investigation of mini specimens whose dimensions were below the standards in the frame of the Small Specimen Test techniques subtask. In the functional materials subproject, the research group participated in the development of the Materials Property Handbook for materials of the fusion reactor vessel components and aimed to advance the development of Materials Databases for functional materials.

Results

In the Tritium Breeder Blanket Module subtask, HUN-REN EK continued the irradiation of 32 pieces of compact tension and 32 pieces of tension, reaching an average 0.2 dpa level during 2025. The subtask has to be continued in the next year. In the Steel Development Qualification program, HUN-REN EK contributed to the selection of steel and ODS grades by conducting mechanical testing of the materials across the full operational temperature window and for properties not addressed in the early development. Tensile tests, fracture toughness tests, hardness tests and fatigue crack-growth measurements are performed in 2025. At the Small Specimen Test Technique subtask, differently designed specimens were manufactured and sent to the EUROfusion partners. The tensile tests will start in the next few months. We have tested some model steels. In the Engineering Design Rules Development subtask, dielectric and physical properties of the materials were collected and evaluated from the research reports of the subgroups and the open literature. The data were uploaded to the database and used to elaborate on the extended functional material's Material Property Handbook. A test matrix was developed that summarises the tests to be performed on the thermo-physical, optical, dielectric, and mechanical properties data of Functional Materials to fulfil the recent demand of the designers. HUN-REN EK develops a suitable technology for measuring the magnetic properties of irradiated materials. The approach combines two magnetic measurement methods. First, an "absolute" technique is used to obtain B–H curves from larger, non-irradiated reference specimens. Second, an improved, HC-approved probe employing a "differential" measurement method—Magnetic Adaptive Testing (MAT)—is used to detect subtle changes in magnetic properties with exceptional sensitivity for aged material. In 2025, the basics of the technology were established, and a calibration measurement was performed. The method of conducting the measurements will be developed during the next few months.

Remaining work

The current work plan for the EUROfusion program is set until the end of 2025, coinciding with the conclusion of the current 5-year Euratom program. In 2026-27, the Euratom program will be extended to ensure that the next 5-year cycle aligns with the EU's 7-year budget plan.

EDUCATION AND TRAINING ACTIVITIES IN RADIATION PROTECTION AND NUCLEAR SAFETY

Tamás Pázmándi, Dorottya Jakab, Éva Széles, Péter Völgyesi

Objective

Capacity building and effective knowledge transfer play a vital role in sustaining radiation protection and the peaceful use of nuclear energy. Exchanging expertise, sharing knowledge, and best practices contribute to the continuous improvement of nuclear safety and radiation protection culture. Recognising the importance of these challenges, the HUN-REN Centre for Energy Research has taken an increasingly active role in education and training. Building on the outcomes of the institute's research and development activities, as well as its experience in higher education, numerous training and tutoring programs have been organised in recent years. The long-term objective is to establish a training centre of both national and international relevance.

Methods

The project „Training and Tutoring for Experts of the Nuclear Regulatory Authorities (NRAs) and their Technical Support Organisations (TSOs) for Developing or Strengthening their Regulatory and Technical Capabilities – MC3.01/20", funded by the European Commission, was implemented between January 2022 and January 2025 to provide professional training to experts from countries outside the European Union.

The international consortium, led by the HUN-REN Centre for Energy Research, involving internationally recognised and distinguished experts, successfully developed and implemented a professional and comprehensive training program. The program included 37 training courses delivered in 16 countries around the world, as well as 23 four-week tutoring courses, i.e. on-the-job training organised in European NRAs and TSOs across 7 European countries. A total of 19 topics were covered across disciplines such as nuclear safety, radiation protection, and Emergency Preparedness and Response (EPR). More than 80 renowned experts contributed to the development and delivery of the training courses, while 10 different institutions hosted tutoring courses offering practical, hands-on experience in real working environments.

In addition to this project's training activities, training courses on "Practical aspects of field response in nuclear and radiological emergencies" were organised for experts of the Nuclear and Radiological Regulatory Commission of the Kingdom of Saudi Arabia in September 2025.

Results

A total of 543 participants benefited from the Training and Tutoring (T&T) activities during the MC3.01/20 project. The effectiveness and efficiency of competence development were clearly demonstrated by participants' improved test performance. Feedback indicated a high level of satisfaction, with an average satisfaction index of 4.7 out of 5.0 (with no course scoring below 4.0) and an average course usefulness rating of 4.8 (out of 5.0, also reaching 4.0 for each course), confirming strong relevance for professional development and the effectiveness of the courses in meeting expectations and professional needs. More than 75 organisations representing 46 countries across 6 regions actively benefited from the project through participation in T&T courses. The project also provided numerous networking opportunities for building professional and personal connections, making significant progress in fostering global cooperation among organisations involved in nuclear safety regulation.

A total of 12 participants attended two courses focusing on the practical aspects of field response in nuclear and radiological emergencies, gaining first-hand experience of challenges encountered by first responders.

Based on the feedback received from the participants, both training courses and tutoring activities achieved their objectives, and the programs provided substantial support in performing their tasks and addressing challenges encountered in their work.

References

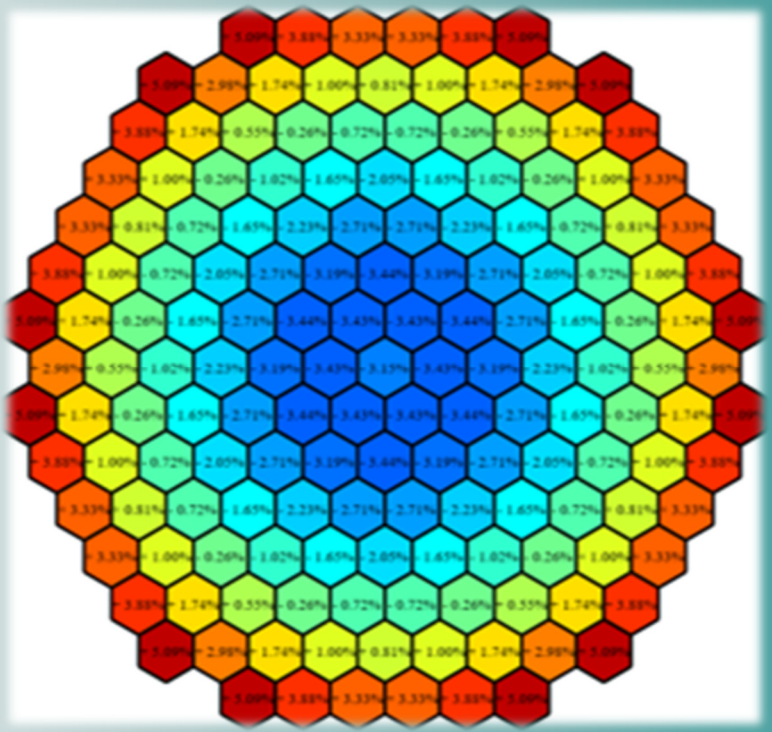
[1] T. Pázmándi, D. Jakab: *Methods and Lessons Learned in Training and Tutoring Activities for Experts of Nuclear Regulatory Authorities*, ICRP 2025: The 8th International Symposium on the System of Radiological Protection

[2] T. Pázmándi, D. Jakab: *Experiences and lessons learned from recent training activities in radiation protection and nuclear safety*, 7th European IRPA Congress 2026 (accepted for presentation)



II. RESEARCH AND DEVELOPMENT RELATED TO NUCLEAR POWER PLANTS





ACTIVITIES OF HUN-REN EK AS THE MAIN CONSULTANT OF PAKS NUCLEAR POWER PLANT

Pál Szentannai, Zsombor Bali, Attila Guba, Áron Hegedűs, György Hegyi, Levente Illés, Márton Király, István Panka, Tamás Pázmándi, Anna Pintérné, Csilla Rudas, Péter Szabó, András Ványi, Nóra Vér

Objective

HUN-REN EK, together with NUBIKI (Nuclear Safety Research Institute), has been the main consultant of Paks Nuclear Power Plant (NPP) for many years. The main consultant supports the NPP in solving safety-related technical issues and helping with strategic planning. The work is done by the most experienced and highly qualified members of the EK staff based on yearly work plans. In 2025, HUN-REN EK undertook the following separate tasks, done by different (groups of) experts:

1. Integration of severe accident dose calculations into the Final Safety Analysis Report (FSAR);
2. Thermo-mechanical analyses of nuclear fuel rods to assess the consequences of load-following operation;
3. Determining the design-basis accident Reactivity Initiated Accident (RIA) analysis under reduced steam generator heat transfer conditions;
4. Investigation of the effect of hydride orientation accumulated in the cladding on mechanical properties.

Methods

Each task required different methods, which are summarised on their specific sheets.

Results

1. Within the framework of a project carried out in 2016–2017, dose calculations were performed for both design-basis and beyond-design-basis operating conditions, during which activity concentrations and dose rates were determined in individual rooms. The results of these analyses had previously been only partially incorporated into the relevant chapters of the Final Safety Analysis Report (FSAR). In the present work, the results obtained for two representative severe accident scenarios were reviewed for each room, and those to be included in Annex M3.9 of Chapter 3 of the FSAR were identified. In addition, proposed amendments to the wording of the Annex and the necessary extensions to the list of source documents were also provided.
2. In the first part of the subsequent subtask, the exact specification of the problem was reviewed, the structure of the time series provided by the plant was described in detail, and the data processing steps performed before the generation of fuel performance input files – together with the auxiliary tools used – were presented. Furthermore, the manufacturing parameters applied in the best-estimate calculations, as well as the nodalisation schemes and model settings used in the individual fuel performance codes, were described. In an appendix to the report, both the previously applied and the newly introduced methodologies for calculating the fast neutron flux impinging on the cladding were also presented. In the second part of this subtask, multi-rod best-estimate calculations were carried out, and the results were analysed. The calculations showed that the maximum cladding hoop stresses were significantly below the applicable limit values. Based on these results, a cumulatively conservative estimate of cladding fatigue was performed. Even under excessively conservative assumptions, the accumulated fatigue in the cladding was found to be an order of magnitude lower than the corresponding limit. To support the multi-rod calculation results, a sensitivity analysis was performed in the final part of the report for the fuel rods considered most heavily loaded in terms of hoop stress. During this analysis, the input time series, manufacturing parameters, applied physical models, and fuel rod types were perturbed individually. Within the project, in cooperation with reactor physicists at the plant, a computational framework was developed that enables rapid and efficient post-calculation of plant fuel rods using two actively developed fuel performance codes. The simulation results and the discrepancies between the codes were discussed in detail. Based on the findings, further detailed investigation of fuel–cladding gap closure using experimental data was recommended. In addition, the development of a Monte Carlo-based comprehensive uncertainty analysis framework was proposed to support the best-estimate results.
3. The next task involved performing the Design-Basis Accident (DBA) RIA analysis to determine whether, under full compliance with current limits, any steam generator operating condition could invalidate previous RIA analyses. The results were documented in the form of a Time Reversal As Self-Supervision (TRASS) report, consistent with earlier analyses. The withdrawal of one element of control rod group 6 was simulated at a conservative power level (94% power), under safety system operation and degraded steam generator heat-transfer conditions. The analysed equilibrium cycle primarily consisted of profiled Russian fuel assemblies containing six gadolinium-bearing rods. The results satisfy the relevant acceptance criteria: even under conservative assumptions, no Departure from Nucleate Boiling (DNB) was observed in the most heavily loaded assembly, and both pressures and cladding temperatures remained within allowable limits despite the degraded steam generator heat-transfer conditions.

4. Specimens of various types were produced, including hydrogen-charged, differently heat-treated, and partially reoriented hydride microstructures. The morphology of the precipitated hydrides was characterised using scanning electron microscopy and image analysis techniques. The results indicate that slow cooling – particularly at lower hydrogen concentrations – leads to an increase in hydride size within the cladding material. The applied reorientation loading slightly increased the fraction of hydrides not aligned with the circumferential direction in ring specimens. However, the effect of these differently structured hydrides on mechanical properties has not yet been investigated. The influence of hydride morphology on ductility is planned to be determined by means of ring compression tests.

Remaining work

This project has been completed.

Related publications

[1] T. Pázmándi, C. Rudas: *Integration of severe accident dose calculations into the FSAR,* EK-TFO-2025-751-03-01-M0, in Hungarian (2025)

[2] A. Ványi: *Thermo-mechanical analyses of nuclear fuel rods to assess the consequences of load-following operation,* EK-TFO-2025-751-04-01-M0, in Hungarian (2025)

[3] Zs. Bali, A. Guba, Á. Hegedüs, G. Hegyi, I. Panka: *Withdrawal of a single element of control rod group 6 at a conservative power level close to 1485 MW, under ÜV-1 operation, for second-generation fuel assemblies optimised for the water-to-uranium ratio, with degraded steam generator heat transfer,* EK-TFO-2025-751-05-01-M0, in Hungarian (2025)

[4] M. Király, N. Vér, P. Szabó, L. Illés, A. Pintérné: *Investigation of the effect of hydride reorientation accumulated in the cladding,* EK-TFO-2025-751-06-01-M0, in Hungarian (2025)

SURET – MODELLING TWO-PHASE FLOW IN SUBCHANNELS WITH A GRAPHICAL USER INTERFACE

Áron Vécsi, Gábor Házi

Objective

In recent years, HUN-REN EK has developed a new subchannel analysis module, SURET (SUbchannel REactor Thermohydraulics). After offline testing, the module was integrated into the VERONA online core monitoring system operating alongside the Paks nuclear power plant units. This integration became possible because the numerical algorithms used in the code were reformulated and accelerated to a level that allowed real-time application.

The present report describes the further development of SURET. Two main objectives guided the work. First, the calculation framework was extended to handle two-phase flow. Second, a graphical user interface was developed in order to simplify the generation of the calculation inputs and to make the software more accessible for engineering use.

Methods

For the treatment of two-phase conditions, the energy equation was modified in a manner consistent with the approach previously used in RETINA, which was developed at our institute and has been in operation in the Paks full-scope simulator for more than ten years. Separate equations are solved for the liquid-water and steam phases, while the thermal coupling between the phases is represented by the heat flux across the interface separating them. In addition, SURET is capable of calculating Critical Heat Flux (CHF).

Earlier versions of SURET did not explicitly model the thermal processes inside the fuel rod. In the current version, the model was extended by introducing a simplified solution of the heat-conduction equations based on an Alternating Direction Implicit (ADI) method. In the present implementation, the fuel rod is assumed to consist of three material regions: uranium fuel, the gas gap and the cladding.

A dedicated graphical user interface was developed for the completed SURET model. The interface supports the geometric definition of both square and hexagonal assembly layouts. Within the program, the user can specify the principal calculation parameters and boundary conditions, define assembly types, and construct arbitrary core configurations from these building blocks.

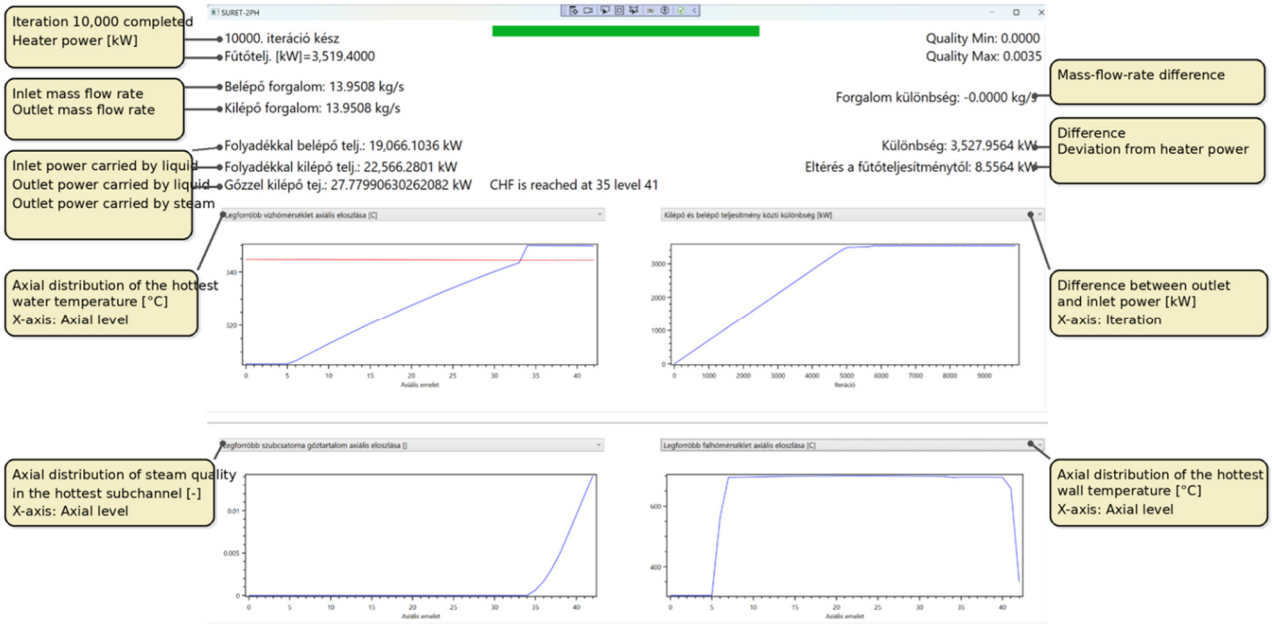


Figure 1: Graphical output during calculation

During the calculation, the program continuously updates the principal results graphically. This provides practical support for identifying convergence problems while the simulation is running. These graphical outputs remain available after the completion of the calculation; an example where CHF is reached is shown in Figure 1. The results are also saved to a file, enabling further post-processing after the run, and they can be displayed directly within the SURET interface itself. An example of crossflow-related results for a given calculation is presented in Figure 2.

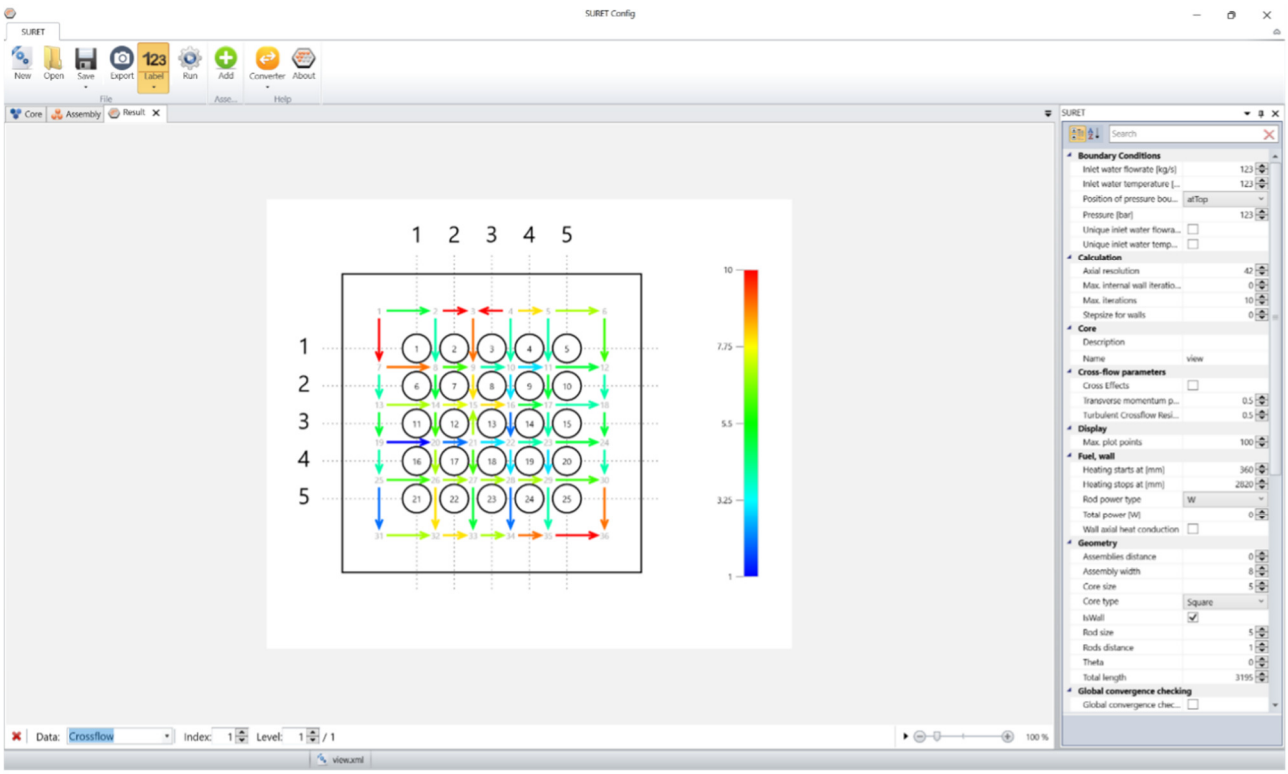


Figure 2: Crossflow results inside the GUI (Graphical User Interface)

Results

The numerical results obtained with SURET were compared with the experimental bundle measurement prepared by EPRI for a 25-rod configuration. For different parameter settings of the code, the comparison yielded acceptable agreement with the measurements as shown in Figure 3. These results indicate that the extended model retains an adequate level of predictive capability while offering the new functionality required for two-phase calculations.

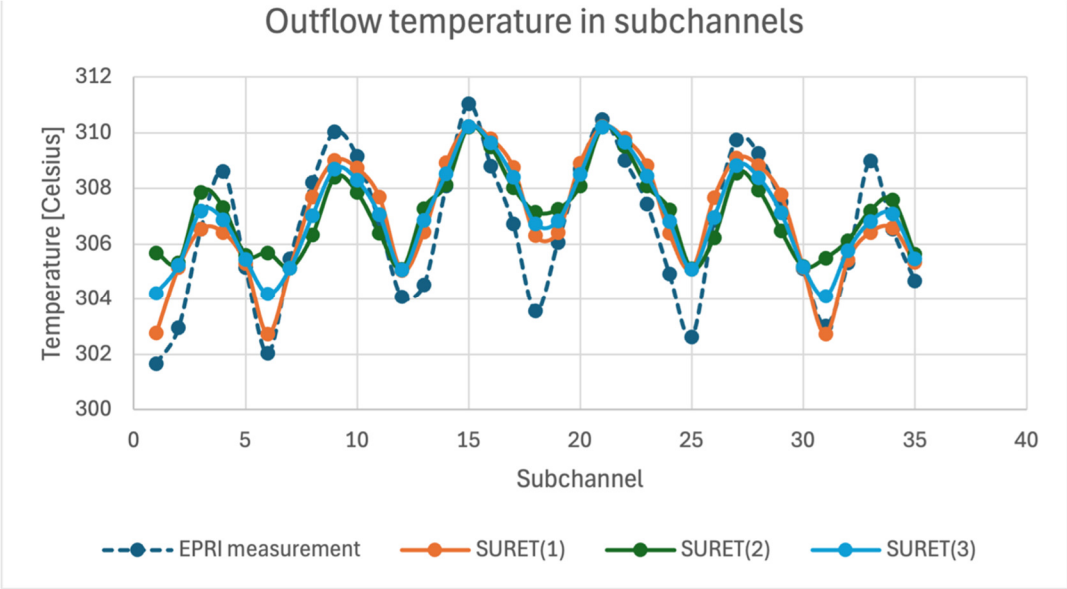


Figure 3: SURET outflow temperature comparison with EPRI measurement

Remaining work

The SURET code, developed for the Paks II Nuclear Power Plant and capable of performing two-phase calculations with a graphical user interface, has been completed and delivered to the customer. The project has therefore been concluded.

The SURET thermohydraulic code still offers significant further development potential, and additional research activities are expected in the future. At present, we are participating in an OECD benchmark project involving subchannel thermohydraulic calculations in liquid sodium. In the longer term, these calculations are intended to be coupled with reactor physics simulations.

INVESTIGATION OF THE CERES FACILITY COOLABILITY LIMIT

Attila Guba, Áron Hegedüs, Attila Nagy

Objective

In the event of a severe accident at a Nuclear Power Plant, the core may melt, as it did in the Fukushima accident. In this situation, the molten core falls to the bottom of the vessel, where density-driven separation takes place. The heavy-density material forms a special crust layer on the wall, which behaves as heat insulation, directing the residual heat to the top layer. The light metal layer concentrates the heat attacking the vessel wall, which may cut the vessel bottom, leading the debris to fall into the concrete bottom. The very unfavourable metal-concrete exothermic reaction should be avoided. For such circumstances, the newer power plants use a so-called "core catcher" to collect and handle the debris. In the already operating power plants, it is unfeasible to build such a device. To prevent it in the Paks NPP, an external core cooling strategy was developed. Water from the sump can be delivered to the reactor cavity, which is intended to remove the attacking heat flux in the outer surface of the vessel. Due to the unfortunate geometry, at the elevation where the light metal layer attacks the wall on the outer side, there is a narrow gap that may reduce the possibility of removing the necessary heat. To test the effectiveness of the heat removal in previous years, several experiments have been performed on the CERES (Cooling Effectiveness on Reactor External Surface) facility, proving that the concept is applicable in the power plant based on very conservative assumptions. The necessary modifications have been implemented in the power plant to decrease the possible adverse effects on the environment, while maintaining vessel integrity. After the experimental series showing the success for the very conservative heat flux, a question arose: how much reserve may there be in the heat flux? To address this, an experiment was planned to increase the heat flux as much as possible, even at the risk of the experiment facility's integrity.

Methods

The CERES facility was prepared to be able to accept the power increase, while most of the heating was focused on the narrow gap. The protection system limit values for the wall and heater rod temperatures were gradually increased, potentially leading to the complete destruction of the whole facility.

Results

With the increase in the power on the outer surface of the vessel, at the narrow gap, bubble formation starts. Since the steam cannot remove the heat from the wall effectively, the connecting metal temperature increases. As the bubble grows, more temperature sensors indicate the heating up of the wall. When the bubble reaches a "critical size", the hot steam may exit the narrow gap, arriving at a much colder water phase, resulting in excessive condensation. Consequently, the bubble collapses rapidly, and the arriving cold water cools down the hot wall. Then this pulsation starts again. As the power is increased, the frequency of the bubble formation period and the maximum wall temperature increase. For us, the maximum wall temperature is important. This experiment was designed to reach the physical limits of the facility and even more. The maximum wall temperature measured on the outer side was 508 °C, while in the heating simulator rod, the maximum was 561 °C. Those values are well beyond the safe operating parameters of the equipment. Since the integrity was challenged after reaching the extreme temperatures, the power was gradually decreased. The power decrease was stopped at the lowest measured power level, checking if the behaviour of the experimental facility was altered due to the extreme load. It was observed that even though the facility was operated well beyond the design limits, the results were still the same as before. The facility was not destroyed. The maximum wall temperatures in the narrow gap are shown in Fig. 1.

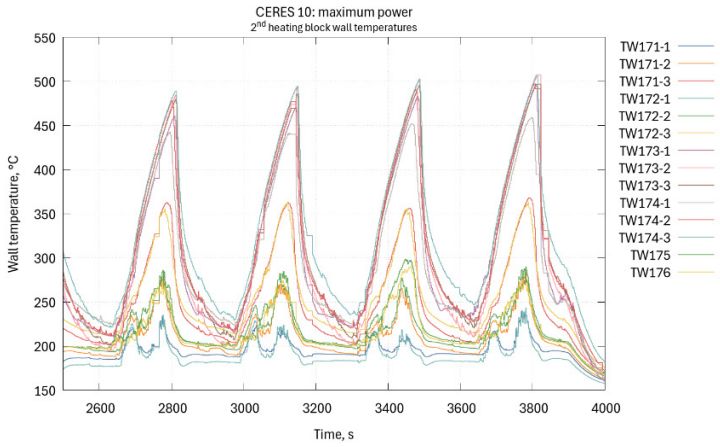


Figure 1: Wall temperatures in the narrow gap at maximum power

Related publication

[1] Gy. Ézsöl, G. Baranyai, L. Perneczky, L. Szabados, I. Tóth: *Modelling of External Cooling for In-Vessel Corium Retention in VVER-440/213 Type Nuclear Power Plants*, 18th International Conference on Nuclear Engineering (ICONE18) 2010

TURBINE EMULATOR DEVELOPMENT FOR THE TURBINE CONTROL SYSTEM OF PAKS NPP

József Páles, Csaba Horváth, Gábor Házi

Objective

Paks Nuclear Power Plant (NPP) has started an Instrumentation and Control (I&C) refurbishment project to replace the Turbine Control Systems (TCS) on the units. The purpose of the project is to introduce a modern Programmable Logic Controller (PLC)-based digital control platform that ensures reliable and safe long-term operation of its turbine control system. As part of the project, it was necessary to develop turbine emulator software that can be used to test and validate the operation of the new TCS hardware and software in a closed loop. The new turbine emulator must be used during the development and commissioning of the new TCS, and later it will also be used for the training of maintenance personnel.

Methods

A turbine emulator software (Fig. 1) has been developed to support the hardware-in-the-loop testing of the new TCS. The emulator software runs on a notebook computer and can be connected to the PLC hardware of the new TCS. The emulator performs real-time simulation of the turbine system and some further important technological systems, which are directly connected to the turbine. The emulator's model system simulates all input measurement signals required for the operation of the new TCS and uses controller commands to change the position of the turbine control valves in the model.

The scope of the simulation was defined so that the system could be used to test all relevant operating modes (speed, power, and pressure control) and functions of the new controller system. To achieve this, the model system contains a detailed simulation of the following important technological systems:

- the six steam generators,
- the main steam system together with its important safety valves and reducers,
- the control oil system and control valves of the turbine,
- the turbine system with all connected moisture separators and reheaters,
- the condenser,
- a simplified generator model with three operating modes (connected to the grid, island and no-load operating modes),
- some further important control logics connected to the above systems (turbine protection, logic for safety valves, power control of the primary circuit, level control in steam generators, etc.).

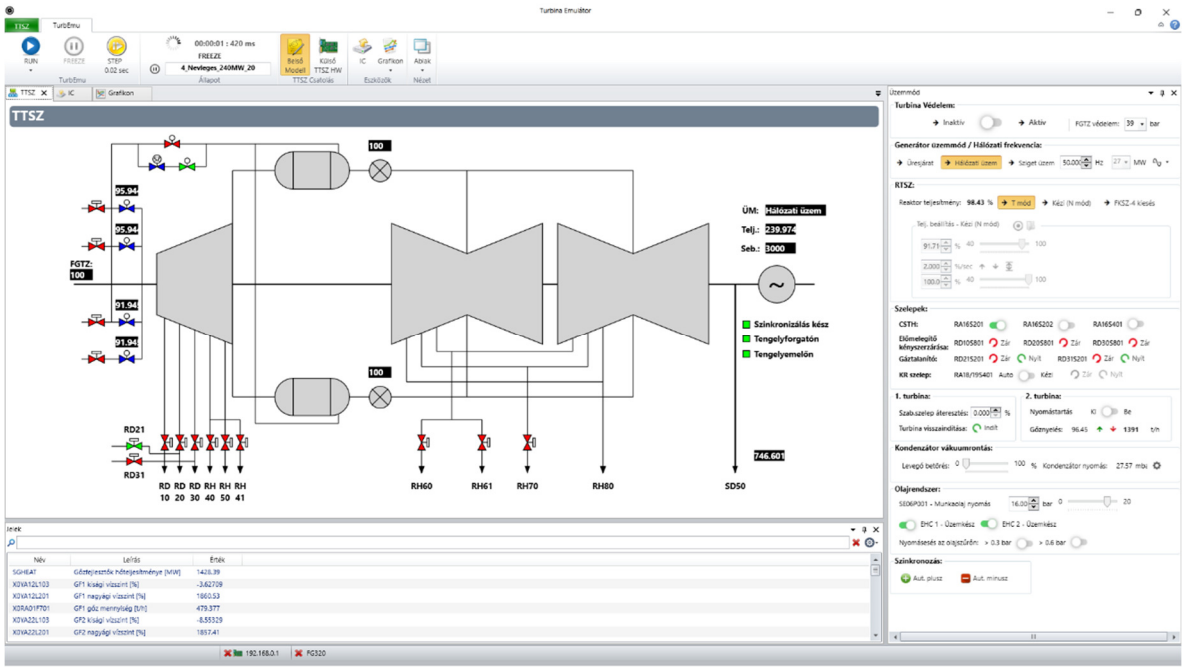


Figure 1: Turbine Emulator Software

The model system of the emulator was created in a graphical simulator development and runtime environment called SIMTONIA (SIMulator Tools for Nuclear Industrial Applications). SIMTONA was developed earlier by HUN-REN EK, and it contains all the necessary tools required for building simulation models of complex technological systems. The environment

contains different types of simulation engines to model different types of processes, such as one and two-phase flow thermohydraulics, control logics, operator panels, etc. The different types of simulation models are connected to each other in the environment to create more complex simulations. The whole model system of the turbine emulator was implemented in SIMTONIA based on the models and parameters available in the full-scope training simulator of Paks NPP.

Results

The turbine emulator software was successfully used for the closed-loop testing of the new turbine control system during the design process, and later during Factory Acceptance Testing (FAT) of the new controller. Using the turbine emulator software in closed-loop, twenty different transient tests were performed to check the operation of the new TCS in all important operating modes and conditions:

- turbine startup in manual, semi-automatic, and automatic modes,
- power control mode tests,
- pressure control mode tests,
- mixed control mode tests,
- checking the operation of limiters under different operating modes,
- handling other special conditions (trip of the main circulating pump, drop of electrical load, etc.).

In later phases of the project, the emulator software will be used for testing during the commissioning of the new controllers, and it will also be used for the training of maintenance personnel.

Remaining work

This project has been completed.

VALIDATION OF THE KARATE CODE SYSTEM AGAINST OPERATIONAL DATA AND STARTUP MEASUREMENTS WITH MODIFIED GROUP CONSTANT LIBRARIES

Vince Hegyi, István Panka

Objective

Over the past decades, KARATE-440 has been continuously developed for the coupled neutron-physical and thermal-hydraulic analysis of VVER-440 reactor cores. The primary objective of the calculations is core design; however, certain safety analyses that can be performed using a static code are also within the scope of KARATE-440. The program supports economical core design while ensuring compliance with the limits established by safety analyses. This capability is also utilised for the periodic independent verification of the core design at Paks Nuclear Power Plant (NPP).

In recent years, several modifications to the VVER fuel design and corresponding core loading patterns have been introduced at Paks NPP to achieve more efficient fuel utilisation. These include, for example, water-to-uranium ratio optimised Gd-doped fuel assemblies. Such developments have required further refinement of the calculation models.

In view of these changes, continuous validation of the KARATE-440 code system is essential. In recent years, comparisons with measurements from Paks NPP have shown larger-than-usual discrepancies for certain parameters. Therefore, a detailed comparison and validation study was undertaken to evaluate the performance of the KARATE-440 code system.

Methods

The following parameters were used for the validation: core-burnup-dependent radial peaking factors derived from assembly-wise in-core temperature rise measurements, core-burnup-dependent operational critical boron concentrations, critical boron concentrations measured at the Minimum Controllable Power (MCP), moderator temperature reactivity coefficients measured during startup tests, and differential control rod group efficiencies. The comparisons were carried out for four consecutive campaigns of each of the four units in reactor cores containing Gd-doped fuel rods. During the validation process, the group constant libraries of the KARATE-440 code system were slightly modified.

Results

According to the validation results, the boron letdown curves show better agreement with the measurements than previously observed. The calculated boron concentrations are generally in good agreement with the measurements, typically within one standard deviation. In addition to the boron letdown results, Fig. 1 shows a comparison between the measured and calculated isothermal temperature reactivity coefficient for Unit 1 using high-enriched Gd-doped fuel. The maximum deviation is approximately 1 pcm/°C, which is within the range of measurement uncertainty. Fig. 2 demonstrates the measured and calculated differential control rod worth as a function of control rod group position for Unit 3. The differences are within 10%, which is considered acceptable.

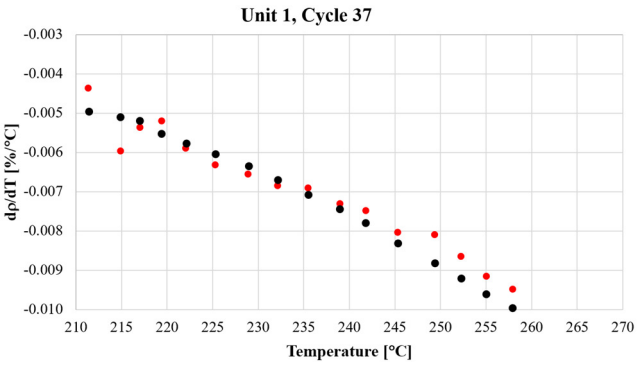


Figure 1: Measured (red dots) and calculated (black dots) isothermal temperature reactivity coefficients for Cycle 37 of Unit 1 as a function of temperature

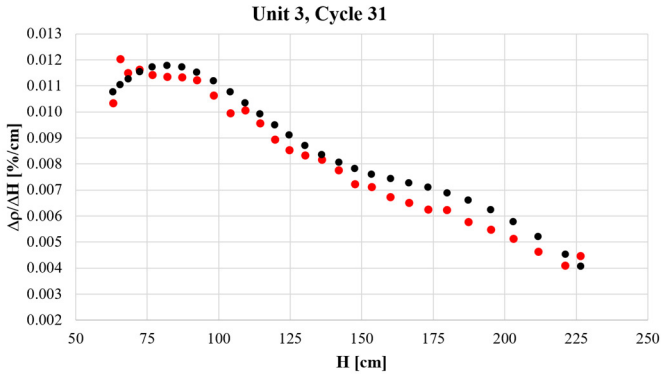


Figure 2: Measured (red dots) and calculated (black dots) differential control rod group worth for Cycle 31 of Unit 3 as a function of control rod group position (H).

Remaining work

The results should be published.

Related publication

[1] H. Vince, I. Panka: *Comparison and validation of KARATE 5.0 code system calculation results with measurement data from Units 1–4 of the Paks Nuclear Power Plant using a modified group constant library,* EK-NBL-2025-739-01-02-M0, in Hungarian (2025)

NEUTRON IRRADIATION LOADING AND HEAT GENERATION ASSESSMENT OF COMPONENTS BETWEEN THE CORE AND REACTOR PRESSURE VESSEL FOR SUBSEQUENT LONG-TERM OPERATION EXTENSION OF THE PAKS NUCLEAR POWER PLANT

Zoltán István Böröczki, György Hegyi, Gábor Hordósy, Csenge Komjáti, István Panka, Petra Pónya, Emese Temesvári

Objective

The objective of this work was to generate heat generation and neutron irradiation loading distributions, expressed in terms of displacements per atom (dpa), required for structural material ageing analyses of components located between the reactor pressure vessel wall and the core over the 70-year subsequent Long-Term Operation (LTO) period. To achieve this objective, a new methodology based on a so-called volumetric source had to be developed.

The methodology was required to generate the source term at the fuel rod level using the KARATE-440 core design code and to perform the subsequent photon and neutron transport calculations with the Monte Carlo N-Particle (MCNP) code.

Methods

The heat generation and dpa loading distributions were determined through a series of coupled KARATE–MCNP calculations using a newly developed so-called volumetric source method. In this approach, the source was defined in the three outermost fuel assembly rows at the core periphery.

From the calculations performed with the KARATE core design code, the rod-segment-wise power density and the number of fissions in the peripheral fuel assemblies were evaluated. These quantities were subsequently used in the Monte Carlo calculations to generate neutrons and photons from within the fuel rod segments. Using a dedicated interface, the calculated neutron source, coolant density distribution, boron concentration, and the fuel assembly types present in the core were incorporated into the MCNP input model. Based on this information, Monte Carlo calculations were performed to evaluate the heat generation and dpa loading distributions in the regions of interest.

In the KARATE calculations, the operating histories of all four units of the Paks Nuclear Power Plant were modelled in detail, covering both the realised operating periods and the projected operation up to a total service life of 70 years.

In the Monte Carlo calculations, the outer three rows of fuel assemblies were considered, and the reactor was modelled radially outward up to the outer surface of the reactor pressure vessel. A horizontal cross-section of the resulting model is shown in Fig 1.

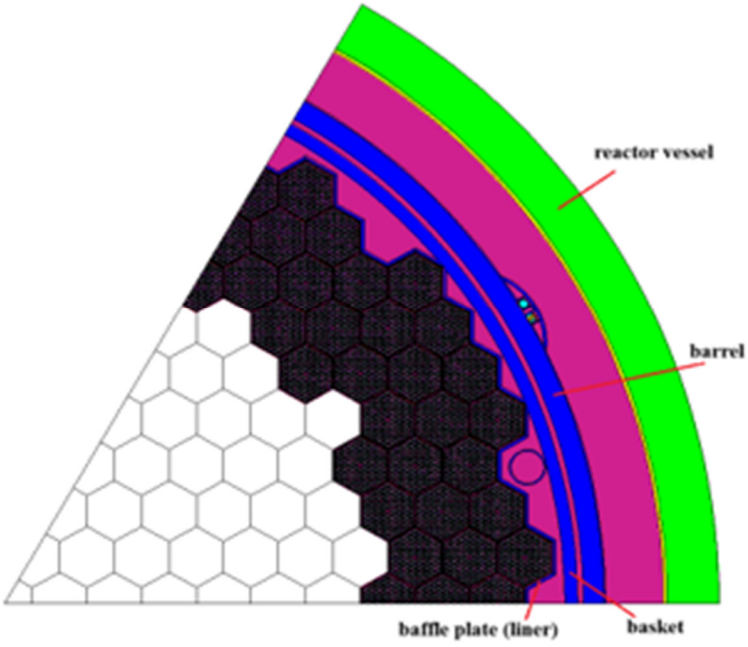


Figure 1: Horizontal arrangement of the model applying the volumetric source method

Results

The calculations were performed for the selected reactor internals regions [1]. Additionally, the evolution of the cycle-integrated average and maximum dpa values in the baffle plate, as well as the average and maximum heat generation rates at the beginning and end of each cycle, was evaluated for each unit over the completed and planned future operating cycles.

It was found that, because of effective cycle planning, neither the power uprate nor the introduction of the C-15 and SLIM fuel assemblies increased the loads. On the contrary, a decreasing trend was observed in both irradiation damage and heat generation (see Figures 2 and 3).

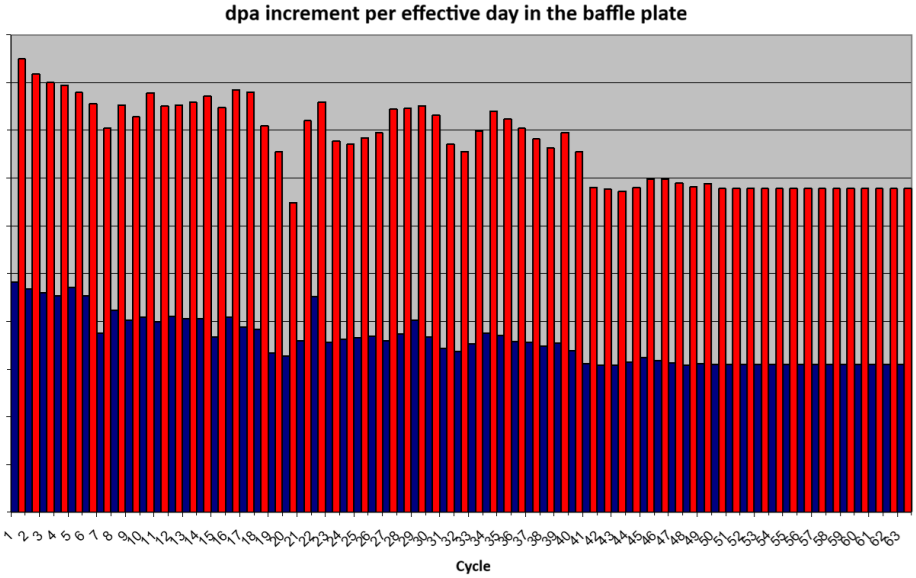


Figure 2: Illustration of volume-averaged (blue column) and maximum (red column) dpa increases (dimensionless) in the reactor baffle plate per effective day for Unit 1 over a 70-year service lifetime

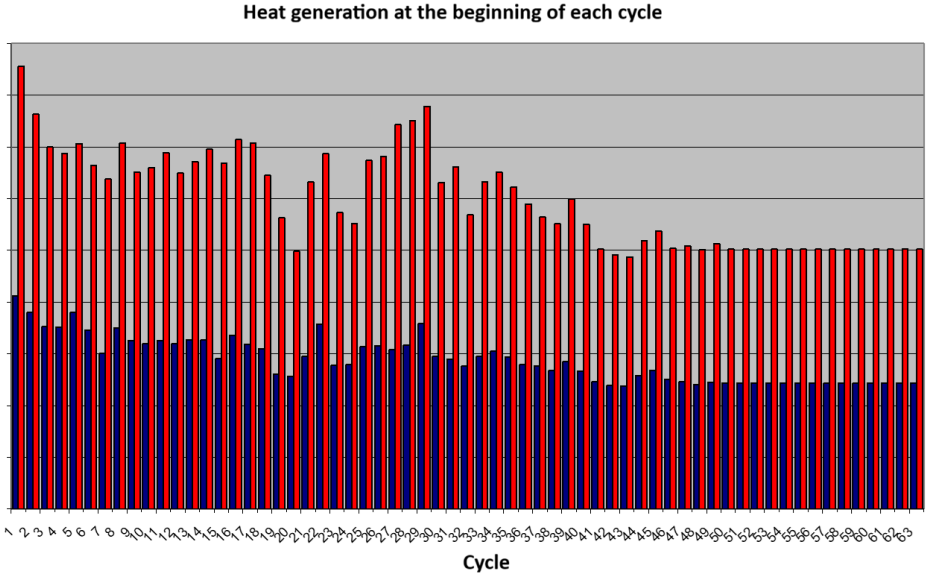


Figure 3: Illustration of volume-averaged (blue column) and maximum (red column) heat generation rate (dimensionless) in the reactor baffle plate at the beginning of each cycle for Unit 1 over a 70-year service lifetime

It should be noted that the results of the validation studies based on measurement data confirmed the adequacy of the applied calculation methodology [1].

Remaining work

The results are planned to be published in 2026.

Related publication

[1] Z. I. Böröczki, Gy. Hegyi, G. Hordósy, Cs. Komjáti, I. Panka, P. Pónya, E. Temesvári: *Neutron irradiation loading and heat generation assessment of components between the core and reactor pressure vessel for subsequent long-term operation extension of the Paks Nuclear Power Plant,* EK-NBL-2026-744-01-03-M2, in Hungarian (2026)

INTEGRAL TESTING OF ACCIDENT TOLERANT FUEL DESIGN UNDER AIR INGRESS CONDITIONS

Róbert Farkas, Nóra Vér, Berta Bürger, Erzsébet Perez-Feró, Tamás Novotny, Anna Pintérné Csordás, Levente Illés, Seif Eddine Habbachi, Zoltán Hózer

Objective

The introduction of Accident-Tolerant Fuel (ATF) at nuclear power plants requires testing under a wide variety of accident conditions. The most promising near-term ATF cladding solution is Cr-coated zirconium alloys.

The main objective of the CODEX-ATF-AIT (Air Ingress Test) was to investigate the behaviour of Cr-coated cladding under air-ingress severe accident conditions ([1],[2],[3],[4],[5]). The access of air to the hot surface of fuel rods during accidents may significantly accelerate core degradation after the failure of the Cr coating, due to the intense oxidation of zirconium alloys. Scenarios leading to air ingress (such as lower head failure, open reactor, or spent fuel storage pool accidents) can be critical from the point of view of radiological consequences, since the loss of cladding integrity can lead to the oxidation of ruthenium and the formation of gaseous radionuclide species.

It was expected that a comparison with the reference test CODEX-AIT-3, carried out with uncoated cladding tubes, would provide information on the role of Cr coating in accident progression and fuel degradation phenomena, and that conclusions could be drawn on the potential extension of coping time.

Methods

The experimental scenario was designed to investigate key phenomena of fuel rod behaviour during accident conditions, including cladding burst, oxidation, nitriding, and eutectic formation. During the preparatory phase, the facility was heated to 600 °C under a steam-argon atmosphere (Fig. 1). In the subsequent pre-oxidation phase, the rod heating power was increased stepwise, leading to pressurisation and cladding burst between 750–800 °C in most rods (Fig. 2). The burst openings allowed coolant ingress, initiating chemical reactions on both sides of the cladding.

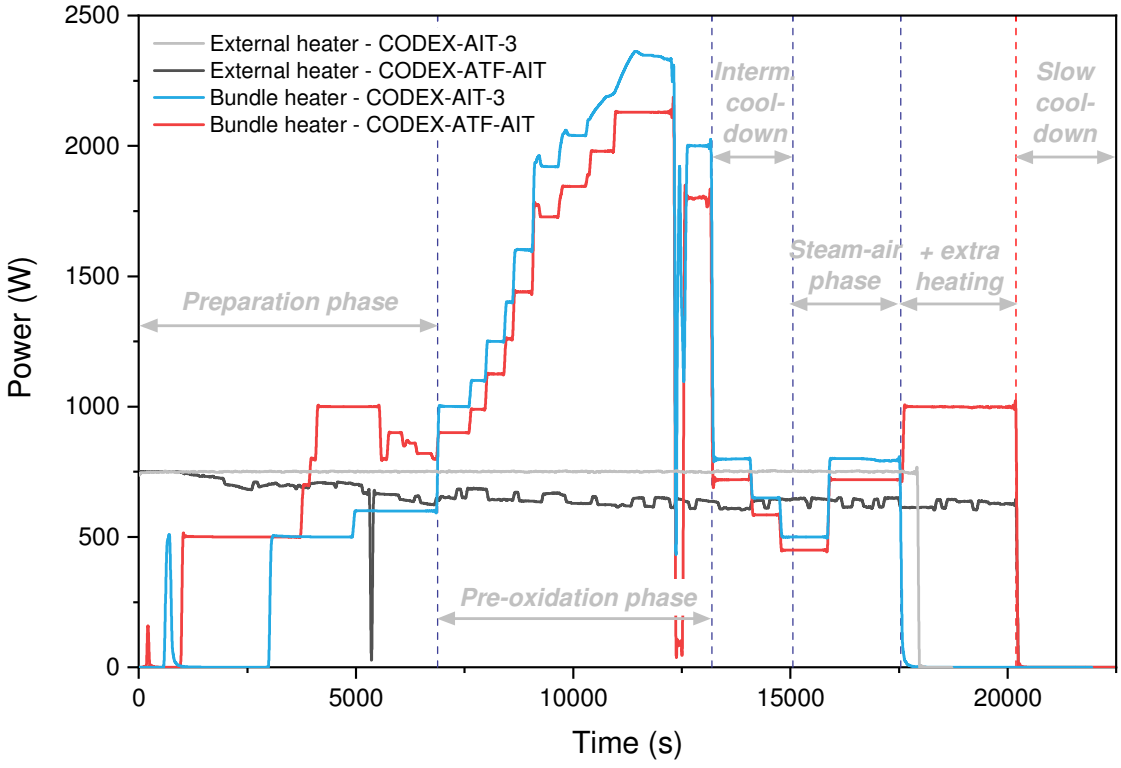


Figure 1: Comparison of power histories of the CODEX-AIT-3 and CODEX-ATF-AIT tests

In the air ingress phase, the temperature rise was significantly slower and smoother compared to the reference experiment CODEX-AIT-3, demonstrating the protective effect of the Cr coating. The duration of the air ingress phase was extended to 1.5 hours (compared to 1 hour in the reference test), with a maximum cladding temperature of 1545 °C (compared to 1600 °C). The temperature profile shifted during this phase, with the peak moving from the upper bundle section to lower elevations due to intense chemical interactions in the less oxidised regions.

Gas analysis confirmed steam and oxygen starvation conditions during air ingress. The partial consumption of nitrogen indicated nitride formation. A total of 1.4 g of hydrogen was generated during the pre-oxidation phase, followed by 3.3 g during the air ingress phase. A controlled cool-down in argon flow was performed to avoid further reactions.

Post-test examinations (endoscopy, light optical microscopy, scanning electron microscopy, energy-dispersive X-ray spectroscopy) were performed to identify degradation mechanisms.

The results confirm the protective role of the Cr coating under air ingress conditions and provide detailed insight into the associated complex material interaction phenomena.

Results

An air ingress experiment was performed in which the experimental bundle was assembled from chromium-coated rods. By comparison with the previous experiment (CODEX-AIT-3), in which no chromium-coated rods were included, the usefulness of chromium coating on fuel element tubes could be assessed.

The bundle was successfully assembled, and during the test, the maximum set temperature was reached. Measurements were conducted in the reference atmosphere. The internally pressurised fuel rods were ballooned and burst, allowing the inner surfaces of these rods to chemically react with steam and air. In comparison with the reference test (CODEX-AIT-3), it was observed that the chromium layer proved beneficial, as high-temperature escalation was delayed and the rod surfaces were protected by the coating. The CODEX-ATF-AIT also revealed that very high temperatures could lead to Cr-Zr eutectic formation and local melting on the surfaces of chromium-coated components. In the case of a nuclear power plant accident, the application of chromium coating could extend the coping time in air ingress type severe accidents, thereby allowing additional time for mitigation actions by the staff.

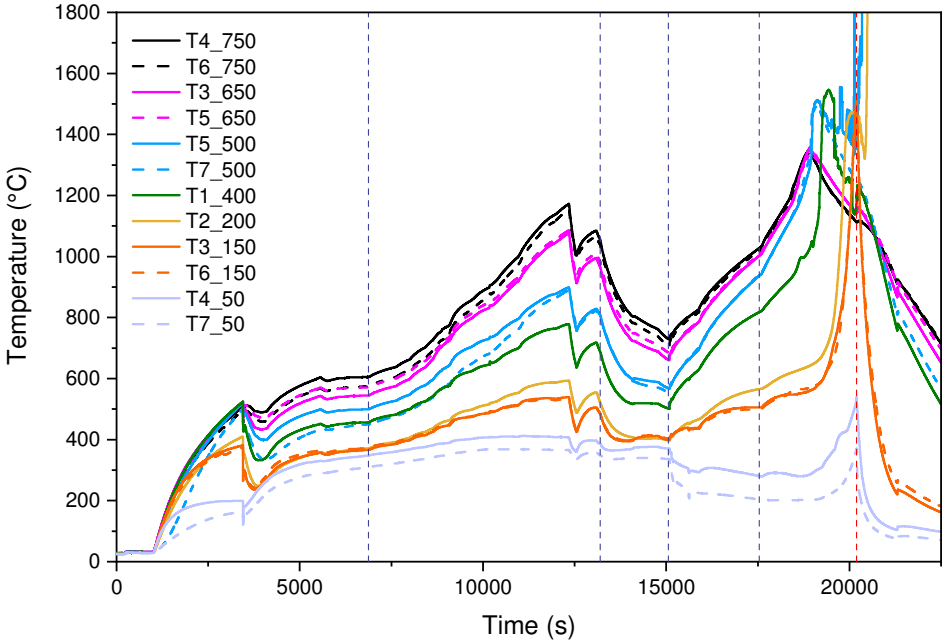


Figure 2: Cladding temperatures in the CODEX-ATF-AIT

Related publications

[1] Z. Hózer, R. Farkas, N. Vér, B. Bürger: *CODEX-ATF: Integral Bundle Test with Accident Tolerant Fuel,* Proceedings of TOPFUEL 2024, Grenoble, ENS

[2] R. Farkas, N. Vér, B. Bürger, A. Pintér Csordás, L. Illés, Z. Hózer, U. Stegmaier: *The CODEX-ATF-AIT integral air ingress experiment,* 29th International QUENCH Workshop, Karlsruhe, 2024-11-19

[3] R. Farkas, N. Vér, B. Bürger, Z. Hózer: *Post-test examination of the integral air ingress experiment CODEX-ATF-AIT,* 30th International QUENCH Workshop, Karlsruhe, 2025-12-16

[4] Z. Hózer, R. Farkas, N. Vér, B. Bürger, A. Pintér-Csordás, M. Király, P. Szabó, S. E. Habbachi, M. Ševeček, M. Steinbrück, J. Stuckert, M. Grosse: *Integral Testing of ATF Fuel under High Temperature Accident Conditions in the CODEX Facility,* (IAEA Technical Meeting on Advanced Technology Fuels, Vienna, 28-31 October 2025)

[5] R. Farkas, N. Vér, B. Bürger, Z. Hózer: *The integral air ingress CODEX-ATF-AIT experiment,* 12th European Review Meeting on Severe Accident Research Conference, Madrid, 2026-05-18

ACOUSTIC EMISSION LABORATORY ACCREDITATION PROJECT

Nagy Attila Gábor

Objective

The primary objective of the 2025 activity is to achieve formal accreditation of the Acoustic Emission (AE) Laboratory according to the **MSZ EN ISO/IEC 17025:2018** standard. Accreditation will validate the laboratory's technical competence in advanced AE-based structural integrity assessments and enable participation in nationally and internationally recognised testing activities.

Methods

To support the accreditation process, a structured approach was adopted:

- Consultation with an external expert experienced in laboratory accreditation frameworks to ensure compliance with legal and technical requirements;
- Development of the full quality management documentation package in line with ISO/IEC 17025, including a Quality Manual, procedures, work instructions, and standardised forms;
- Supporting **procedures and standardised forms** for all testing and quality activities;
- Documentation of **internal audits**, **management reviews**, and **method verification**;
- Participation in an inter-laboratory comparison (round-robin test) to demonstrate measurement competence. The test involved monitoring acoustic emission signals during pressure cycling of a vessel (Figure 1) and performing planar source localisation tests to verify spatial resolution (Figure 2);
- Establishment of **data and IT control systems** ensuring traceability and security.

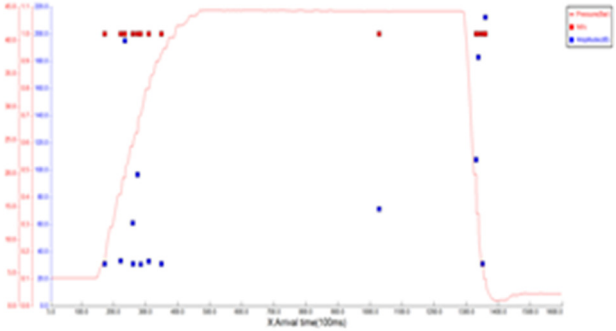


Figure 1: Correlation between vessel pressure (red line) and acoustic emission parameters (hit rate in red squares, amplitude in blue squares) during a pressure cycle test, demonstrating measurement consistency in the inter-laboratory comparison

Results

By November 2025, all required documentation was completed and internally reviewed.



Figure 2: Experimental setup for the inter-laboratory comparison

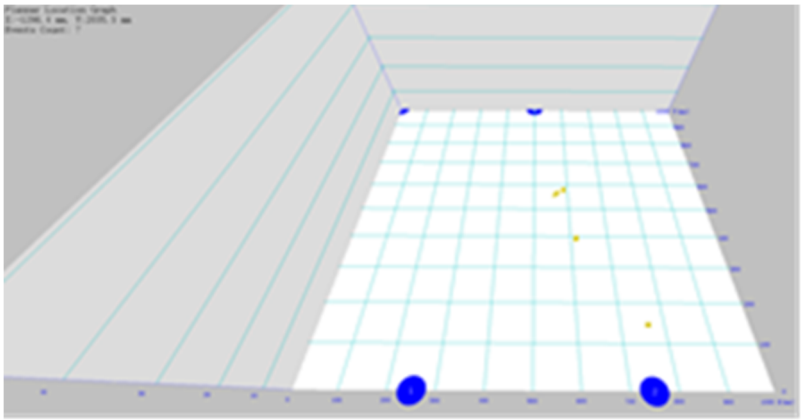


Figure 3: Planar source localisation graph showing seven detected AE events (yellow dots) on a 1000 mm × 1000 mm test plate. Blue circles indicate sensor positions (1-4).

To enhance the credibility and visibility of the laboratory, I actively participated in two national conferences, delivering presentations on AE methodology. Two peer-reviewed articles have been published in Hungarian technical journals, and an English-language manuscript is currently under review for international publication. The inter-laboratory comparison confirmed the laboratory's measurement consistency and reliability, as demonstrated by the clear correlation between pressure transients and AE event parameters (Figure 1). Furthermore, planar localisation tests (Figure 3) verified the system's ability to accurately identify source positions within the monitored structure. The quality system—including data integrity protocols and document control—is fully operational.

Remaining work

Submit the documentation to the accreditation authority.

Related publications

[1] Nagy A. G., Gémes Gy. A.: *Akusztikus emisszióval (AE) történő korróziós folyamatok és vasbetonszerkezetek vizsgálata (Acoustic emission (AE) testing of corrosion processes and reinforced concrete structures),* 2025, Anyagvizsgálók Lapja (Journal of Materials Testing), 2025/I_II.

[2] Nagy A. G., Szabó P. I.: *Az akusztikus emisszió (AE) haditechnikai alkalmazásai (Military applications of acoustic emission (AE)),* Haditechnika (Military technology), accepted, expected to appear in issue 2026/2.

[3] A. G. Nagy, G. A. Gémes: *Mathematical Methods in Acoustic Emission Analysis: Source Localization, Waveform Processing and Noise Filtering,* Institute of Physics (IOP) Conference Series: Materials Science and Engineering, (under review)

EFFECT OF STEAM PRE-OXIDATION ON THE AIR OXIDATION OF SLIM CLADDING

Erzsébet Perez-Feró and Tamás Novotny

Objective

In an air ingress accident, the zirconium-based fuel cladding can undergo significant oxidation. In a real accident scenario, the cladding is already oxidised in water or steam during normal operation or in the initial phase of the accident, before coming into contact with air. The oxide layer formed on the surface – depending on its quality and thickness – can significantly influence the cladding's air oxidation.

Methods

Two oxide layers with different thicknesses (3 µm and 10 µm) were produced on the surface of the SLIM samples in steam at 800 °C and 1100 °C. The thickness and quality of the formed oxide layer were measured using an optical microscope. The pre-oxidised samples were then oxidised in a pure air atmosphere at high temperature. The oxidations were carried out under isothermal conditions at 1000 °C and 1200 °C. The tests were also performed on E110 cladding, and the results for the two cladding types were compared.

Results

The experiments demonstrate a marked difference between the air-oxidation kinetics of the SLIM and E110 claddings (Figure 1). At the same time, the results clearly show that even a relatively thin (3 µm), compact oxide layer can slow down the air oxidation of both materials. A thicker oxide layer further reduces oxidation more effectively. The dense oxide scale formed during steam pre-oxidation impedes the penetration of the oxidising atmosphere to the underlying metal surface.

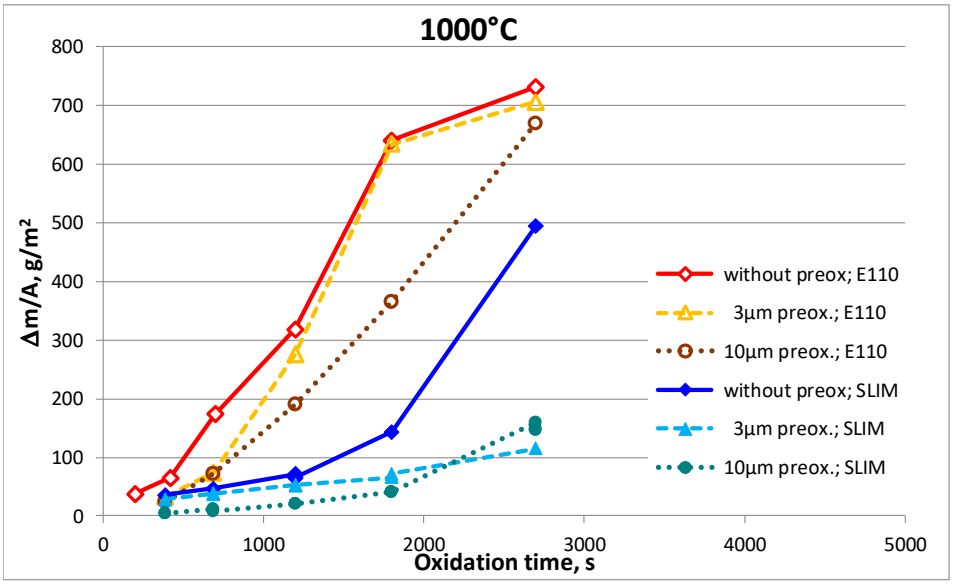


Figure 1: Oxidation kinetics of SLIM and E110 alloys in pure air at 1000 °C

Remaining work

The work has been completed.

Related publications

[1] E. Perez Feró, T. Novotny, M. Horváth: *Effect of steam pre-oxidation on the air oxidation of SLIM cladding,* HUN-REN-EK-FRL-2025-146-1-1-M0, in Hungarian (2025)

PARAMETERISED CROSS-SECTION LIBRARY GENERATION WITH THE SERPENT 2 CODE AND TESTING IN VVER-1200 CORE GEOMETRY WITH THE KIKO3DMG NODAL SIMPLIFIED SPHERICAL HARMONICS (SPN) CODE

Dániel Sebestény, Zoltán István Böröczki, István Pataki, István Panka

Objective

Calculation of core neutronics is generally undertaken in two steps, with the first being a detailed calculation of some regions in the core (e.g., a fuel assembly model) that produces group constants and the second being the calculation of the full core using the aforementioned simplifications and the group constants as input data.

Running the first step every time the second step run is computationally demanding, especially when a large number of core-level calculations are needed, e.g., in core optimisation, in transient calculations, or when iterating with thermal-hydraulic feedback. Therefore, a common practice is that the group constants are generally calculated at many different burnup and state parameter values, and a model is fitted to these results.

Our present research focused on the parameterisation of Monte Carlo-generated group constants. A novel polynomial regression-based method supplemented by automated hyperparameter optimisation (CORK) was the algorithm used in our current work for a VVER-1200-type assembly model. The goal of this study was to apply and test the elaborated parameterisation package in a versatile two-step calculation chain that can be used for various core geometries within a wide range of burnup and state parameters, including both normal and transient conditions.

Methods

The physical model was an assembly of the VVER-1200 reactor in the case of SERPENT 2 for the determination of the parameterised group constant library according to 5 features: burnup, boron concentration, fuel temperature, coolant temperature, and coolant density. For the SERPENT reference calculation and KIKO3DMG multigroup diffusion nodal calculation, a simplified VVER-1200 core model was set up, and the core model was the same in both the KIKO3DMG and the reference calculation.

To verify the method across the state space, the coupled KIKO3DMG results were compared to reference SERPENT 2 calculations in 48 different states with respect to the effective multiplication factor (k_{eff}), the assembly-level power distribution (k_{q}), and the reactivity coefficients.

An important part of the methodology concerned the handling of the different group constants. Two improvements were applied, which increased the numerical stability of the calculations. The total cross section was not fitted directly, but its parts were fitted separately, resulting in a slight improvement of the results.

Another, less straightforward but more impactful step was the fitting of only the S scattering matrix and the difference between the SP (Scattering Production) and S matrices, which significantly enhanced the accuracy of the group constants used for the fitting, decreasing the k_{eff} discrepancy coming strictly from the fitting from the order of several hundred pcm to within 10 pcm.

Results

In comparison to the reference SERPENT full core model, the two-step test calculations with SERPENT and KIKO3DMG using the novel models were well within the desired accuracy when compared to the respective reference SERPENT full core calculations. Both the effective multiplication factors and the approximated reactivity coefficients were in good agreement. The former had a discrepancy of 61.6 pcm in the RMS error metric for 48 test states with various burnup and state parameter values. The latter were estimated with difference quotients, and their discrepancies were found to be well within the 1σ of the applied engineering limits [1].

A baseline linear interpolation was substituted in the calculation pipeline in place of the CORK procedure to showcase the latter's usefulness. While linear interpolation also produced decent results, they were falling well short of those of the CORK algorithm, with an RMS error of k_{eff} of 125.3 pcm as opposed to 61.6 pcm of the CORK algorithm for 48 test states. Reactivity coefficient approximations were within the 3σ of the applied engineering limits but exceeded the 1σ limits in some cases [1].

At the same time, the radial power distribution (k_q) had a consistent discrepancy of around 1-3% in the MAPE (Mean Absolute Percentage Error) metric, which came neither from the two-step methodology nor from the error of the group constant fitting, but from the effects of the homogenization, energy condensation, and diffusion approximation employed by the nodal code. These differences in k_q were observed several times in other similar studies. The results are demonstrated in Fig. 1 and Fig. 2 at different burnup levels in a selected case.

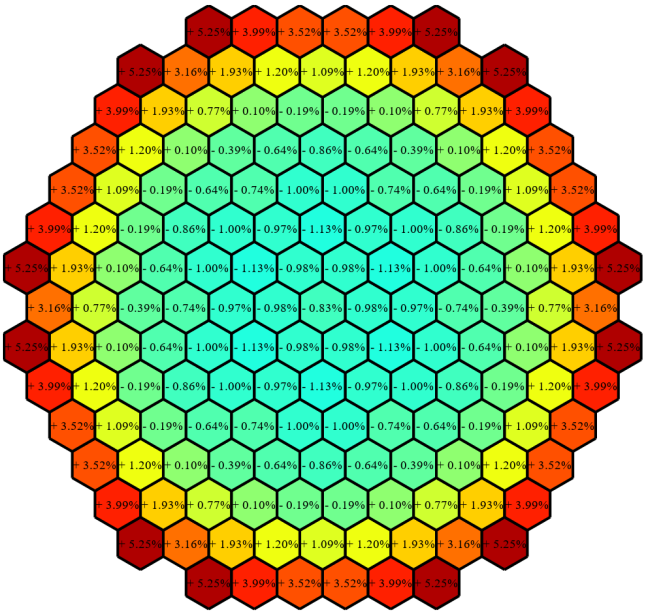


Figure 5: Relative difference between the assembly-wise normalised power distribution of the KIKO3DMG calculation with parameterised group constants and the reference Serpent full core calculation (BU = 0 MWd/kgU; CB = 8.0 g/kg; T_f = 600.0 K; T_m = 400.0 K; ρ_m = 0.900 g/cm³).

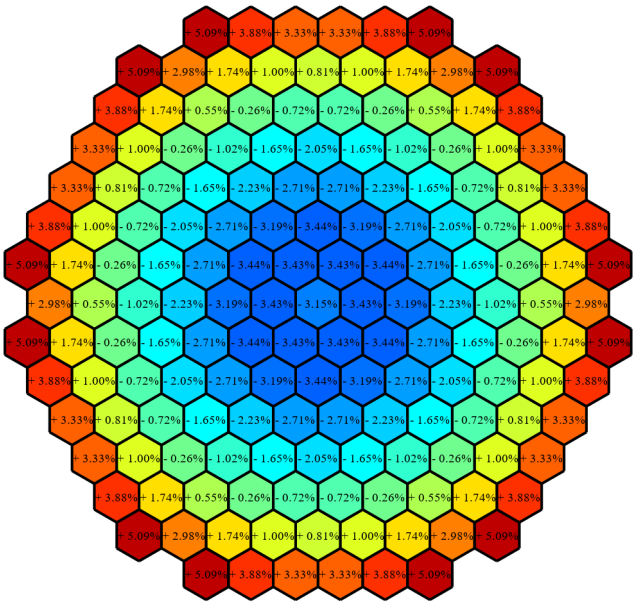


Figure 2: Relative difference between the assembly-wise normalised power distribution of the KIKO3DMG calculation with parameterised group constants and the reference Serpent full core calculation (BU = 20 MWd/kgU; C_B = 8.0 g/kg; T_f = 600.0 K; T_m = 400.0 K; ρ_m = 0.900 g/cm³).

Remaining work

We plan to publish the results in an international journal soon.

Related publication

[1] D. Sebestény, Z. I. Böröczki, I. Pataki, I. Panka: *Testing of Monte Carlo-based, machine learning parameterised group constant generation*, XXII. Nukleáris Technikai Szimpózium (Nuclear Technical Symposium), Szeged, Hungary, November 19-21, 2025. (in Hungarian)

BENCHMARKING AND IMPROVING COMPUTATIONAL TOOLS FOR SMR ANALYSIS

Zoltán István Böröczki, Csenge Komjáti, István Pataki, Áron Vécsi

Objective

In recent years, Small Modular Reactors (SMRs) have received significant attention at both global and local levels. These nuclear reactors with electric power output below 300 MW per module are designed to be produced in series, easily transported, and deployed to meet a wide range of industrial and economic needs. However, the design and operation of SMRs present numerous challenges, which are currently being extensively studied by the scientific community.

The reactor cores of SMRs are significantly smaller than those of traditional reactors, and many designs are Generation IV reactor types, utilising liquid metal or helium as coolant and operating in a fast-neutron spectrum. Due to their size and fast spectrum, these reactors are characterised by high neutron leakage and significant flux anisotropies, which complicate modelling and necessitate the assessment of the applicability of codes and methods used in the Nuclear Safety Department (NBL).

Methods

In recent years, several investigations have been conducted for three benchmark exercises and the corresponding reactor designs, with different aims, to evaluate the capabilities of commonly used codes and methods in the NBL for small-sized nuclear reactors:

- First, a purely neutronics benchmark of the NuScale Integrated Pressurised Water Reactor (IPWR) concept was chosen primarily to test different group constant generation techniques and the effects of the higher-order transport approximations on these types of designs.
- The South-West Experimental Fast Oxide Reactor (SEFOR) benchmark was selected as a basis for fast reactor designs. The benchmark is still under development by the OECD/NEA sub-group on Uncertainty Analysis in Modelling (UAM) for Design, Operation, and Safety Analysis of Sodium-cooled Fast Reactors (SFR-UAM), providing an opportunity for scientific cooperation to compare and evaluate neutronics and thermal-hydraulic calculations.
- Moreover, the PRATIC benchmark exercise was also announced as part of the Light-Water Small Modular Reactors (LW-SMR) benchmark program by the OECD/NEA Working Party on Scientific Issues of Reactor Systems (WPRS), offering detailed descriptions of geometric, reactor physics, and thermohydraulic benchmarks.

For the various benchmark exercises, deterministic and Monte Carlo (MC) codes are used to perform various analyses, testing the capabilities of the programs available at our laboratory. The Serpent 2, SCALE KENO and MCNP Monte Carlo codes are used, models were developed, and reference solutions were determined for the diverse reactor states. These results provided the reference solutions for the effective multiplication factors (k_{eff}), reaction rates, various reactivity feedback coefficients, and pin- and assembly-wise power distributions, which were used to evaluate the deterministic models.

Deterministic codes require group constants for their calculations, which can be generated using different methods, significantly influencing the final results. A Python-based program is now being developed to collect, manipulate, parameterise, or format these group constants originating from various sources, such as Serpent 2 or SCALE NEWT. The new code is developed with high flexibility in mind to satisfy the various needs of the final deterministic solvers and to describe the diverse original problems. It also needs to leave room for fast-paced testing capabilities to analyse the different group constant generation approaches.

The deterministic calculations are performed using the PARTISN multigroup discrete ordinates neutron transport code and the KIKO3DMG nodal diffusion and SPn transport code developed at our laboratory. The performance of the KIKO3DMG in various benchmarking exercises is one of the primary subjects of our investigation.

Results

Calculations for the NuSCale benchmark

The NuScale-type benchmark was published in 2023, which includes detailed 3D fuel assembly and core geometries, as well as material compositions and operational parameters. The benchmark presents reference results generated by the Serpent 2 Monte Carlo code for the reactivity worth of control rods and radial pin, assembly-wise power distributions.

Detailed 3D models were created for the MCNP and Serpent 2 Monte Carlo codes to generate reference solutions for the benchmarking exercise. Few-group cross-sections were generated using the Serpent 2 Monte Carlo code and the SCALE NEWT deterministic code. The performance of the deterministic KIKO3DMG model was tested with both sets of cross-sections; furthermore, the mesh and the effects of higher-order transport approximations were also investigated in this geometry. Results indicated that the accurate modelling of a small-sized IPWR core requires SP_3 approximations.

Calculations for the SEFOR benchmark

In this year, three simple test cases for thermal-hydraulic simulations have been announced in the framework of the SEFOR benchmark exercise: an assembly model, representing a single isolated fuel assembly; a lattice model, simulating a regular

array of assemblies; and a SEFOR-like model, which serves as a simplified representation of the SEFOR reactor geometry. The SURET (SUbchannel REactor Thermohydraulics made by EK) code was chosen for these simulation exercises, and work on modifying the code has begun to extend its capabilities for the accurate simulation of the sodium cooling medium. Preliminary results indicated good agreement with the benchmark participants, highlighting the differences between the modelling approaches and places for further code and model development.

Calculations for the PRATIC benchmark

In 2024, the PRATIC, a soluble-boron-free pressurised water-cooled SMR reactor benchmark, was introduced, which now forms a subtask in the Light-Water SMR (LW-SMR) NEA WPRS working group. Its fuel enrichment ranges between 2.5% and 5%, and it also contains gadolinium fuel rods —between 0 and 36 pins per assembly. The task description includes detailed geometrical, reactor-physics, and thermohydraulic specifications. The reference results distributed with the benchmark were produced using the deterministic codes APOLLO2 and CRONOS2.

Assembly and full-core models were created for the Serpent 2 Monte Carlo code. Burn-up calculations were performed for the various types of assemblies using different modelling approaches, and the effective multiplication factors were compared to APOLLO2 results. Sensitivity analysis was conducted during the burn-up calculations for the radial meshes in the fuel pins, as shown in Figure 1.

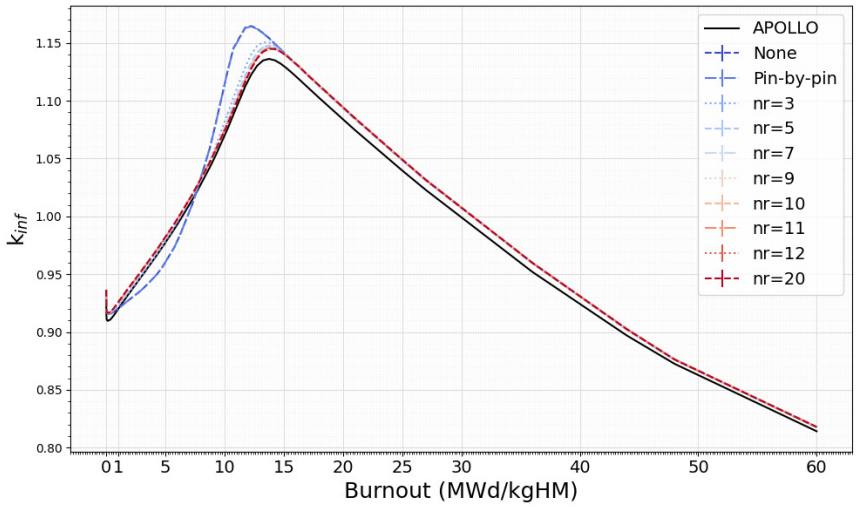


Figure 1: Effect of the radial mesh in the gadolinium pins on the effective multiplication factor. (nr denotes the number of equal volume radial divisions in the pins)

Remaining work

In the future, we would like to refine and further develop the Python package used for group-constant preparation to enhance our testing capabilities in the deterministic calculations. The numerous options during energy condensation and homogenization directly affect the results of the deterministic calculations; therefore, multiple analyses will still need to be performed to identify best practices in simulating SMR reactors.

Related publications

[1] E. García, L. Buiron, N. G. Herranz, A. Jiménez-Carrascosa, Y. Cao, Z. I. Böröczki: *Status of the SEFOR benchmark Phase I: Isothermal tests,* Proceedings of Best Estimate Plus Uncertainty International Conference (BEPU 2024), Lucca, Italy, May 21-26, 2024.

[2] Z. I. Böröczki, I. Pataki: *Deterministic and Monte Carlo model developments for the SEFOR benchmark exercise,* WPRS Benchmarks Workshop 2024, Lucca, Italy, May 19-23, 2024.

[3] Cs. Komjáti, Z. I. Böröczki, I. Pataki: *Számítások NuScale-jellegű reaktorfizikai benchmarkhoz (Calculations for a NuScale-like reactor physics benchmark).* XXI. Nukleáris Technikai Szimpózium (Nuclear Technical Symposium), Budapest, Hungary, November 28-29, 2024.

[4] Z. I. Böröczki, I. Pataki: *Részvétel a SEFOR benchmark feladatban (Participation in the SEFOR benchmark task),* XXI. Nukleáris Technikai Szimpózium (Nuclear Technical Symposium), Budapest, Hungary, November 28-29, 2024.

[5] Z. I. Böröczki, Á. Vécsi: *SEFOR Subchannel Simulation with SURET,* WPRS Benchmarks Workshop 2025, Cambridge, United Kingdom, June 30 – July 4, 2025.

[6] Cs. Komjáti, Z. I. Böröczki, I. Pataki: *Reaktorfizikai kódok felkészítése SMR-ek elemzésére (Preparing reactor physics codes for SMR analysis),* XXII. Nukleáris Technikai Szimpózium (Nuclear Technical Symposium), Szeged, Hungary, November 19-21, 2025.

SUPPORT FOR THE PREPARATION OF SMALL MODULAR REACTORS IN HUNGARY

Márton Király, Ildikó Boros, Margit Fábián, Attila Imre, Tamás János Katona, Tamás Pázmándi, Éva Széles, Szabina Török, Péter Völgyesi, Péter Zagyvai

Objective

Recent international trends and domestic nuclear-industry developments indicate that Hungary should begin near-term preparation for one or more potential Small Modular Reactor (SMR) projects. This work, therefore, does not recommend a single "best" reactor, but proposes an executable, risk-managed roadmap: first, quantify national objectives and define priority use cases; then clarify the regulatory/licensing pathway and site-selection logic; in parallel, establish supplier and human-resource capabilities; and only then narrow technology options and prepare first projects. The decision goal is not a purely technical optimum, but a coherent pathway that is financeable, repeatable, and robust under uncertainty. SMRs are treated as systems with different deployment and operating logic than large units, where value is measured not only in electricity cost but also in total system cost and delivered services (electricity, heat, hydrogen, flexibility).

Methods

The assessment combined policy/program design with techno-economic and infrastructure screening. We identified three complementary strategic application domains: (1) accelerating power-sector decarbonisation with flexible low-carbon capacity supporting renewable integration; (2) decarbonising heat markets, especially district heating and high-temperature industrial heat; (3) providing a reliable low-carbon supply for hydrogen and data-economy loads. National readiness was structured around the IAEA Milestones approach and its 19 infrastructure areas, leveraging Hungary's non-newcomer status (operational NPP, research reactor, waste management, mature regulatory system) while highlighting SMR-specific gaps (modular construction, non-water-cooled concepts, multi-product applications). A staged site-selection methodology was outlined: regional screening (grid access, heat sink capability, land use, exclusion zones, protected areas), followed by detailed technical safety refinement (meteorology, hydrology, geology/seismology/geotechnics/ hydrogeology), with early inclusion of public acceptance, logistics, expandability, security, and emergency preparedness; brownfield industrial/energy sites were prioritised. Capability building was mapped into parallel workstreams: early regulatory dialogue and standards adaptation; supplier ecosystem development (open call and database, competence screening, audits and gap-closing, capacity management); modular workforce training from nuclear fundamentals to SMR operation, maintenance, cyber-security, and non-LWR competencies. Technology coverage included 18 SMR concepts across Light-Water Reactor (LWR) and non-LWR families, with six water-cooled reference designs reviewed in depth using a consistent template (fuel cycle, systems, safety philosophy, supply chain, licensing status, project maturity).

Results

The work delivers an implementation-oriented framework for launching Hungarian SMR projects as a structured national program rather than a one-off technology choice. SMRs offer potential advantages—reduced capital at the unit level, modular construction and factory assembly that may lower schedule risk (still to be demonstrated), and passive, physics-driven safety concepts—while their system value depends on multi-product services and integration needs. A coherent decision logic is emphasised: "what, where, and how" (use cases, siting, deployment model) must be resolved before "with what, for how much, and by when" (technology, cost, schedule). Key near-term actions include quantitative power-system and heat-market modelling to size demand and integration requirements; early site concept development and supplier pre-qualification; and structured pre-licensing engagement to adapt methodologies for modular and multi-purpose facilities. The analysis finds that water-cooled reference SMRs benefit from stronger licensing precedents that can improve predictability, yet higher system-value directions (district heating, high-temperature heat, thermal storage and balancing, hydrogen coupling) should remain in the option space for mid- to long-term strategy. Financing is identified as a primary First-Of-A-Kind (FOAK) barrier; a toolbox is proposed (Power Purchase Agreements / Heat Purchase Agreements (PPA/HPA) structures, capacity/availability mechanisms, regulated asset base-type approaches, and targeted public risk sharing), with milestone-based disbursement to control risk. Overall, the reports provide a repeatable pathway from strategic fit and regulatory clarity through siting and social conditions to supplier/H.R. readiness and financeable business models—supporting credible prospects for SMR deployment that can deliver electricity and, where justified, heat and hydrogen while strengthening flexibility, security of supply, and climate objectives.

Remaining work

Based on the reports generated in this project that served as the scientific background study for a governmental proposal, at the end of 2025, the Hungarian Parliament confirmed the plans to move forward with the Hungarian SMR project.

OPTIMISED MANOEUVRING OF NUCLEAR POWER PLANTS: THE ACTUAL CONSTRAINTS AND CONSEQUENCES

Pál Szentannai and Tamás Fekete

Objective

Apart from the increasing share of uncontrollable renewables in the energy mix, and aside from the successive stopping of traditional, fossil-fueled power plants, the consumption–production balance of the grid must be permanently assured. This necessitates the controllability of many nuclear power plants, too.

Methods

Traditional load control solutions focus only on the controlled variable; as an upgrade, a more comprehensive optimum seeking approach is proposed by the authors. If a nuclear power plant is in the manoeuvring regime, the actual constraints and consequences of the nonstationary transitions have to be recognised, formulated, and considered. The external expectations are stated from the grid operator's side – generally as time-dependent constraints on the electrical load output. The internal aspects are the versatile side effects of the transients, mostly caused by thermal stresses. To find the optimal balance between fast electrical load change and low damage on the reactor side, a cost function is needed, which considers and weights the consequences while adhering to the constraints. The resulting actuator trajectories indicate that a simple slowing down of the reactor's load change is far from the optimal load-following strategy.

Results

A schematic overview of the optimisation process developed by us is shown in the following figure. Note that this is not an online controller; its output is the optimal trajectory for the investigated case, as targeted at the beginning of the research work. Besides this, many other variables along the optimal pathway are also delivered, which can be used for a technical overview, or, e.g., as a comparative reference pathway for any controller realisations.

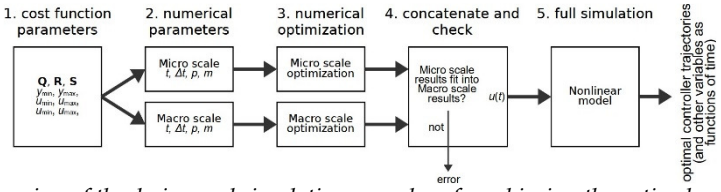


Figure 1: Overview of the design and simulation procedure for achieving the optimal actuator trajectories

A few further details of the nonlinear optimisation procedure are shown in the next figures.

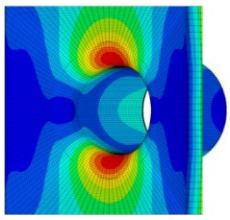


Figure 2: Thermal stress field within the solid body around the nozzle corner in the course of increasing the unit load

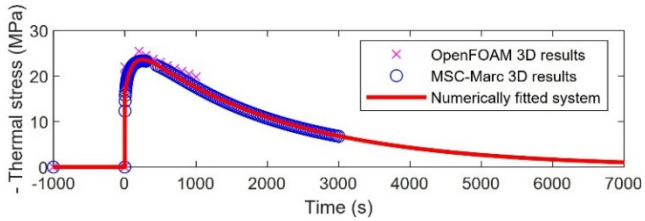


Figure 3: Step response function fitted to the outcomes of the 3D calculations

Remaining work

Involving the fuel behaviour and investigations under further criteria formulated by the grid operator.

Related publications

[1] B. Pudleiner, T. Szucs, T. Fekete, P. Szentannai: *Dynamical modeling of the thermal stress in the nozzle corner of reactor pressure vessels for model-based power maneuvering control design,* Nucl Eng Des **445:** 114529 (2025) https://doi.org/10.1016/j.nucengdes.2025.114529

[2] P. Szentannai, T. Fekete: *The actual constraints and consequences of the maneuvering operation of PWRs - An optimum seeking approach,* Nucl Eng Des **445,** 114480 (2025) https://doi.org/10.1016/j.nucengdes.2025.114480

[3] B. Pudleiner, L. Désesquelles, C. Matter, T. Fekete, P. Szentannai: *Optimisation of the control curves of load-changing nuclear power units taking into account thermal stress,* Archives of Thermodynamics 45, (2025)

[4] P. Szentannai, T. Fekete: *Life-Time Considering Control (LTCC) of Load Changes in Nuclear and Conventional Power Plants for Reducing Ecological Footprint.* In: Lackner M, Sajjadi B, Chen W-Y, editors. Handbook of Climate Change Mitigation and Adaptation, New York: Springer; 1–69. (2025) https://doi.org/10.1007/978-1-4614-6431-0_172-3

[5] P. Szentannai, T. Szucs, B. Pudleiner, T. Fekete: *Transient phenomena and their consideration in load-following control of nuclear power plants,* Thermal Science **28:** 3183–93 (2024) https://doi.org/10.2298/TSCI230805052S

FINITE ELEMENT ANALYSIS OF THE NECKING OF TENSILE TESTS

Tamás Fekete, Dániel Antók, Levente Tatár

Objective

To ensure the safety of large-scale pressure systems used in the nuclear industry, the reliability of structural integrity computations must be enhanced. Recently, we have developed the Digital Twin method to determine **the strength and fracture mechanics of structural steels. As several advanced methods for structural integrity computations** depend heavily on the plastic properties of metals, to support our calculations, the reliability of the assessment of plastic material properties needs to be improved. Several methods exist to obtain a material's flow curve using tensile test results, each with its own advantages and disadvantages. Our goal was to develop a new, improved method for processing tensile test results.

Methods

The flow curve can be determined using simple analytical formulas until necking occurs. As necking evolves, the initially uniaxial stress and strain fields become triaxial, and the flow curve obtained from these formulas no longer accurately reflects the material's behaviour. Several correction methods have been developed to address this issue, including the Bridgman, Siebel-Davidenkov-Spiridonova, Szczepinski, and Gromada methods. The commonality of these correction methods is characterised by the utilisation of the radius of curvature (R) at neck formation (see Figure 3). Majzoobi developed a novel method that does not utilise the radius of curvature, which is difficult to measure during tensile tests. The team is currently engaged in the development of a novel correction method (Tatár), which involves the measurement of only cross-section diameters. The approach is grounded in the principle of elastic relaxation.

Tensile test experiments were simulated using the finite element method (Figure 1). The geometry was axially symmetric, and a homogeneous and isotropic material was assumed. Von Mises yield criterion and large strain theory were used in all models.

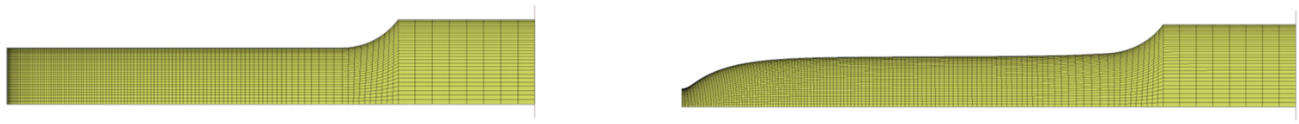


Figure 1: Finite Element Model of a Tensile Test Specimen; Initial and Final State

Ten different artificial "input" flow curves (Figure 2) were used in the simulations. The results provided strain and stress values. Using these results, the radius of the cross section (a) and the radius of the curvature at the necking (R) could also be determined (Figure 3). These data were then processed using the aforementioned correction methods. Ultimately, "output" flow curves were created. Comparing the "input" and "output" flow curves allows one to estimate the accuracy of the correction methods.

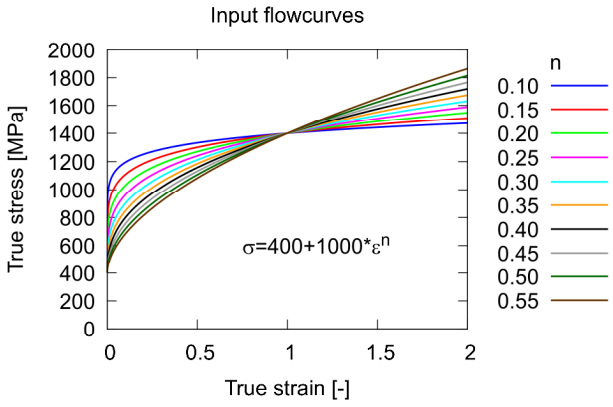


Figure 2: Input Flow Curves

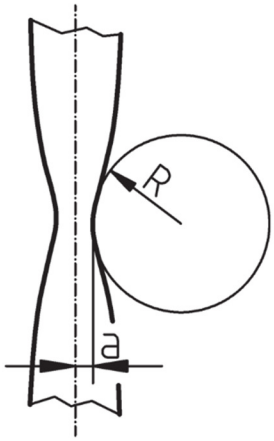


Figure 3: Cross-section and Curvature

Results

The "output" flow curves can be seen in Figure 4. Considering all "input" flow curves, one can create bands representing the accuracy of the correction methods by calculating the difference between the "input" and "output" curves (Figure 5).

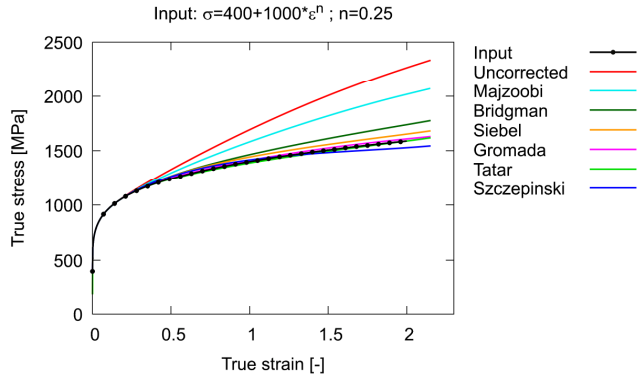


Figure 4: Output Flow Curves

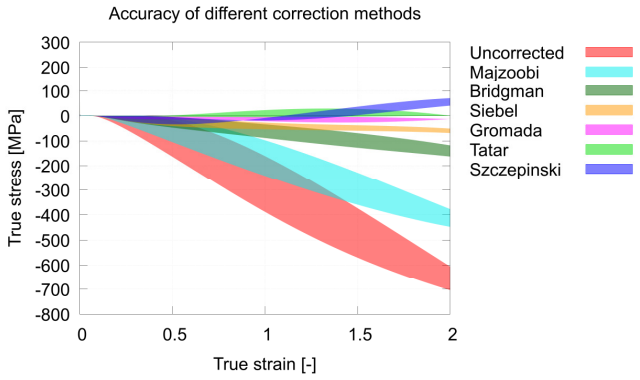


Figure 5: Correction Method Accuracy

Analysis of the uncorrected "output" curves indicates a significant discrepancy from the "input" curves, thus rendering them unsuitable for use in the simulation of large plastic deformations. The Majzoobi correction method, which does not utilise curvature, produced the poorest results among the methods examined in the study when applied to deformation ranges above 0.5. The Bridgman method, a well-known technique in the field, is arguably the most widely employed. However, its precision is inadequate at significant deformation levels. The Siebel and Szczepinski correction methods have been shown to yield outcomes that surpass those of the Bridgman method; however, they are not as frequently employed due to the fact that they were not initially published in English. The Gromada method has been demonstrated to produce optimal results; however, its formulas are characterised by a high degree of complexity.

The Tatar method is a relatively straightforward technique that has yielded encouraging results.

Remaining work

As the artificial flow curves used in this work include only a strain hardening region, the accuracy of the correction methods needs to be assessed based on artificial flow curves with a considerable flow region.

The Tatár correction method is a purely empirical one. Its applicability has to be further checked and optimised against different artificial and realistic flow curves.

Related publication

[1] L. Tatar, D. Antok: *Szakítóvizsgálat kontrakciós szakaszának közelítései (Approximations of the contraction phase of tensile testing)*, XXII. Nuclear Technical Symposium, Szeged (in Hungarian)

A NEW CONCEPT FOR THE METHODOLOGY OF STRUCTURAL INTEGRITY COMPUTATIONS

Tamás Fekete

Objective

Large-Scale Engineering Systems (*LSES*s) are designed for a specified service lifetime, referred to as the Design Service Lifetime (*DSL*). During the third quarter of the 20th century, the *DSL* of an *LSES* was typically 30–40 Operating Years (*OY*). Conversely, the *DSL* of a newly constructed plant, such as a Nuclear Power Plant (*NPP*), is currently 60 OY. The Operating License (*OL*) of a newly constructed plant is typically granted for the duration of the plant's *DSL*. Large-scale pressure systems (*LSPS*s) are of paramount importance for the safety of power plants, such as nuclear power plants (*NPP*s), and heavy chemical facilities. The overall service life of an industrial plant is contingent upon the service life of its safety-critical *LSPS*s. During the design phase, Design Safety Calculations (*DSC*s) are implemented to demonstrate the safety of *LSPS*s, at least up to the *DSL*. During operation, Structural Integrity Computations/Calculations (*SIC*s) are conducted to ascertain the conditions and timeframes—up to the Technically Allowable Lifetime (*TAL*)—under which the safety of an *LSPS* can be expected. The issuance of an Extended Operating License (*EOL*) to an operating plant is contingent upon the demonstration by the Structural Integrity Calculations (*SIC*s) that the *TAL* of its *LSPS* exceeds the Extended Operating Time (*EOT*) designated for the facility's original design. A significant number of *NPP*s constructed around the world during the latter third of the 20th century have been granted an *EOL*, referred to as the "first-phase *EOL*", in most cases for a period of 20 *OY*. Presently, *NPP* proprietors are preparing to submit applications for a "second-phase *EOL*", with the objective of obtaining supplementary 20-year licenses. These *NPP*s will operate within the Long-Term Operation (*LTO*) range, which extends from 70 to 80 *OY*. The methodology employed in *SIC* projects during the "first-phase *EOL*" procedures was identical to that implemented for *DSC*s. However, as preparations for the "second-phase *EOL*" are underway, several previously unaddressed issues have come to the fore, requiring novel and rigorous safety assessments. This is because the ageing of *LSPS* structural materials over the course of decades of operation has led to a significant shift in the conditions deemed necessary for safe operation. Consequently, a careful re-examination of the *SIC* methodology from its foundational principles has become imperative.

The objective of the research was to formulate and develop a novel theory for *SIC*s that is consistent with the prevailing theory, where applicable, but goes beyond the limitations of the disciplinary framework and is valid under a broader range of conditions.

Methods

The research was based on the key hypothesis that human culture is a unified whole, in which every cultural discipline carries partial information about the world. That is to say, the hypothesis was that cultural disciplines are characterised by incomplete, fragmented knowledge, which complement each other in such a way that together they provide a good description of the whole. This constitutes the fundamental principle of a holistic worldview. In contemporary technological civilisations, the assurance of adequate everyday living conditions gives rise to increasingly complex engineering problems, the resolution of which calls for more rational development of the Engineering Sciences. The rational development of Scientific Theories falls within the realm of Philosophy. A conceptual model was employed to take into account the requirements of a holistic worldview. This model was used to support the research methodology. As illustrated in Figure 1, the methodological model demonstrates the interrelation between Philosophy, Science, Engineering, and Practice. The research methodology was based on a pragmatic combination of methods incorporating philosophical, scientific, theoretical, and engineering application aspects, following the Conceptual Model.

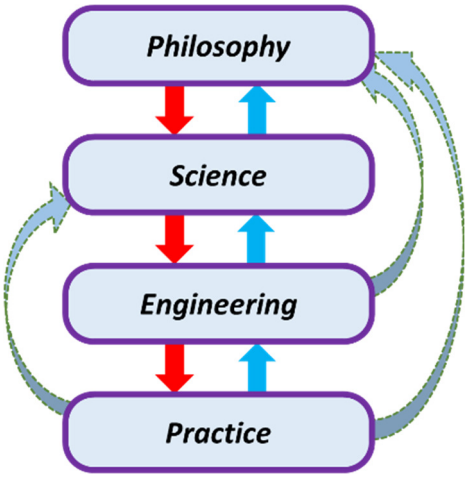


Figure 1: The relationship between Philosophy, Science, Engineering, and Practice in the Conceptual Model.

The research program commenced with general studies concerning research methodology, underpinned by philosophical tenets, to elucidate the existence of a methodology that can be employed to address tasks transcending the realm of model development within individual scientific disciplines. These tasks necessitate a more profound examination, including the relationship between different disciplinary theories, which extends beyond the scope of routine/day-to-day scientific practice and necessitates a more comprehensive investigation. The second phase of the research was based on the results of research methodology studies. In the initial phase, a thorough, contemplative evaluation of the theoretical underpinnings of the *SIC* methodology was conducted, with particular emphasis on the principles underpinning each discipline. In the subsequent step, hypotheses were formulated on the basis of the results of the evaluation, with the aim of ensuring that inconsistencies between the fundamental principles of the original disciplines were eliminated. In the third step of the process, a scientific theory was sought that could serve as a metadiscipline for the original disciplines. In the third phase of the research, the most significant theoretical connections of the scientific framework theory were summarised. In the fourth phase of the research, simulations carried out as part of an industrial case study confirmed that the engineering models derived from the framework theory are promising for future safety analyses.

Results

The development of the novel methodology for *SIC*s required a paradigmatic shift from the prevailing disciplinary-based theoretical framework to a conceptually novel, holistic framework. This shift was methodologically justified and constituted a pivotal step in the research. Philosophy, as a framework, was founded to address general conceptual issues systematically, and therefore, this problem was solved using philosophical methods. It is evident that the disciplinary and the holistic approaches to science represent two discrete paradigms. Consequently, an epistemological method was required that would not only facilitate the development of a scientific discipline and its associated models but also serve as a suitable instrument for developments impacting the system of scientific disciplines and encompassing significant philosophical inquiries. The Aristotelian Analytic-Synthetic Method (*ASM*), as illustrated in Figure 2 (left side), serves as the foundation for contemporary scientific methodology, yet it is not well-suited for this undertaking. Concurrently, the adequate methodological basis for resolving problems involving a paradigm shift, which is recognised as a major philosophical task, is a new version of the Analytical Method (*AM*) –adapted to contemporary requirements– which was also practised in early antiquity but was first documented by Plato. This novel approach is delineated on the right-hand side of Figure 2. The *AM* has been demonstrated to be an effective method that can be used not only in the development of models within scientific disciplines, but also as a suitable tool for the process of creating new theories from existing ones, where a Conceptual Shift (*CS*) is required. The Aristotelian *ASM* and the *AM*, as expounded by Plato, can also be regarded as two paradigms. The *ASM* posits that scientific disciplines are closed systems in terms of information, whereas the *AM* is predicated on the concept of open systems in terms of information. During the transition from *ASM* to *AM*, *CS* is implemented by a shift from the closed system concept to the open systems concept.

As a preliminary step towards scientific-level investigations, a reflexive evaluation of the disciplines comprising the international best practice-based *SIC* methodology was performed. These disciplines include thermal conductivity calculations, strength calculations, and fracture mechanics calculations. The analyses demonstrated that the various theories were developed from divergent worldviews. The thermal conductivity calculations were based on irreversible fundamentals, while the strength and fracture mechanics analyses were based on reversible ones. The fundamental principles of the theory employed for ageing calculations remain opaque to the present day. Moreover, the development of the individual disciplines was undertaken in accordance with the principles of the closed system concept.

From a scientific standpoint, the *AM* furnished the methodological basis for the theoretical development and its verification, encompassing the *CS* and the generalisation of the extant theoretical framework, thereby ensuring compatibility with the original framework within its area of validity. From a philosophical perspective, the *CS* represented a shift from the disciplinary approach to science that was prevalent in the 19th century to a holistic concept that has become a central tenet of modern science. The classical methodology of *SIC*s was developed from a disciplinary perspective, while the new methodology of *SIC*s is based on holistic principles. The novel *SIC* methodology is rooted in the premise that irreversibility is an inherent feature of the universe. This finding indicates that the theoretical models of heat transport, mechanical and fracture mechanics calculations, and ageing analyses are all dissipative. The overarching theoretical framework underpinning dissipative systems is that of Modern Thermodynamics or, in the case of solids, Modern Thermomechanics. In this framework, the second law of Thermodynamics serves to integrate and coordinate the various subsystems representing different disciplines, thereby forming a unified whole. Consequently, Modern Thermodynamics is a holistic theory. The physical umbrella theory of the new *SIC* methodology is a branch of Modern Thermodynamics, namely Nonequilibrium Continuum Thermodynamics/Thermomechanics. This is a metadiscipline comprising heat transport theory, continuum mechanics, fracture mechanics and ageing theory. For a visual representation of the conceptual shift, refer to Figure 3.

The advent of modern Non-Equilibrium Continuum Thermodynamics/Thermomechanics as the prevailing overarching theory for *SIC*s has paved the way for a novel approach to the structural materials of engineered systems investigated through *SIC*s. In this regard, structural materials are to be regarded as inhomogeneous, out-of-equilibrium thermodynamic systems, and their time-dependent behaviour is to be interpreted within the framework of this unified conceptualisation. One of the most significant theorems of the novel Nonequilibrium Thermodynamics-based framework theory for engineering professions is that, under general conditions, the ***J***-integral is path-dependent –i.e. local $\hat{\boldsymbol{J}}$ values and far-field $\bar{\boldsymbol{J}}$ values are shown to be different, which is an inevitable consequence inherent in the description of inhomogeneous materials. It therefore

follows that the ***J***-integral type description is also valid for inhomogeneous materials. However, around the crack edge, an inhomogeneous $\bar{J}$ field generally develops, which is the sum of the $\hat{J}$ calculated at the crack edge and a $C_{inh}(r,\varphi)$ term, i.e. $\bar{J}(r,\varphi) = \hat{J} + C_{inh}(r,\varphi)$. The novel ***J***-integral concept represents a substantial extension of the classic Rice *J*-integral.

The findings of a transient fracture mechanics analysis, grounded in the novel *SIC* methodology and conducted for an industry-relevant transient, demonstrate that during a Pressurised Thermal Shock (*PTS*) transient characterised by rapid cooling followed by y reheating, the ***J***-integral is path-dependent, during the entire *PTS* transient – i.e., not solely during unloading but additionally during loading. As Figure 4 shows, $C_{inh} \neq 0$ throughout the *PTS* transient.

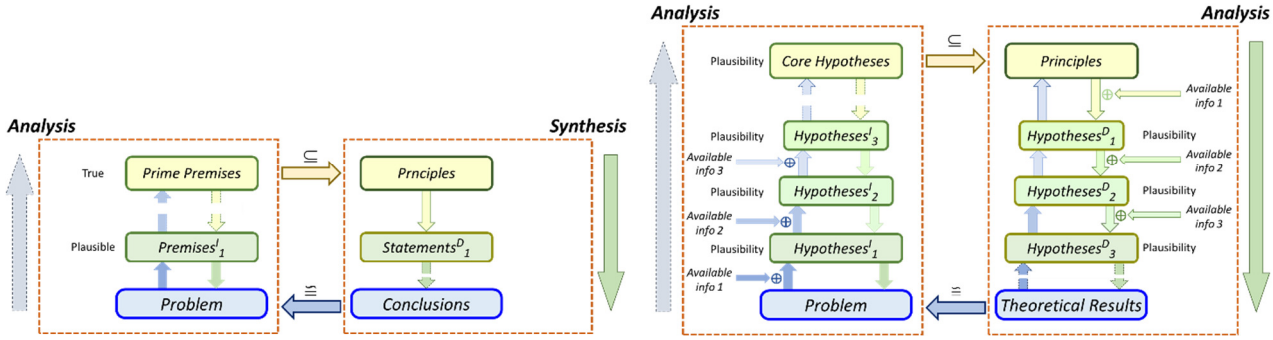


Figure 2: (left) The Scheme of Aristotle's Analytic-Synthetic Method; (right) The modern Analytic Method

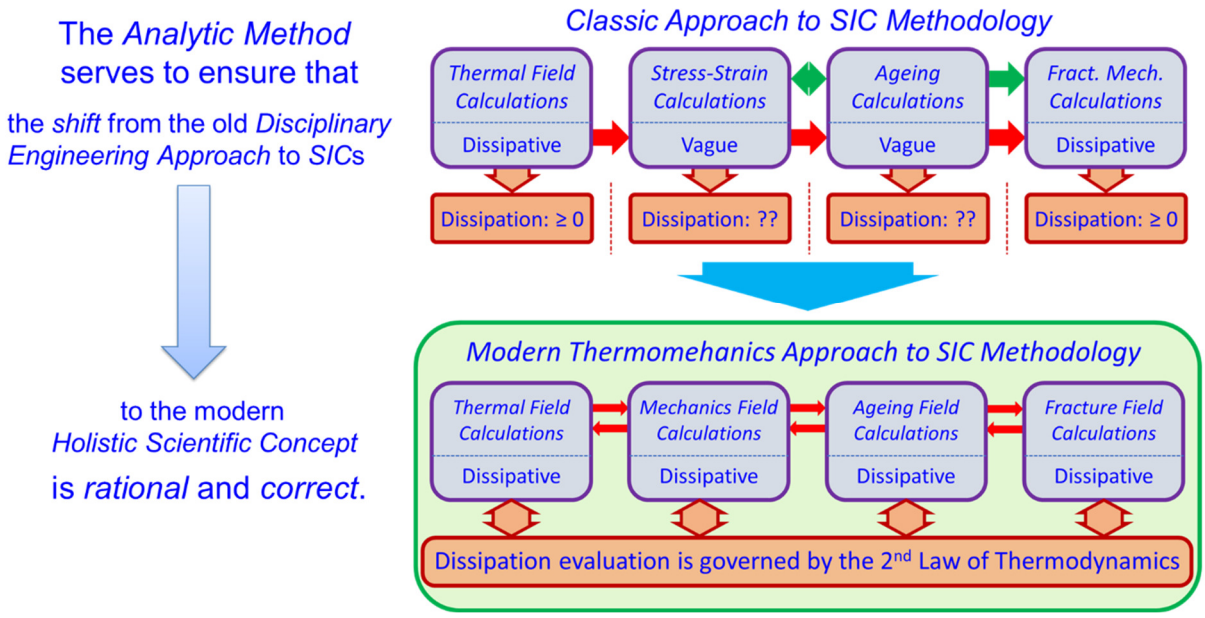


Figure 3: The Conceptual Shift supported by the AM during the methodological development of SICs

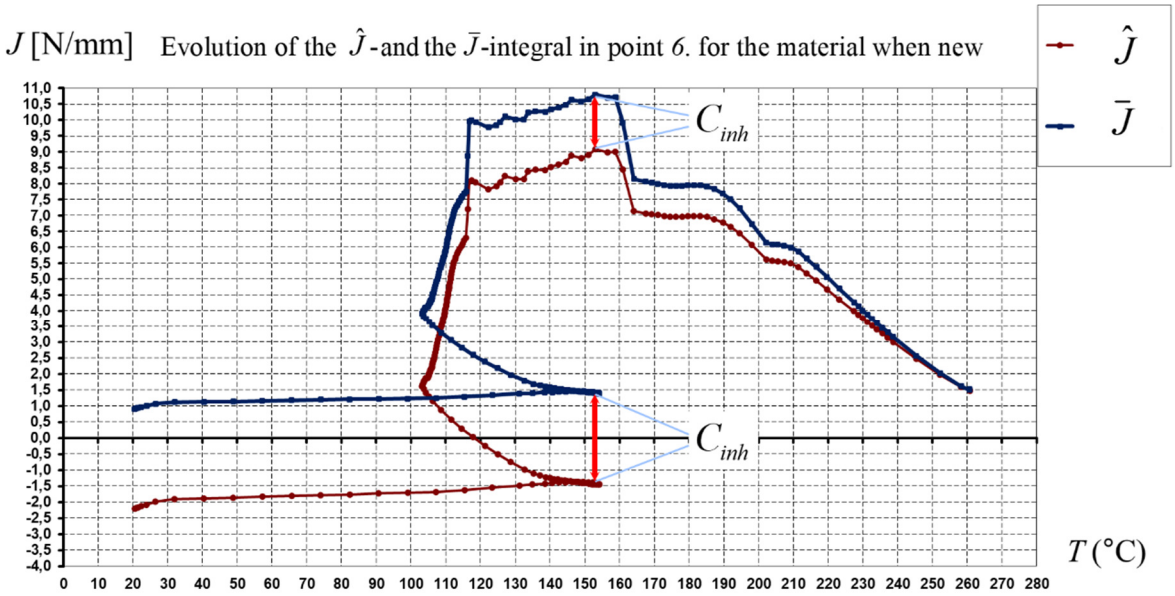


*Figure 4: Evidence for the path dependence of the **J**-integral during the PTS transient*

Remaining work

Subsequent research will concentrate on industrial applications of the novel theoretical framework.

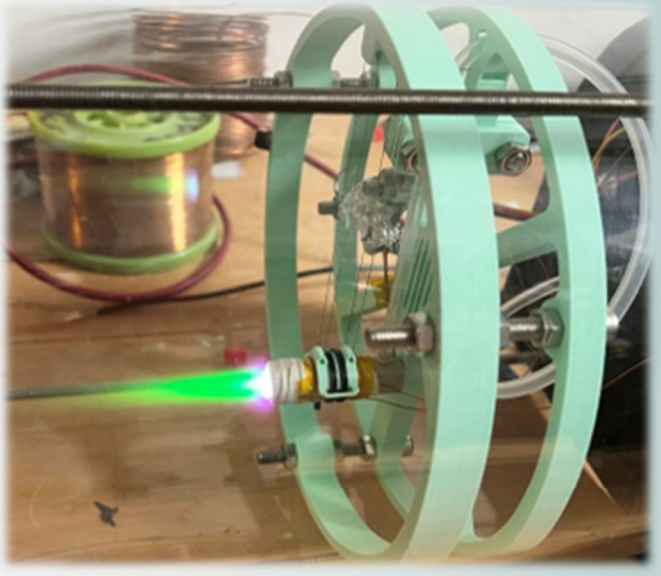
Related publication

[1] T. Fekete: *A new Concept for Large-Scale Pressure Systems Structural Integrity Computations,* Procedia Structural Integrity **68,** 925–921 (2025) https://doi.org/10.1016/j.prostr.2025.06.150





III. NUCLEAR SECURITY, DOSIMETRY AND SPACE RESEARCH





DEVELOPMENT AND IMPLEMENTATION OF CULTURAL HERITAGE PRESERVATION USING IONISING RADIATION TECHNOLOGY

Péter Völgyesi, Hedvig Nagy, Tünde Tóth, András Kovács

Objective

The radiation-induced preservation of Cultural Heritage (CH) artefacts, planned for regular implementation in Hungary, is an efficient complementary technology worldwide for removing woodworms, moths, bacteria, mould, etc. from wooden, textile, leather, bone, and cellulose items without generating radioactivity in the irradiated objects. To explain the advantages and characteristics of this nuclear preservation technology, scientific visits are initiated, and exhibitions and conferences are organised with experts and restorers from museums and archives. To achieve this goal, our first task is to utilise the knowledge and experience of the already existing research team, consisting of experts from the Hungarian National Museum and the HUN-REN Centre for Energy Research (HUN-REN EK) for the selection and education of the relevant stakeholders (i.e. management and restorers of Hungarian museums, art galleries, archives, churches, private collectors, etc.) by disseminating and demonstrating the recent achievements of these technologies performed at high-standard foreign institutions and companies. At the same time, discussions are planned with the management of the concerned museums and galleries to establish a database containing the most endangered CH artefacts. The second task is the selection of suitable gamma and electron irradiation facilities available in Hungary depending on the type of the CH artefact in question. The next step planned is to work out suitable gamma and electron irradiation technologies for different types of CH objects composed of various materials in order to select the most suitable irradiation conditions, including reliable process control methods by using standardised dosimetry systems. In this phase, first experimental irradiations are planned, followed by technological irradiations utilising the experience of the experimental studies. To facilitate the initiation and implementation of this technology in Hungary, the utilisation of the already existing knowledge and experience is planned through scientific visits and bi- and multilateral cooperation programmes as well as within the framework of the ongoing IAEA European Regional Technical Cooperation programmes (RER1024).

Methods

Two gamma irradiation facilities, i.e. (1) the pilot irradiation facility of the Institute of Isotopes (IoI) Co. Ltd., (Fig. 1(a), and the industrial irradiation facility of Agroster Co. Ltd.,(Fig. 1 (b)) available for the radiation treatment of cultural heritage objects in Hungary, have been characterised for large-scale irradiation of CH objects with respect to dose distribution in the irradiation room, potential irradiation locations and to the availability of standardised dosimetry systems (ECB (ethanol-monochlorobenzene), GEX B3 film, FWT-60 film, Fricke solution, red Perspex, Al-oxide TL dosimeters, etc.).



Figure 1: Gamma irradiation facility of (a) IoI Co. Ltd. and (b) of Agroster Co. Ltd.

The main dosimeter system at both irradiation facilities is the oscillometric ECB solution, which took part in the recent calibration verification and dosimetry inter-comparison exercises organised by the IAEA RER1021 project for quality assurance reasons. In both cases, the performance of the oscillometric ECB dosimeter system was very good.

The LPR-4 type linear electron accelerator of HUN-REN EK (Figure 2 (a)) was characterised and tested for the potential irradiation of cultural heritage objects (mainly paper and textile). The irradiation geometries (using scanned beam and/or with or without an Al scatter plate) were selected, and the electron irradiation geometries, with respect to dose, were tested using Polystyrene (PS) calorimeters (Figure 2 (b)). Besides ECB, Sunna film, GEX B3 film, FWT-60 film, and alanine aqueous solution dosimeters can also be used for dose measurements.

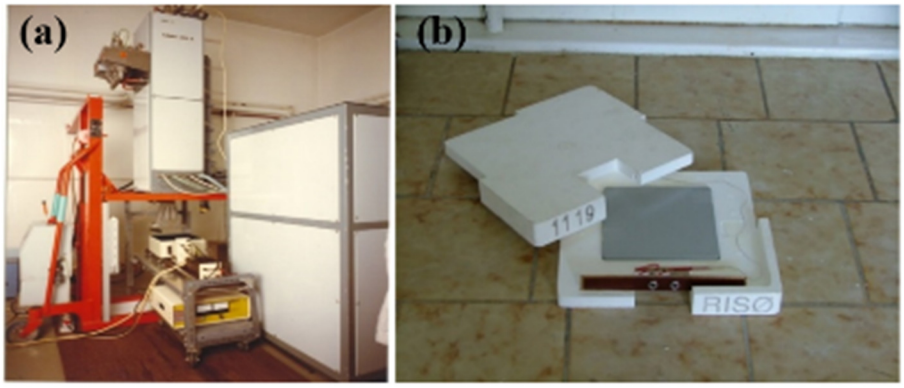


Figure 2: (a) LPR-4 linear electron accelerator of HUN-REN EK, (b) PS routine calorimeter

Results

1. Dissemination through national conferences

An IAEA-supported National Seminar on „Cultural Heritage Preservation Using Ionising Radiation Technology" was organised for the representatives of relevant Hungarian stakeholders at the HUN-REN EK on the 21st of November 2023 to introduce the basics, advantages, application possibilities and worldwide use of the special irradiation technology applied for the preservation of cultural heritage objects. The invited lecturer was Dr V. Moise, IAEA expert, Head of the IRASM Irradiation Centre, Bucharest, Romania. Dr K. Dúzs, from the Hungarian National Museum, also gave an oral presentation on "Cultural Heritage Preservation in Hungary". 28 participants, mainly restorers, took part in the meeting from the following institutions: Museum of Fine Arts, Museum of Applied Arts, Semmelweis Medical History Museum, Hungarian National Museum, National Gallery, National Archives, Agroster Irradiation Co. Ltd., IoI Co. Ltd., National Atomic Energy Authority of Ghana and Türkiye (guests), HUN-REN EK (Figure 3).



Figure 3: National Seminar on "Radiation Preservation of Cultural Heritage Objects" at the HUN-REN EK

The HUN-REN EK also participated in the „Annual Conference of the Association of Hungarian Church Archivists and Association of Church Museologists (26-28. June 2024, Pápa, Hungary). An oral presentation on the "Use of Ionising Radiation in Heritage Protection" was given by Dr H. Nagy (HUN-REN EK).

2. Dissemination through scientific visits

Experts from the Roman Catholic Bishopric of Pécs (the Capital of Baranya County) visited HUN-REN EK to discuss the irradiation of various types of textiles (e.g., silk and wool curtains, carpets, pillows, vestments, copes, and stoles) contaminated by moths.

HUN-REN EK was visited by the leadership and experts (restorers and archaeologists) of the Kiscelli Museum (which is part of the Budapest History Museum) for study and discussion on the potential use of the irradiation technology for their relevant collection.

The radiation experts of HUN-REN EK visited the Budapest City Archives and discussed the irradiation of mouldy paper documents from the II. World War period. Experts from the National Evangelical Collection Museum, from the Székesfehérvár Diocesan Museum and from the Museum of Ethnography visited HUN-REN EK for discussion on radiation preservation of

cultural heritage objects and to visit the gamma irradiation facility of the IoI Co. Ltd. and the electron irradiation facility of HUN-REN EK.

3. *Dissemination through exhibition*

In the framework of the Museum Street Plus festival in Pécs, organised by the Janus Pannonius Museum, a small exhibition was held at the Episcopal Treasury between 16 and 19 August 2024. The exhibition was prepared by colleagues from the Bishopric of Pécs and HUN-REN EK. In addition to a poster presenting the main characteristics and applications of radiation-based preservation of cultural heritage objects, textiles —such as cushions (Fig. 4)—previously treated with ionising radiation due to moth infestation were also displayed.



Figure 4: Exhibition in the Episcopal Treasury, Bishopric of Pécs

4. *Dissemination through establishment of a scientific cooperation program*

To get acquainted in more detail with the radiation preservation method of various cultural heritage objects, the experts of the Museum of Fine Arts initiated a bilateral cooperation project with HUN-REN EK to investigate and analyse this technology together on specific, especially film products stored under different conditions. The details of this cooperation project are under discussion.

5. *Gamma and electron irradiation of textile items of Pécs Bishopric*

Due to the preliminary discussions and to visit the gamma irradiation facility of IoI Co. Ltd., the experts of the Bishopric of Pécs sent several moth-contaminated textile samples for experimental irradiation. These samples include sewn and/or woven stoles, cushions, cloaks, curtains, tapestries, and copes made of silk, wool, velvet, and brocade. They also contain silk, wool, cotton, straw, and metal strings (Figures 5, 6).



Figure 5: Moth-contaminated tapestry and cope of Pécs Bishopric

These samples were packed into cardboard boxes of 40x40x40 cm. Four cardboard boxes were placed on top of each other, supplied with ECB dosimeters, located at the reference locations for dose control and irradiated for 2 x 48 hours. According to the dosimeter measurements, the products were irradiated in the dose range of 2.8 – 5.05 kGy.

One stole sample was irradiated with the 4 MeV linear electron accelerator using a scanned beam as shown in Figure 6. The doses were 3.0 kGy and 5.0 kGy, as measured by the PS calorimeter and B3 film dosimeters.



Figure 6: Stole from Pécs Bishopric irradiated at the 4 MeV linear accelerator of HUN-REN EK

6. *Gamma irradiation of wooden objects*

Bench ends, contaminated with wood-boring insects from the National Evangelical Collection Museum (Figure 7), and a carved, painted fretwork statue of St. Michael Archangel of the Székesfehérvár Diocesan Museum (Figure 7) were irradiated against auger-worms in the gamma irradiation facility of the IoI Co. Ltd.



Figure 7: St. Michael Archangel of the Székesfehérvár Diocesan Museum and bench end of the National Evangelical Collection Museum

Remaining work

Besides the further irradiation of the textile samples against moth-contamination, and the gamma irradiation of wooden samples to eliminate woodworms and wood-boring insects, ceramics, archaeological animal bones, as well as books and paper documents will also be irradiated against moulds. Preliminary investigations with respect to moulds, a bilateral cooperation project has been initiated with the Microbiology Department of Eötvös Loránd University to study and analyse the microbiological contamination of relevant objects and documents for more accurate determination of the required irradiation dose, as well as for post-irradiation control.

DEVELOPMENTS IN PERSONAL DOSIMETRY: PART 3

Tamás Pázmándi, Dorottya Jakab, Annamária Pántya, Zsófia Rékasi, Csilla Rudas, Márton Zagyvai, Péter Zagyvai

Objective

The goal of this work is to establish a research centre dedicated to occupational personal dosimetry that can effectively address real-world challenges, analyze events and incidents involving potential or confirmed exposures, estimate doses and contribute to reducing and mitigating exposure risks.

Methods

1) Determination of detector response using Monte Carlo simulations: The response of gamma-ray detectors applied in whole-body and partial-body monitoring was modelled through Monte Carlo–based simulations to support a more realistic assessment of internal exposure. In parallel, methodological developments were conducted to enable selective and rapid monitoring of thyroid radioactivity following accidental intake, to facilitate fast screening of potentially exposed individuals.

2) Development of analytical procedures for quantifying isotopes relevant to internal exposure that are difficult to measure, with particular emphasis on determining ^{90}Sr uptake from urine samples. Rapid but less accurate methods are distinguished from time-consuming methods comprising ^{90}Y ingrowth to secular equilibrium.

3) Further improvements were made to gamma spectrometry procedures to enhance the accuracy and precision of measurements in biological samples.

4) Evaluation of measurement uncertainty and identification of methods for its mitigation in both active and passive measurement methods used in external personal dosimetry. We demonstrated that accounting for irradiation conditions when evaluating external dosimetry measurements can significantly reduce uncertainties. To achieve this, the energy distribution and incidence properties of radiation fields were determined by modelling. A series of measurements was conducted to evaluate the characteristics of the radiation fields in the Budapest Research Reactor (BRR), in collaboration with researchers from SCK-CEN (Belgium). Two types of neutron monitors were used to measure the neutron ambient dose equivalent: two units of the conventional neutron survey meter Berthold LB6411, and a Raylab DIAMON (Direction-aware Isotropic and Active Neutron Monitor) neutron spectrometer that provided directional and spectral data.

Results

1) Progress was made in modelling the detector response using Monte Carlo simulations. The preliminary simulation runs confirmed the feasibility of using this approach for assessing internal exposure. In addition, the first steps toward developing a selective rapid-monitoring method for thyroid activity were completed, including identifying suitable measurement conditions.

2) Steps with opportunity for further improvement and optimisation were identified, offering different solutions for procedures for screening and long-term medical follow-up, respectively.

3) The gamma spectrometry measurement procedure for biological samples was further enhanced, with a focus on identifying and evaluating additional key factors that influence measurement accuracy and precision.

4) The neutron field characterisation revealed clear spatial variability in the neutron spectra within the BRR reactor hall, with intensity and contributions from thermal, epithermal, and fast neutron energy ranges significantly differing by location and position. These are caused by the reactor's structural composition, shielding characteristics and operational factors. Such location-dependent variations in the neutron spectra lead to significant variations in the dose rates, too, highlighting the importance of using local correction factors adjusted to the field characteristics, such as specific energy distribution and angular dependence, to improve measurement accuracy.

Remaining work

Type-testing and calibration of newly purchased directly readable Electronic Personal Dosimeters (EPDs) intended for monitoring individual workflows, especially when higher radiation exposure is anticipated within BRR, to improve accuracy and reduce uncertainties in real-time occupational dosimetry.

Related publication

[1] S. Pinasti, O. Van Hoey, C. Mihailescu, M. Abdelrahman, D. Jakab, A. Pantya, T. Pázmándi, C. Rudas, M. Zagyvai, F. Vanhavere, & N. Pauly: *Computational neutron personal dosimetry at the Budapest Research Reactor,* Radiation Measurements **184,** 107420 (2025) https://doi.org/10.1016/j.radmeas.2025.107420

IMPROVEMENTS IN PERSONAL DOSIMETRY

Tamás Pázmándi, Annamária Pántya, Zsófia Rékasi, Márton Zagyvai, Péter Zagyvai

Objective

It is important to consider individual parameters in personal dosimetry, as these factors can vary significantly among workers under regular radiation control and among members of the general public. Current personal dosimetry systems generally do not account for characteristics such as age, lifestyle, or underlying health conditions.

This project aimed to integrate these individual parameters into personal dosimetry systems in order to achieve more accurate dose assessments and thereby reduce radiation-related risks. In addition, the work also continued on the wound-dosimetry project initiated in 2023. The goal was to compare different measurement and dose-assessment methods and to establish a comprehensive measurement protocol, supported by case-study evaluations.

Methods

In order to evaluate age-specific parameters, we participated in the whole-body counter intercomparison organised by EURADOS, focused primarily on children. The intercomparison aimed to improve radiation protection capacity for vulnerable population groups and to incorporate sex-related differences into monitoring practices. The participating laboratories had to calibrate their in vivo monitoring systems and develop person-specific measurement protocols. The provided phantoms representing different age groups (1 year to adult female) were assembled using polyethylene bricks according to the instructions provided by the organising laboratory. Each phantom contained predefined cavities for the placement of radioactive sources. Both known-activity and unknown-activity sources were provided for the exercise. All measurements were performed using an HPGe detector equipped in a routinely used measuring booth. The measurements were conducted with the phantoms in a lying position. The detector scanned along the body's length during each acquisition. The measurement time for the phantoms was 20 minutes and 1 hour for blank measurements. Three types of measurements were performed for each phantom:

1) Calibration measurements were conducted using the known-activity sources to establish detector response functions for each age group.
2) The unknown sources were used to determine the isotope and estimate the activity using the previously obtained calibration curves.
3) Blank measurements were performed to determine the background counts, which were used for the calculation of detection limits for certain predefined radionuclides.

In 2024, our laboratory submitted results for the ICIDOSE#2 intercomparison, which included a wound dose assessment. Multiple dose assessment methods were applied, although the final submission was based on manual evaluation. In 2025, the previously used methodology was reassessed in light of the recommended solution provided by the organisers, enabling a comparison of approaches and the evaluation of the accuracy of our original assessment.

Results

As the intercomparison is still ongoing, only preliminary conclusions can be drawn. The measurement system was calibrated using all phantom configurations, and the calibration curves enabled the identification of the unknown isotopes. These sources were determined to be Cs-134 and Cs-137, and their activities were quantified for all age groups, with generally low uncertainties. The exception was the long blank measurement series, where the low count rates resulted in higher uncertainty. Finally, detection limits for radionuclides relevant in medical applications were calculated, with higher values for isotopes emitting gamma photons with lower yield.

As part of the evaluation of wound contamination scenarios, the dose assessment performed for Case 4 of the ICIDOSE#2 intercomparison showed good agreement with the recommended reference values. The analysis also indicated that using a mixed approach can provide a more accurate and detailed assessment compared to relying on a single method.

Remaining work

For the children's whole-body counting intercomparison, the next step will be to evaluate our results in the context of the overall intercomparison findings, to identify strengths and areas for improvement in our measurement and assessment procedures.

ORGANISATION OF AN INTERNATIONAL COMPARISON ON THE DETERMINATION OF INTERNAL EXPOSURE (ICIDOSE#2) – PART 2

Tamás Pázmándi, Annamária Pántya, Zsófia Rékasi

Objective

In recent years, new recommendations have been introduced for assessing internal radiation exposure in the workplace. To support their practical implementation and evaluation in occupational internal dose assessment, the EURADOS Working Group 7 (WG7)—which brings together European experts in internal dosimetry—has launched an international intercomparison exercise. Our role in this initiative was to coordinate the organisation of the exercise and oversee the assigned tasks. The primary aim of the intercomparison was to assess internal dose determinations performed by participating laboratories using current recommendations and accreditation standards.

Methods

The intercomparison exercise comprised five case studies of varying complexity, which were designed to address routine and less common challenges in internal dosimetry. The cases differed in data availability, monitoring intervals, and scenario type, ranging from limited early-phase data to long-term datasets extending up to one year. These scenarios covered routine monitoring, follow-up assessments after negative results and incidents that required special evaluation.

Participants could choose which case(s) they wanted to answer. For each selected case, only one solution could be submitted, although participants were allowed to revise their submissions until the deadline. Following the submission deadline, all collected results were analysed and evaluated in detail.

A workshop for the participants was subsequently organised in Budapest on 13–14 May 2025 to discuss the findings, methodological approaches, and lessons learned. After the workshop, an anonymous survey was distributed to all ICIDOSE#2 participants to assess the quality of both the intercomparison exercise and the workshop.

Results

A total of 41 participants from 22 countries submitted results to the ICIDOSE#2 intercomparison exercise. 34 participants were based in Europe, while 7 participants represented institutions outside Europe.

Altogether 164 submissions were received across the five case studies. Only 4.89% of the participants provided results for a single case, and an additional 4.89% submitted solutions for two cases. A larger proportion of participants responded to three cases (21.95%) or four cases (21.95%). Notably, 46.34% of the participants submitted results for all five cases, and on average, participants responded to four cases. Participation was high for Case 1 and Case 2, with almost all participants submitting solutions. For the more complex scenarios (Case 4 and Case 5), over half of the participants responded.

At the workshop, 24 participants attended in person, while 11 participants joined online. Following the workshop, an anonymous survey was distributed, yielding 37 responses. The feedback confirmed that the intercomparison exercise was successful. Participants expressed satisfaction with both the number and the difficulty of the cases, and they considered the timing of the exercise to be appropriate. The overall workshop was rated as excellent by the respondents. Furthermore, 97% of respondents indicated that they support the continuation of internal dosimetry intercomparisons on a regular basis, highlighting the importance and value of such exercises.

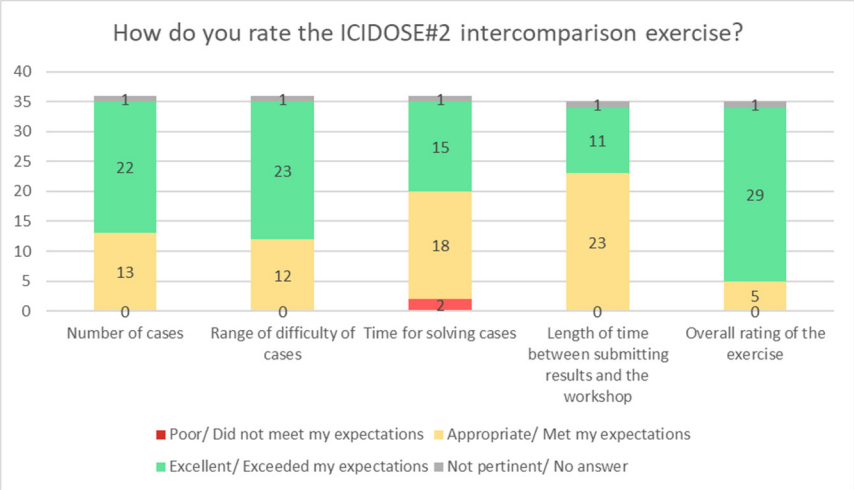


Figure 1: Feedback received from intercomparison participants

Based on the results and experiences, recommendations were formulated for the enhancement of international guidelines. The EURADOS Report and a scientific paper summarising the results of the project are being finalised and submitted.

Related publications

[1] T. Pázmándi, D. Bingham, B. Breustedt, D. Broggio, C. M. Castellani, G. Drouet, P. Fojtík, A. Giussani, S. Löscher, J. Osko, A. Pántya, Z. Rékasi, V. Rovenská, D. Spencer: *EURADOS ICIDOSE#2 InterComparison of Internal DOSE assessment #2 – Analysing the intercomparison results,* EURADOS Report 2026-01, March 2026. https://doi.org/10.12768/qwak-ej64

[2] A. Giussani, A. Pántya, Zs. Rékasi, T. Pázmándi, D. Bingham, B. Breusted, D. Broggio, C. M. Castellani, G. Drouet, P. Fojtík, S. Löscher, V. Rovenská, D. Spencer: *The ICIDOSE#2 intercomparison exercise on internal dose assessement,* ICRP 2025: The 8th International Symposium on the System of Radiological Protection, 2025

[3] D. Bingham, B. Breusted, D. Broggio, C. M. Castellani, G. Drouet, P. Fojtík, A. Giussani, S. Löscher, J. Osko, A. Pántya, T. Pázmándi, Zs. Rékasi, V. Rovenská, D. Spencer: *Insights into Internal Dosimetry Practices through the ICIDOSE#2 Intercomparison,* 7th European IRPA Congress 2026 (accepted for presentation)

EXAMINATION OF THE POTENTIAL APPLICATIONS OF BIG DATA ANALYSIS FOR RADIATION PROTECTION PURPOSES

Dorottya Jakab, Attila Hirn, András Kocsonya, Tamás Pázmándi, Patrik Pinczés, Zsófia Rékasi, Csilla Rudas, Péter Zagyvai

Objective

Big data is a branch of data science concerned with handling and analysing extremely large and complex datasets. The analytical process typically involves data acquisition and processing, such as cleaning and transformation, followed by the application of advanced analytical methods that go beyond traditional statistical techniques—such as machine learning, artificial intelligence, and data mining. These approaches enable a deeper understanding of complex datasets, support the identification of hidden patterns, and allow predictive analyses that are often not achievable with conventional methods.

The objective of this project was to explore and understand the methodology of big data analysis and assess its applicability within the field of radiation protection. Specifically, it aimed to evaluate how these modern data science tools can be applied to large datasets generated over decades of radiation-monitoring activities. This included investigating the potential of these methods to identify possibly hidden patterns, determining the underlying causes of observed trends, and providing predictive insights based on historical monitoring data.

Methods

A comprehensive literature review was carried out before the analytical work, focusing on big data methodologies, their current use in radiation protection, and their potential for future application. This review also examined how similar analytical approaches are employed in related scientific fields. The main findings were summarised and presented as a poster at the NENE 2025 Conference in Slovenia (8–11 September).

Following the literature review, relevant datasets were obtained from EK's Environmental Protection Service. These consist of dose-rate measurements and variant meteorological data collected at 10-minute intervals between 2014 and 2025, which served as the basis for an initial test analysis. The data were processed by converting them into appropriate formats, performing cleaning procedures, and conducting basic statistical evaluations to ensure data quality and consistency. These preparatory steps established a solid foundation for the subsequent application of advanced analytical techniques—such as data mining, clustering, anomaly detection, and machine-learning-based predictive modelling—to explore patterns, trends, and potential insights within the datasets.

Results

The literature review indicated that big data analytics offers substantial opportunities for advancing radiation protection by enabling the integration and interpretation of large, complex datasets. Relevant applications were identified across numerous areas, including environmental and workplace monitoring, personal and internal dosimetry, biodosimetry, and medical applications. Within these fields, key analytical objectives—such as prediction, anomaly detection, pattern recognition, and decision-support—highlight the value of data-driven methodologies. A wide range of techniques is currently in use, ranging from traditional statistical modelling to advanced machine learning and hybrid approaches, with the choice of method largely dependent on the structure, quality, and complexity of the available data. Despite challenges such as data heterogeneity and variable data quality, existing applications already demonstrate clear benefits, including improved reliability, enhanced efficiency, and the ability to uncover complex relationships and previously hidden patterns.

The preliminary analysis of the datasets obtained from the Environmental Protection Service revealed several practical considerations for future work. Preparing the data for analysis required careful formatting and cleaning. Although the datasets contain numerous missing values, their overall size and temporal resolution allow for effective handling and potential imputation during subsequent analysis. Additionally, several extreme values were identified, which may represent outliers, requiring further investigation and appropriate treatment. Nonetheless, the datasets appear sufficiently robust and comprehensive to support the application of machine-learning algorithms and other advanced analytical techniques in future stages of the project.

Remaining work

The next steps of the project will focus on applying advanced analytical algorithms to the cleaned datasets to identify hidden patterns, trends, and anomalies, as well as to develop predictive models. Once these methodologies have been successfully applied, they will be extended to other relevant datasets to further explore and demonstrate the potential of big data analytics in radiation protection.

Related publication

[1] Zs. Rekasi, D. Jakab, T. Pazmandi, P. Zagyvai, Cs. Rudas: *Exploring the applicability of big data analytics in radiation protection*, In NENE 2025 Conference Proceedings - 34th International Conference Nuclear Energy for New Europe, Nuclear Society of Slovenia, Ljubljana **169,** 109-116 (2025) ISBN 978-961-6207-61-4
https://www.djs.si/upload/nene/2025/NENE_2025_Conference_Proceedings.pdf

REVISION OF ENVIRONMENTAL RADIOLOGICAL CONSEQUENCE ASSESSMENTS AND DEVELOPMENT OF AN UNCERTAINTY ANALYSIS FRAMEWORK

Csaba Glavák, Tamás Pázmándi, Csilla Rudas

Objective

In this work, two research activities related to the assessment of environmental radiological consequences resulting from accidental atmospheric releases of radioactive materials from nuclear facilities are presented, this activities constitute an essential part of nuclear safety analyses.

The objective of the first project was the revision of environmental consequence calculations associated with Large Break Loss-Of-Coolant Accidents (LB LOCA) belonging to Design Basis Condition 4 (DBC4) scenarios, as described in Chapter 15.2 of the Final Safety Analysis Report (FSAR). Earlier analyses conservatively assumed 100% fuel rod failure; however, recent evaluations demonstrated that such an assumption is excessively conservative. Based on updated analyses, a revised – and still conservative – assumption of 33% fuel rod damage was introduced, requiring recalculation of release source terms and resulting environmental doses.

The objective of the other work was to initiate the development of an advanced analytical framework (CARC Expert) for evaluating uncertainties associated with atmospheric dispersion and dose calculations. This includes the identification and systematic analysis of uncertainties in input data and model parameters, as required by regulatory frameworks, through sensitivity analysis methods.

Methods

For the LB LOCA reassessment, release source terms were updated based on the 33% fuel rod damage assumption. Environmental dispersion and dose calculations were performed using the CARC (Calculations for Atmospheric Release Criteria) code for selected accident scenarios defined in the FSAR. Meteorological input data and previously established dispersion parameters were applied consistently with earlier analyses. Short-term (2-day and 7-day) and long-term (lifetime-integrated) committed effective doses were determined for representative receptor locations, taking into account all relevant exposure pathways, including cloudshine, groundshine, inhalation, and ingestion.

In parallel, the CARC Expert development project focused on the systematic identification of input data and model parameters influencing dispersion and dose calculations. These include release characteristics, meteorological conditions, population habits, and model-specific parameters related to atmospheric transport, deposition, food chain transfer, and dose conversion. A sensitivity analysis framework was outlined, where selected parameters are perturbed within defined ranges, and the resulting changes in calculated dose values are quantified for specified percentiles (e.g., median, 95th percentile). The methodology aims to ensure computational efficiency while enabling robust uncertainty evaluation.

Results

The recalculation of environmental consequences for LB LOCA scenarios using the revised 33% fuel rod damage assumption was carried out. Based on the findings, updates to relevant sections of the FSAR were conducted.

Within the CARC Expert project, the first phase successfully established the framework for uncertainty and sensitivity analysis. Key input parameters and model components influencing calculation results were identified, and requirements for their systematic evaluation were defined. Preliminary considerations highlighted the importance of efficient data handling, as large-scale sensitivity analyses may significantly increase computational and memory demands. Potential optimisation strategies, such as improved data storage and result handling, were identified for further investigation.

Remaining work

The revision of dose calculations for LB LOCA has been completed. The next phase of the work regarding the uncertainty analysis framework will focus on the development and implementation of the sensitivity analysis methodology, and the extension of the CARC code to support automated uncertainty evaluations. In the final phase of the work, the validation of the approach will be carried out through benchmark calculations.

Related publications

[1] T. Pázmándi, Cs. Rudas: *Recalculation of environmental radiological conditions, reassessment of LB LOCA calculations in FSAR Chapter 15.2 using a source term corresponding to 33% fuel rod damage,* EK-SVL-2025-718-01-01-01, in Hungarian (2025)

[2] T. Pázmándi, Cs. Glavák, Cs. Rudas: *Analyses for the evaluation of uncertainty in environmental radiological consequence assessments; Identification of parameters relevant for sensitivity analysis,* EK-SVL-2025-752-01-01-M0, in Hungarian (2025)

[3] Cs. Rudas, Cs. Glavák and T. Pázmándi*: Uncertainty Evaluation in Radiological Consequence Modelling with CARC Expert tool,* 7th European IRPA Congress 2026 (*accepted for presentation*)

DOSE-RATE ASSESSMENTS FOR DESIGN BASIS ACCIDENTS WITHIN THE PAKS NUCLEAR POWER PLANT

Dorottya Jakab, Annamária Pántya, Tamás Pázmándi, Csilla Rudas

Objective

Since the latest comprehensive assessment of the radiation conditions of certain areas and rooms inside the Paks Nuclear Power Plant (NPP) in 2006, there have been several technological developments and changes (e.g. introduction of a new fuel type, extension of fuel cycle) which affect the resulting dose rates in certain locations within the building. In addition, recent investigations have expanded the range of radionuclides contributing to the primary circuit coolant activity, and in some cases, modifications of activity concentrations were indicated based on the measured values. These findings have also highlighted the need for the revision of primary circuit water activity data, for which updated analyses have recently been completed in 2020. Considering the modified source terms and parameter sets under both normal and accident conditions, it has become necessary to review the set of analysed accident scenarios and to further develop the applied calculation methodologies. In addition to the updated assessment of radiation conditions for normal operation finished in 2022, the revision of airborne and liquid radioactive sources and releases in normal operation was also completed in 2024 [1].

The overall objective of the present project was to systematically repeat and update the full set of dose-rate calculations in case of Design Basis Accident (DBA) conditions for the affected equipment and plant areas, and to establish an updated dose-rate map for the plant. The work was carried out in three phases, including the selection of accident scenarios and associated source terms, the development of calculation models and input data sets, and the execution of the accident dose-rate calculations. The final aim of the work is to integrate the results of the revised analyses into Chapter 15.2 of the Final Safety Report (FSR) [2].

Methods

In the first phase of the project, previous studies related to DBA conditions within the plant were reviewed in detail, and their main findings and lessons learned were summarised. Based on these, the accident scenarios to be analysed were selected in accordance with those defined in Chapter 15.2 of the FSR, as no new types of accident scenarios were identified despite the implemented technological modifications. These accident scenarios include representative containment overpressure events, as well as selected non-overpressure transients, accidents in shutdown and open reactor conditions, and cases related to the spent fuel pool.

The associated source terms were determined taking into account the updated core inventory, revised primary circuit water activity data, and the results of recent thermohydraulic analyses reflecting the current operational conditions. The set of equipment and plant areas to be investigated was identified, focusing on those locations where significant airborne radioactive contamination may occur during DBA conditions. These include the containment as well as adjacent areas connected directly or indirectly through leakage paths or ventilation systems. The analysed areas were also grouped according to their associated ventilation systems, and chains of connected rooms were examined.

In the second phase, the computational models were reviewed and updated for the simulation of radioactive material release, transport, and dispersion within the plant building, including the releases from the containment and propagation through interconnected rooms and ventilation systems. The necessary input data for the calculations were defined and finalised in consultation with relevant plant experts.

Results

In the final phase of the project, dose-rate calculations for DBA conditions were performed using the developed models and established input data sets. The activity concentrations in the air and on the surfaces within the affected rooms were determined for the selected design basis accident scenarios, taking into account the release and transport of radioactive materials from the primary systems and their dispersion within the building. Based on these results, the resulting external and internal dose rates for personnel present in the considered areas were calculated.

The analyses confirmed that the most significant radiological impact occurs in the adjacent areas to the containment, where radioactive materials may be transported due to pressure differences and leakage pathways. The results provide a consistent and up-to-date basis for the assessment of radiation conditions during accident scenarios within the plant buildings.

Based on the results of this work, the related parts of Chapter 15.2 of the Final Safety Report can be fully updated.

Remaining work

This project has been completed.

Related publications

[1] D. Jakab, A. Pántya, T. Pázmándi, Cs. Rudas: *Revision and recalculation of airborne and liquid radioactive source terms and releases under normal operation, and the associated outdoor and room dose rates,* EK-SVL-2024-709-02-01-01, in Hungarian (2025)

[2] Final Safety Report of the Paks Nuclear Power Plant, Version 19, in Hungarian (2024)

ENVIRONMENTAL IMPACT ASSESSMENT PROCEDURE FOR THE SUBSEQUENT SERVICE LIFE EXTENSION OF THE PAKS NUCLEAR POWER PLANT

Dorottya Jakab, Annamária Pántya, Zsófia Rékasi, Csilla Rudas

Objective

The main objective of this work is to establish the basis of the Environmental Impact Assessment (EIA) procedure related to the planned subsequent service life extension of the four reactor units of the Paks Nuclear Power Plant (NPP) by another 20 years (up to 2052 and 2057). The EIA report will contain the estimation of the expected environmental impacts and the extent of the impact area associated with the plant's continued operation during the service life extension period, drawing on 13 specialised Examination Programmes (WPs). We are responsible for coordinating and implementing two WPs: WP11 – Assessment of the radiation exposure to the population living in the vicinity of the Paks NPP, and WP13 – Examination of potential transboundary impacts.

Methods

Within WP11, the radiation exposure of the general public living within a 30 km radius of the site was assessed, and the results were utilised to estimate the anticipated impacts of the continued operation of the Paks NPP on nearby residents. WP13 included the evaluation of both radiological and non-radiological impacts with potential transboundary implications. The work involved reviewing previous analyses, conducting updated assessments with the most up-to-date data and modelling tools available, and performing an analysis of expected changes throughout the extended service life.

The analyses of radiological impacts included modelling of both actual and potential gaseous and liquid radioactive releases from the NPP under various operating conditions using models developed in-house. The activity concentrations of released radioisotopes at the receptor points were determined, and the exposure of the population was then calculated by taking into account the relevant exposure pathways. Atmospheric dispersion was modelled using real meteorological measurement data series covering several years. For assessing the radiological consequences due to liquid radioactive discharges, it was assumed that the plant's liquid releases would ultimately be discharged into the Danube as the receiving water body and as the radioactive contamination discharged into the river water disperses, its activity concentration decreases due to dilution and radioactive decay. Aquatic dispersion was modelled considering the hydrological characteristics of the Danube.

In addition to modelling gaseous and liquid radioactive releases, direct and scattered radiation from plant operation, along with other man-made sources and activities, such as the transport of fresh and spent nuclear fuel and radioactive waste, and the use of radioactive sources for industrial radiography, were also evaluated to provide a comprehensive estimation of overall radiological impacts.

Results

In the second year of the work, activities focused on performing the detailed analyses, calculations, and evaluations of the expected impacts associated with the planned service life extension of the Paks NPP. The previously developed methodologies, analytical tools, and compiled input datasets were applied in the assessments.

Gaseous and liquid radioactive releases from the NPP were modelled for normal operation, anticipated operational occurrences, and design basis accidents. Population doses for adults and 1-year-old age groups were determined for each release scenario. For gaseous radioactive releases, these included external dose from the radioactive cloud, external dose from the contaminated soil, internal dose from inhalation, and internal dose from ingestion via the food chain. For liquid emissions, external dose from contact with and immersion in contaminated water, and internal dose from ingestion via the aquatic food chain were calculated.

The analyses were carried out with consideration of potential changes in environmental impact arising from evolving conditions, which may influence exposure during the extended service life. The sensitivity analyses performed showed the degree to which potential variations in meteorological conditions, Danube water flow, and shifts in lifestyle and consumption habits could affect doses to the population and exposure levels.

Based on the results of the analyses, the magnitude of population radiation exposure and the extent of potential transboundary impacts were quantified and evaluated within the framework of the EIA, to characterise the impacts associated with the planned service life extension.

Remaining work

This work lasts until 2026.

DEVELOPMENT DIRECTIONS FOR SPACE WEATHER AND SPACE DOSIMETRY DETECTOR SYSTEMS

Patrik Pinczés, Attila Hirn, Julianna Szabó, Boldizsár Major

Objective

As part of the detector system development, we are searching for options to improve our existing detectors and advance them with new technologies. Currently, the TRITEL and RADTEL cosmic radiation telescopes are in use and are planned to be launched in the following years on several space vehicles, like the Gateway lunar station, the Distributed Space weather Sensor System (D3S) orbiting the Earth and the Mars Sample Return mission.

The silicon semiconductor used in these instruments is a technology widely used in cosmic particle detectors worldwide. The objective is to upgrade our detectors and look for new technologies to create the next generation of the top-of-the-art space weather and cosmic radiation sensors.

Methods

Our development contains 2 key profiles:

I) new detector configurations with new detector types, geometries and possible new technologies;

II) neural network usage for spectral unfolding. This involves Linear Energy Transfer spectra determination and proton, electron and ion spectra analysis. Our goal is to advance the logic of particle classification and energies.

Results

After studying the related literature, it was found that recent advancements in diamond detectors make them a possible candidate for new technology radiation detectors. Their radiation hardness is better than that of silicon, and they can detect not only charged particles but neutrons as well. Diamond detectors are not sensitive to optical light, but one could measure UV radiation with them, which contains information about the activity of the sun, thus about the space weather.

Another possible candidate is the Perovskite detectors. The best of these semiconducting materials is the $CsPbBr_3$ configuration. The development of these detectors is not as advanced as that of diamond detectors, but one should give special attention to their development in the future.

A third candidate is the Cherenkov detectors. It has promising results in discriminating between electrons and relativistic protons.

New methodologies in data analysis were also considered. Neural networks have advanced a lot in recent years and are widely used for the determination of the origin of cosmic radiation (for example, solar or galactic) and for the identification of particle types.

Partly as a result of the work performed here, our group won a European Space Agency (ESA) call led by the French Aerospace Lab ONERA: “Particle Radiation Instrument and Spectrometer for Europe (PRISE)”. In this project, a concept for a system with a wide measurement range and efficient particle discrimination is going to be developed.

Remaining work

The development of new detectors should be monitored closely in the following years.

Our current detector configuration will get advanced geometries, and data analysis will be updated.

INVESTIGATION OF METHODOLOGICAL DEVELOPMENT DIRECTIONS FOR THE JOINT EVALUATION OF TRITEL AND RADTEL MEASUREMENTS PERFORMED IN PARALLEL ON BOARD MULTIPLE SPACECRAFT

Patrik Pinczés, Attila Hirn, Julianna Szabó, Boldizsár Major

Objective

The measurement of cosmic radiation is important due to its impactful changes in interplanetary space and near Earth. Future space missions with HUN-REN EK contribution and devices (TRITEL & RADTEL radiation detector telescopes) require preliminary knowledge about the expected space weather environment and about the changes in radiation conditions. The complexity of this research increases the goal of operating multiple radiation detectors with the same configuration in different locations in the Solar System. These locations include low-Earth orbit, Lunar orbit, interplanetary space and possibly Mars orbit.

Methods

Cosmic radiation is a complex topic; changing conditions and limited measurements require intense modelling and good use of available data. Comparison of interdisciplinary measurements is required: these are the data from solar observing satellites like SOHO and STEREO-A with space radiation telescopes like ACE or RADCUBE. This includes radiation dosimetry measurements from Pille-ISS aboard the International Space Station and data from the BUDApest Neutron Monitor, too.

From an engineering point of view, conditions across different locations in the Solar System can vary widely. Modelling the space weather environment helps to determine what electric charges and magnetic fields can be expected near Earth, in interplanetary space and at other planets like Mars. Precise assessment of conditions is required to ensure instrument safety and accurate measurements.

The methods also include solar wind modelling in close collaboration with HUN-REN Wigner Research Centre for Physics.

Results

The following development directions were identified based on measurement data, research and modelling:

- Data analysis from the RADTEL detector (flown on the RADCUBE space weather monitoring satellite in low Earth orbit between 2021-2024) with comparison to other cosmic radiation detectors, including the Euglena Combined Regenerative Organic Food Production in Space (Eu: CROPIS) and Radiation Measurements in Space (RAMIS) instruments from the German Aerospace Centre (DLR).
- Research on the achievable scientific goals and the conditions near space weather probes in different locations in the Solar System.
- Comparison of space weather models to determine which are the best for multi-spacecraft measurements. Analysis of the PFFS (Potential Field Source Surface), WSA (Wang-Sheeley-Arge) and ENLIL space wind and MHD (magnetohydrodynamics) models.
- Analysis of the Solar-MACH magnetic field connection configurations.
- Combination of theoretical models with measurements in interplanetary space.
- A PhD topic entitled 'Multi-Spacecraft Measurements with Silicon Detector Telescopes in the Earth's Magnetosphere and in Interplanetary Space' has been started based on these findings.

Remaining work

The project incorporates multiple years of work. The next steps include further refining of space weather models and the preparation of instrumentation for the space missions.

Related publication

[1] P. Pinczés, A. Hirn, T. Berger, D. Matthiä, K. Marsalek, M. Rohde, M. Radenhäuser, M. Kasemann, B. Przybyla: *RADCUBE-RADMAG instrument: technology demonstration & measurements,* 28th Workshop on Radiation Monitoring for the International Space Station, Cologne, Germany (2025)

DEVELOPMENT OF A PLASMA THRUSTER FOR POCKET SATS

Miklós Palánkai, Bence Práth, Kenichiro Takahashi[a], and Gábor Veres

[a] - *Institute of Science Tokyo*

Objective

The development aims to design and test a sufficiently small and lightweight thruster to be deployed onboard very small, so-called cube- or pocket sats for orientation/altitude control and/or de-orbitation. Since cube- and pocket sats are relatively cheap devices, any equipment used for their altitude control must also be very compact and simple, yet robust and reliable. Our compact electro-thermal plasma thruster fulfils these requirements and offers the right thrust necessary for cube- and pocket sats at the size and weight compatible with the dimensional restrictions.

Methods

Cube- and pocket sats are at the lower end of the size- and weight-spectrum of small satellites. As stated in NASA's report NASA/TP—2022–0018058 (State-of-the-Art Small Spacecraft Technology), "Since 2013, the flight heritage for small spacecraft has increased by over 30% and has become the primary source of space access for commercial, government, private, and academic institutions." The number of cube- and pocket sats (also called nano- and pico-satellites) has increased even more dramatically.

Thrusters for the altitude control of pocket sats at the moment are not available on the market. The reason is that no thruster is available in the size of a pocket sat (approx. 50x50x50 mm^3) that offers the required thrust of a few 10 mN. Pulsed plasma thrusters are available in the required small size, but their thrust is far too low, in the few 10 microN range. Existing warm gas and electro-thermal thrusters can deliver the required thrust, but they consume electrical power in the magnitude unavailable onboard of a pocket sat.

For cube sats, the situation is more relaxed, but even that market can profit from our compact thruster that combines the advantages of the warm gas and electro-thermal thrusters.

Results

Continuing the previous year's developments, we have concentrated our work on the measurement of the thrust generated by the thruster.

For this, we have designed a pendulum that holds the thruster, which pushes a small force cell capable of measuring forces down to the mN range.

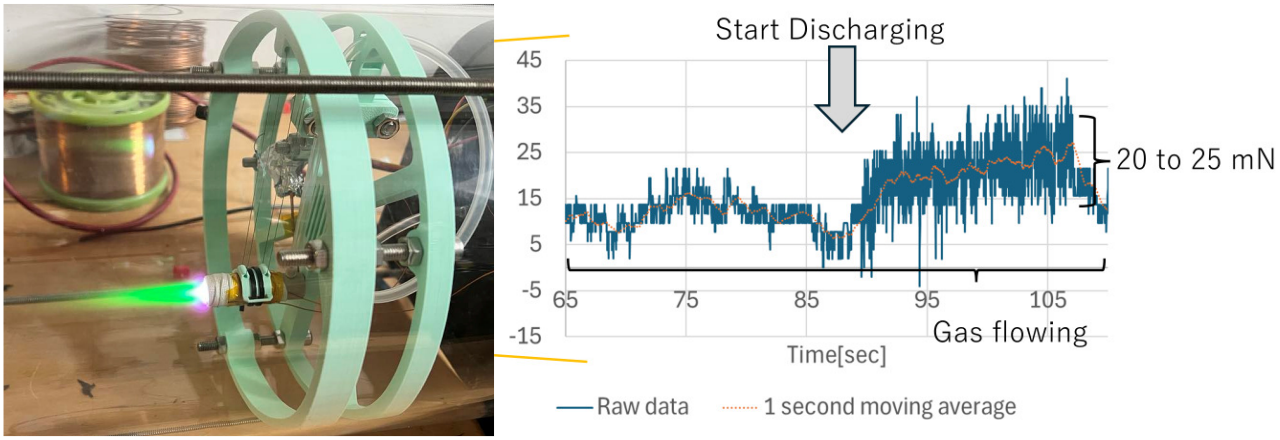


Figure 1: The pendulum with the thruster (left) and the result of the measurement (right)

The results show that the gas flow caused a force of around 10 mN, while switching on the discharge added a 10-15 mN extra force. This is in approximate agreement with our FEA predictions of the previous year. Unfortunately, the measurements are quite noisy, which is due to the charged particles that build up the plasma and generate electric noise in the force-cell itself and its electronic unit. Shielding of the electronics helps a bit, but not too much.

We also re-measured the spectrum of the plasma plume, and the improved evaluation of the line intensities gave us a plasma temperature of 1 eV. This is pretty much what one would expect from such a partially ionised argon plasma.

Remaining work

Although there is some increase in the thrust with the discharge relative to the thrust of the neutral gas itself, for this thruster concept to be viable, the contrast needs to be greatly improved. For this, we will redesign the nozzle to improve its flow characteristics.

WIRELESS GAMMA RADIATION DETECTOR SYSTEM FOR ENVIRONMENTAL MONITORING, DOSE RATE MAPPING AND SEARCH FOR RADIOACTIVE SOURCES

Attila Hirn, István Apáthy, János Volk

Objective

The radiation detector system described below was developed within the framework of an umbrella project aimed at developing environmental monitoring sensors for use in emergency conditions. The main objective was to develop a wireless gamma radiation detector system for environmental monitoring, dose rate mapping and the search for radioactive sources. The system is intended for flexible deployment, including fixed installations, mounting on unmanned or passenger vehicles, and portable use.

Methods

The detector system is based on the Geiger-Müller (GM) counter technology developed by the HUN-REN EK Space Research Department for operation in harsh environments, including aboard stratospheric balloons and sounding rockets. The system was designed to be compatible with the environmental monitoring system of the Environmental Protection Service at the KFKI Campus.

The mobile gamma radiation detector incorporates two GM tubes with different sensitivities to cover the required dose-rate measurement range. The electronics, data acquisition and communication functions were integrated into a compact, field-deployable unit. The system supports wireless data transmission via LoRaWAN and records dose-rate data together with the corresponding measurement time and position information. The prototype was tested under field conditions, including long-term outdoor operation, to validate its functionality and stability in a real environmental monitoring scenario.

Results

The development objectives were successfully achieved. A mobile gamma radiation detector prototype was designed, the electronics were assembled and integrated, and the complete system was successfully validated under field conditions.

The combination of two GM tubes with different sensitivities provides coverage of the required measurement range. LoRaWAN-based communication enabled reliable wireless transmission of dose-rate data, while the data acquisition and visualisation functions operated reliably during field tests. The prototype demonstrated stable operation during long-term outdoor measurements and proved suitable for mobile environmental radiation monitoring and dose-rate mapping.

An example of a dose-rate profile recorded during a field test is shown in Fig. 1. Dose-rate maps contain sensitive location information and therefore cannot be included in this report.

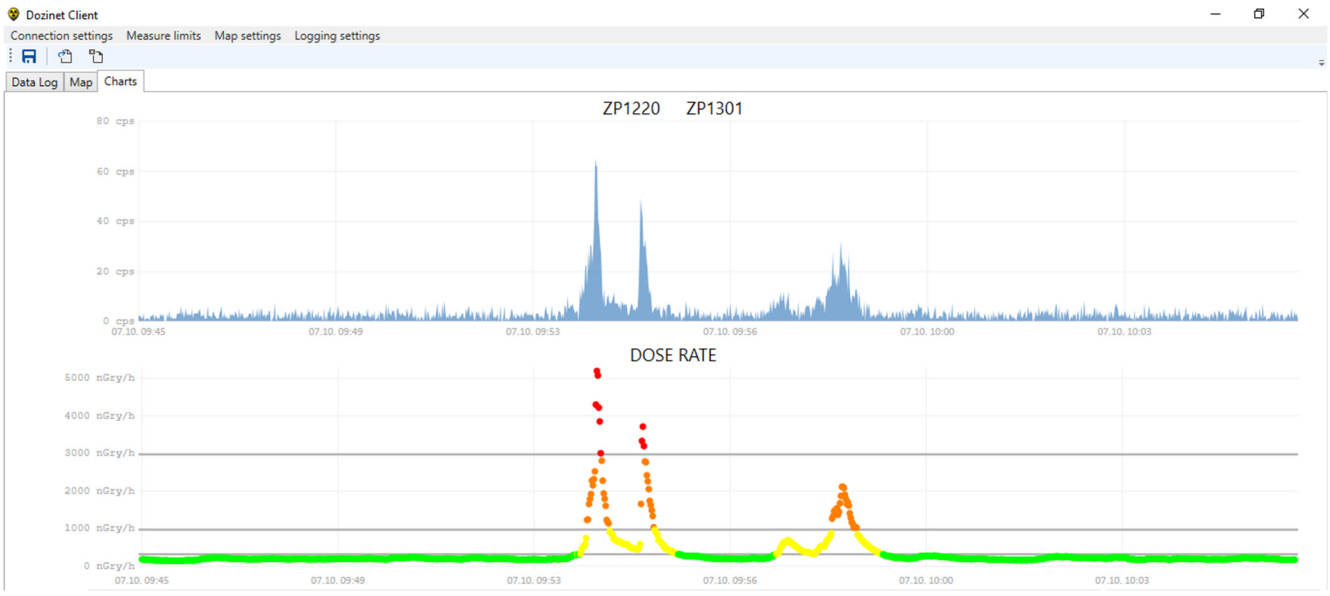


Figure 1: Dose-rate profile obtained using the mobile gamma radiation detector prototype during field measurements

Although the detector technology employed is less advanced than that of compact scintillation detectors capable of providing spectroscopic information, the developed system fulfilled the defined functional requirements and successfully passed field validation. The development demonstrated that a customised, robust and wireless radiation monitoring system can be implemented within a relatively short development timeframe for environmental monitoring applications.

Remaining work

The development objectives have been achieved, and the project has been completed. No further development work is planned within the frame of the project.

Acknowledgment

The activity reported in the present paper was conducted within the framework of the Thematic Excellence Program 2021, grant number TKP-16-6/PALY-2021.

DOSE DISTRIBUTION INSIDE THE INTERNATIONAL SPACE STATION-3D / DOSIS 3D

Julianna Szabó, Attila Hirn, Boldizsár Major

Objective

The aim of the DOSIS 3D project is the measurement of the radiation environment inside the International Space Station (ISS). The project is organised by the European Space Agency (ESA) under the leadership of the German Aerospace Centre (DLR), with the participation of research groups from all around the world. The Centre for Energy Research (EK) is responsible for the provision of passive radiation detectors for the measurement of the absorbed dose (D), Linear Energy Transfer (LET) spectra and dose equivalent (H). These activities are funded within the framework of the ESA PRODEX Experiment Arrangement No. 4000124183. DOSIS 3D was started in the year 2012, and after several extensions, it was prolonged till the remaining lifetime of the ISS. It consists of approximately half-year-long exposure cycles (phases). The current report presents the results from the last two phases (25 and 26), which were flown on the ISS between March 2024 and March 2025.

Methods

Thermoluminescent Detectors (TLDs) and Solid State Nuclear Track Detectors (SSNTDs) are applied by the EK Space Research Department to investigate the dose contribution of the low (< 10 keV/µm) and the high (> 10 keV/µm) LET cosmic radiation. The detector boxes contain two SSNTD sheets and six or eight TLD pellets. In each phase, there are 10 single boxes and a set of 3 boxes (arranged in the three directions of space: X, Y, Z) installed inside the European Columbus module of the ISS. A ground-based intercalibration program is also part of the project, in which the detectors are regularly irradiated at high-energy particle accelerators.

Results

The parameters mostly affecting the radiation environment onboard the ISS are the solar activity, the altitude of the ISS and the local shielding. The last two phases of DOSIS 3D took place at the maximum of solar cycle 25, with the highest solar activity in July 2024. The altitude of the ISS was practically unchanged during this period. Our results are in accordance with these circumstances. Figs. 1 and 2 present the absorbed dose rates and the dose equivalent rates for phases 25 and 26. There is only a slight difference between the two phases, the D values decreased by ~12% in average, while the H values decreased by ~6%. For both exposure missions, we see a similar pattern of the dosimetric quantities over the 13 positions in Columbus. The lowest doses are obtained at Box 9, while the highest values are at Box 2. The reason for this pattern lies in the different local shielding thicknesses for the different positions inside the Columbus Laboratory.

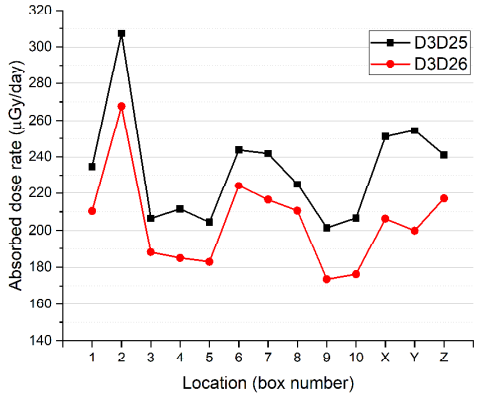


Figure 1: Absorbed dose rates measured during phases 25 and 26

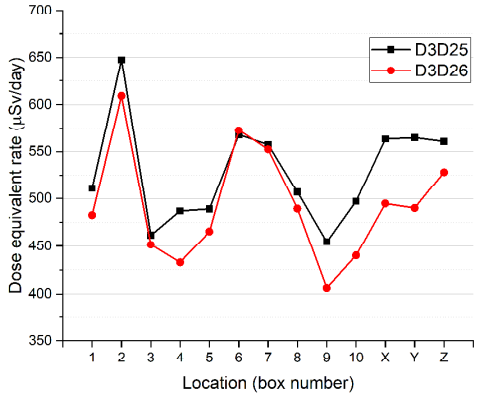


Figure 2: Dose equivalent rates measured during phases 25 and 26

Remaining work

According to the current plan, the project continues until the end of 2026. The measurements related to the actual phases and the interpretation of the vast amount of data are in progress. Building an interactive database has started, serving the scientific community and holding essential information for the application of radiation protection standards for manned spaceflight and for any radiation-susceptible experiment in space.

Related publication

[1] T. Berger, ... , J. Szabó, A. Strádi, A. Hirn, J.K. Pálfalvi, et al.: *DOSIS and DOSIS 3D - Active and Passive Radiation Measurements in Columbus from 2009 – 2025*, 28th Workshop on Radiation Monitoring for the International Space Station, Cologne, Germany (2025)

RADMAG SPACE WEATHER INSTRUMENT DEVELOPMENT

Attila Hirn

Objective

Earth's space environment is highly influenced by several physical parameters, including magnetic field variability, cosmic ray intensity, solar activity and atmospheric conditions. Because of the magnetosphere's complexity and dynamics, effective space weather monitoring requires high spatial and temporal resolution. To address this need, the European Space Agency (ESA) defined the Distributed Space Weather Sensor System (D3S) concept, utilising hosted primary and secondary payloads for operational space weather monitoring on as many platforms as possible. HUN-REN EK initiated the development of a space weather instrument suite, called D3S-RadMag. The major goal of the development is to combine radiation and magnetic field measurement capabilities into a single payload that can be utilised within the D3S hosted payload concept. In 2025, the main objectives of the project were to complete the Preliminary Design Review (PDR), further consolidate the RadMag design, and refine the radiation monitor design based on radiation performance analyses.

Methods

The generic RadMag development follows a phased project management approach in accordance with the recommendations of the European Cooperation for Space Standardisation (ECSS). The preliminary design was reviewed and verified within the framework of the PDR, covering the system-level design, requirements, interfaces, analyses and planned Assembly, Integration and Verification (AIV) activities.

Radiation performance analyses of the RadMag radiation monitor particle telescope were performed to assess the expected instrument response over the relevant particle flux and energy ranges and to identify potential saturation effects in high-flux environments. The performance of the telescope significantly degrades at count rates above 10^5 counts per second (cps) in individual detectors due to increased dead time and pulse pile-up. Based on the results of these analyses, the detector configuration and telescope geometry were reassessed in cooperation with ONERA, the French aerospace research laboratory. Design modifications were investigated with the aim of reducing the geometrical factor and thereby extending the usable measurement range of the instrument towards higher particle fluxes. The modified configuration is intended to reduce the effective geometrical factor and prevent saturation of the detector system in high-flux radiation environments while maintaining the required measurement performance.

Results

The PDR of the RadMag development was successfully completed in 2025. The review confirmed the maturity of the preliminary design and provided the basis for proceeding with the subsequent design consolidation phase.

As part of the radiation performance assessment, the RadMag particle telescope was analysed with respect to its response in high particle flux environments. The analysis indicated that the initial telescope configuration could reach saturation in the front three detectors of the telescope in regions with particularly high particle fluxes, such as during intense solar particle events or in certain regions of the Van Allen radiation belts. In cooperation with ONERA, a modified detector configuration was therefore proposed to reduce the geometrical factor of the telescope and extend its operational range.

The proposed modification foresees the use of annular detectors for the first three detectors and the introduction of additional shielding and a pinhole at the telescope entrance aperture. These measures are expected to reduce the particle acceptance of the telescope and mitigate saturation effects in high-flux environments. The modified configuration will be further assessed as part of the ongoing design consolidation.

Remaining work

In 2026, the main objective will be to consolidate the RadMag design and requirements with particular emphasis on ensuring compatibility with the AURORA-D mission. The modified RadMag radiation monitor telescope configuration will be further analysed and incorporated into the consolidated design, as appropriate. The requirements and relevant system-level design documentation will be updated accordingly.

Acknowledgment

The activity reported herein was performed under ESA Arrangement No. 4000142147/23/D/MRP (generic development) and No. 4000143083/23/D/AP (AURORA-D consolidation).

THE INTERNAL DOSIMETRY ARRAY FOR GATEWAY, THE SPACE STATION OF THE ARTEMIS PROGRAM

Attila Hirn, Ádám Marton

Objective

The Internal Dosimeter Array (IDA) would be the very first European-led internal payload to be hosted within the US Habitation and Logistics Outpost (HALO) module for Gateway, the future lunar-orbiting space station of the Artemis program. The goal of the IDA payload is to continuously monitor the internal space dosimetry environment with the combination of existing and proven instrument technologies developed by our institute and international partners. Dosimetry measurements for exploration missions are of utmost importance, as the astronauts will not be protected by the Earth's magnetic field or the atmosphere; hence, they could be exposed to up to 700 times the radiation dose of an average human on Earth from space radiation. The IDA consortium is led by the HUN-REN Centre for Energy Research (EK). The primary objective for 2025 was the completion of the engineering phase and the manufacturing, acceptance, and integration preparation of the Proto-Flight Model (PFM), leading towards final system integration and delivery to the European Space Agency (ESA).

Methods

The project is implemented following a phased development approach defined by the European Cooperation for Space Standardization (ECSS). In the previous year, an Engineering Model (EM) was built for development and verification purposes. In this project, the EM is used for qualification, software development and testing, functional testing, and mechanical fit checks at the HALO mock-up and during the flight. Later, it will be used as a ground reference model. During 2025, the project successfully completed the engineering phase and entered the flight manufacturing phase after the successful EM Test Acceptance Review (TAR) and the PFM Manufacturing Readiness Review (MRR). The IDA payload comprises the European Active Dosimeter (EAD) mobile unit from the German Aerospace Centre (DLR), the MediPix radiation detector supplied by ADVACAM s.r.o. (Czech Republic), the three-dimensional silicon detector telescope TRITEL developed by EK and manufactured by REMRED Ltd., and the Passive Dosimetry System (PDS) provided by the Japan Aerospace Exploration Agency (JAXA). The common Electronics Box (E-Box) interfacing with the Gateway subsystems is developed by REMRED Ltd., while the payload structure is designed and manufactured by Airbus Defence and Space.

Results

A major milestone was achieved in March 2025 when IDA successfully passed the National Aeronautics and Space Administration (NASA) Safety Review 2, confirming compliance with the programme's safety requirements. The engineering phase was formally completed through the successful EM TAR, followed by the PFM MRR authorising the start of flight model manufacturing. During the second half of the year, PFM manufacturing progressed according to schedule. The PFM Design Review Boards (PFM DRBs) were successfully completed. The flight dosimetry instruments—including the TRITEL, MediPix and Passive Dosimetry System (PDS)—were manufactured, calibrated, acceptance tested and delivered for integration. The metallic payload structure was also delivered. By the end of 2025, procurement and manufacturing of the Electronics Box (E-Box) had been completed. The Software Preliminary Design Review (SW PDR) was successfully held in December, with the final close-out activities continuing. These achievements established the readiness for final payload integration and system-level verification activities planned for 2026.

Remaining work

The remaining activities include integration of the IDA PFM, system-level functional and environmental testing, completion of software qualification, and final acceptance before handover of the flight hardware to ESA for subsequent delivery to NASA.

Acknowledgment

The IDA payload implementation is conducted under ESA Contract No. 4000136731/21/NL/AT.

DEVELOPMENT AND QUALIFICATION TESTING OF A COMPLEX SPACE DOSIMETRY SYSTEM FOR INTERPLANETARY MISSIONS

Attila Hirn, Győző Tóth

Objective

The Mars Sample Return (MSR) campaign led by NASA/JPL (National Aeronautics and Space Administration / Jet Propulsion Laboratory) aims to convey soil and atmospheric samples from the Mars surface to Earth. An important contribution of the European Space Agency (ESA) to the program is the Earth Return Orbiter (ERO) spacecraft. The Space Dosimetry System (SDS) experiment, composed of a space radiation monitor (RADTEL space radiation telescope) and a dosimetry monitoring system (TRITEL 3-dimensional silicon detector telescope), had been proposed for ERO to monitor space radiation and related dosimetry quantities during the Earth-Mars cruise, in orbit around Mars and during the return trip from Mars to Earth, supporting future human Mars exploration missions.

In 2025, the SDS development activities focused on experimental verification of the instrument performance and environmental robustness of the design. Radiation performance measurements with electrons and protons were performed at the Paul Scherrer Institute (PSI), while environmental testing, including random vibration tests, was conducted to verify the mechanical integrity and functional performance of the developed hardware under representative spaceflight conditions.

Methods

The engineering activities are performed by Hungarian subcontractors with relevant spaceflight heritage, while project management and product assurance requirements, system-level consolidation, experiment approach definition, and radiation analyses are conducted by the HUN-REN Centre for Energy Research (EK).

Calibration and performance testing were conducted at instrument level. Dedicated Instrument Calibration Enclosures (ICE) were designed and manufactured to enable radiation measurements at relevant facilities. Following integration into the ICEs and functional testing, dedicated particle-beam measurements were performed at the PSI. Electron and proton beams were used to investigate the response and performance of the radiation detectors under controlled irradiation conditions. The measurements provided experimental data for the characterisation and verification of the RADTEL and TRITEL detector systems and for comparison with simulation results.

Following completion of the performance tests, the instruments were removed from their ICEs and integrated into the SDS engineering model. The environmental test campaign included mechanical environmental testing, with random vibration tests performed to verify the structural integrity of the payload and its ability to withstand the mechanical loads associated with spacecraft launch. Functional checks were performed before and after the environmental tests to identify any degradation or changes in instrument performance.

Results

In 2025, the SDS development progressed from component and subsystem-level development towards experimental verification of the integrated engineering models.

A dedicated measurement campaign was conducted at the Paul Scherrer Institute using electron and proton beams. The measurements provided experimental data on the detector response under controlled particle irradiation conditions. The obtained data confirmed the functionality of the instruments and the expected linear response (Fig. 1). However, the measurements also revealed that the parameter settings of the peak detection algorithm require adjustment.

The environmental test campaign also got underway. The hardware was subjected to random vibration testing at representative qualification levels. During those tests, two of the silicon detectors of RADTEL were damaged. Preliminary analysis indicates that the damage was not caused by the instrument design but rather by a manufacturing defect in the detectors. A more detailed investigation will be conducted in 2026, with involvement of the detector manufacturer. The environmental test campaign can proceed only after the issue has been resolved.

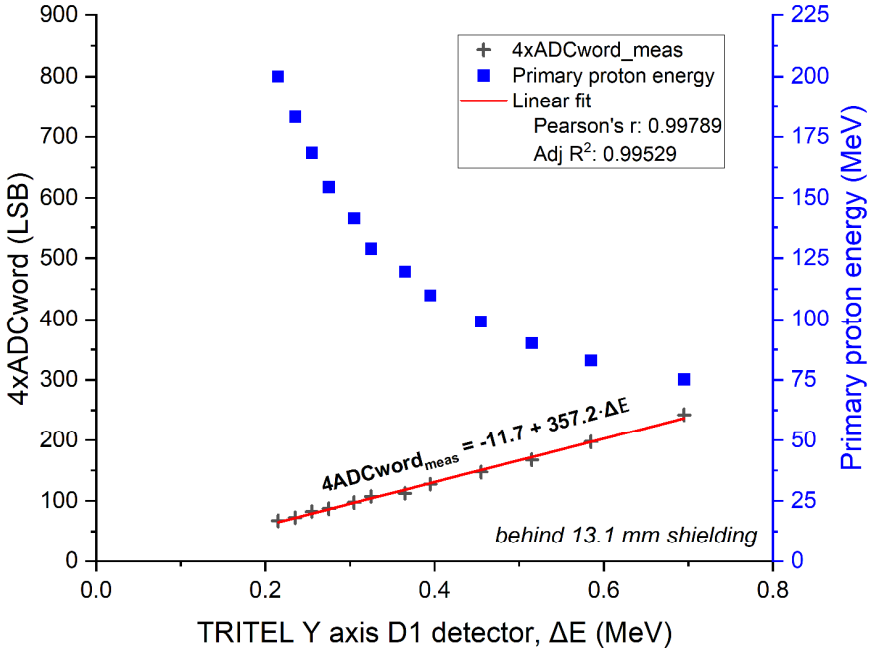


Figure 1: Measured peak amplitude versus energy deposition in the TRITEL Y-axis D1 detector in proton-beam measurements (linearity check)

Remaining work

The results obtained from the 2025 test campaigns will be used to consolidate the detailed design of the SDS and to define the final configuration of the flight hardware. Further development activities will include the continuation and completion of the environmental test campaign, completion of the design consolidation, manufacturing and integration of the flight hardware, followed by the required qualification and acceptance testing. Performance testing of the RADTEL and TRITEL instruments with optimised parameter settings will be continued at PSI. The measurement data will be further analysed and compared with Monte Carlo simulations to support the final performance characterisation of the instruments.

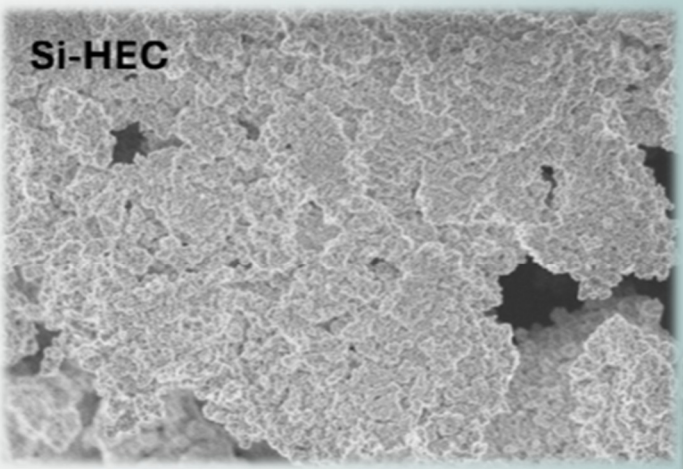
Acknowledgment

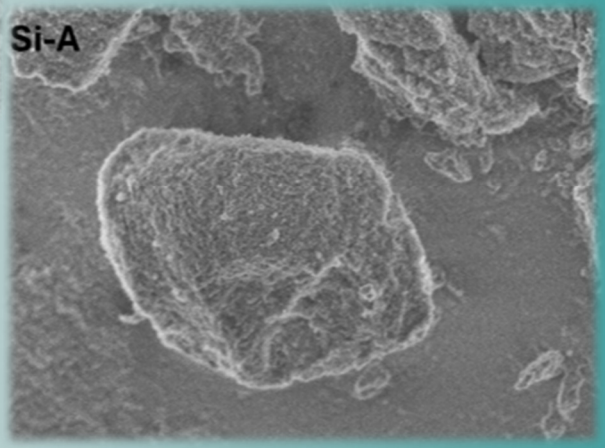
The implementation phase of the SDS development is financed under ESA Contract No. 4000137393/22/NL/DB.





IV. ENERGY SECURITY AND ENVIRONMENTAL STUDIES





ENERGY STRATEGY AND NETWORK RESEARCH FOR FUTURE LOW-CARBON ENERGY SYSTEMS

Lilla Barancsuk, Endre Börcsök, Tímea Erdei, Veronika Groma, Bálint Hartmann, Tamás Soha

Objective

A key objective in future energy mix research is to identify the technological, economic, and system-level conditions required for establishing a stable, sustainable, and decarbonised electricity system. One important research direction focuses on the role of nuclear fusion, with particular emphasis on critical factors such as investment costs, deployment speed, tritium supply, and the limitations of renewable energy sources, all of which may determine the long-term integration of fusion energy into the global energy system.

To investigate the applicability of international approaches in Hungary, it also became necessary to develop a GIS-based Multi-Criteria Decision-Making (MCDM) methodology capable of determining the optimal spatial allocation of energy alternatives, particularly renewable energy projects. Our study evaluated the suitability of different regions for energy system developments at a national scale by considering a total of 24 technical, environmental, and socio-economic factors.

One of the key prerequisites for the stable operation of future energy systems is the condition and resilience of the electricity grid. To address this issue, complex network-theoretical modelling approaches were applied to analyse the long-term structural evolution of the electricity distribution network in Southern Transdanubia. The research investigated whether certain topological characteristics and the resulting inherent vulnerabilities persist despite the substantial expansion of the network. Our study was later extended to a comparative meta-analysis of the high-voltage electricity transmission networks of four European countries — the Czech Republic, Hungary, the Netherlands, and Slovakia — examining their topological evolution, resilience, and vulnerability over a 50–70 year period.

One of the greatest challenges associated with the integration of renewable energy sources is the stochastic nature of photovoltaic power generation, which can cause significant fluctuations in electricity systems. Accurate ultra-short-term forecasting represents an important tool for mitigating these effects. The related research aimed to develop a resource-efficient solar irradiance forecasting model capable of simultaneously predicting global and diffuse horizontal irradiance at 1-, 5-, 10-, and 20-minute forecasting horizons. The objective was to create a solution that combines high forecasting accuracy with low computational demand, making it suitable even for embedded or edge computing devices.

Methods

Several complementary modelling and data analysis approaches were applied to investigate the technological, spatial, and network-related characteristics of future energy systems. To analyse the evolution of the global energy mix, the EUROfusion TIMES Model (ETM), a technology-oriented optimisation-based energy system model, was employed to simulate the development of the global energy system up to 2100 under different decarbonisation pathways. The analysis was based on 24 distinct scenarios that examined long-term energy system development by varying the share of renewable energy sources, the market entry date of nuclear fusion, deployment dynamics, and investment costs.

To determine the spatial suitability of domestic energy alternatives, a GIS-based Multi-Criteria Decision-Making (MCDM) methodology was applied. The method included preprocessing various geospatial datasets, defining buffer zones and suitability categories, applying weighting procedures, and executing raster-based spatial operations. The analysis integrated national and European datasets, including Corine Land Cover, Natura 2000, infrastructure-related, and nature conservation databases, in order to provide a comprehensive assessment of territorial suitability for energy developments.

Complex network-theoretical approaches were employed to investigate the stability and vulnerability of electricity networks. In the case of the medium-voltage distribution network of Southern Transdanubia, four historical snapshots of the network (1950, 1955, 1960, and 1965) were reconstructed from historical maps and analysed using graph-based models. Various complex network metrics were calculated, including degree, closeness, and betweenness centrality, as well as network efficiency. In addition, the impacts of node and edge failures on system performance were examined through 10,000 simulation runs.

Within the framework of the international comparative study, a historical topological database with annual resolution was established for the transmission networks of four European countries — the Czech Republic, Hungary, the Netherlands, and Slovakia. The networks were analysed using graph-theoretical methods, with particular emphasis on small-world properties, global efficiency, clustering characteristics, and the occurrence of specific network motifs such as loop and star structures. The analysis also included the investigation of infrastructure age and the long-term evolution of network topology.

To model the temporal variability of renewable energy generation, a Feature-based Long Short-Term Memory (FbLSTM) neural network was developed, combining pre-processed sky-camera image features and meteorological parameters as input variables. The model was trained and validated using more than three years of minute-resolution all-sky camera and meteorological measurement data, and its performance was compared against a ConvLSTM-based benchmark model.

Results

The results demonstrated that nuclear fusion could play a significant long-term role in the decarbonisation of the global electricity system; however, the extent of its contribution strongly depends on the deployment rate of the technology and the maturity of supply chains, particularly tritium availability. According to the modelling results, the share of fusion energy in global electricity generation by 2100 may range from a few per cent up to 21%. The analyses further revealed that rapid industrial-scale deployment is a more critical factor for the success of fusion technology than either early market entry or low investment costs alone. In addition, limiting the share of renewable energy sources may create more favourable conditions for the expansion of fusion technologies. [1,2]

The GIS-based suitability assessment indicated that approximately 31,031 km² of Hungary is suitable for wind energy development, representing nearly one-third of the country's total area. The most favourable regions accounted for 9.7% of the national territory. Furthermore, the applied GIS-based MCDM methodology effectively identified areas that should be excluded from energy developments due to environmental, social, or infrastructural constraints, while also providing detailed spatial support for strategic decision-making processes.

The structural analysis of electricity networks revealed that, despite the expansion of the Southern Transdanubian distribution network, its fundamental topological characteristics — such as low clustering and tree-like structure — remained largely unchanged over the long term. This resulted in persistent vulnerability, as even small proportions of node or edge failures caused significant reductions in network efficiency. The findings also showed that, despite the developments implemented between 1950 and 1965, the resilience of the system improved only marginally. [3]

The international comparative analysis showed that European transmission networks not only expanded in size over recent decades but also became increasingly structurally complex. At the same time, the principal topological indicators stabilised after approximately 25–30 years, suggesting long-term structural consolidation of the networks. Motif analysis revealed that a gradual balance emerged between robustness and efficiency: the systems became progressively less centralised while certain redundant loops were retained to ensure operational flexibility. [4]

The FbLSTM model developed for short-term renewable energy forecasting outperformed both persistence-based and ConvLSTM-based benchmark models across most forecasting horizons, while maintaining substantially lower computational requirements. The use of extracted image features enabled approximately a 4,250-fold reduction in input data volume compared to raw camera images, while the model achieved an approximately 10% improvement in forecast skill relative to persistence-based forecasting methods. [5]

Remaining work

Future work will focus on extending the GIS-based spatial suitability modelling framework to additional energy technologies, including Small Modular Reactors (SMRs), nuclear fusion facilities, and other emerging low-carbon energy alternatives. These developments will require the integration of technology-specific technical, environmental, safety, infrastructural, and socio-economic criteria to support comprehensive territorial assessment and long-term energy planning.

Another important research direction is the further improvement of PV power generation forecasting models through the integration of spatial suitability assessment results. Incorporating territorial suitability and local environmental characteristics into forecasting frameworks may improve the accuracy and robustness of PV production predictions, particularly under highly variable meteorological conditions. This integrated approach could contribute to more reliable renewable energy integration and enhanced grid stability in future energy systems.

Related publications

[1] V. Groma, E. Börcsök, A. Terjék, C.A. Bustreo: *European Comparative Study of Public Perception and Evidence-Based Information on Energy Production Alternatives,* Sustainability **17(22)**, 143 (2025) https://doi.org/10.3390/su172210043

[2] C. Mantilla, C. Bustreo, F. Gracceva, Y. Lechòn, T. Baroncelli, M. Bauer, N. B. Ayed, M. Biberacher, E. Börcsök, S. Broekers, V. Groma, L. Savoldi, L. Siciliano, A. Kanudia: *Fusion at Scale: Critical Enablers in Global Energy Transitions,* submitted to Energy Policy

[3] B. Hartmann, T. Soha, M. T. Cirunay, and T. Erdei: *Inherent structural vulnerabilities in power distribution networks: a longitudinal complex network analysis*, Appl Netw Sci **10**, 31 (2025) https://doi.org/10.1007/s41109-025-00724-9

[4] B. Hartmann, M. T. Cirunay: *Empirical cross-system meta-analysis of long-term transmission grid evolution*, International Journal of Electrical Power & Energy Systems **173**, (2025) https://doi.org/10.1016/j.ijepes.2025.111447

[5] L. Barancsuk, V. Groma, B. Kocziha: *Hybrid ultra-short term solar irradiation forecasting using resource-efficient multi-step long-short term memory*, Renewable Energy **247(10),** 122962 (2025) https://doi.org/10.1016/j.renene.2025.122962

IMPROVEMENT OF ENERGY SECURITY BY THE UTILISATION OF LOW-TEMPERATURE HEAT SOURCES AND BY ENERGY STORAGE

Attila R. Imre

Objective

The research focuses on enhancing the security and resilience of energy supplies, addressing critical aspects such as advanced energy storage technologies and improvements in overall energy efficiency. Special emphasis is placed on the effective utilisation of existing low-temperature heat sources, including geothermal energy as well as industrial waste heat, which represent significant untapped potential. To achieve this, the applicability of traditional Organic Rankine cycles was studied, as well as innovative thermodynamic cycles are being designed and optimised to maximise power output while keeping costs at an acceptable level. In the field of energy storage, the work concentrates on large-capacity solutions such as high-temperature heat storage (Carnot batteries), hydrogen and its derivatives, and other high-density storage systems. These approaches aim to support grid stability and enable sector coupling for sustainable energy integration. Furthermore, the research explores the feasibility of establishing a nationwide network of on-site hydrogen production facilities combined with hydrogen refuelling stations in Hungary, creating a decentralised infrastructure that supports both mobility and industrial applications.

Methods

Thermodynamic data were taken from RefProp database and NIST Webbook. Calculations were done mostly using our own codes.

Results

This study introduces an innovative system for recovering waste heat from exhaust air following a regenerative thermal oxidiser process, integrating a Carnot battery with Photovoltaic (PV) modules. The Carnot battery combines an Organic Rankine Cycle (ORC) equipped with a recuperator, Thermal Energy Storage (TES), and a heat pump. Waste heat is first captured in TES, while additional energy is extracted via a heat pump to raise the temperature of a secondary fluid, effectively charging TES from both direct and indirect sources. The stored heat enables electricity generation through the ORC. Results indicate a heat pump COP (Coefficient of Performance) between 2.55 and 2.87, ORC efficiency ranging from 0.125 to 0.155, and Carnot battery power-to-power ratios between 0.36 and 0.40. PV modules contribute 1.35 GWh annually, primarily powering the heat pump and ORC pump, leading to a total annual net generation of 4.30 GWh. Economic analysis across four configurations shows favourable returns, ranging from 25% to 160%. Evaluations comparing systems with and without PV integration and ORC recuperation reveal that incorporating both significantly boosts power output, offering a highly viable and sustainable energy solution. [1]

The Carnot principle indicates that raising the hot source temperature or lowering the cooling source temperature improves cycle efficiency. For ORC systems operating under subcritical conditions, increasing evaporation and/or condensation temperatures can enhance efficiency within certain ranges until a maximum is reached, which depends on the working fluid. Beyond this point, efficiency may decline near the critical region for some configurations. Preliminary findings suggest that elevating evaporation temperature above the critical point, followed by expansion to subcritical conditions—known as transcritical ORC—can improve performance when condensation temperature is fixed. However, this trend is strongly influenced by the isentropic efficiency of the expander. This study presents a theoretical analysis of ORC configurations from subcritical to transcritical operation, including two-phase expansion systems such as trilateral and partially evaporated ORC. Several working fluids were evaluated in simulations. Considering material limits and fluid stability, 350 °C was chosen as the maximum evaporation temperature. Results indicate that higher evaporation temperature does not always guarantee better efficiency; optimal performance depends on fluid selection and operating conditions. Notably, transcritical ORC systems using CO_2 demonstrated promising efficiency for future energy conversion applications. [2]

A novel approach is introduced to visualise the thermodynamic sub-processes within ORC. Special emphasis is placed on examining various working fluids—both wet and dry—and their characteristic state changes during ORC operation. The analysis covers transitions starting from saturated states and ending in different saturated conditions, including liquid-liquid, liquid-critical, liquid-gas, gas-liquid, gas-critical, and gas-gas processes. Particular focus is given to isothermal, isobaric, and isenthalpic transitions, which strongly influence ORC performance and efficiency. The visualisation technique provides a clearer representation of these complex thermodynamic interactions, improving understanding of the relationships between cycle behaviour and fluid properties. The impact on cycle efficiency, expansion characteristics, and heat recovery potential has been assessed for different fluid types. This method offers value for both educational and industrial applications: 3D models help students grasp ORC principles and fluid differences, while industry professionals can use them to select optimal working fluids, enhancing cycle efficiency and adapting systems to diverse heat sources. [3]

Several existing heat sources, such as geothermal energy or industrial waste heat, have temperatures sufficient for electricity generation, yet their heat flow rates (typically a few tens to hundreds of kWth) are too low for efficient utilisation with conventional solutions like ORC systems. Achieving viability requires either more efficient devices or a reduction in self-

consumption. For smaller ORC units, pumps and air-cooling systems account for significant internal losses, cutting net power output by 30–50%. Our approach eliminates this issue by replacing the pump and isobaric liquid heater with an isochoric heating device, enabling the formation of a trilateral transcritical cycle without a pump. This design not only improves efficiency but also reduces installation and maintenance costs by minimising component complexity. The concept will be demonstrated using working fluids such as propane, cyclopropane, and xenon. [4]

Although hydrogen technology in private and public transport is expanding, its growth remains far behind battery-electric vehicles due to persistent supply and demand-side inertia. The limited number of hydrogen-powered vehicles initially hinders the development of a comprehensive refuelling infrastructure, creating a classic chicken-and-egg problem. A promising approach is to establish a decentralised, on-site hydrogen production network, which avoids the high capital costs of centralised systems and accelerates early deployment. This concept can be further strengthened by employing methane splitting (pyrolysis) instead of electrolysis, using biomethane sourced from existing biogas plants as feedstock. Such a solution could support refuelling stations along the Hungarian section of the Trans-European Transport Network (TEN-T) and other major routes, improving accessibility and sustainability. A case study near Szarvas, adjacent to the M44 highway, demonstrates feasibility: hydrogen production powered by geothermal energy, with an ORC system generating over 1000 kW_{el} and providing residual heat for district heating. This integrated approach significantly improves economic viability while leveraging renewable and waste heat resources. [5,6]

Overall, these studies provided valuable insights into the performance of ORC and similar processes, the usability of Carnot battery technology, the possibility of using a novel cycle for the utilisation of small heat sources and a viable way to establish a public hydrogen refuelling station network.

Related publications

[1] P. D. Prajna Paramita, S. Daniarta, A. R. Imre, and P. Kolasinski: *Techno-Economic Analysis of Waste Heat Recovery in Automotive Manufacturing Plants,* Applied Sciences **15**, 569 (2025) https://doi.org/10.3390/app15020569

[2] S. Daniarta, P. Kolasínski, A. R. Imre: *Design and Analysis of Organic Rankine Cycle From Subcritical to Transcritical Operations,* Proceedings of the 8th International Seminar on ORC Power Systems (Eds.: Turunen-Saaresti, Teemu; Crespi, Francesco; Spinelli, Andrea; Uusitalo, Antti; White, Martin T.), Lappeenranta-Lahti University of Technology LUT, LUT Scientific and Expertise Publications **25-09,** 277-286 (2025) https://urn.fi/URN:ISBN:978-952-412-288-7

[3] R. Kustán, A. R. Imre: *Visualization of the Simple Thermodynamic Processes Related to Heat-to-power and Power-to-heat Cycles,* Proceedings of the 8th International Seminar on ORC Power Systems (Eds.: Turunen-Saaresti, Teemu; Crespi, Francesco; Spinelli, Andrea; Uusitalo, Antti; White, Martin T.), Lappeenranta-Lahti University of Technology LUT, LUT Scientific and Expertise Publications **25-09,** 21-30 (2025) https://urn.fi/URN:ISBN:978-952-412-288-7

[4] A. R. Imre, R. Kustán: *How Can Self-consumption for Heat Engines be Reduced to Make Them a Viable Alternative to Utilize Small Heat Sources for Power Production?* Proceedings of the 8th International Seminar on ORC Power Systems (Eds.: Turunen-Saaresti, Teemu; Crespi, Francesco; Spinelli, Andrea; Uusitalo, Antti; White, Martin T.), Lappeenranta-Lahti University of Technology LUT, LUT Scientific and Expertise Publications 25-09, 11-20 (2025) https://urn.fi/URN:ISBN:978-952-412-288-7

[5] K. Kummer, A R. Imre: *Supply of the hydrogen refuelling stations in the Hungarian part of the Trans-European Transport Network – comparison of the methane splitting and water electrolysis,* International Journal of Hydrogen Energy **186C,** 152084 (2025) https://doi.org/10.1016/j.ijhydene.2025.152084

[6] K. Kummer, A. R. Imre, R. Kustán: *Decentralized Hydrogen Refuelling Station Concept: Achieving Security of Supply through Geothermally-Powered Onsite Biomethane Pyrolysis,* 20th Conference on Sustainable Development of Energy, Water and Environment Systems (SDEWES), 05-10 October, 2025, Dubrovnik, Croatia, https://www.dubrovnik2025.sdewes.org/ (oral presentation, will be published in the proceeding book)

SYNCHRONISATION MODELLING AND DEVELOPMENT OF POWER GRIDS

Géza Ódor, Bálint Hartmann,
Kristóf Benedek, István Papp, Michelle T.Cirunay

Objective

Cascade failures in power grids occur when the failure of one component or subsystem triggers a chain reaction that propagates through other components or subsystems, ultimately leading to a widespread blackout or outage. Controlling cascade failures on power grids is important for many reasons, such as economic impact, national security, public safety, and even ripple effects on transportation systems. Monitoring the networks at the node level has been suggested by many, either by controlling all nodes of a network or by subsets. Using our Kuramoto-based network synchronisation methods and tools this year, we focused on the prediction of power grids' development towards more stable High Voltage (HV) electrical systems in Europe.

Methods

Predicting, controlling, and avoiding blackouts and helping to design more error-prone networks and methods have been the subject of many other studies. Most of them use approximations and try to isolate the most vulnerable points by a frequency analysis of solitary nodes. Here, we contributed to the modelling of cascades based on the complete Kuramoto equations, without any linearization, by numerical simulations on large European high-voltage power grids. We investigated the effects of changing network topology on the synchronisation and cascade failure dynamics in several ways. The first path is purely static, based on the network community analysis and aims to determine the effects of the addition or removal of bridges between communities. The second path is dynamic; it uses the solution of the swing equations and identifies the nodes of lowest local synchrony. By bypassing these nodes, via the addition of edges of the same number as the bridge links, we can compare the methods.

While there are numerous well-known order parameters to characterise these dynamics, shortcomings of these metrics are also recognised. To capture all transitions from phase-disordered states over phase locking to fully synchronised systems, new metrics were proposed and demonstrated on homogeneous models. We aimed to address a gap in the literature, namely, to examine how gradual improvement of power grid models affects the goodness of certain metrics. To study how the details of models are perceived by the different metrics, 12 variations (scenarios) of a power grid model were created, introducing varying levels of heterogeneity through the coupling strength, the nodal powers and the moment of inertia. The grid models were compared using a second-order Kuramoto equation and an adaptive Runge-Kutta solver, measuring the values of the phase, the frequency and the universal order parameters. Finally, the frequency results of the models were compared to grid measurements.

Another way of power-grid improvement suggested by DC and linearization modelling is the inclusion of High-Voltage Direct Current (HVDC) lines instead of normal AC connections. To implement this with our nonlinear Kuramoto solver, we substituted certain AC lines in the European 2016 power grid (known to be HVDC lines in reality) with constant and adaptive power sources and sinks at the ends of these lines.

Results

Regarding the different network improvement strategies, dynamical bypassing was found to improve synchronisation the best, while the average cascade sizes are the lowest with static bridge additions. However, for very large or small global couplings, these network changes do not help; they seem to be useful near the synchronisation transition region, where self-organisation drives the power grid. Thus, we provide a demonstration of Braess' Paradox on continent-sized power-grid simulations and uncover the limitations of this phenomenon. We also determined the cascade size distributions and justified the power-law tails near the transition point on these grids [1, 2, 3].

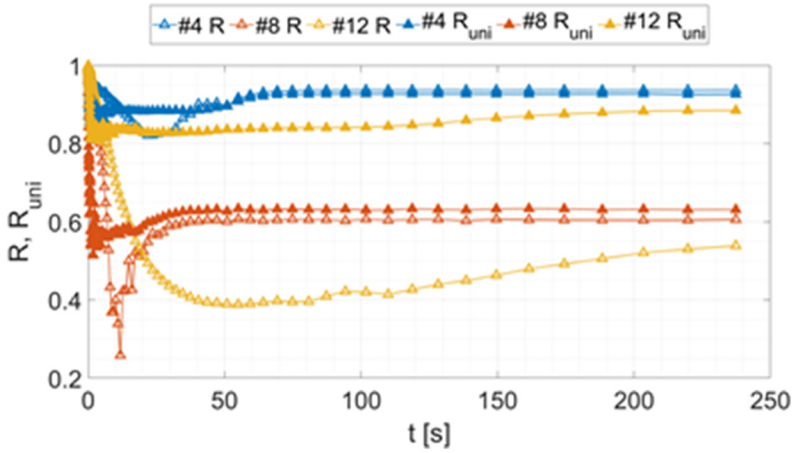


Figure 1: Evolution of R and R_{uni} for phase-ordered initial conditions at λ = 0.5 (close to the synchronisation point). The level of heterogeneity increases with the scenario number.

Regarding the different order parameters, we found that the universal order parameter ($\boldsymbol{R}_{uni}$) was able to capture more details of the grid models, especially in cases of decreasing moment of inertia, than the standard Kuramoto order parameter ($\boldsymbol{R}$). The most heterogeneous models showed lower synchronisation and thus suggest a limitation of the second-order Kuramoto equation. However, even the most heterogeneous models showed notable synchronisation, encouraging the use of such models (see *Fig. 1*). We also found that decreasing the inertia of the system is more distinctly presented across the different scenarios but does not inhibit synchronisation.

Finally, we showed local frequency results related to the multi-peaks of static models, which implies that spatial heterogeneity can also induce such multi-peak behaviour [4]. Note that according to our knowledge, this is the first time that heavy-tailed, q-Gaussian frequency distributions could be well described via modelling of the whole power grid, as shown in Figure 2.

Regarding the HVDC improvements, our first results, involving the BME EE BSc student Aron Weidinger, showed that the substitutions of 37 HVDC lines with AC ones on the EU2016 grid, which we analyzed earlier, did not alter the synchronisation results too much [5]. However, our more precise study has shown that static DC lines improve phase stability and the cascade sizes above the synchronisation threshold. Adaptive frequency-dependent HVDC lines proved to be even better in the steady state, at the expense of long transients [12].

This HVDC study has been extended by taking into account the DC power levels adaptively. This was done by rewriting our present simulation C-code by PhD student Kristof Benedek. Extensive simulations found improvements in the cascade sizes, but still in the weakly coupled region. This work was done in consultation with the researchers of the Institute of Complex Systems at the University of Baleares, Mallorca, where similar research has been started under the lead of Prof. Pere Colet. Publication of the results is scheduled for this year. In the half-year extension in 2025, a comparison of different network improvements on the Hungarian HV power grids was investigated. For the Hungarian power grid, we have knowledge of detailed electrical parameters, and we compared the Kuramoto model approach results with those from standard electrical engineering. We tested the validity of the Braess paradox for different network upgrades and compared the results coming from the full European simulations with those of the Hungarians. We also compared these results with those of standard electrical engineering load methods [8] [9]. Furthermore, there have been network analysis studies on the Hungarian MW power grids, too [10-11].

Besides the mainstream power-grid results, we performed some additional studies of the Kuramoto model in higher dimensions to investigate heterogeneity effects, which was a completion of a work started with Shengfeng Deng [6] and another research conducted with Robert Juhasz (Wigner FK), in which we investigated glassy dynamics in two dimensions [7]. These results provide a better understanding of the heterogeneity effects on the Kuramoto model, which ultimately appear in power grids. For example, negative couplings can describe capacitive stabilising elements.

We mention that these results were presented at several international conferences as invited talks: Netsci2024 (Quebec, Canada), CCS2024 (Exeter, UK), Dynamic Days Europa 2024 (Bremen, Germany), ICMGIII (India), DSS-2024 (Istanbul, Turkye), ENACS (Max Planck, Dresden) 2025, DDS2025 Thessaloniki and a seed of an international research network has been set up, led by us, who submitted an application for the COST action fund in 2024.

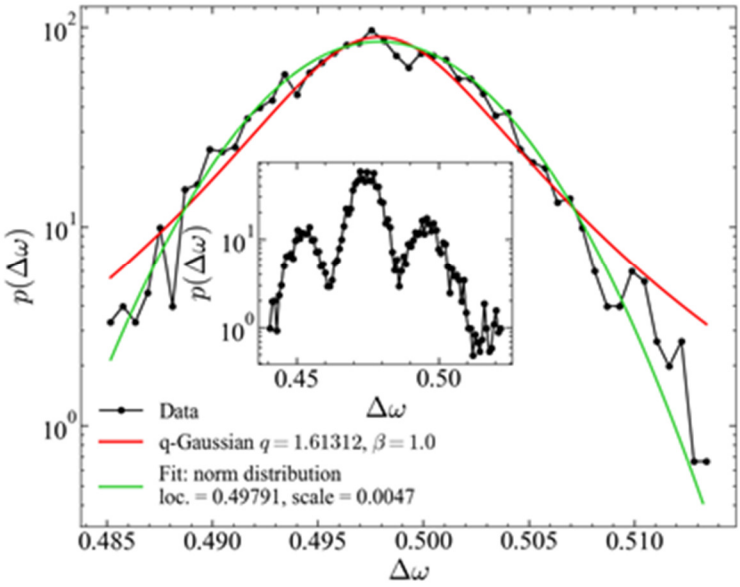


Figure 2: Local frequency fluctuation distributions with respect to Ω_i=50 Hz, obtained for scenario 9, corresponding to Békéscsaba substation for transmission rate λ = 0.5, with different numerical fits. The best fit is obtained with the Student's t-distribution. The q-Gaussian provides $q \simeq 1.61$, close to the measurements. This particular node was chosen because real data were fitted for the same substation in one of our previous works. Similar distribution results were obtained for the other substations (e.g. Detk, Győr) as well. The inset shows the typical multi-peak behaviour in the case of $\lambda = \lambda_c$ at the same node, in the present case, for λ = 0.6.

Related publications

[1] G. Ódor, I. Papp, K. Benedek, B. Hartmann: *Improving power-grid systems via topological changes or how self-organized criticality can help power grids*, Phys. Rev. Res. **6,** 013194 (2024) https://doi.org/10.1103/PhysRevResearch.6.013194

[2] B. Hartmann, G. Ódor, I. Papp, K. Benedek, S. Deng, J. Kelling: *Dynamical heterogeneity and universality of power-grids,* Sustainable Energy, Grids and Networks **39,** 101491 (2024) https://doi.org/10.1016/j.segan.2024.101491

[3] K. Benedek: *Szinkronizációs és stabilitás dinamika tanulmányozása és topológiai változtatások hatásainak vizsgálata nagyfeszültségű villamoshálózatokon (Study of synchronization and stability dynamics and the effects of topological changes on high-voltage electrical networks)*, MSc Thesis work at BME TTK.

[4] B. Hartmann, G. Ódor, K. Benedek, I. Papp: *Power-grid modelling via gradual improvement of parameters,* Chaos **35,** 013138 (2025) https://doi.org/10.1063/5.0237050

[5] A. Weidinger: *The impact of renewable energy production on the stability of the electric power system,* BME BSc Thesis work, 2025 December.

[6] G. Ódor, S. Deng, J. Kelling: *Frustrated synchronization of the Kuramoto model on complex networks,* Entropy **26(12),** 1074 (2024) https://doi.org/10.3390/e26121074

[7] R. Juhász and G. Ódor: *Finite-size scaling and dynamics in a two-dimensional lattice of identical oscillators with frustrated couplings,* Chaos **35,** 053119 (2025) https://doi.org/10.48550/arXiv.2411.02171

[8] B. Hartmann, G. Ódor, K. Benedek, I. Papp and M. T. Cirunay: *Quantitative comparison of power grid reinforcements,* Chaos & Solitons & Fractals, **200(9),** 117095 (2025) https://doi.org/10.1016/j.chaos.2025.117095

[9] Hartmann B., Ódor G., Benedek K., Papp I., M. T. Cirunay: *Hálózat megerősítési módszerek kvantitatív összehasonlítása (Quantitative comparison of network reinforcement methods),* Electrotechnika **118,** 30-32 (2025) https://real.mtak.hu/id/eprint/224810

[10] B. Hartmann, T. Soha, M. T. Cirunay, T. Erdei: *Uncovering the inherited vulnerability of electric distribution networks,* arXiv:2409.06194

[11] M. T. Cirunay, B. Hartmann, T. Erdei, T. Soha*: Investigating the emergent invariant properties of Hungarian electric distribution networks,* arXiv:2506.04009

[12] K. Benedek, G. Ódor: *The effect of HVDC lines in power-grids via Kuramoto modelling,* arXiv:2512.24122

PARTICULATE MATTER LOAD AND LUNG DEPOSITION OF AEROSOL PARTICLES DURING THE USE OF DIFFERENT GYM EQUIPMENT

Szilvia Kugler, Péter Füri, Árpád Farkas, Attila Nagy, Veronika Müller***

**HUN-REN Wigner Research Centre for Physics, 1121 Budapest, Konkoly-Thege Miklós út 29-33*
*** Semmelweis University, Department of Pulmonology, 1083 Budapest, Tömő u. 25-29*

Objective

The objectives of this work were:

- to measure indoor Particulate Matter (PM) concentration elevation during different physical exercises by healthy adults using various gym equipment in a physiotherapy exercise room;
- to measure indoor PM concentration elevation during breathing exercises and stationary bicycling of COPD patients in a physiotherapy exercise room used for pulmonary rehabilitation therapy;
- to check the different respiratory parameters of the healthy adults during ergospirometry measurements to obtain accurate input parameters for the stochastic lung model;
- to calculate the lung deposition pattern of the measured pollutants during physical activity.

Methods

The measurement setup for healthy adults

The study was conducted on randomly selected days, involving healthy adults engaged in physical exercise across different seasons of the year. One measurement was conducted in spring, four in summer and one in autumn. The Department of Pulmonology's rehabilitation gym at Semmelweis University served as the study site. Two stationary bicycles, an elliptical trainer and a treadmill were used for the training. Six Optical Particle Counters (OPCs) (OPC-N3, Alphasense, Essex, Great Britain) were installed in the room, each placed horizontally at one meter from the presumed position of the participants' mouths. Figure 1 shows the schematic setup of the rehabilitation room with a size of 7.8 m × 5.0 m × 3.2 m. The OPCs measured every 1.398 seconds the PM concentrations (0.35 µm¬40 µm range) in the air. From these data, 1-minute averages and the trendlines were calculated for the different activities.

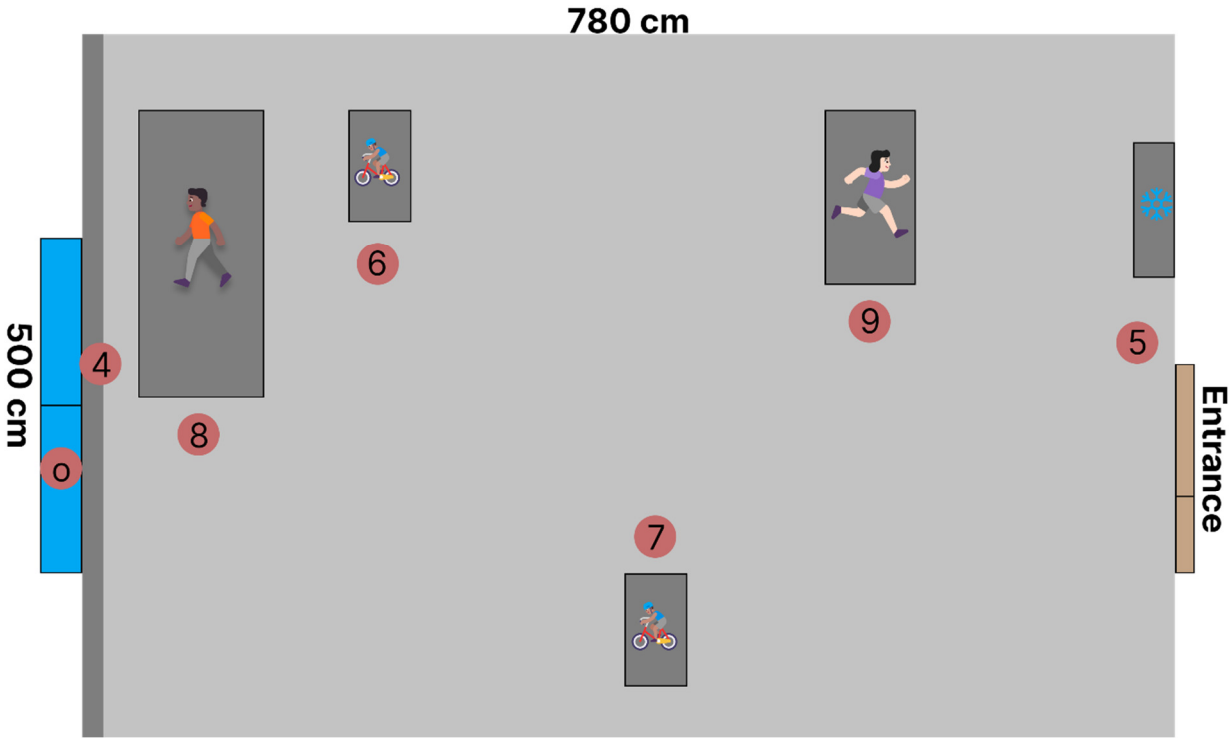


Figure 1: The schematic setup of the exercise room. Numbers represent OPC placements. OPCs 1, 2 and 3 were not used in this setup. Next to 9: Elliptical trainer; next to 8: Treadmill; next to 6 and 7: Stationary bicycle; The representation of all equipment is to scale. The OPCs 4 and 5 served for background measurements.

The measurement setup for COPD patients

The same rehabilitation gym was used for the COPD patients. In the respiratory rehabilitation of COPD patients, two types of therapy are typically performed: the first consists of breathing exercises performed in a seated position as a structured set of movements, followed by stationary bicycling. The study was repeated several times during the summer. Usually, two patients were present during the measurements. Both exercise types lasted for 30 minutes. Eight OPCs (OPC-N3, Alphasense, Essex, Great Britain) were installed in the room, and the same method was used as for the healthy adults.

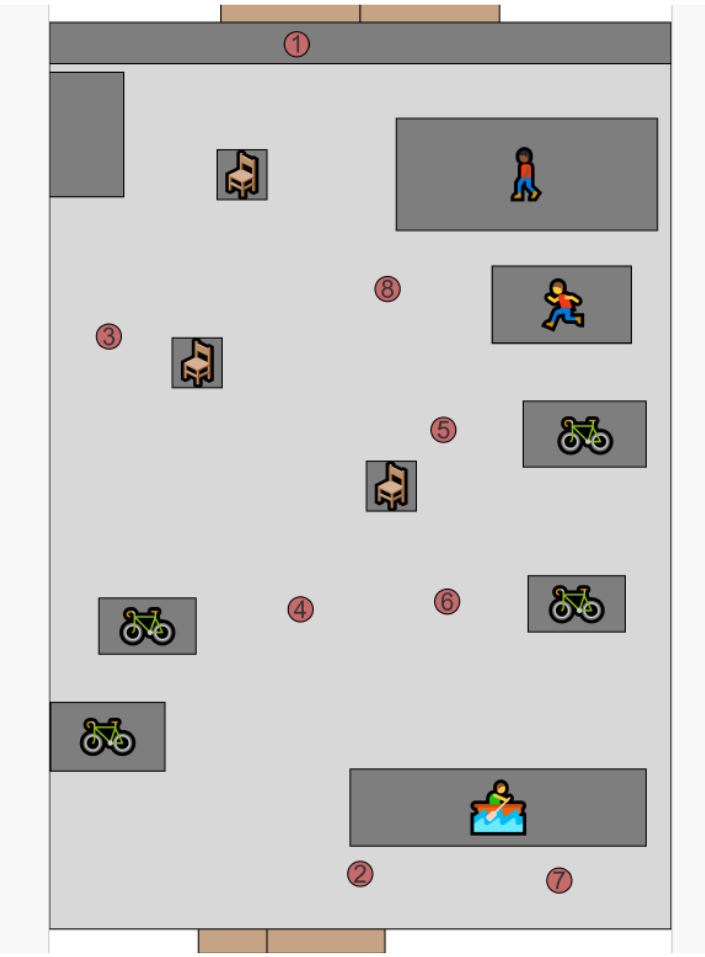


Figure 2: The schematic setup of the exercise room. Numbers represent OPC placements. Next to 8: Elliptical trainer and Rowing machine (ergometer), next to 4 and 6: Stationary bicycle; next to 3 and 5: Chair. The representation of all equipment is to scale. OPCs 1 and 2 served for background measurements.

Ergospirometry measurements of healthy adults

Ergospirometry is used to measure respiratory parameters under different loads. In this case, a stationary bicycle was used. All healthy adults participated in this measurement to provide input data for the deposition modelling.

Stochastic Lung Model

The deposition distribution of aerosol particles measured in the gym was calculated using the Stochastic Lung Model. Deposition in the upper airways was determined using Cheng YS's (2003) formula for mouth breathing. The fraction of particles deposited in the lung by diffusion, impaction and gravitational deposition was calculated in randomly selected airway geometries.

Results

PM load during the different activities of healthy adults

Before the training started, the windows and the door were opened for a short time to ventilate the room. The conditioning of the room lasted for 30 minutes before the training session started; this is the so-called „sedimentation" period. The physical exercises on the bicycle, treadmill and elliptical trainer lasted 30 minutes. Women used the treadmill and the elliptical trainer at a stationary intensity of 50 W, and the two bicycles were used by men at an intensity of 100 W. Figure 3 demonstrates the 1-minute averages and the trendline of a summer (A) and an autumn (B) day. The average background concentrations of PM2.5 were 4.16 ± 0.17 μg/m^3 (summer) and 4.93 ± 1.0 μg/m^3 (autumn). The average PM2.5 loads were 10.03 ± 1.04 μg/m^3 (summer) and 11.83 ± 1.03 μg/m^3 (autumn), indicating no high seasonality in the measured values.

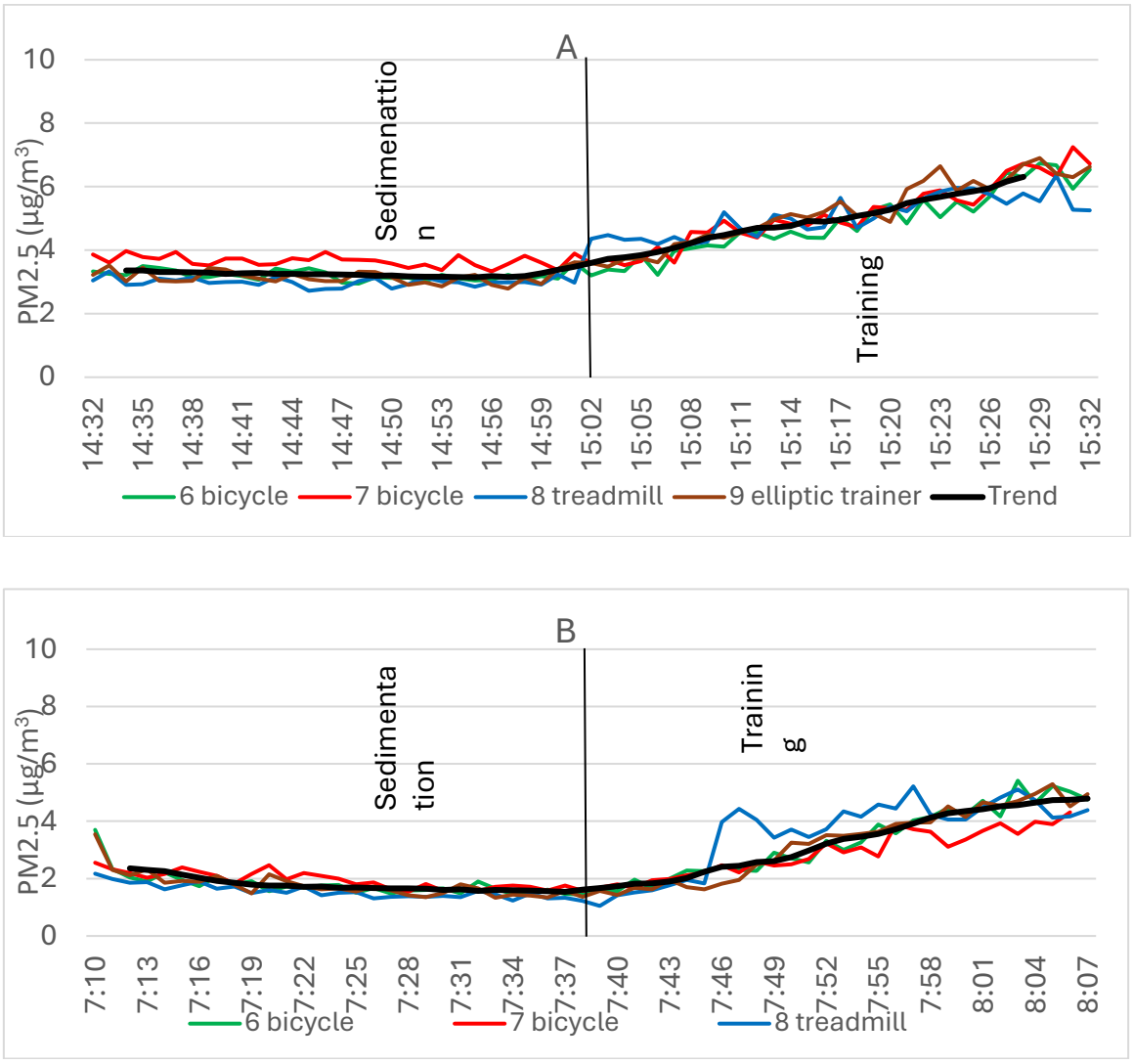


Figure 3: The PM2.5 concentrations measured at the numbered sites in the room and the trendline in summer (A) and in autumn (B). In both cases, two men were using stationary bicycles at 100 W, and two women were using the treadmill and the elliptical trainer at 50 W.

Figure 4 compares the concentration trends of the different PM fractions on a summer day. It is important to highlight that the PM1 fraction showed only a small increase during the exercises, while PM2.5 doubled. The average PM10 load increased from 13.53 ± 4.07 µg/m³ to 29.76 ± 7.88 µg/m³, with a maximum value of 44.76 µg/m³.

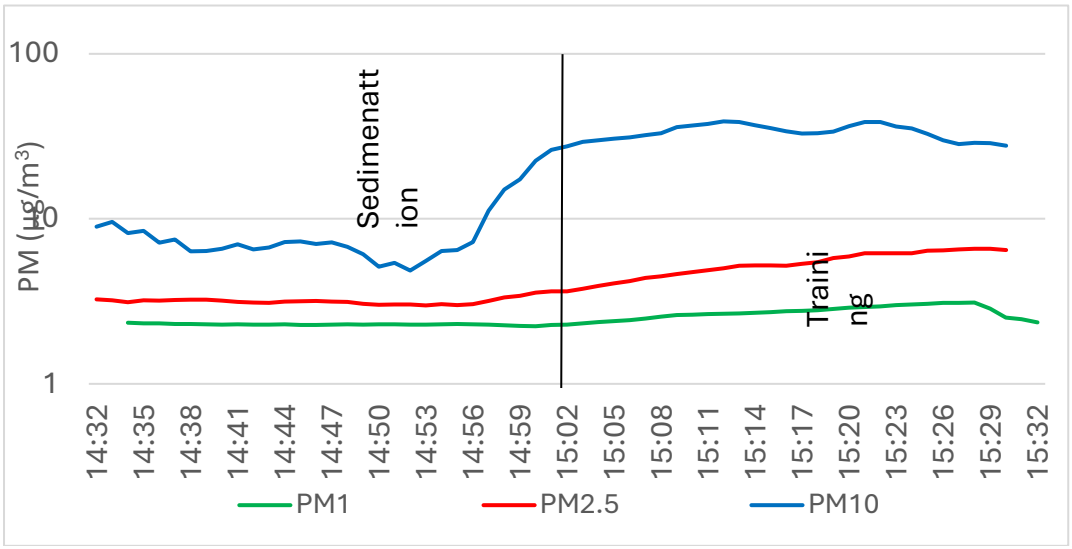


Figure 4: The trend of PM concentrations measured in the room during the sedimentation and training period. The trend is the average of OPCs 5-9.

Since all windows and doors were closed during the exercises, only internal sources could raise PM concentrations. Probably the main source was resuspension, and the aerosol particles were generated during machine use. The highest source was the treadmill, as shown in Figure 3.

Comparison of the PM load of the COPD patients and healthy adults

Before starting the exercise, average PM2.5 background concentrations were 2.62 ± 0.12 µg/m³, whereas during the breathing exercises of the two COPD patients, these values increased to 4.2 ± 0.43 µg/m³. When the two patients cycled as part of their rehabilitation program, the PM2.5 concentration reached 5.85 ± 0.25 µg/m³. When the four healthy adults used the different equipment, the concentration increased to almost four times the initial background value (11.1 ± 0.85 µg/m³). The background PM10 values were 6.02 ± 2.49 µg/m³ at the beginning. During the breathing exercise, it doubled (16.84 µg/m³) or tripled (21.47 µg/m³). The average values during the workout for healthy adults ranged from 42.55 ± 7.77 µg/m³ to 62.12 ± 6.66 µg/m³. This is summarised in Figure 5. Both PM fractions are close to or above the limiting values of the WHO air quality guideline recommendations.

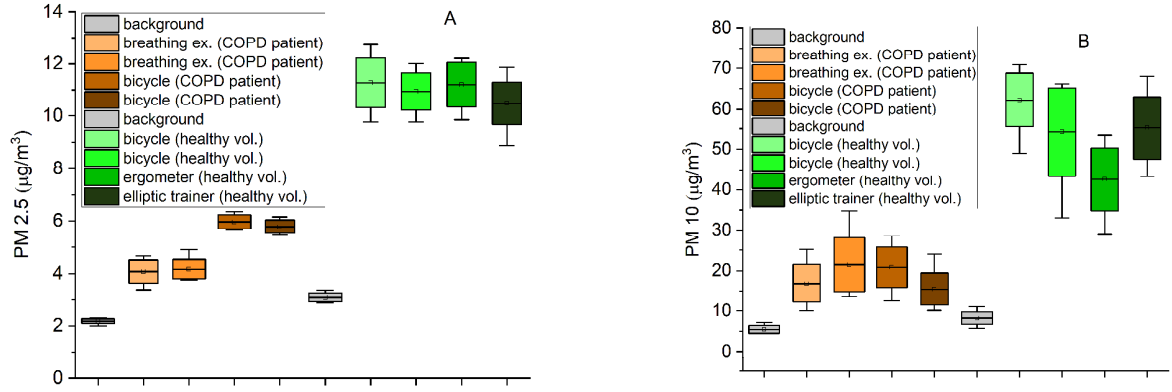


Figure 5: Measured PM2.5 (A) and PM10 (B) concentrations during the different activities of the COPD patients and healthy adults. The box plots show the mean and standard deviation, and the error bars indicate the minimum and maximum values.

Lung deposition of the measured aerosol particles

As shown in Table 1, both the inspiratory volume and respiratory rate increased significantly as the subject spent more time on the training device. The number of particles per second measured in all measurement channels also increased (131/sec (min), 137/sec (avg) and 157/sec (max)).

Table 1: Breathing parameters used to calculate airway deposition distribution (inspiratory volume, minute respiratory rate and breathing time (inhalation + exhalation))

	Ve (l/min)	Inspiratory volume (l)	Respiratory rate (1/min)	Breathing time (s)
Minimum	14	0.79	17.72	3.39
Average	36.6	1.2	30.50	1.97
Maximum	65.3	1.8	36.28	1.65

It is clearly visible that at all three time points, most particles are deposited in the acinar part of the lungs between the eighteenth and twenty-second airway generations. This is because the majority of the measured particles are larger than 350 nm but smaller than 1 µm in diameter, so diffusion does not affect them significantly; however, they are still too small for impaction and sedimentation. A large part of these particles therefore reaches the deeper airways. The higher air velocity from increased physical activity drives inhaled particles deeper into the acinar airways. Based on the results shown in Figure 3, it can be concluded that good air quality is very important during activities that involve increased physical activity (and consequently a larger volume of inhaled air), such as treadmills, exercise bikes, or other gym equipment. If there is a lot of dust in the gyms, a significant amount of particles, up to one hundred thousand per minute, can settle in the acinar airways. This can increase the likelihood of respiratory diseases and also elevate the risk of circulatory illnesses.

Figure 6 shows the airway deposition rate (deposited particle/min) of inhaled aerosol particles in the upper airways, bronchial and acinar airways in the 1st minute (minimum), 15th minute (average) and 29th minute (maximum).

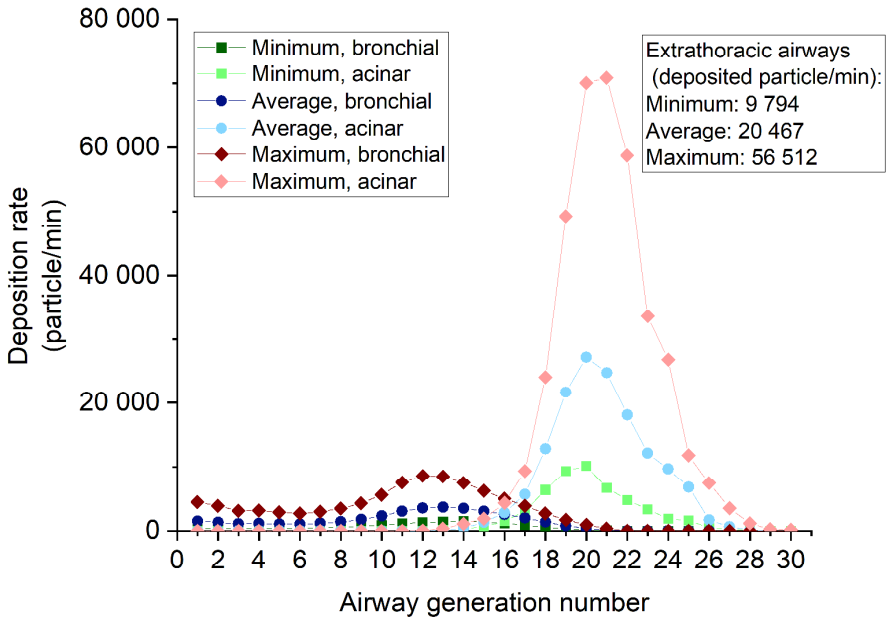


Figure 6: Airway deposition rate of the inhaled particles in the extrathoracic, bronchial and acinar airways for the 1st (min), 15th (average) and 29th (max) minutes

This study involves human participants and was approved by the Semmelweis University Ethical Board (ID: 114/2024). The study adheres to the principles outlined in the Declaration of Helsinki for experiments involving human subjects. Before participation, participants received detailed information about the study procedure, data storage, confidentiality, and anonymity. Written informed consent was obtained from all participants.

Remaining work

All the undertaken tasks were completed.

Related publication

[1] Sz. Kugler, K. A. Kup, T. Erdélyi, J. T. Varga, Sz. Török, A. Nagy, V. Müller: *Indoor exercise and particulate matter: PM2.5 resuspension during the use of different gym equipment.* (Under submission)

SELECTIVE BINDING OF RARE EARTH ELEMENTS WITH SILICA ADSORBENTS: ENVIRONMENTAL PROTECTION AND METAL RECOVERY

Zoltán Dudás, Selay Sert Çok, Dániel Pércsi, Adél Len, László Almásy, Sarvarjon Kurbonov, István Tolnai, Krisztina Frey, Attila Sulyok, Roberto Fernández de Luis

Objective

The increasing demand for Precious Heavy Metals (PHMs) and Rare Earth Elements (REEs) in advanced technologies—such as renewable energy systems, catalysts, and electronic devices—has created an urgent need for sustainable recovery strategies from secondary sources, particularly aqueous waste streams. Conventional separation and extraction methods often suffer from high chemical consumption, poor selectivity, and environmental drawbacks. In this context, adsorption-based recovery using functional hybrid materials has emerged as one of the most promising, eco-friendly, and cost-effective approaches for reclaiming these critical elements.

The main objective of this project was therefore to design, synthesise, and evaluate novel functionalized silica-based hybrid adsorbents with tailored surface chemistry for the selective binding and removal of PHMs and REEs from aqueous environments. To this end, it was aimed to develop sustainable sol–gel-derived silica hybrid materials integrating inorganic robustness with organic/biopolymeric functionality and to correlate structural, morphological, and chemical characteristics with adsorption performance.

By combining silica's intrinsic stability and high surface area with amine-, thiol-, and biopolymer-derived donor sites, this work contributes to the development of next-generation sorbents aligned with circular-economy and critical-raw-materials recovery goals.

Methods

Sixty different silica samples were synthesised during the project using a one-step sol–gel route. Six hybrid samples, based on a silica precursor (tetraethylorthosilicate) co-condensed with various functional or biopolymeric modifiers, were selected from these samples (Table 1) and presented as a case study. The sol–gel process was conducted under mild conditions, enabling uniform hybridisation between silica and the organic components. Samples were dried under ambient conditions to yield xerogel-type materials.

Table 1: Sample IDs and compositions

Sample ID	Sample Content	Compositions (by mol %)
Si-A	Silica+ Amine	75:25
Si-T	Silica + Thiol	75:25
Si-A-T	Silica + Amine + Thiol	50:25:25
Si -HEC	Silica + Hydroxyethyl Cellulose	80:20
Si-BG	Silica + Bovine Gelatine	80:20
Si -SSC	Silica + Shrimp Shell Chitin	80:20

A comprehensive set of physicochemical and structural characterisation methods was employed to evaluate the composition, morphology, and adsorption-relevant surface chemistry of the synthesised hybrid materials. These analyses provided key insights into the successful incorporation of organic or biopolymeric components into the silica matrix and their influence on textural properties.

Fourier Transform Infrared Spectroscopy (FTIR): FTIR spectra of the xerogel powders were recorded in the range 4000–500 cm^{-1} to verify the presence of characteristic silica and functional-group vibrations, confirming the successful incorporation of organic functionalities within the silica network.

Solid-State ^{29}Si Nuclear Magnetic Resonance (NMR): To further confirm network formation, solid-state ^{29}Si Magic-angle-spinning (MAS) NMR spectroscopy was performed on representative hybrid samples. The spectra were deconvoluted into Q^n and T^n components, corresponding respectively to silicon atoms in inorganic ($Si(OSi)_{4-n}(OH)_n$) and organosilane ($R–Si(OSi)_{3-n}(OH)_n$) environments.

Scanning Electron Microscopy (SEM): SEM was employed to evaluate the morphology and porosity of the hybrids, revealing distinct textural differences depending on the modifier type.

N_2 Sorption: Textural properties were quantified from nitrogen sorption isotherms recorded at 77 K. Specific surface area Brunauer, Emmett and Teller (BET) total pore volume, and average pore width (Barrett–Joyner–Halenda (BJH)) were calculated to assess mesoporosity.

X-ray Photoelectron Spectroscopy (XPS): XPS analyses were carried out after metal adsorption to investigate the surface chemical environment and binding interactions. Survey and high-resolution spectra were recorded for Si 2p, O 1s, C 1s, N 1s, S 2p, and the relevant metal core levels (e.g., Eu 3d).

Adsorption tests: Sorption experiments were conducted to assess the metal uptake potential of each hybrid. The tests were performed in batch mode using aqueous solutions of representative REE and PHM ions at known initial concentrations (typically 20 mg L^{-1}). Fixed masses of xerogel samples were dispersed in 25–50 mL of solution, and the suspensions were shaken under controlled temperature and pH for predetermined contact times (ranging from 30 min to 24 h). After equilibration, the supernatants were separated by filtration and analyzed spectrophotometrically by Inductively Coupled Plasma Mass Spectrometry (ICP-MS) to determine residual metal concentrations. The removal efficiencies (R%) were calculated using standard mass-balance equations:

$$R\% = (C_0 - C_e)/C_0 \times 100$$

where C_0 and C_e are the initial and equilibrium concentrations (mg L^{-1}).

In addition to batch equilibrium studies, preliminary dynamic column adsorption tests were performed to evaluate the real-time uptake behaviour of the most promising hybrid adsorbent. The setup consisted of a peristaltic pump system (Figure 1) connected to a glass column (inner diameter ~ 1 cm, bed height ~ 5 cm) packed with the xerogel adsorbent. The feed solution containing model metal ions (e.g., As(III)) was continuously circulated at a controlled flow rate of 0.5 mL min^{-1}. Effluent samples were collected at specific time intervals and analyzed spectrophotometrically to determine the temporal variation of normalised concentration (C/C_0).



Figure 6: Laboratory setup of the dynamic column adsorption experiment

Results

Chemical Properties

The structural integrity and chemical functionality of the synthesised silica-based hybrid xerogels were verified by FTIR and ^{29}Si MAS NMR spectroscopy, and the obtained spectra of the samples are given below.

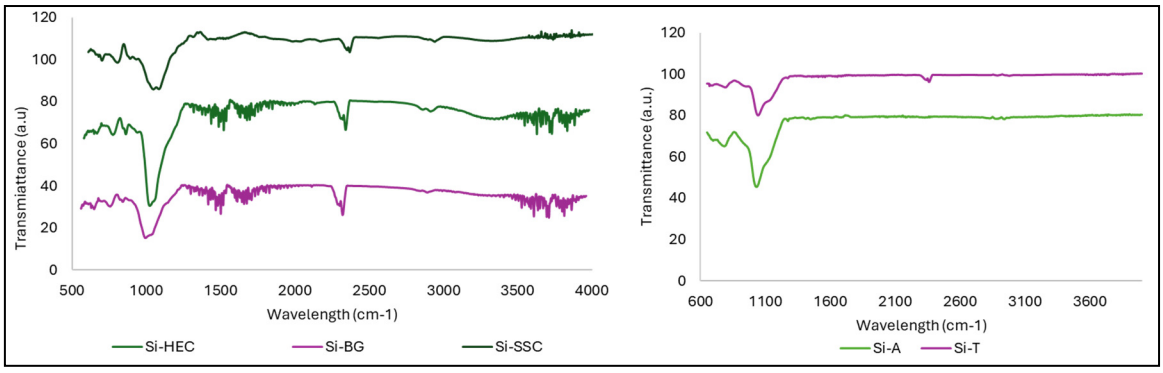


Figure 2: FTIR spectra of the silica hybrids

The FTIR spectra of all xerogels exhibited the characteristic vibrational features of the silica network, including the strong asymmetric Si–O–Si stretching band around 1080 cm^{-1}, the symmetric stretching near 800 cm^{-1}. The broad absorption near 3400 cm^{-1} and the weak band at ~1630 cm^{-1} correspond to the O–H stretching and H–O–H bending of surface silanols and physisorbed water, respectively. Distinct spectral features arising from organic and biopolymeric modifiers were also evident. The amine-functionalized sample (Si-A) displayed N–H bending (~1550 cm^{-1}) and C–N stretching around 1400 cm^{-1} bands, confirming the incorporation of amine groups. The thiol-containing sample (Si-T) exhibited a weak S–H stretching band at approximately 2570 cm^{-1}, indicating successful grafting of mercaptopropyl moieties. In contrast, the biopolymer-modified samples (Si-BG, Si-HEC, Si-SSC) showed strong absorptions attributable to the organic backbones: amide I (C=O stretching, ~1650 cm^{-1}) and amide II (N–H bending, ~1550 cm^{-1}) for gelatin; C–O–C and C–OH vibrations (1200–1000 cm^{-1}) for hydroxyethyl cellulose; and characteristic polysaccharide/chitin-related bands (amide and C–O modes) for shrimp shell chitin.

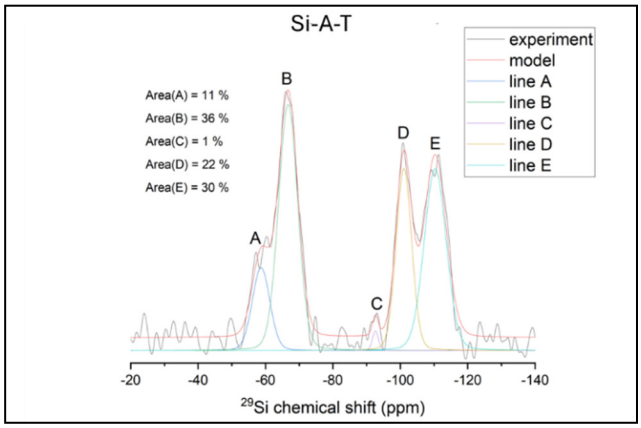


Figure 3: ^{29}Si MAS NMR spectra of the sample Si-A-T

The ^{29}Si MAS NMR spectrum recorded for the representative Si-A-T hybrid exhibited well-defined Q^n (Q^2, Q^3, Q^4) and T^n (T^2, T^3) resonances. The dominance of Q^3 (–102 ppm) and Q^4 (–110 ppm) species indicates a highly cross-linked siloxane network, while the presence of T^2 (–57 ppm) and T^3 (–67 ppm) signals confirms covalent bonding between the silica framework and the organosilane functional groups. The coexistence of Q and T sites supports an interpenetrated hybrid structure, where organic functionalities are homogeneously distributed within the inorganic matrix rather than merely surface-grafted. Overall, FTIR and NMR results collectively demonstrate that the obtained chemical diversity provides multiple coordination sites for metal ion interaction, laying the foundation for efficient PHM/REE sorption behaviour.

Morphological Properties

The SEM micrographs of the silica-based hybrid xerogels reveal distinct morphological differences arising from the nature of the incorporated organic components, as displayed in Figure 4.

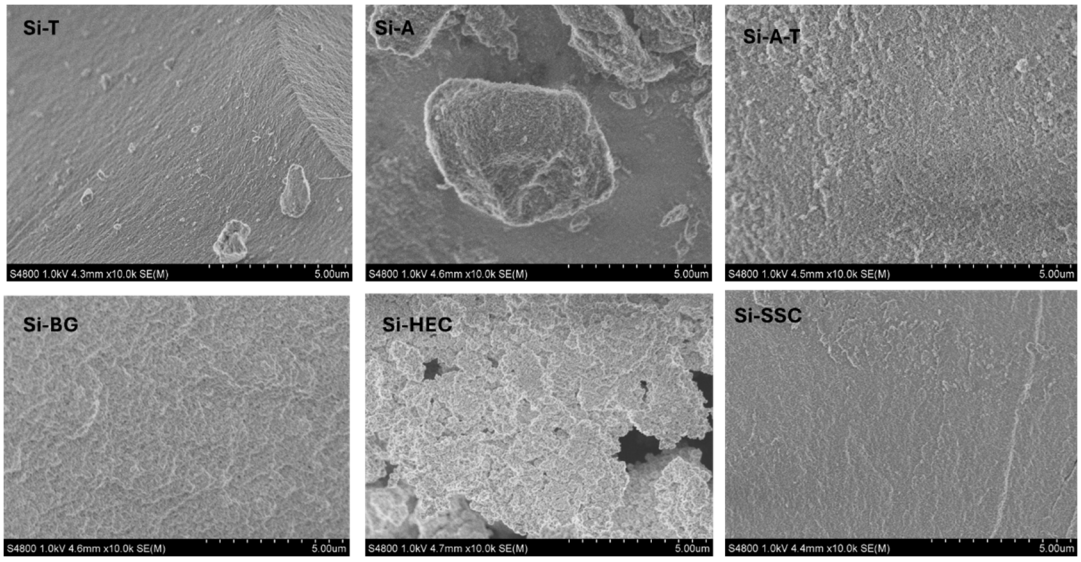


Figure 4: SEM micrographs of the samples

All samples exhibit nanoscale particulate features typical of sol–gel-derived silica, yet their surface textures and porosities vary considerably. Si–A shows a smooth, compact morphology with well-connected nanoparticles, indicating homogeneous condensation and structural coherence. In contrast, Si–T displays a rougher, more open network of loosely aggregated particles, suggesting that thiol incorporation increases mesoporosity and surface accessibility. The ternary Si–A–T hybrid exhibits an intermediate structure, where the combined amine and thiol functionalities yield a balanced morphology with both cohesion and porosity. The biopolymer-based systems demonstrate more heterogeneous textures: Si–HEC features a fibrous, sponge-like structure with interconnected voids; whereas Si-BG and Si-SSC displayed a more compact surface, with partially fused particles and reduced interstitial porosity.

Textural Properties

The porosity and surface characteristics of the xerogels were evaluated by N_2 adsorption–desorption analysis at 77 K. All samples exhibited type IV isotherms, typical of mesoporous materials, with hysteresis loops varying according to the incorporated organic component (*Table 2*). The organosilane-modified xerogels (Si-A, Si-T, Si-A-T) retained high surface areas (430–640 m^2/g), confirming that co-condensation of amine and thiol groups did not disrupt mesostructural formation. The slight reduction in pore width and volume for Si-A-T suggests increased network cross-linking and partial pore constriction by organic groups.

Table 2: N_2 sorption results of the hybrid xerogels

Sample ID	Surf. area, m^2/g	Pore width, nm	Total pore volume, cm^3/g	Type of isotherm
Si-A	644.1	4.2	0.75	Type IV-H2a
Si-T	574.5	4.1	2.01	Type IV-H2b
Si-A-T	429.0	2.4	0.24	Type IV-H4
Si-BG	75.1	5.9	0.10	Type IV-H4
Si-HEC	29.7	5.8	0.05	Type IV-H4
Si-SSC	25.0	6.3	0.04	Type IV-H4

In contrast, the biopolymer hybrids (Si-BG, Si-HEC, Si-SSC) exhibited markedly lower surface areas (< 80 m^2/g) and small pore volumes, consistent with pore blocking or partial collapse of the mesoporous network during drying. Nevertheless, their broader pore size distributions and H4-type hysteresis loops indicate the presence of slit-like mesopores formed by layered or irregular aggregates. This confirms that the silica framework remains tuneable through the choice of modifier: organosilane hybrids provide high porosity and accessibility, while biopolymer incorporation yields denser, functionally rich surfaces potentially advantageous for selective metal coordination.

Sorption Results

Batch adsorption experiments revealed that the adsorption efficiency of the synthesised xerogels toward REE and PHM ions is strongly governed by the nature of the organic component. In contrast to what might be expected from surface-area considerations alone, the biopolymer-based hybrids (Si-BG, Si-HEC, Si-SSC) consistently exhibited higher REE uptake (removal efficiency > 85%) than the organosilane-functionalized samples, despite their significantly lower BET surface areas (Figure 5). This enhanced performance can be attributed to the high density of oxygen- and nitrogen-donor sites (–OH, –COOH, amide and acetamide groups) in gelatin, hydroxyethyl cellulose, and chitin, which provide multidentate coordination environments ideally suited for hard trivalent cations such as Eu^{3+}. The organosilane-modified xerogels (Si-A, Si-T, Si-A-T) still showed measurable adsorption performance with removal efficiency reaching 60%, particularly for heavier or softer PHMs, but their performance in REE removal remained inferior to that of the biopolymer composites, underscoring the dominant role of chelation chemistry over total porosity.

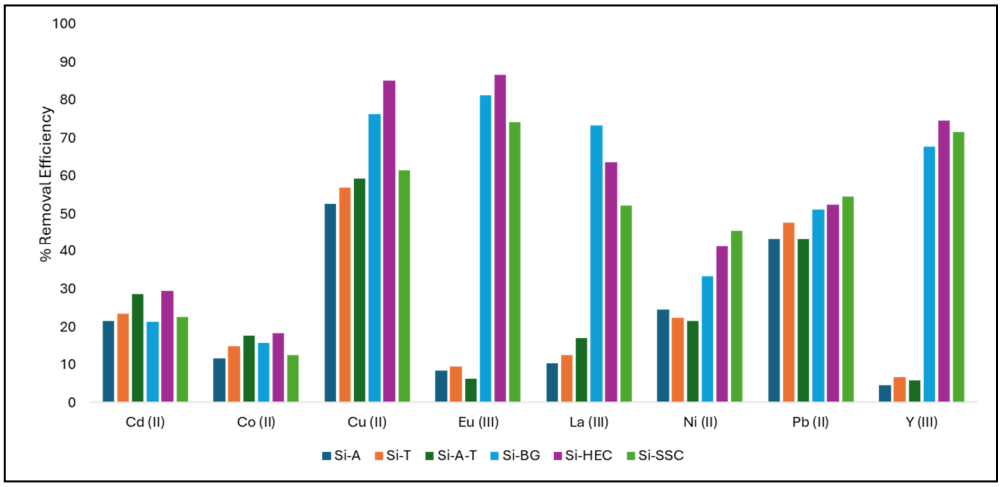


Figure 5: Batch sorption removal efficiencies of the hybrid xerogels for various REEs and PHMs

To elucidate the adsorption mechanism of rare-earth ions on the biopolymer–silica hybrids, XPS was performed on the Si-HEC sample after Eu^{3+} adsorption, and the obtained spectra were displayed in Figure 6. The survey spectrum clearly showed the presence of europium through the characteristic Eu 3d doublet, confirming that Eu ions were successfully immobilised on the hybrid surface. The shape and position of the Eu 3d peaks are consistent with europium in the trivalent state (Eu^{3+}), indicating that the oxidation state of the metal was preserved during the adsorption process. In addition to Eu signals, the O 1s and C 1s regions exhibited components attributable to the hydroxyethyl-cellulose framework and its interaction with the adsorbed metal. The O 1s envelope contained contributions that can be assigned to metal–oxygen bonds and to hydroxyl/ether oxygen in the biopolymer, suggesting that Eu^{3+} is coordinated predominantly through oxygen donor sites. The C 1s region showed features corresponding to C–C/C–H and C–O/C–O–C environments, consistent with the polysaccharide backbone, and supports the role of these functional groups in metal binding. No additional peaks indicative of counter-ions or strongly Eu–Si-specific environments were evident, implying that europium adsorption proceeds mainly via chelation with the hydroxyl- and ether-rich domains of the HEC phase, rather than direct interaction with the silica network. Overall, the XPS data provide spectroscopic evidence that Eu^{3+} ions are anchored to the Si-HEC surface through coordination with O-containing functional groups of the biopolymer, in agreement with the high Eu uptake observed in batch sorption experiments.

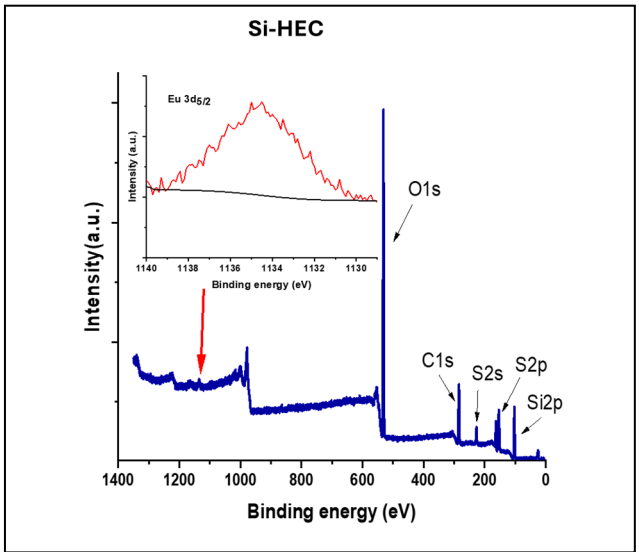


Figure 6: XPS spectra of the sample Si-HEC

Dynamic Sorption Studies

To further assess the performance of the most promising hybrid sorbent under practical conditions, dynamic column adsorption experiments were conducted using the Si-HEC composite, which had already demonstrated the highest REE uptake in batch tests. In this experiment, the same material was evaluated for the removal of As(III) from aqueous solution to explore its broader applicability toward different contaminant classes. The influent As(III) solution was continuously passed through the packed bed, and effluent samples were collected at defined intervals for concentration analysis. The relative concentration ratio (C/C_0) was then plotted as a function of time to obtain the breakthrough profile (Figure 7).

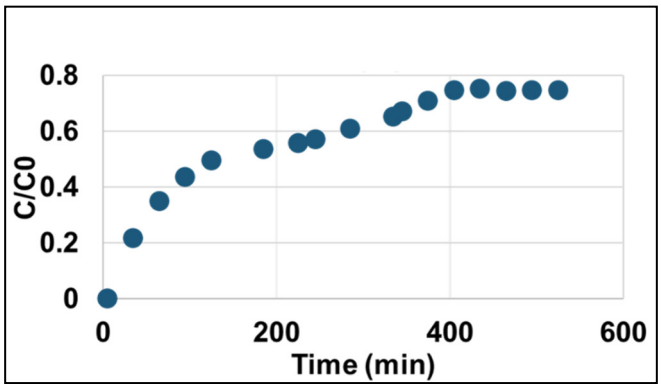


Figure 7: Breakthrough curve (C/C_0 vs time) for As(III) adsorption on Si-HEC hybrid sorbent under continuous-flow conditions

The obtained curve displayed the expected sigmoidal shape typical of diffusion-controlled adsorption processes. An initial mass-transfer region (0–150 min) reflected rapid uptake of As(III) on readily accessible surface sites, followed by a gradual increase in C/C_0 as intraparticle diffusion and site saturation became dominant. Near-equilibrium was approached after approximately 450–500 min, at which point $C/C_0 \approx 1.0$, indicating bed exhaustion. The material exhibited good mechanical integrity and retained its sorption activity throughout the continuous-flow operation, confirming that Si-HEC possesses stable adsorption characteristics under dynamic conditions.

These preliminary results suggest that the same hybrid framework effective for REE capture can also function efficiently for oxyanion-type pollutants such as As(III). The data will serve as a baseline for further kinetic modelling (e.g., Thomas and Yoon–Nelson models) and scale-up design in future work.

Remaining work

The results obtained so far clearly demonstrate the strong potential of the synthesised hybrid xerogels for efficient adsorption of rare-earth and heavy-metal ions. Ongoing work focuses on completing the dynamic column experiments for As(III) removal to establish breakthrough capacity and kinetic parameters under different flow conditions. In parallel, regeneration and reusability tests will be conducted to confirm the long-term stability of the most effective sorbents. These steps will provide a solid basis for scaling up the process toward practical recovery and purification of REEs and other critical metals from aqueous streams.

The results of this research, conducted with support from the project, will be summarised in three scientific publications.

CHARACTERISATION AND LUNG DEPOSITION OF HARMFUL AEROSOL PARTICLES

János Osán, Berta Börcsök, Árpád Farkas, Péter Füri, Veronika Groma, Balázs Gergely Madas

Objective

Air pollution is a key environmental concern with significant public health risks. Particulate Matter (PM) is among the most harmful pollutants in ambient and indoor air, especially fine ($PM_{2.5}$) and ultrafine ($PM_{0.1}$) particles that can bear harmful chemical compounds and radon progeny, which are associated with respiratory, cardiovascular and other diseases. Domestic combustion of solid fuel (coal, wood, or occasionally domestic waste) is a significant aerosol pollution source in rural settlements, especially during the heating season. The emission of domestic stoves burning different solid fuels was tested using a dedicated laboratory experiment. Ambient air sampling was performed during winter at a rapidly expanding rural settlement near Budapest (Solymár, Hungary), where, in addition to traffic, biomass burning and presumably waste combustion represent significant sources.

Health effects of aerosol particles through the inhalation pathway can be calculated using lung deposition modelling. For the same exposure, it is an important question of radiation protection how the individual characteristics of the subjects, like age or health status, affect the dose distribution in the nuclei of the radiosensitive cells of the airway epithelium. As a large population is affected by the radiation burden caused by the decay of the radon progeny and there is a well-established dose–effect relationship, investigating individual variability upon radon exposure may be especially important.

Methods

Particulate emissions of a conventional household stove were investigated during combustion of various solid fuels (wood, lignite, household waste) in a targeted laboratory experiment. The laboratory experiments were supplemented with a six-week winter sampling campaign at Solymár. The particle size distribution in the diluted flue gas and ambient air was monitored using a Scanning Mobility Particle Sizer (SMPS) and Optical Particle Counter (OPC), while an aethalometer and Total Carbon Analyser (TCA) were also operating in parallel for monitoring of carbonaceous aerosols. Size-fractionated particulate samples were collected on Si wafers using a 9-stage May-type cascade impactor from ambient aerosol and diluted flue gas of the stove combustion experiment. The combination of cascade impactor sampling and Total-reflection X-ray Fluorescence (TXRF) analysis was found to be an effective tool for determining the mass size distribution of chemical elements or compounds in a wide size range of 70 nm to 10 µm. $PM_{2.5}$ aerosol samples were collected on quartz filters over 24-hour intervals and analysed using thermo-optical methods to quantify organic (OC) and elemental carbon (EC) fractions, enabling more accurate source apportionment. Video surveillance was used to document the operational patterns of residential boilers near the sampling site.

Regarding lung deposition calculations, we compared the radiation burden of the bronchial airway epithelium for a sitting healthy adult man, a man with severe asthma and a 5-year-old healthy child. To determine how the age of the subject and airway diseases, like asthma, affect the absorbed energy in the bronchial airways, we used the Stochastic Lung Model and a combined mucociliary clearance and alpha dosimetry model. The Stochastic Lung Model was used to simulate the deposition distribution of radon progeny in the airways. For the child, the airway dimensions were scaled down according to the data of Phalen and Oldham (2001). For the asthmatic subject, the probability and extent of airway contraction were determined by consulting with pulmonologists. Using the deposition distributions, in every airway generation, the mucociliary clearance model determined the number of alpha decays of ^{218}Po and ^{214}Po. Finally, the dosimetric model created alpha paths from the emitter atoms to the nuclei of the target cells. The absorbed energy was calculated in every part of the alpha path. The absorbed energy in the nuclei of the basal and secretory cells was used to determine the absorbed doses for the cells.

Results

Differences were observed in the shape of the particle size distributions measured in the flue gas of the stove experiment for the fuels burned. The maximum of the size distributions fell between 20–70 nm for most fuels, while the maximum was between 200–500 nm for the combustion of bicycle tyres, cardboard and polystyrene foam. TXRF results of flue gas samples taken with a cascade impactor showed that the emission of K, Cl, Br and Zn was significant in the submicron size range during wood burning. These elements were also present in the air of the selected rural site, their concentration showed a maximum in the 0.25-0.5 µm fraction, confirming that wood burning is the main aerosol source. The combustion of parquet was associated with an increased content of lead and zinc in the fine fraction of the emitted aerosol, while the fine fraction of copper and bromine was characteristic of the combustion of coloured bedding and cardboard [1].

Regarding the ambient aerosols collected at Solymár, our approach, relying on the traffic- and biomass-related aerosol contributions separated by the Aethalometer model and their comparison with EC and OC time series, enabled the assessment of EC and OC as source-specific markers and facilitated the identification of potential illegal waste burning events. Results indicate extreme episodic pollution events linked to inefficient residential biomass combustion and likely to illegal waste burning, with 1-minute $PM_{2.5}$ concentrations reaching 212 µg/m³ and Black Carbon (BC) peaking at 23.8 µg/m³—substantially above background levels measured at the nearby suburban station (Fig.1) [2].

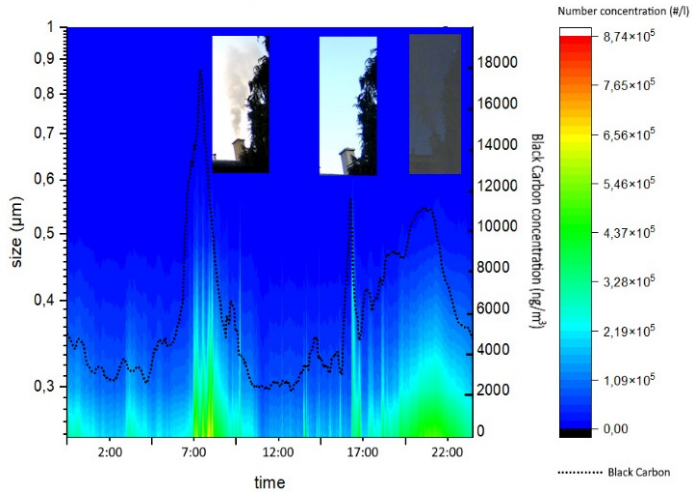


Figure 1: Particle size distribution and black carbon concentration at Solymár on 19 February, supplemented with video snapshots selected for those periods when pronounced increases in aerosol particle concentrations were detected

By optimising the correlations between the temporal variations of markers associated with the same emission sources, the Ångström exponents required for the Aethalometer model for both biomass burning (α_{BB}) and fossil-fuel (α_{FF}) combustion were determined, yielding α_{FF} = 1.15 and α_{BB} = 2.2 values. The elevated α_{BB} value may reflect episodic contributions from illegal household waste burning, a possibility further supported by concurrent increases in additional tracers such as EC2 (temperature-resolved fraction of elemental carbon commonly associated with intense combustion sources). We derived this conclusion by comparing days classified as typical, purely biomass-burning periods, with days that clearly deviated from this pattern. On the latter, the relative proportions of biomass-burning markers shifted systematically, and the magnitude of this deviation showed a strong linear relationship with the contribution of more refractory elemental carbon, as represented by the EC2 thermal–optical fraction (Fig. 2). This indicates that part of the biomass burning was replaced by a fuel source producing more thermally stable (refractory) elemental carbon, consistent with combustion processes known to generate more refractory elemental carbon, such as plastic-containing waste. These findings contribute to the refinement of emission inventories and the development of targeted mitigation strategies, while ongoing work expands marker databases to improve pollutant source apportionment [2].

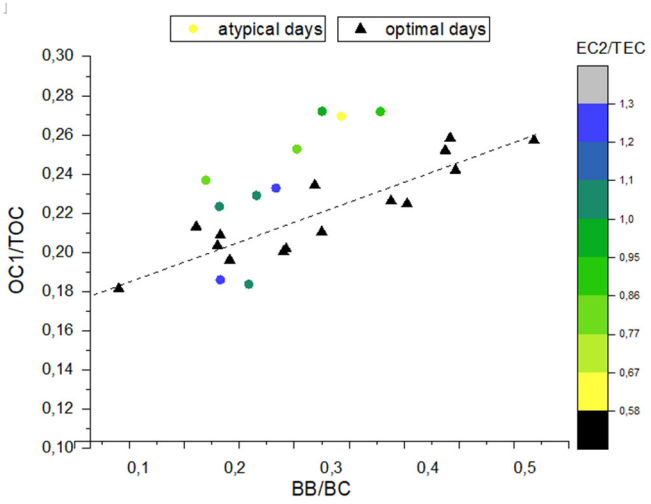


Figure 2: Relationship between the normalised values of biomass-burning-related components (BB and OC1), with days characterised by purely biomass-burning influence ("typical") shown as black triangles and days affected by additional sources ("atypical") shown as coloured dots. The dashed line represents the linear regression determined for the optimal days, while the colour scale indicates the EC2/TEC value associated with each measurement point.

For inhaling the same air with the same radon progeny activity concentration (40 Bq/m^3), for a 5-year-old child, in the big bronchial airways (BB), although less radon progeny is deposited, the dose rates are higher than for a healthy adult man. This is the effect of the smaller airways in the child, what cause higher hit probability and higher deposited energy in the target cell nuclei. In contrast with that, in the small bronchi (bb), the dose rates are lower for the child. This is caused by the smaller inhaled air volume, which cannot carry the particles so deep into children's lungs. For an asthmatic subject, the dose rates are higher in every airway generation than for a sitting healthy man. This is the synergistic effect of the more deposited radon progeny and the shorter alpha tracks due to the airway contraction. These results indicate that the individual characteristics of the subjects have a strong effect on the radiation burden (Fig. 3) [3].

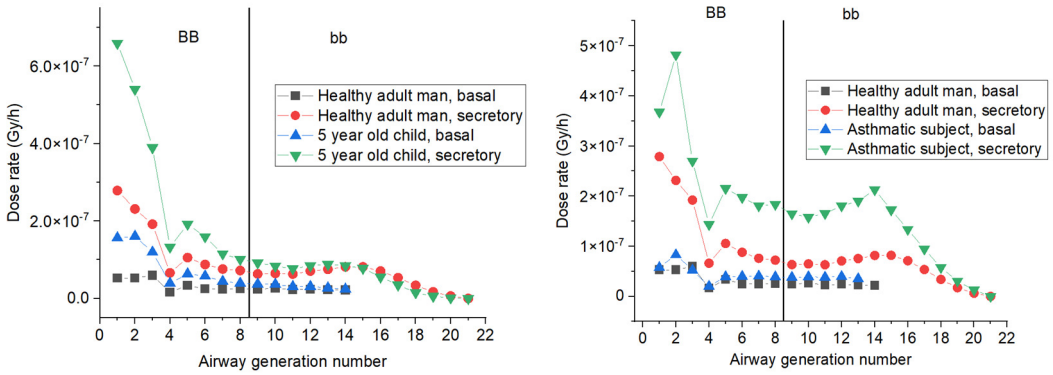


Figure 3: Absorbed dose rates in the nuclei of the basal and secretory cells of the bronchial airway epithelium for a healthy adult man, a 5-year-old child and a subject with severe asthma

Remaining work

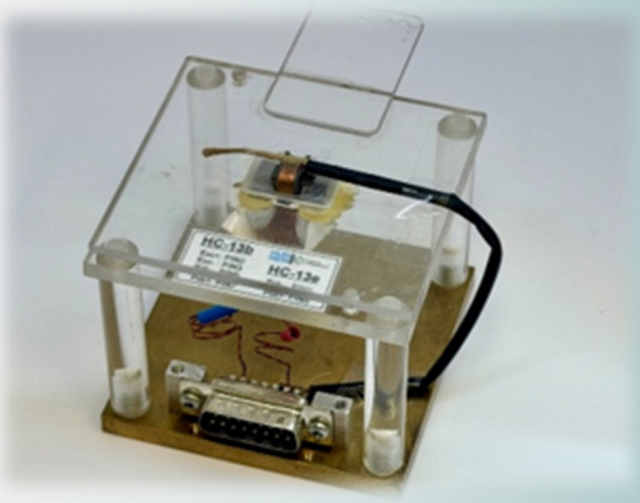
Research is ongoing for the identification of markers for wood and waste combustion based on the size distribution of emitted aerosol particles, and for estimating health effects of combustion-related particles through lung deposition modelling. Investigations are performed in the frame of the SNN- 150615 project supported by the Hungarian Research, Development and Innovation Fund.

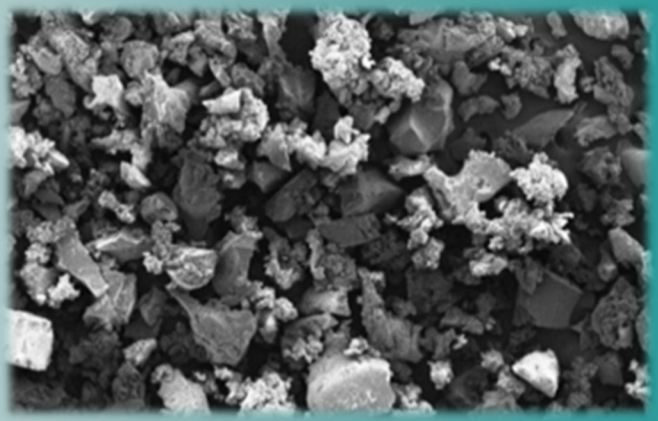
Related publications

[1] J. Osán, B. Börcsök, B. Jancsek-Turóczi and V. Groma: *TXRF analysis of airborne particulate matter originating from resuspension and combustion,* TXRF 2025 Conference, Kielce, Poland, (2025)

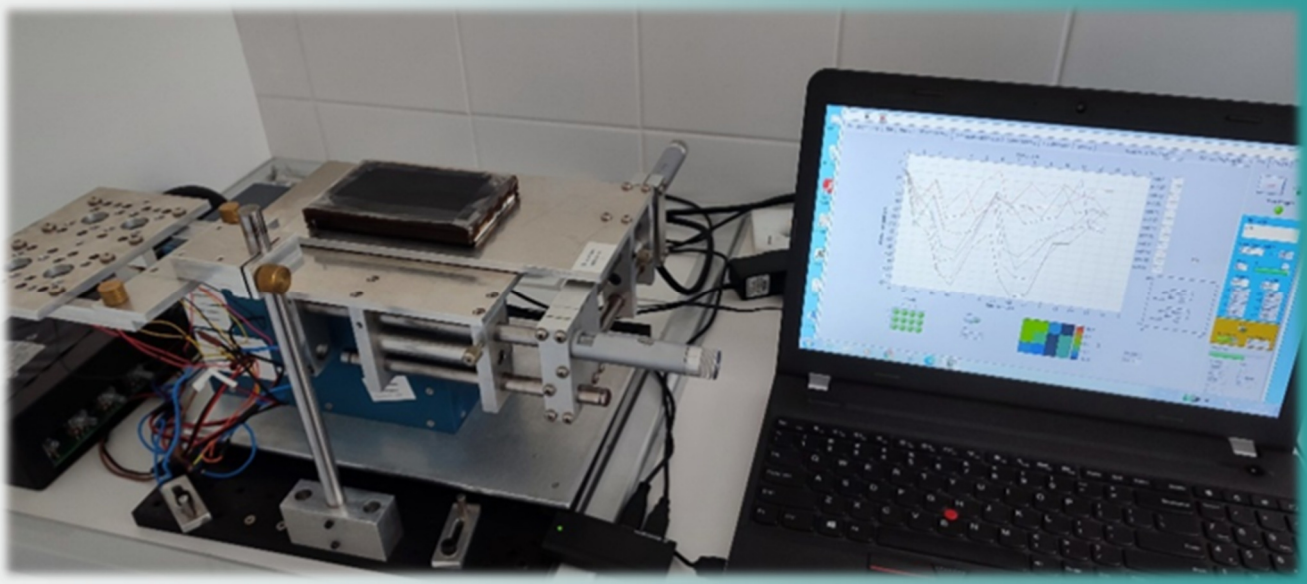
[2] S. Kheirandish, B. Alföldy, P. Füri, J. Osán, Á. Farkas, M. Rigler, A. Gregorič and V. Groma: *Characterization of carbonaceous aerosol particles emitted by solid fuel combustion in rural areas,* Environmental Monitoring and Assessment, under review (2026)

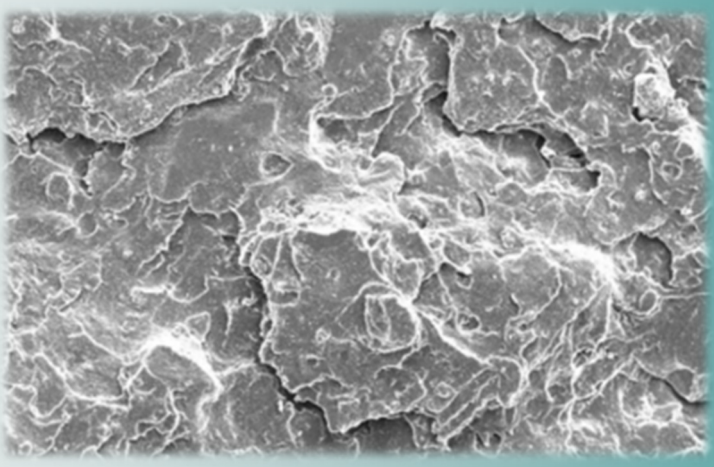
[3] P. Füri, Á. Farkas, W. Hofmann and B.G. Madas: *The role of individual characteristics of human subjects on the radiation burden of the bronchial airways from radon progeny,* Radiation and Environmental Biophysics **64**, 629–635 (2025) https://doi.org/10.1007/s00411-025-01148-w





V. NUCLEAR ANALYSIS AND CHEMISTRY





ENERGY CARRIER AND RAW MATERIAL PRODUCTION VIA CHEMICAL (CATALYTIC) METHODS AND ENERGY-EFFICIENT WATER PURIFICATION

Krisztina Kovács, Anna Tegze, Kornél Fél, László Wojnárovits, Renáta Homlok, Erzsébet Takács, Anita Nagyné Horváth, Miklós László Németh, Tamás Korányi, Andrea Vargáné Beck, Mahitha Udayakumar, József Sándor Pap, Tímea Benkó, Krisztina Frey, Nóra Győrffy-Fürcht, Irfan Khan, Zsolt Gábor Kerner, Tamás Ollár

Objective

The scientific research conducted at the HUN-REN Centre for Energy Research in 2025 focuses on developing sustainable chemical technologies for energy production, raw material recovery, environmental protection, and advanced materials research. The main research directions include enhancing hydrogen generation through photoelectrochemical and catalytic methods, advancing methane pyrolysis for the production of hydrogen and carbon-based nanomaterials, and exploring the broad application of high-energy ionising radiation in environmental, chemical, microbiological, and polymer research. These activities include radiation-based removal of environmental contaminants from water, the study of radical-mediated reaction pathways, investigations of microbial responses to irradiation, and the modification and performance enhancement of polymer materials.

Methods

1. **Water Splitting:**

In (photo)electrocatalytic systems, standard methods like linear sweep, cyclic voltammetry, electrochemical impedance spectroscopy, and pulse techniques are applied for detailed analysis of the catalytic performance. Chronometric techniques are coupled with product analysis to assess Faraday or charge efficiency (selectivity). Pre- and post-catalytic analysis of the electrolyte (Ultraviolet-visible (UV-vis), Dynamic Light Scattering (DLS)) and the electrode (X-ray Photoelectron Spectroscopy (XPS), Scanning (Transmission) Electron Microscopy - Energy Dispersive X-ray Spectroscopy (S(T)EM-EDX), Raman, Fourier Transform Infrared (FTIR), X-Ray Diffraction (XRD)) supplies important complementary information about the fate of the catalysts. Beyond experiments, collaborators contribute with high-level computational capacities.

2. **Methane Reforming and Pyrolysis:**

Powder catalyst samples using MgO as a support were prepared by different chemical methods, while model catalyst samples were produced by magnetron sputtering of Ni and Mo onto a TEM grid. Structural analysis was performed using Temperature Programmed Reduction (TPR), XRD, TEM, XPS and Raman spectroscopy in the reduced state and after methane decomposition tests. Catalytic performance of the supported samples was investigated i) in a highly diluted CH_4 flow in a fixed bed reactor under temperature ramp and ii) in 50% CH_4/Ar using a horizontal reactor at 800 °C. Treatment of the model sample under the flow of CH_4 at 800 °C was used to induce carbon deposition, to be investigated by TEM and XPS.

3. **Application of high-energy ionising radiation in environmental, chemical, microbiological, and polymer research:**

In the field of water treatment, the main approaches include gamma radiolysis and pulse radiolysis to generate reactive species in aqueous solution and to identify the transient intermediates, oxidation kinetics, and radical-mediated degradation pathways of organic contaminants. The studies were complemented by kinetic experiments and by the application of conventional wastewater analytical methods.

In the microbiological study, the methodology involved exposing sensitive and resistant bacterial strains to different doses of gamma irradiation, applied alone or in combination with antibiotics, followed by Matrix-Assisted Laser Desorption/ Ionisation Time-Of-Flight (MALDI-TOF) mass spectrometry to characterise treatment-induced changes in bacterial protein profiles.

In polymer research, radiation-based treatments were combined with conventional materials characterisation techniques such as mechanical testing, vulcanisation analysis, swelling measurements, and FTIR spectroscopy to evaluate structural and performance-related changes.

Results

1. **Water Splitting:**

We further studied the applicability of first-row transition metal complexes in photo- and electrocatalysis. As part of this work, we published the structural and spectroscopic characteristics of a copper-containing coordination polymer. Various oxide and chalcogenide nanoparticles have long been at the centre of photocatalysis research.

We participated in uncovering the optical and photoelectrochemical properties of phase-pure, p-type semiconductor Cu_2S quantum dots, which were generated through the reaction of β-mercaptoethanol and sacrificial Cu_2O nano-octahedra. Given that properties can be further enhanced with metal nanoparticles, new opportunities are emerging for the development of photofunctional nanomaterials produced *via* controlled sulfidation.

By modifying the surface of hematite nanorods with Magnesium-iron Layered Double Hydroxide (MgFe-LDH), we demonstrated that this material combination significantly improves the efficiency of photoelectrochemical water oxidation. The presence of the layered double hydroxide promotes charge carrier separation and reduces the activation energy, resulting in a substantial improvement in the photoelectrochemical performance.

On a two-dimensional MoS_2 support, we stabilised semiconductor platinum clusters only two atomic layers thick, which possess unique catalytic characteristics due to the bandgap appearing in their electronic structure. These semiconducting Pt layers far outperform the activity of commercially available nanoparticles while requiring three orders of magnitude less noble metal during the hydrogen evolution reaction.

We demonstrated that high-curvature gold nanocone (AuNC) patterns, through geometric and plasmonic collective effects, enable photocathodes to utilise the Near-Infrared (NIR) range during hydrogen evolution. The AuNC-Ru antenna-reactor exhibits outstanding efficiency and durability, operating stably in an alkaline medium under both visible and NIR light at an extremely low overpotential for over 500 hours.

2. **Catalytic Methane Conversion**:

The NiMo/MgO powder catalysts with the same metal content, prepared in two different ways (sol-gel and wet impregnation), showed different catalytic activities in the pyrolysis of methane. In all cases, a bimetallic alloy was formed, but with different compositions and sizes. The addition of H_2 during methane decomposition improved the stability of the catalysts, resulting in higher carbon yields. Omitting the reduction pretreatment resulted in much smaller metal particle sizes and thinner carbon nanotubes, as well as higher initial activity, but faster deactivation.

To investigate how Ni and Mo loading influences the catalyst's catalytic activity and coke formation ability, a new microcombinatorial TEM method was used to produce Mo-Ni clusters on a SiO_x-coated Au TEM grid by magnetron sputtering and an additional high-temperature hydrogen treatment. Although the composition of the NiMo particles changed linearly along the grid, carbon formation after CH_4 flow at 800 °C could not be detected. The reason for the coke formation anomaly was that the Au diffusing from the grid and alloying with the metal particles hindered CH_4 dissociation and caused partial segregation of the NiMo nanoparticles.

3. **Application of high-energy ionising radiation in environmental, chemical, microbiological, and polymer research:**

In the degradation of Trimethoprim, a detailed picture was obtained of the hydroxyl-radical-induced reaction pathways. The treatment led to progressive oxidation, a faster decrease in Chemical Oxygen Demand (COD) than in Total Organic Carbon (TOC), improved biodegradability, and the disappearance of initial toxicity at higher treatment levels.

In the microbiological study, the results showed that MALDI-TOF MS could effectively distinguish between sensitive and resistant *Staphylococcus aureus* and *Escherichia coli* strains, especially at lower absorbed doses. The combined application of irradiation and antibiotics produced dose-dependent changes in bacterial protein profiles, revealing potentiation effects and different adaptive responses between sensitive and resistant strains.

In the polymer-related studies, irradiation-based material modification led to clear performance improvements. In the ground tyre rubber study, radiation-assisted surface activation improved compatibility in rubber mixtures and enhanced mechanical performance, including higher tensile strength and a slight increase in tear strength without sacrificing elongation at break. In the photopolymer additive-manufacturing study, gamma post-treatment markedly improved stiffness, strength, and thermal resistance.

Remaining work

Our previous research yielded detailed knowledge on the radiolytic degradation mechanisms of several micropollutants. Based on these findings, our objective is to examine possible correlations between degradation efficiency and the molecular structure of pharmaceutical compounds under various matrix conditions. At the same time, we aim to investigate the broad potential of ionising radiation in polymer research, particularly with regard to its application in material modification and the improvement of functional properties.

Related publications

1. K. Kovács, D. Székely, A. Tegze, R. Homlok, A. Bezsenyi, L. Wojnárovits: *Gamma and pulse radiolysis of trimethoprim in aqueous solutions: Intermediate radicals, rate of oxidation, toxicity,* Journal of Water Process Engineering **69,** 106743 (2025) https://doi.org/10.1016/j.jwpe.2024.106743
2. L. Wojnárovits, E. Takács: *Comparison of the Rate Constants of $^{\bullet}OH$, $SO_4^{\bullet-}$, $CO_3^{\bullet-}$, $Cl_2^{\bullet-}$, $Cl^{\bullet}$, $ClO^{\bullet}$ and $H^{\bullet}$ Reactions with Organic Water Contaminants,* Molecules **30:(18),** 3741 (2025) https://doi.org/10.3390/molecules30183741
3. A. Haider, R. Homlok, C.M. Farkas, T. Kocsis: *Characterizing Antimicrobial Effects of Radiation and Antibiotic Interactions on Staphylococcus aureus and Escherichia coli Using MALDI-TOF MS,* Antibiotics **14:(1),** 41, (2025) https://doi.org/10.3390/antibiotics14010041

4. Kiss, L., Szakács, Á., Homlok, R., Tegze, A., Mészáros, L.: *Gumiőrlemény felületaktiválása víz közegű, elektronsugárzásos kezeléssel és alkalmazása gumikeverékekben (Surface Activation of Ground Tire Rubber via Water-Based Electron Beam Irradiation and its Applicability in Rubber Mixtures)*, Polimerek (Polymers) **11:(3),** 90–96 (2025)

5. Sz. Krizsma, L. Kiss, A. Suplicz, R. Homlok, L. Mészáros: *Gamma-irradiation post-treatment in photopolymer-based additive manufacturing: An efficient method for improved performance,* Materials Today Communications **49,** 114205 (2025) https://doi.org/10.1016/j.mtcomm.2025.114205

6. B. Tatár, R. Homlok, L. Mészáros: *Enhancing the shape memory performance of self-reinforced cross-linked polyethylene composites by the optimization of the production temperature,* Nuclear Engineering and Technology **57:(9),** 103617 (2025) https://doi.org/10.1016/j.net.2025.103617

7. M.O. Plutenko, I.A. Golenya, V.M. Plavkov, T. Matus, J.S. Pap, and S. Shova: *Crystal Structure, Hirshfeld Analysis and Electrochemical Properties of poly[diaquabis[μ6-2-Cyano-2-(oxidoimino)acetato]copper(II)disodium],* Acta Crystallographica Section E: Crystallographic Communications **81:(10),** 972–976 (2025) https://doi.org/10.1107/S2056989025008126

8. D. Kovács, G. Z. Radnóczi, Z. E. Horváth, K. Frey, A. Sulyok, Z. Fogarassy, J. S. Pap, A. Deák, D. Zámbó: *Photoassisted Chemical Transformation of Cu_2O Nanooctahedra into Cu_2S Quantum-Dot Superstructures: Structural and Photoelectrochemical Properties,* ACS Materials AU **5:(6),** 1018–1028 (2025) https://doi.org/10.1021/acsmaterialsau.5c00106

9. I. Khan, T. Benkó, S. Keszei, A. Deák, D. Zámbó, S. Shen, Y. Wang, et al.: *Mechanistic and DFT Insights Into Co-Catalytic MgFe-LDH/Hematite Interfaces for Efficient Photoelectrochemical Water Oxidation,* Chemistry-A European Journal (2026) https://doi.org/10.1002/chem.202502623

10. T. Ollár, P. Vancsó, P. Kun, AA. Koós, G. Dobrik, EV. Sukhanova, ZI. Popov, et al.: *Semiconducting Pt Structures Stabilized on 2D MoS_2 Crystals Enable Ultrafast Hydrogen Evolution,* Advanced Materials **37:(37),** (2025) https://doi.org/10.1002/adma.202504113

11. F. Zhang, L. Ren, Q. Wang, Y. Ding, J.S. Pap, S. Shen, J. Wei, and J. Chen: *Near-Infrared-Driven Photoelectrochemical Hydrogen Evolution Reaction Enabled by Plasmonic Gold Nanocone Arrays with High Curvatures,* Small Methods **9:(8),** (2025) https://doi.org/10.1002/smtd.202500121

12. A. Horváth, M. Németh, A. Beck, D. Olasz, M. Serényi, G. Sáfrán: *Dramatic interference of Au TEM grid with model and supported MoNi/ MgO catalysts during high temperature reduction and methane decomposition,* Materials Today Nano **32,** 100690 (2025) https://doi.org/10.1016/j.mtnano.2025.100690

REAL-TIME MONITORING OF CELL RESPONSE/CELL DEATH DUE TO IONISING RADIATION DOSE EFFECT BY TRACKING CELL NANOMOTION

Attila Gulyás, Renáta Homlok, Dorina Szin, László Takács, Zsolt Csalótzky, Ágnes Belák, Krisztina Kovács, András Kovács, Károly Bodor, Sándor Kásás, Zoltán Dicső, Róbert Horváth, Inna Székács, Péter Völgyesi

Objective

To develop and implement novel real-time nanomotion microscopy systems compatible with high-dose ionising radiation, capable of tracking the nanoscale oscillations of individual adherent cells during the adhesion process. The platform aims to:

System development: design and construct a radiation-resistant nanomotion microscope compatible with high-dose environments. Characterisation of adhesion dynamics: identify characteristic oscillations resulting from the dynamic activity of filopodia and lamellipodia, which are associated with morphological changes of the cell (from spherical to flattened states). Discrimination between live and dead cells: compare the oscillatory patterns of living and dead cells, demonstrating that the measured nanomotions serve as reliable markers of general cell function. Nanomotion definition and mathematical analysis: test and apply various biological nanomotion definition approaches and implement advanced mathematical methods for analysing nanomotion data quantitatively. Investigation of radiation dose effects: correlate nanomotion measurements with radiobiological effects, enabling the system to monitor cell responses and cell death in real time under different radiation dose conditions.

Methods

Microscopy-based nanomotion analysis. Nanomotion microscopy can be implemented in several ways: the more expensive approach uses atomic force microscopy, whereas a cheaper alternative is plain optical microscopy (Optical Nanomotion Detection, ONMD), which involves optical image and data processing. In this study, widely used in biological research Saccharomyces cerevisiae cells were irradiated with a linear accelerator, and their post-irradiation motion was recorded using an optical microscope with a 40× objective. Cells were confined in a custom a few10 µm thick chamber between two glass slides to eliminate directional drift. The cells, which are a few micrometres in size, consist of a few 100 pixels with the objective magnification (40x) used and the video image resolution (1920x1080). We recorded 10–20 s videos at 25 fps (frames per second), and these recordings were processed by a self-developed MATLAB script to detect nanomotion signals of a single cell or a cell population; the software computes the nanomotion signal by few second time-integrating the pixel-wise light intensity differences between successive frames. Figure 1 A shows the first frame of a movie recorded on S. cerevisiae after irradiation with a dose of 10 Gy. The program automatically selects cells (as blobs) of a defined size and analyzes their nanomotion (cells surrounded by a yellow curve). Figure 1 B shows only the selected cells and their corresponding labels (numbers that appear close to the cells). Each of the selected cells has its nanomotion analysed and displayed as depicted in Figure 2. It is important to note that the nanomotion of cells in solution consists of two effects: the externally generated Brownian motion and the internally generated nano-oscillation of the cells. In our tests, we can measure the sum of the two as a function of time and/or dose. It makes sense that if the cell dies, the Brownian motion remains, while the nano-oscillation of the cells disappears. In the nanomotion signal, the nano-oscillation of the cells is a small but not negligible part compared to the Brownian motion. The measurement uncertainty is large, and this requires serious metrological care, such as repeatability, reproducibility and control samples.

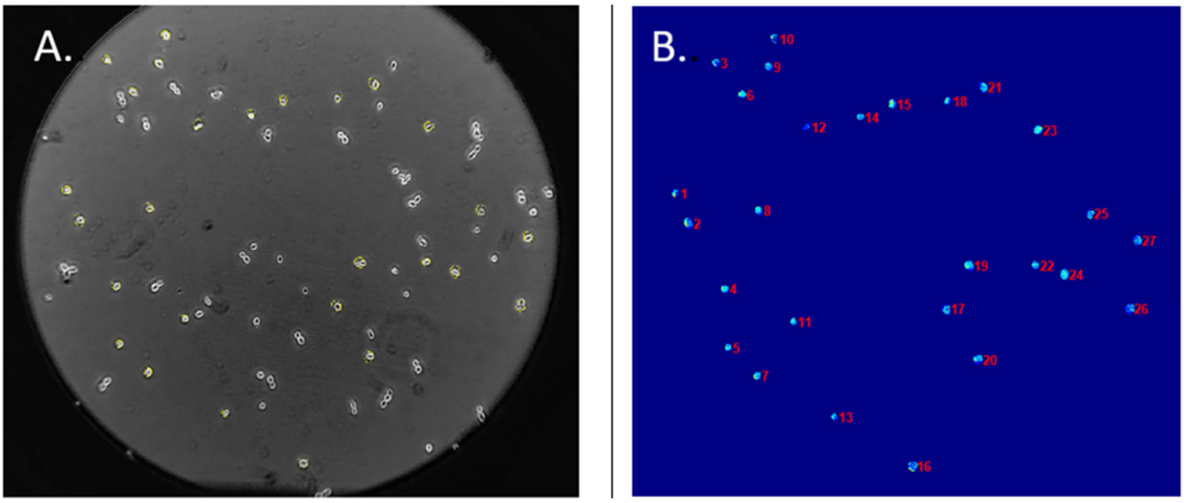


Figure 1: Microscopic image of cells A. and their highlighting B. for evaluation of nanomotion

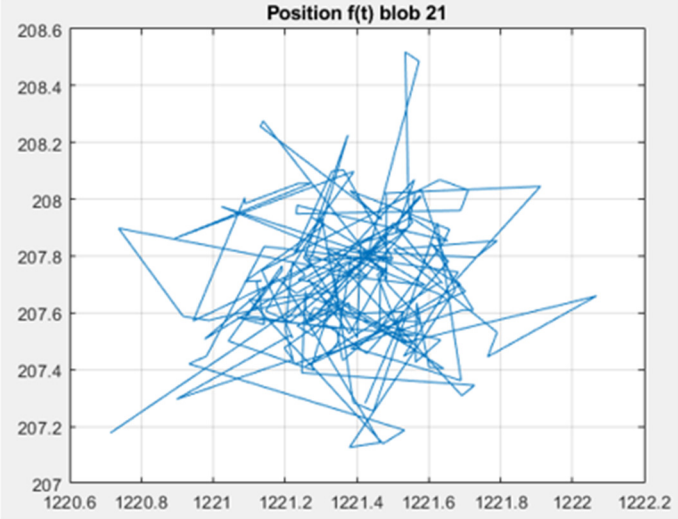


Figure 2: Subpixel displacements of a cell as a function of time (about 5 s) after an irradiation of 1000 Gy. Nanomotion displacement units are given in pixels.

The sum of the differential intensity of the pixels composing the 'DifImage' is eventually normalised by the surface occupied by the cells in the original image. Figure 3 depicts the activity of 25 cells after an irradiation of 1000 Gy. The time axis represents 6.6 seconds as 199 DifImages, the colour scale represents the nanomotion activity, which is intensity, whereas the Blobs axis (lines) corresponds to the different cells. It is important to note that the nanomotion of cells in solution consists of two effects: the externally generated Brownian motion and the internally generated nano-oscillation of the cells. In our tests, we can measure the sum of the two as a function of time and/or dose. It makes sense that if the cell dies, the Brownian motion remains, while the nano-oscillation of the cells disappears. In the nanomotion signal, the nano-oscillation of the cells is a small but not negligible part compared to the Brownian motion. The measurement uncertainty is large, and this requires serious metrological care, such as repeatability, reproducibility and control samples.

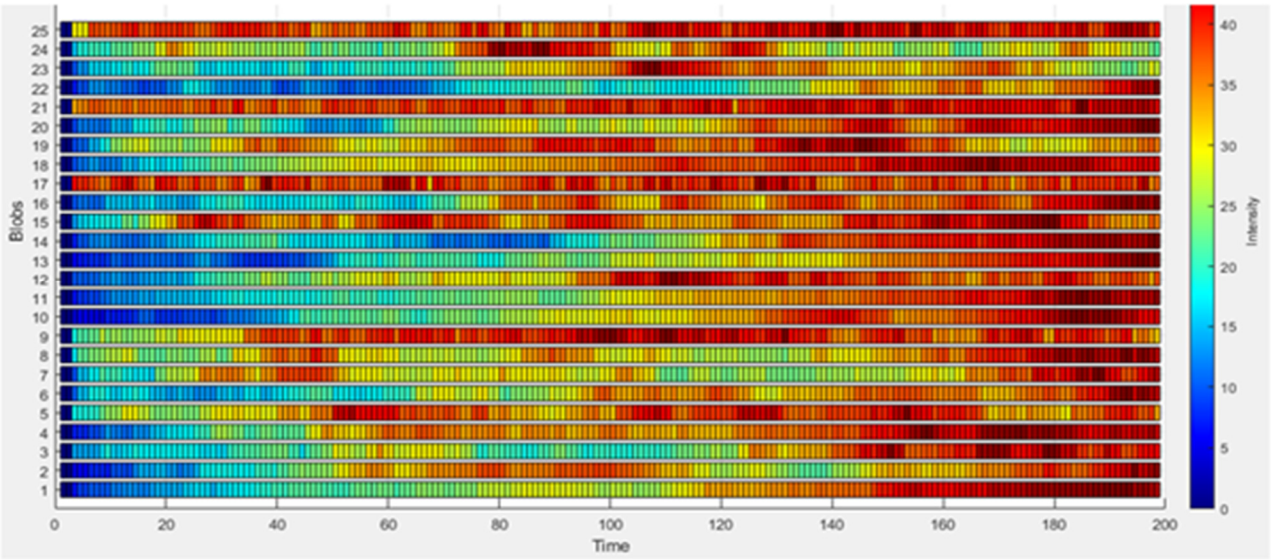


Figure 3: Nanomotion activity of 25 cells as a function of time covering 6,6 seconds

RWG biosensor adhesion assay. The Corning Epic Cardio (Fig. 4) used in the measurements is a label-free optical biosensor based on RWG (Resonant Waveguide Grating) technology. Brief operating principle: Light waves propagating along the surface of the waveguide penetrate the region above the sensor to a depth of approximately 150 nm, known as the evanescent field. If the refractive index of the material within this region changes (for instance, when a cell settles and adheres to the surface of the sensor), it leads to a shift in the resonant wavelength. This wavelength shift is detected, allowing the device to monitor cellular adhesion processes or responses to various stimuli in real time. The sensors are composed of an 80×80 grid of pixels, each with an edge length of 25 μm. The maximum sampling frequency is 60 Hz. This spatial and temporal resolution enables the instrument to observe changes of a magnitude similar to the movements of cell lamellipodia. In the experiments, we typically used two different measurement modes: one was the low sampling frequency mode, which recorded a data point every 3 seconds, and most of the measurements lasting 90-210 minutes were conducted in this mode, while the 60 Hz measurements were performed in 5-minute intervals, repeated 1-3 times during the course of the experiment.

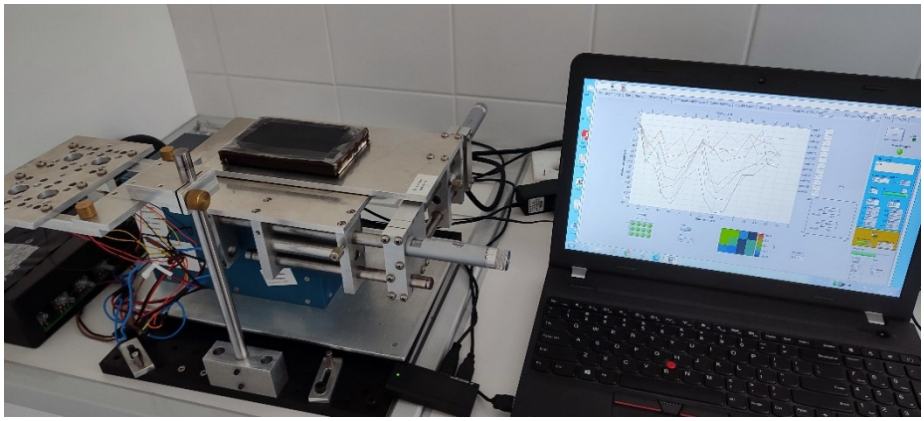


Figure 4: The Corning Epic Cardio setup

The experiments were conducted using HeLa cell line. The cells were passaged for at least 2 days, but no more than 4 days, before the measurement. The following protocol was used for cell preparation: cells were washed with Dulbecco's Phosphate Buffered Saline (DPBS), then treated with 0.05% (w/v) trypsin, 0.02% (w/v) Ethylenediaminetetraacetic acid (EDTA) solution for 2 minutes and subsequently aspirated. The cells were washed with 1 mL of complete Dulbecco's Modified Eagle Medium (DMEM) high glucose medium, centrifuged at 200×g for 5 minutes, and the supernatant was discarded. The cells were then resuspended in 1 mL of HEPES-HBSS (4-(2-hydroxyethyl)-1-piperazineethanesulfonic acid) – Hank's Balanced Salt Solution) buffer, and after cell counting, the appropriate dilution was pipetted into the wells of the Epic plate. The measurement begins with a 30-60-minute baseline recording with only buffer in the wells, after which the cell suspension is pipetted into the wells, followed by at least 90 minutes of additional measurement. After completing the Cardio measurement, Invitrogen Blue/Green fluorescent dyes were added to the cell-containing solution in the plate wells, and the cells were photographed using a 20× objective lens. Based on the images obtained, we were able to determine which cells were alive or dead at the end of the measurement, thus validating the analysis of our biosensor measurements.

Results

Microscopy-based nanomotion analysis. We have established stable experimental conditions and evaluation know-how for the study of cell nanomotion after radiation energy absorption. We performed nanomotion studies after different (0-100,000 Gy) doses, over a time ranging from a few minutes to several hours. Figure 5 depicts results obtained on S. cerevisiae after exposure to increasing levels of radiation. After a dose of 100,000 Gy, which is theoretically a thousand times the half-lethal dose of these yeasts, immediate death is likely, meaning only Brownian motion can be detected. A similar effect, that cells oscillate more actively before the moment/period of their death, was previously observed in bacteria upon exposure to increasing antibiotic doses.

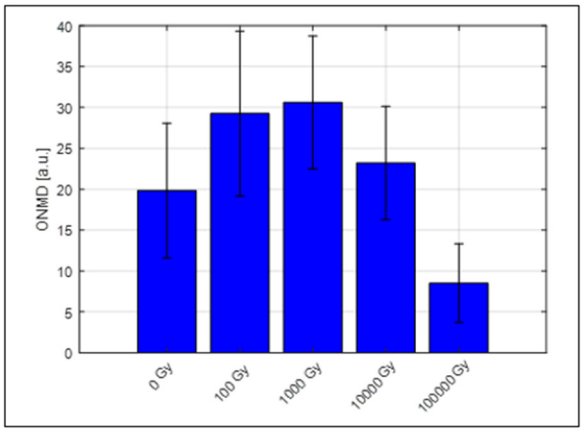


Figure 5: Nanomotion activity of the same yeast cell solution depending on the absorbed dose, samples irradiated separately with 4 MeV electron radiation

RWG biosensor adhesion assay. The wavelength shifts observed in living cells are greater than those measured in dead cells and the background (Fig. 6). To illustrate the methods used for oscillation analysis, we employed the results of an experiment in which HeLa cells adhered to an RGD-functionalized PLL-*g*-PEG surface. We investigated the optimal method for defining nanomotion in the analysis of oscillations, specifically determining the time-scale jumps at which the calculated nanomotion provides useful information. Our results indicated that, given the 25-micrometre spatial resolution, high-frequency measurements at 60 Hz are actually not necessary. This is because the limitations of spatial resolution mean that the detectable oscillations stem from slower morphological changes, such as cell adhesion and cell division. For detecting these processes, a sampling interval of 3 seconds was sufficient. By examining the nanomotion defined as the difference between consecutive data points (with 3-second intervals) (Fig. 7C, 7F), we found that individual living cells exhibit increasing rolling variance in their pixels during the establishment of stable adhesion, in contrast to dead cells (Fig. 7B).

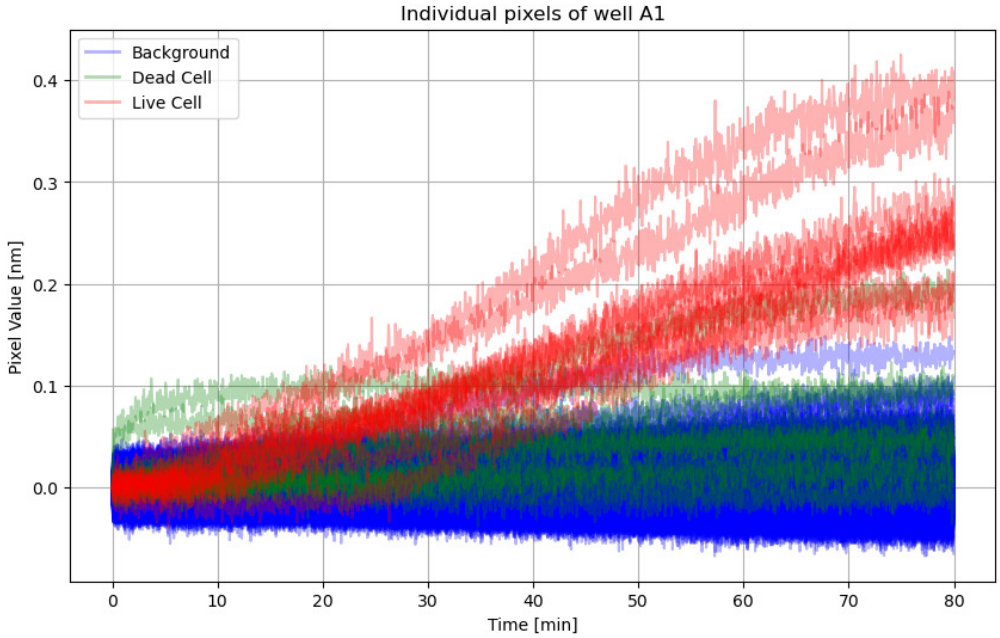


Figure 6: Comparison of the wavelength shift signals from pixels covered by the centres of individual cells (red: living cell, green: dead cell) and the signals from background pixels (blue)

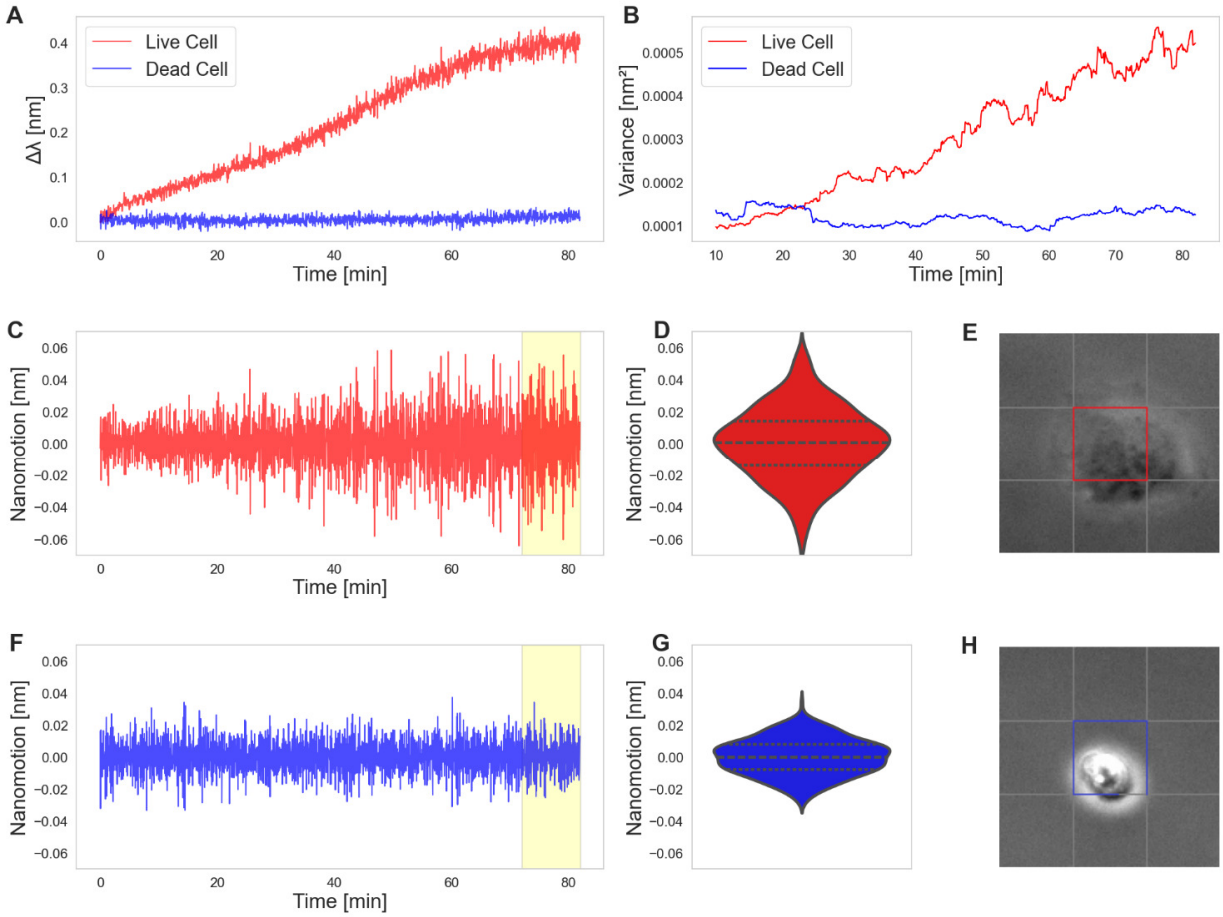


Figure 7: Representative temporal evolution of wavelength shift signals from Individual Live and Dead Cells Centre Pixels (A) Wavelength shift (Δλ) over time during the cell attachment process for a live cell (red) and a dead cell (blue).(B) Rolling variance of the nanomotion signal during the attachment process, indicating higher variability in live cells.(C) Nanomotion signal (consecutive frame differences) over time for the live cell.(D) Violin plot of nanomotion from the highlighted 20 minute time window in (C). (E) Phase-contrast image of the adhered live cell; the coloured square indicates the central pixel from which the time-series data in the plots were extracted. (F–H) Corresponding data for a representative dead cell: nanomotion signal (F), violin plot (G), and phase-contrast image with the blue-marked pixel (H).

We plotted the variance of individual cells calculated over 20 minutes of stable adhesion formation in a histogram, which shows that the distributions for dead and living cells differ significantly from each other (Fig. 8). The variance-based thresholding method achieved 93% accuracy in distinguishing live and dead cells.

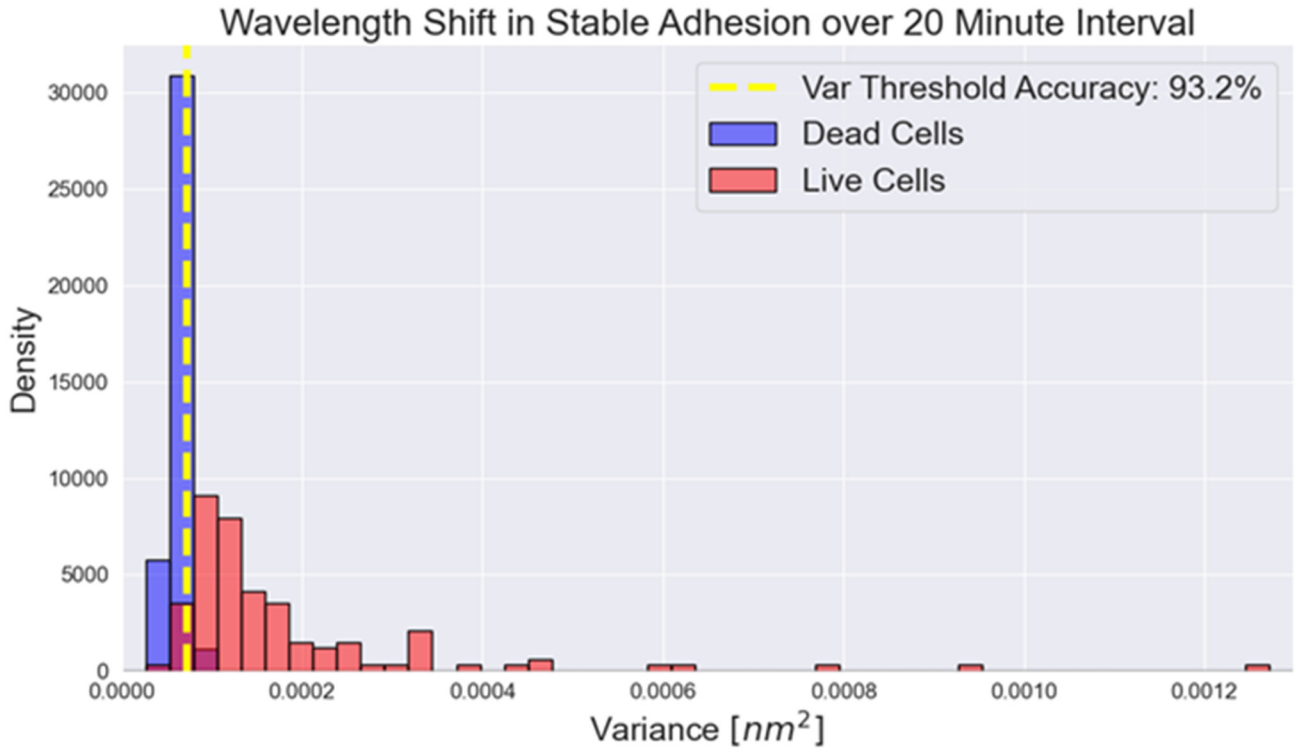


Figure 8: Histogram of variance of signal fluctuation over a 20 min time interval and thresholding to differentiate live and dead cells

For nanomotion calculated with larger time intervals (3 seconds), the violin plots of individual living cells, dead cells, and cell-free pixels show characteristic differences: the violin plots of living cells exhibit a broader spectrum compared to those of dead cells and background pixels (Fig. 9).

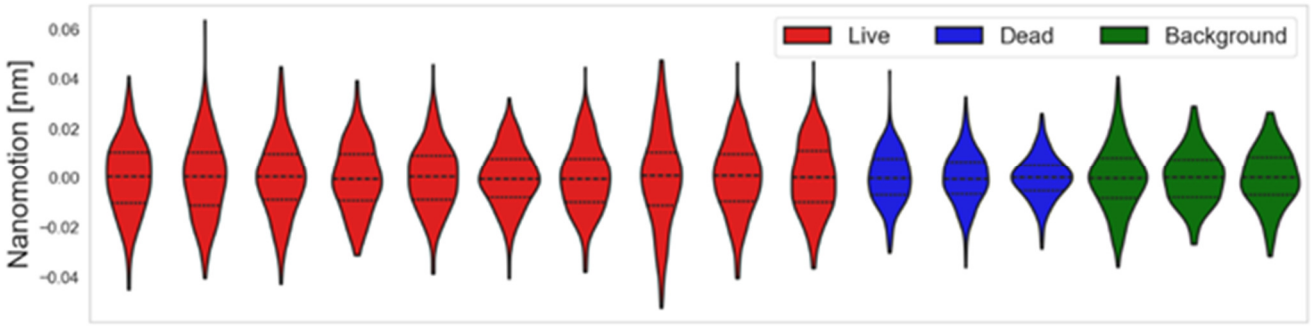


Figure 9: Violin plots of individual pixels nanomotion

To examine the temporal changes in wavelength shifts and nanomotion calculated with different window sizes for pixels covered by living and dead cells, we applied a wavelet transformation. Using the Morlet wavelet, we analyzed the changes in dominant frequency throughout the duration of the measurement. The results of the wavelet transformation revealed distinct differences between pixels corresponding to living cells, dead cells, and the empty background (Fig. 10).

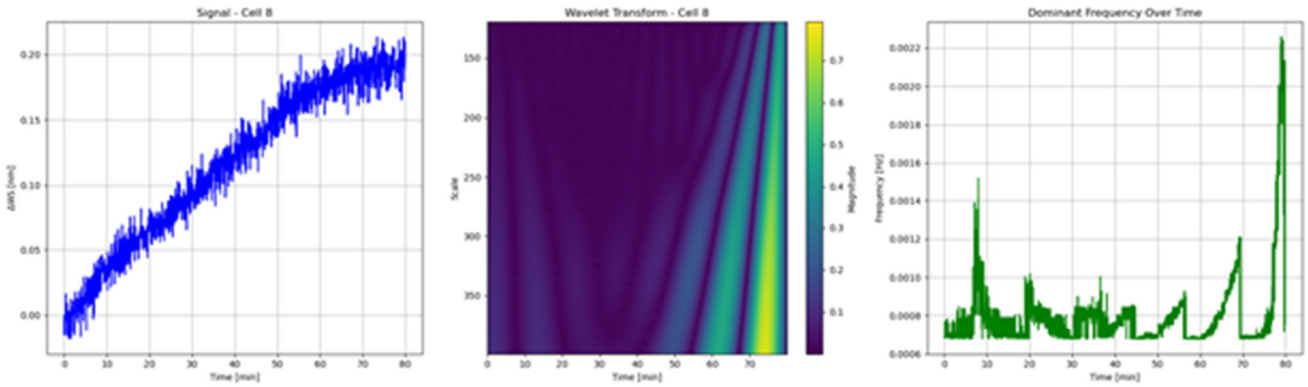


Figure 10: The result of the wavelet transformation for a randomly selected living cell.

Remaining work

Develop an advanced chamber design to completely eliminate unidirectional drift of cells during nanomotion assays. Incorporate more radiation-sensitive biological models (HeLa cells) and integrate real-time monitoring capabilities during irradiation. Extend the MATLAB motion analysis software with frequency-domain analyses (e.g., FFT) to uncover nuanced radiation-induced nanomotion patterns. Integrate data streams from the Corning Epic Cardio system to jointly analyse adhesion dynamics under irradiation. Investigate the combined effects of ionising radiation and antifungal agents (e.g., Actidibon) on cell nanomotions, complementing existing radiobiological findings. Characterise adhesion behaviour and nanoscale oscillations of cancer cell lines with varying metastatic potentials (4T1-T2, 4T1-LM2, 4T1-BM2) on different surfaces (laminin, RGD, fibronectin, uncoated glass) to explore predictive markers of metastasis. Adapt the methodologies beyond S. cerevisiae to other complex eukaryotic systems (e.g., various tumour cell lines and primary cultures) to broaden the applicability and validation of nanomotion-based assays.

APPLICATION OF ELECTRON BEAM IRRADIATION IN GROUND TIRE RUBBER RECYCLING

Lóránt Kiss, Renáta Homlok, Anna Tegze, Krisztina Kovács, Péter Völgyesi, Erzsébet Takács, László Mészáros

Objective

The purpose of the present report is to summarise the results achieved within our project entitled *Application of Electron Beam Irradiation in Rubber Granulate Recycling*, which received support under the HUN-REN EK Priority Budget Topic Programme (KKTP).

Our research aimed to develop a novel, water-based electron beam irradiation technology capable of activating the surface of Ground Tyre Rubber (GTR) produced from end-of-life tyres. When incorporated into new rubber compounds, this surface activation improves interphase adhesion, thereby broadening the potential application areas of materials containing recycled rubber and ultimately contributing to the reduction of waste tyres in the environment.

Within the framework of the project, we conducted a comprehensive assessment of the irradiation-induced modifications in GTR, targeting both the surface (Fourier-Transform Infrared Spectroscopy, FTIR; and Scanning Electron Microscopy, SEM) and its bulk phase (Soxhlet extraction, crosslink-density measurements). The irradiated GTR was incorporated into natural-rubber matrices, after which we examined the vulcanisation characteristics of the compounds and subsequently produced vulcanised sheets. The mechanical properties of these materials were then evaluated by tensile and tear testing, and "Shore A" hardness measurements. Furthermore, to elucidate the interfacial interactions between phases, morphological analysis was carried out using SEM micrographs.

Methods

Radiation treatment of ground tyre rubber by electron beam

The surface activation of the ground tyre rubber was carried out using electron-beam irradiation. During the irradiation process, a TESLA LINAC LPR-4 accelerator delivered 4 MeV electrons with a pulse duration of 800 ns. In compiling the experimental setup and determining the parameters of the accelerator, we used our experience gained from our wastewater treatment experiments.

In each experiment, 25 g of GTR was irradiated in 100 mL of distilled water containing 0.5 mL of surfactant, added immediately before continuous irradiation, ensuring proper suspension and dispersion of the GTR particles in the aqueous medium. Without this surfactant, the hydrophobic GTR would float on the water surface, thereby reducing the efficiency of the irradiation process.

During irradiation, air bubbling was applied through a silicone tube under continuous stirring to provide a sufficient amount of oxidising species for radiolysis and to prevent sedimentation of the GTR at the bottom of the vessel. After irradiation, the GTR was filtered through 615 MN creped filter paper and dried at room temperature until a constant mass was reached. The absorbed doses were 5, 10, 20, 40, 60, 80, and 100 kGy. The arrangement of the treatment can be seen in Figure 1.

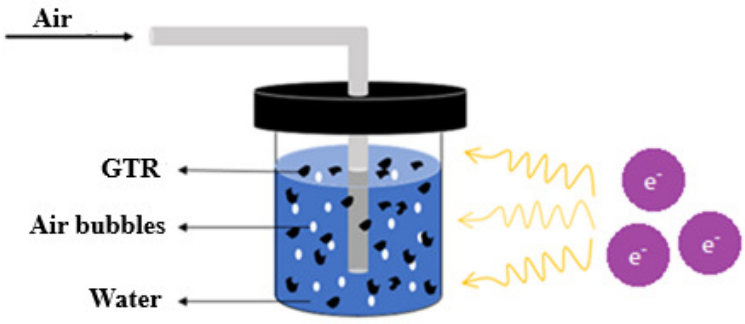


Figure 7: The experimental setup for the electron beam treatment of the GTR

For dosimetry, we prepared a 0.1 M L-alanine solution as a chemical dosimeter. Two types of solutions were used: (i) 120 mL of 0.1 M L-alanine in water and (ii) 100 mL of 0.1 M L-alanine containing 25 g of GTR and 0.5 mL of surfactant. The irradiation was carried out in the same container setup and measurement arrangement using continuous LINAC irradiation for 5, 10, and 20 minutes, while the solutions were constantly mixed and aerated. After irradiation, 2.5 mL ampoules were filled and later gamma-irradiated to establish a calibration series. For dose evaluation, oscillometric readout was applied: in the first step, a calibration curve was constructed from the oscillometric response of the gamma-irradiated alanine solutions, and this calibration curve was subsequently used to determine the absorbed dose in the electron-beam-irradiated solutions.

Recipes and compounding

For the preparation of the vulcanizates, a so-called two-step mixing method was employed. In the first step, the ground tyre rubber was mixed with the vulcanisation system so that the irradiation-induced active sites generated on the GTR surface could react with the curative components and form an even more reactive intermediate system. This mixture is referred to as the GTR premix, and its composition is listed in Table 1. The premix was prepared for each absorbed-dose level of GTR. The mixing order followed the sequence shown in the table, from top to bottom.

Table 1: Composition of the GTR premixes

Materials	Amount (phr)
Zinc-oxide	5
Stearic acid	2
GTR	100
Oil	10
N-cyclohexyl-2-benzothiazolesulfenamide (CBS)	1.25
Tetramethylthiuram-disulfide (TMTD)	0.6
Sulphur	0.6

In the second step, the GTR masterbatch was incorporated into a natural-rubber-based formulation using a semi-efficient sulphur vulcanisation system (Table 2). This system is widely used and provides a balanced set of mechanical properties. The mixing order followed the sequence shown in the table.

Table 2: Composition of the natural rubber based vulcanises

Materials	Amount (phr)
Natural rubber	100
Carbon black	60
Zinc-oxide	5
Stearic acid	2
GTR	100
Oil	10
N-cyclohexyl-2-benzothiazolesulfenamide (CBS)	1.25
Tetramethylthiuram-disulfide (TMTD)	0.6
Sulphur	0.6

The GTR masterbatches and the natural rubber compounds were prepared using a Brabender Plasti-Corder mixer (Brabender GmbH & Co. KG, Duisburg, Germany). The mixing zone temperatures were uniformly set to 50 °C with a rotor speed of 40 rpm. After all ingredients had been added, mixing was continued for an additional 2 minutes to ensure sufficient homogeneity. A 50 cm^3 mixing chamber was used with a 70% fill ratio.

Vulcanisation properties and vulcanisation

After preparing the compounds, the next step was the evaluation of their vulcanisation characteristics. For this purpose, a MonTech D-RPA 3000 rubber process analyzer (MonTech Werkstoffprüfmaschinen GmbH, Buchen, Germany) was used. For each test, a 4.5–5 g disk specimen was cut from the compounds produced with the internal mixer.

The parameters set on the RPA were as follows:

- 1° amplitude,
- 160 °C temperature,
- 15-minute measurement time.

Subsequently, vulcanised sheets were produced from the compounds using a Teach-Line Platen Press 200E hydraulic press (Dr Collin GmbH, Munich, Germany). The dimensions of the resulting sheets were 200 mm × 200 mm × 2 mm. Pressing was carried out at 2.8 MPa and 160 °C, and for each compound, the curing time corresponded to the respective t_{90} value obtained from the RPA measurements. At the beginning of the pressing, a brief degassing step was performed during mould closure to ensure uniform material distribution and that there was no air trapped inside the rubber.

Analytical methods for investigating bulk and surface modifications in ground tyre rubber

The soluble fraction (also referred to as sol content) of the irradiated ground tyre rubber samples was determined by Soxhlet extraction in accordance with ISO 1407:2023. Toluene was heated in the flasks located at the bottom of the apparatus. Above

the heated solvent, three specimens from each irradiation dose were placed in cellulose thimbles. The thimbles were lined with cotton wool to ensure proper sealing. During extraction, the vapour of the heated solvent passed through the thimbles, dissolving the non-crosslinked, low-molecular-weight components, and subsequently condensed into the lower flask containing the solvent. The experiment was carried out for 16 hours. Water cooling and electric heating were used throughout the process. After extraction, the samples were dried at 80 °C to constant mass.

The crosslink density was determined by a swelling method in accordance with ASTM D 6814-02. In this procedure, pre-weighed GTR samples were swollen in toluene at room temperature for 72 hours. After the swelling period, the solvent was decanted, and the surface of the swollen samples was gently blotted with paper towels to remove any adhering solvent and thereby avoid incorporating excess surface solvent into the swollen mass measurement. The samples were then dried at 80 °C to constant mass and subsequently weighed again to obtain the solvent-free dry mass. For each dose level, the measurements were performed on five specimens. Crosslink density values were calculated using the Flory–Rehner and Ellis–Welding equations.

Testing of the vulcanises

Tensile tests were performed in accordance with DIN 53504, using a gauge length of 60 mm and a crosshead speed of 500 mm/min. Tear resistance tests were conducted according to ASTM D624, with a crosshead speed of 500 mm/min and a gauge length of 56 mm. Before testing, a 1 mm notch was introduced on the inner side of each specimen to ensure a defined initiation point for failure. All mechanical tests were carried out at room temperature using a Zwick Z005 universal testing machine (Zwick GmbH, Ulm, Germany).

The "Shore A" hardness of the specimens was measured using a Zwick H04.3150 hardness tester (Zwick GmbH, Ulm, Germany). For each material, 15 measurements were taken to obtain a representative hardness value. The dwell time for each measurement was 3 seconds.

The morphology of the GTR particles and the fracture surfaces of the tested specimens was examined using a JEOL JSM 6380LA scanning electron microscope (JEOL Ltd., Tokyo, Japan). Before SEM analysis, the samples were coated with a thin layer of gold.

Results

Effects of radiation on the bulk properties of ground tyre rubber

The results of the Soxhlet extraction and crosslink density analyses (soluble fraction, crosslink density, and its variation) are summarised in Table 3.

Table 3: Results of Soxhlet extraction and crosslink density measurements of electron-beam-treated GTR

Absorbed dose (kGy)	Sol-content (%)	Crosslink density (10^{-4} mol/cm^3)	Difference in the crosslink density (%)
0	8.70 ± 0.45	10.41 ± 0.86	0
5	9.33 ± 0.31	9.22 ± 0.71	-11.36
10	9.29 ± 0.30	10.14 ± 0.65	-2.53
20	9.04 ± 0.38	10.37 ± 0.53	-0.35
40	9.48 ± 0.49	10.53 ± 0.45	1.18
60	9.14 ± 0.21	10.72 ± 0.76	3.07
80	8.97 ± 0.37	10.61 ± 0.18	1.98
100	8.95 ± 0.31	10.53 ± 0.73	1.19

The soluble fraction of the irradiated GTR increased for all irradiation doses compared to the untreated reference. However, the magnitude of this increase was only about 1–2%. The higher soluble fraction indicates that irradiation induces chain scission, during which small molecular fragments are cleaved from the long polymer chains and subsequently extracted by toluene. The relatively small increase suggests that no significant degradation occurred.

At lower doses (5, 10, 20 kGy) the crosslink density decreased, resulting in negative values for the change in crosslink density, whereas at higher doses (40, 60, 80, 100 kGy) it showed an increasing trend, yielding positive changes. The sample irradiated at 5 kGy stands out from the others, exhibiting an unusually large decrease (–11.36%). This is most likely due to measurement error, as such a substantial reduction cannot be explained at such a low dose. For the remaining doses, the change in crosslink density was typically within the range of 1–3%.

Both the soluble fraction and the crosslink density show only very minor changes, suggesting that the internal chemical structure of the GTR was not significantly affected by irradiation. Instead, the primary process is presumed to be the radiolysis of water. The oxidative intermediates formed from water radiolysis can activate the surface of the GTR, explaining the observed increase in crosslink density. The highest crosslink density was obtained at 60 kGy, after which the value began to decline again. Overall, the results demonstrate that it was possible to develop a surface activation method without substantially altering the chemical structure of the material.

Effects of radiation on the surface of the ground tyre rubber

Micrographs of the treated and untreated GTR particles are shown in Figure 2. Both images exhibit particles in similar sizes, except for a few larger GTR granules. The finely porous particle surfaces resulting from the grinding process are clearly visible in both cases. As discussed in the literature, certain treatments can significantly enhance adhesion. For example, acid treatments can generate complex surface morphologies, leading to a substantial increase in the specific surface area of GTR particles. In the present study, no significant morphological changes were observed, suggesting that electron-beam irradiation does not markedly influence the surface morphology of GTR. Consequently, the improvement in adhesion is not attributed to morphological modification but rather to the formation of surface-activated functional groups.

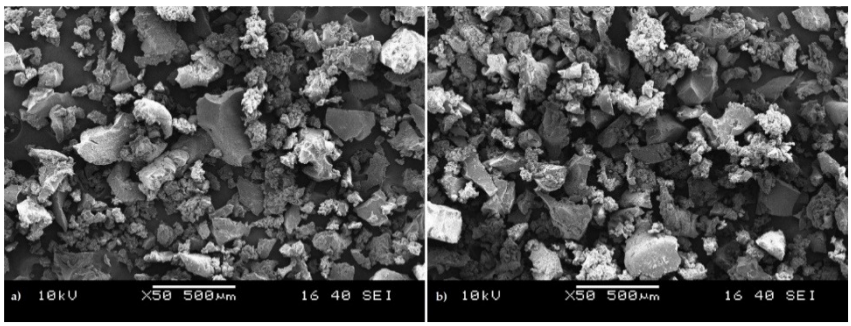


Figure 8: Scanning electron micrographs of the untreated (a) and the 100 kGy electron-irradiated (b) ground tyre rubber particles at 50× magnification

Results of vulcanizate testing

The tensile strength values measured for the two-step vulcanizates are summarised in Figure 3. It is evident that the tensile strength of the irradiated two-step samples increased compared to the reference (8.25 MPa). At lower doses, this increase was more pronounced, reaching 10.49 MPa at 10 kGy, which corresponds to a 25% increase. After 10 kGy, a decreasing trend is observed, although the values remain above the reference. The lowest tensile strength was recorded at the highest dose (7.99 MPa). The increase in tensile strength suggests that during the first step of the two-step mixing process, the active groups formed on the surface of the irradiated GTR were able to react with the vulcanisation system. This effect was further enhanced in the second mixing step, resulting in the formation of particularly active sites that were able to establish even better interactions with the matrix.

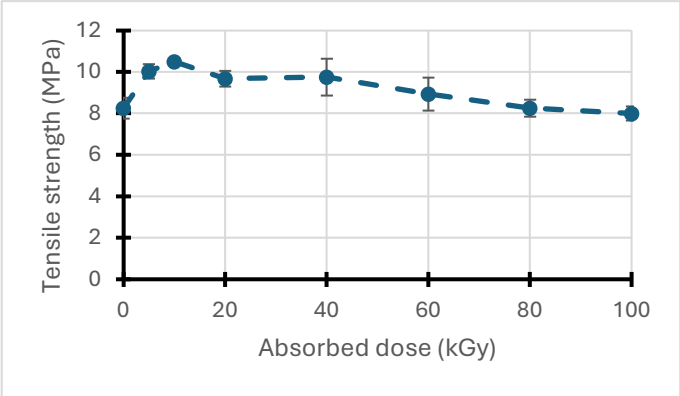


Figure 9: Tensile strength of the vulcanisates

The elongation at break values determined from the tensile tests are shown in Figure 4. The elongation of the various samples ranged between 290% and 340%, with the lowest value (294%) observed for the 100 kGy dose and the highest (335%) for the 10 kGy dose, representing an approximately 20% increase compared to the reference value (316%). Similar to the tensile strength results, the elongation at break shows that low doses lead to an increase in elongation, reaching a maximum at 10 kGy, after which a decreasing trend is observed; however, values remain above the reference except for the highest dose. Considering the high filler content of these systems, these elongation values are excellent. The elongation values of the two-step vulcanisates exceeded those of the one-step compounds. As with the tensile strength results, this improvement can be attributed to the two-step mixing process: in the first step, the GTR reacts with the vulcanisation system, and this reaction continues in the second step, resulting in improved interfacial interactions between the phases.

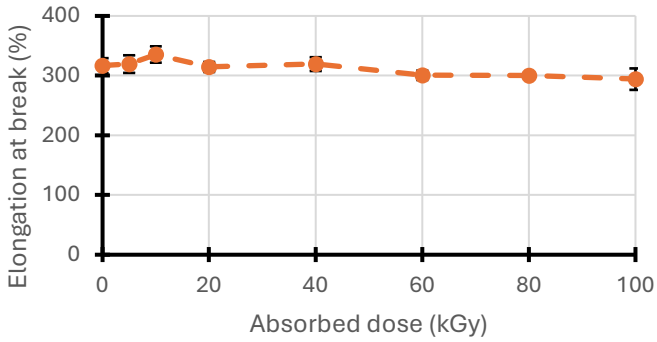


Figure 10: Elongation at break values of the vulcanisates

The tear strength values for the two-step vulcanisates are presented in Figure 5. The same trend observed for tensile strength and elongation at break is also evident here. Compared to the reference (22.8 kN/m), electron irradiation generally increased the tear strength, except for the 5 kGy sample (17.4 kN/m), where a significant decrease was recorded. This is most likely due to a notch-related error, which may have initiated premature failure in the specimen, thus skewing the average value for this dose. The highest tear strength was observed for the 40 kGy sample (29.5 kN/m), corresponding to an outstanding 70% increase relative to the non-irradiated reference. Beyond this dose, tear strength gradually decreased with increasing irradiation; however, even at the highest dose of 100 kGy (25.1 kN/m), the values remained above the unirradiated reference. The increase in tear strength was further enhanced in the two-step mixing process (reaching approximately 25.0 kN/m), whereas in the one-step samples, values were around 8.0 kN/m. This increase reflects improved interfacial adhesion, as cracks naturally initiate at the weakest location, i.e., the phase boundary, and propagate from there. The combined effect of electron irradiation and the two-step mixing process led to the greatest improvement in tear strength, providing clear evidence of successful surface activation.

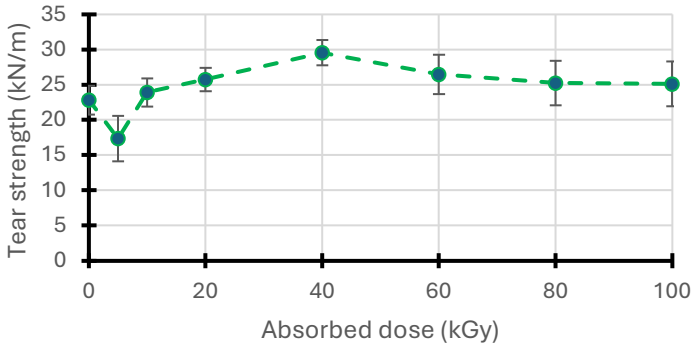


Figure 11: Tear strength of the vulcanisates

The "Shore A" hardness values of the two-step mixed vulcanisates are presented in Figure 6. The hardness values range between 50 and 56. The highest value was recorded for the reference sample (0 kGy, 55.5), while the lowest was observed at 100 kGy (49.7). The trend of the curve indicates a slight decrease in hardness with increasing irradiation dose, which is supported by the minor fluctuations in the measured values. Overall, the differences between the measured values are small, suggesting that electron-beam irradiation has minimal impact on hardness. This observation supports the hypothesis that electron irradiation in water does not significantly affect the chemical structure of the material, but primarily serves to activate the surface. It is noteworthy that the "Shore A" hardness of the two-step vulcanisates is higher than that of the one-step samples, for both the reference and the irradiated GTR-based compounds. This can be attributed to the higher sulphur content in the two-step formulations, which leads to increased crosslink density.

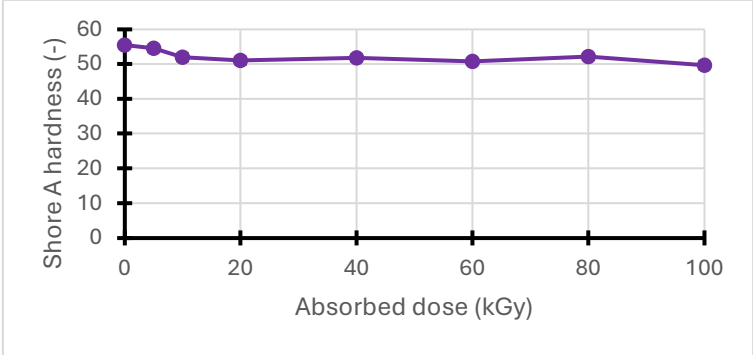


Figure 12: "Shore A" hardness of the vulcanisates

For the morphological characterisation of the compounds, the fracture surfaces of the tear test specimens were examined. The corresponding micrographs are shown in Figure 7.

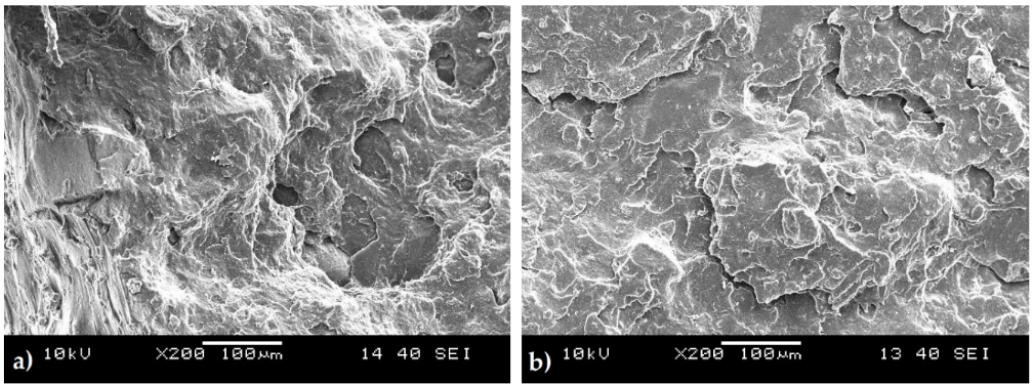


Figure 13. SEM images of the fracture surfaces of two-step vulcanite tensile specimens: a) untreated (0 kGy) and b) 60 kGy electron-irradiated samples

It can be concluded that in both the untreated (Figure 7a) and the irradiated samples (Figure 7b), the GTR was able to integrate properly into the matrix, forming a nearly homogeneous structure, which is essential for efficient stress transfer between the matrix and the GTR particles, reducing stress and contributing to improved and more reproducible mechanical performance.

Conclusion

This study demonstrated that water-based electron-beam irradiation is an effective method for activating the surface of GTR without significantly altering its bulk chemical structure. While only minor changes were observed in sol content and crosslink density, the irradiated GTR showed markedly improved mechanical performance when incorporated into natural-rubber compounds. Lower absorbed doses (around 10–40 kGy) led to the most pronounced increases in tensile strength, elongation at break, and tear resistance, confirming enhanced interfacial adhesion between GTR and the rubber matrix. SEM analyses further supported the formation of stronger interphase interactions rather than morphological alterations. Overall, the developed irradiation-based activation process improves the compatibility and performance of recycled rubber, offering a promising route to higher-value applications and contributing to more sustainable tire-recycling technologies.

Remaining work

All commitments were completed fully, and one article was published in the Polimerek (Polymers) journal.

Related publications

[1] Kiss L., Szakács Á., Homlok R., Tegze A., Mészáros L.: *Gumiőrlemény felületaktiválása víz közegű, elektronsugárzásos kezeléssel és alkalmazása gumikeverékekben (Surface activation of rubber crumb by aqueous electron beam treatment and its application in rubber mixtures),* Polimerek (Polymers) **9,** 90-96 (2025)

[2] Kiss L., Homlok R., Tegze A., Takács E., Mészáros L.: *Hulladék abroncs gumiőrlet értéknövelt újrahasznosítása ionizáló sugárzás segítségével (Value-added recycling of waste tire rubber crumb using ionizing radiation),* előadás (oral presentation), 2025 October 13-15. Őszi Radiokémiai Napok (Autumn Radiochemical Days), Balatonszárszó

[3] Kiss L., Homlok R., Tegze A., Takács E., Mészáros L.: *Hulladék abroncs gumiőrlet értéknövelt újrahasznosítása ionizáló sugárzás segítségével (Value-added recycling of waste tire rubber crumb using ionizing radiation)* XXX. Őszi Radiokémiai Napok (Autumn Radiochemical Days), Budapest, Magyarország: Magyar Kémikusok Egyesülete (Hungarian Chemical Society) (MKE) **140,** 32-35 (2025) ISBN 978-615-6018-33-5

[4] L. Mészáros, L. Kiss.: (Budapest University of Technology and Economics – Hungary), D. Constantinescu (S.C. Monofil S.R.L.), K. Harre, U. Gohs (HTW Dresden) – Germany, M. Stelescu (National R&D Institute for Textiles and Leather): *Recycling of Waste Tyre Rubber Containing Natural Rubber with the Aid of Ionising Radiation,* IAEA-CN-332/809

One MSc Thesis was completed in the course of the project:

[5] Szakács Á.: *Elektronsugárzással kezelt gumiőrlemény alkalmazhatósági lehetőségei gumikeverékekben (Application possibilities of electron beam treated rubber crumb in rubber mixtures),* Budapesti Műszaki és Gazdaságtudományi Egyetem (Budapest University of Technology and Economics), Gépészmérnöki kar (Faculty of Mechanical Engineering**)**, Polimertechnika Tanszék (Department of Polymer Engineering).

MAGNETIC CHARACTERISATION OF RADIOACTIVE MATERIALS

Antal Gasparics, Ildikó Szenthe,
Kristóf Csikós and István Mészáros

Objective

The nuclear industry's growing interest in innovative materials is being driven by emerging technologies such as nuclear fusion and various types of small modular reactors. Ensuring operational safety requires advanced structural health monitoring, which in turn creates a need for additional material characterisation based on the principles of different Non-Destructive Evaluation (NDE) techniques, including electromagnetic methods. Recently, the concept of a "material passport" has been introduced. This passport aggregates not only the primary mechanical and chemical properties of a material but also those characteristics relevant to NDE inspections. Such material passports play a crucial role in the earliest stages of structural design and serve as a foundation for developing new materials. In response to a specific request from the Fusion collaboration, HUN-REN EK has undertaken magnetic characterisation of EUROFER '97 material exposed to various operational conditions. This effort led to the establishment of methods and laboratory capabilities suitable for examining the magnetic properties of irradiated, radioactive materials within a hot-cell (HC) environment.

Methods

In the applied-research phase of material development, only small-volume test specimens are typically examined due to biological risks, high irradiation costs, and the challenges of managing radioactive waste. A well-known technique—the Vibrating-Sample Magnetometer (VSM), or Foner magnetometer—was developed decades ago and is suitable for magnetic characterisation of small samples. However, VSM systems are large, costly, and difficult to operate in a HC environment, making them impractical and not economical for this purpose. To address this limitation, a project was initiated to develop an experimental setup capable of replacing the VSM technique in hot-cell conditions for characterising specimens with volumes of only a few cubic millimetres.

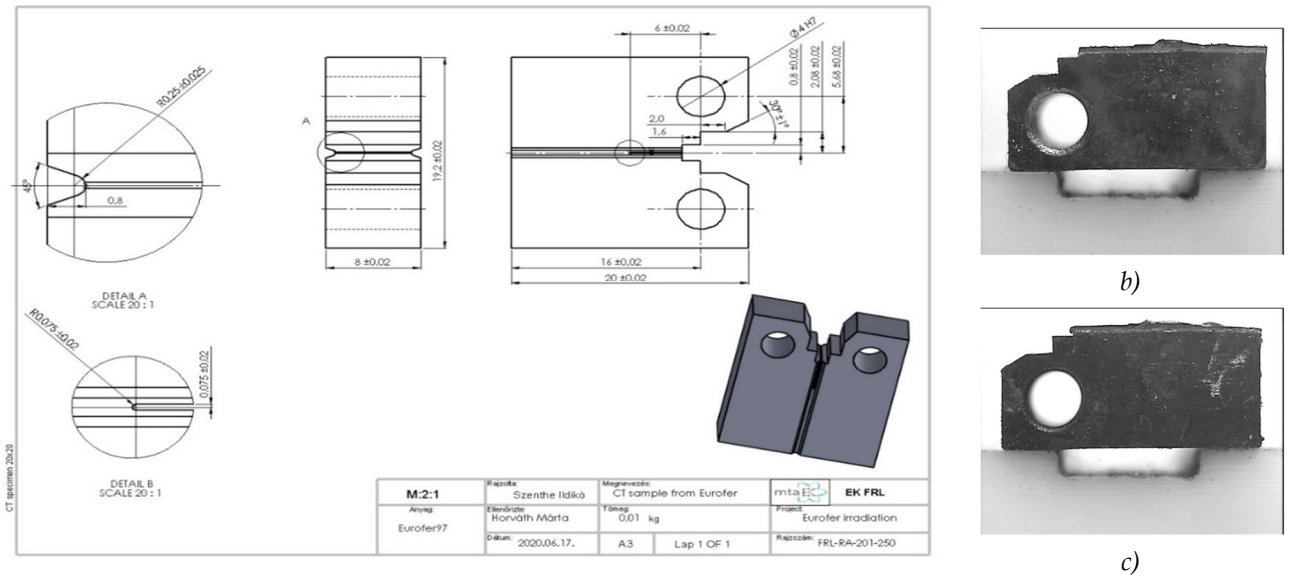
Our approach combines two magnetic measurement methods. First, an "absolute" technique is used to obtain B–H curves from larger, non-irradiated reference specimens. Second, an improved, HC-approved probe employing a "differential" measurement method—Magnetic Adaptive Testing (MAT)—is used to detect subtle changes in magnetic properties with exceptional sensitivity. These changes may arise from neutron irradiation or mechanical/thermal treatments. The absolute method determines the baseline magnetic characteristics of unirradiated material and enables proper calibration of the MAT results.

The project was carried out through collaboration among three parties: the Institute for Atomic Energy Research, which provided the hot-cell facility and sample preparation capabilities; the Institute of Technical Physics and Materials Science, which contributed expertise and instrumentation for the MAT method; and the Department of Materials Science and Engineering at the Budapest University of Technology and Economics, which provided magnetic characterisation expertise and facilities.

Results

During the execution of the project, the requirements for the measurement setup changed several times. No dedicated test samples were originally designed for magnetic characterisation; this need emerged only after the specimens had already been selected for their operational environment, subjected to various irradiation conditions, and even used in destructive mechanical tests. As a result, only the leftover fragments from these mechanical tests were available for magnetic measurements (see Fig. 1).

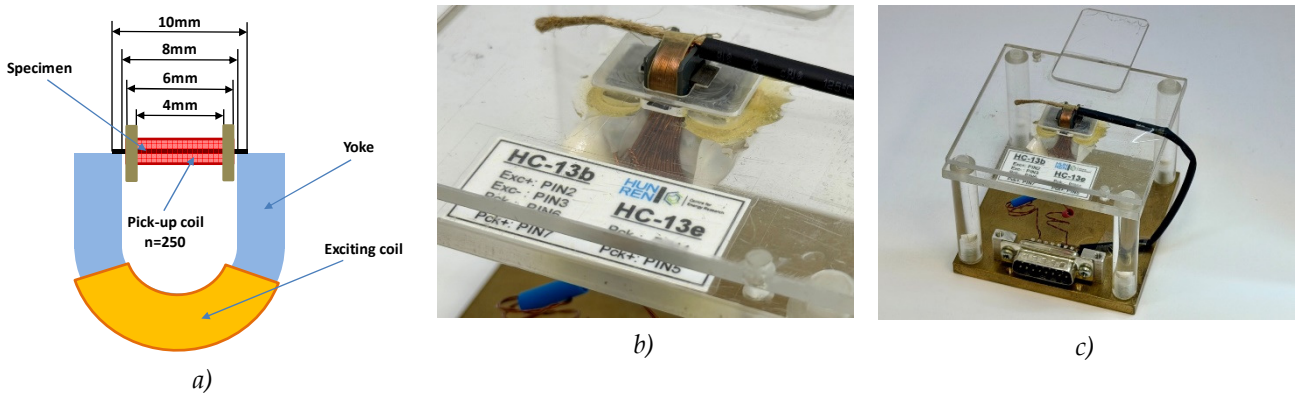
Because the destructive tests produced fragments with highly variable geometries, we were ultimately forced to define a very small, standardised rectangular sample size that could be cut from most of the remaining material. The final agreed dimensions for the magnetic characterisation specimens were 10 × 5 × 1 mm.



a) b) c)

Figure 1: The geometry of the mechanical test samples
a) Schematics of geometry; b) and c) the two fragments of the destructive test

Magnetic characterisation requires driving the specimen into magnetic saturation, which in turn demands a high excitation field. This can only be achieved using a magnetic yoke with a sufficiently large excitation coil. Furthermore, the yoke's cross-section must be significantly larger than that of the test specimen along the magnetisation direction to prevent the yoke from saturating before the sample does. These conditions impose strict limits on the minimum feasible size of both the yoke and the test specimen. The developed HC-13e probe reached the lower limit of applicability: the magnetic coupling area between the yoke and the specimen is effectively the same as the cross section of the specimen itself—approximately 5 mm² (see Fig. 2a).



a) b) c)

Figure 2: The developed MAT probe: 'HC-13e'
a) Schematic of the set-up; b) target specimen inside the pick-up coil; c) the whole probe

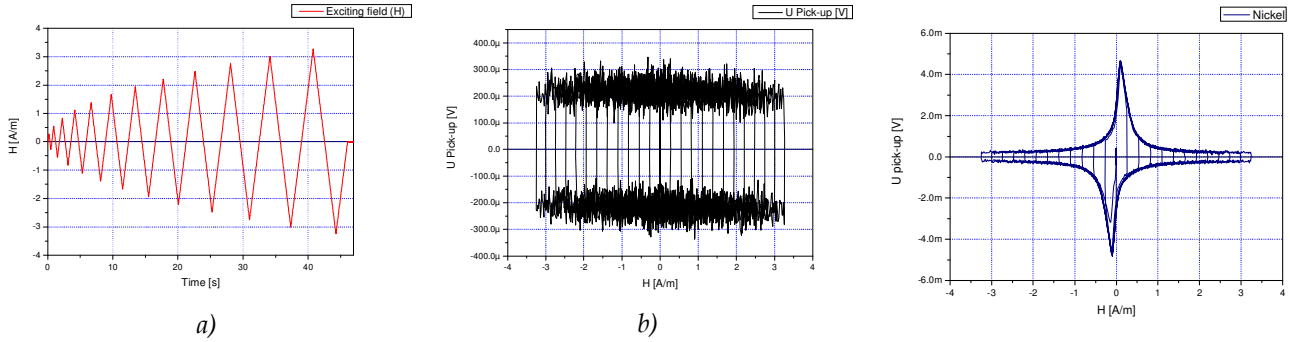
Operating at the limits of applicability meant that even small mechanical inaccuracies in sample dimensions or in positioning the specimen relative to the yoke became major sources of measurement error. The HC environment further complicates sample handling, making precise manipulation difficult. Additionally, the HC-13e probe employs extremely small pick-up coils made from delicate wires only 130 µm in diameter.

To address these challenges, a special transparent plastic holder was developed to ensure accurate specimen positioning and to allow reliable manipulation using HC tools. The pick-up coils and their connecting wires are protected by reinforced wire guides and plastic coverings (see Fig. 2b and Fig. 2c).

The operational validation of the HC-13e probe and its computer-controlled measurement system aimed to verify whether the intended magnetic behaviour of test specimens could be accurately recorded, and to identify the system's error sources—including noise, uncertainties, and signal asymmetries—that ultimately limit precision and reliability. The entire setup was evaluated by measuring responses both without a specimen ("in air") and with a high-purity nickel sample whose magnetic properties are well established.

Instead of using a single-frequency (sinusoidal) excitation field, the MAT system applies a linearly varying time function, in which the field increases stepwise to its final value during each reverse magnetisation cycle. This linear excitation allows for easy separation of the system's linear response from the nonlinear behaviour caused by the material's intrinsic magnetic properties.

Operational validation results show that in the linear case (i.e., without a test specimen), the induced signal in the pick-up coil remains constant at the microvolt level (see Fig. 3a), is symmetrical, and is nearly two orders of magnitude lower than the peak response observed with a nickel specimen (see Fig. 3c) and the measured noise level is definitely lower than 50μV These results confirm that the system setup is capable of accurately recording the magnetic response of these small volume specimens, achieving a resolution of approximately 5%.

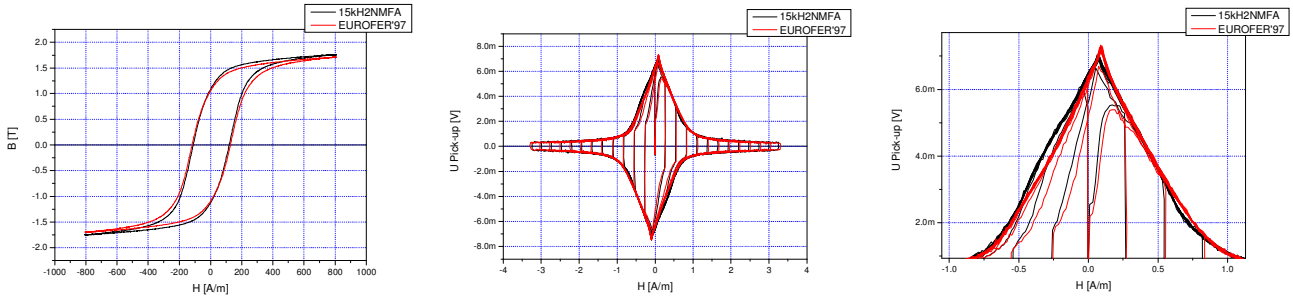


a) *b)* *c)*

Figure 3: The operational validation of the HC-13e probe and the MAT system
a) Time function of the applied exciting field; b) Response without specimen; c) Response with nickel specimen

The MAT method was developed to compare the magnetic properties of different specimens by eliminating the common components of the signal, thereby enhancing resolution without requiring a large signal dynamic range or separating the contributions from the yoke and the specimen. Because of this, the method is not suitable for calibration purposes. However, it is exceptionally sensitive to even subtle changes in material properties that affect magnetic behaviour. Consequently, measuring target specimens with MAT also provides the opportunity to monitor material degradation as an additional benefit for the future.

To demonstrate these capabilities, different reactor structural materials, namely '15KH2NMFA' and EUROFER '97, were also compared (see Fig. 4). This illustrates the advantage of comparing the full resultant permeability curves rather than just a few characteristic points of the B–H curves. Since the MAT method generates a large dataset from a series of minor reverse magnetisation loops, it allows the selection of specific parameter pairs (so-called magnetic descriptors) from a given loop that show the highest correlation with the degradation process, enabling the most reliable monitoring of material changes.



a) *b)* *c)*

Figure 4: Experimental results
a) 'Absolute' measurement of B-H curve;
b) Comparison of MAT Resultant permeability curve series;
c) Comparison of MAT Resultant permeability curve series - enlarged

The effects of the initial material inhomogeneity in the mechanical test specimens (see Fig. 1) are clearly visible for both 15KH2NMFA and EUROFER '97 materials. This was observed when measurements were performed on inactive or as-quenched specimens cut from the bulk material in three different orientations: 'S–L', 'S–T', and 'L–T' respectively. Here, 'L' refers to the primary direction of rolling, extrusion, or the forging axis; 'T' denotes the long-transverse direction; and 'S' represents the short-transverse direction or the material thickness. While not surprising, this is an important consideration. These inhomogeneities are further amplified after irradiation campaigns and even more so following destructive mechanical tests. Consequently, interpreting measurement results obtained from fragments of mechanically tested specimens is problematic. For this reason, we have proposed preparing a separate set of specimens designed exclusively for magnetic characterisation. This will require either a new irradiation campaign or the use of other already irradiated specimens that have not undergone mechanical testing.

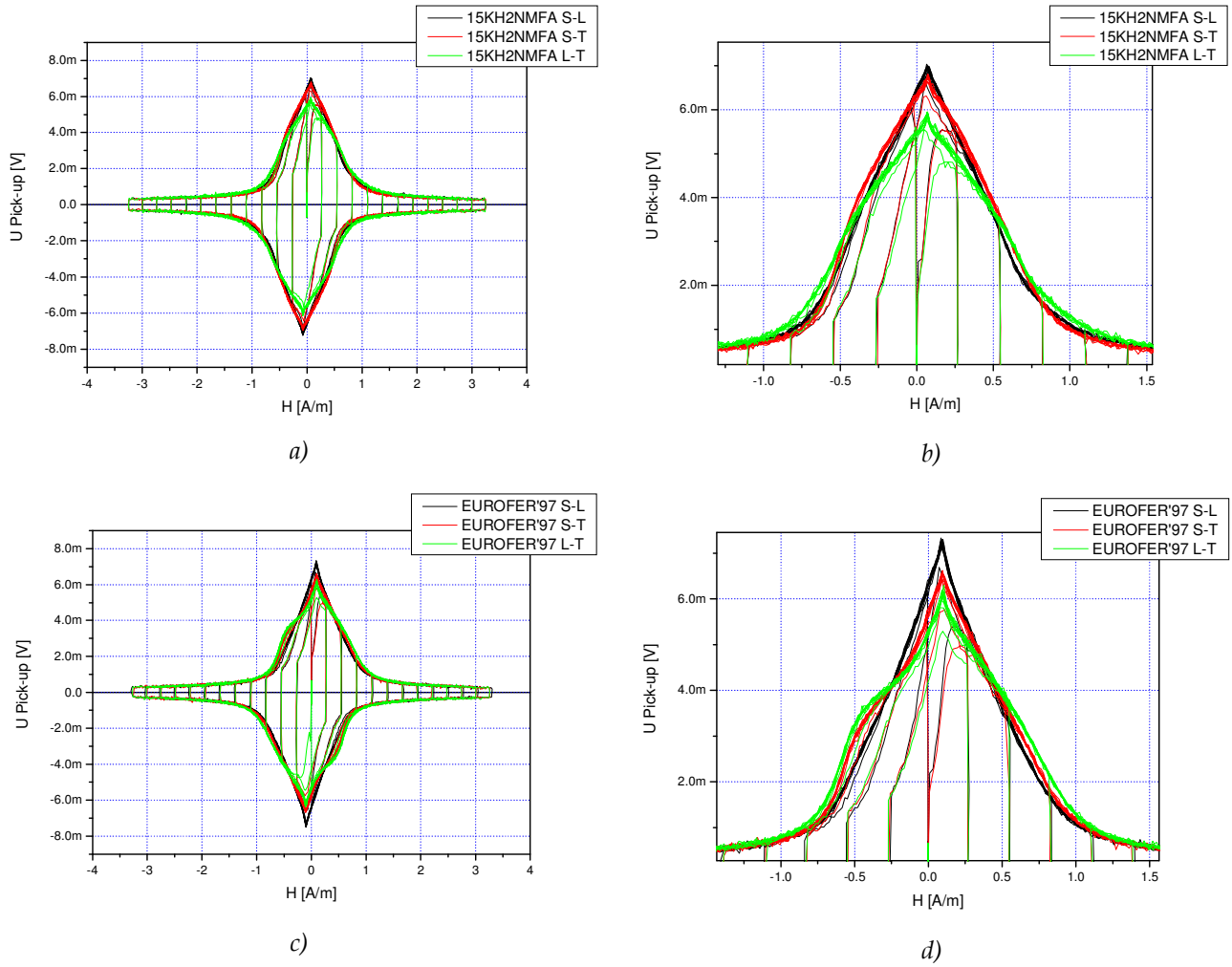


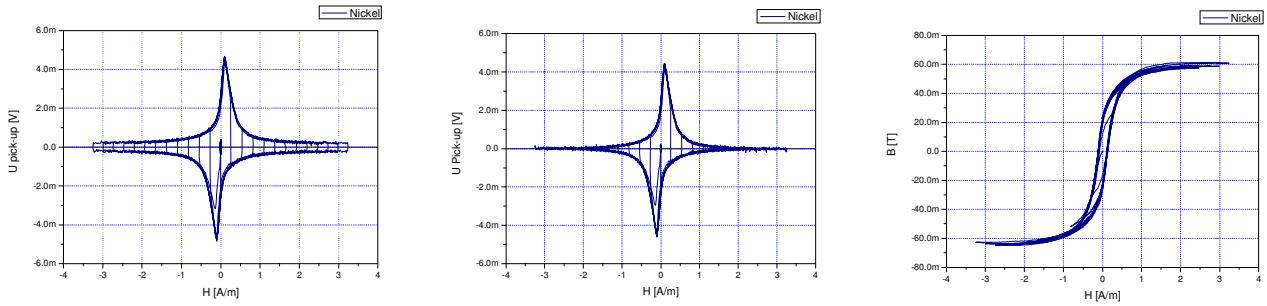
Figure 5: Comparison of specimens cut out from different orientations: 'S-L', 'S-T' and 'L-T'
a) MAT Results on 15KH2NMFA; b) MAT Results on 15KH2NMFA – enlarged
c) MAT Results on EUROFER'97; b) MAT Results on EUROFER'97 - enlarged

In conclusion, a new magnetic probe—the HC-13e—has been developed for the magnetic characterisation of radioactive materials intended for use in High-Contamination (HC) environments. The probe has demonstrated its ability to magnetically saturate the test specimens and to generate response signals of sufficient quality for analysis.

During the project, the original concept of replacing the VSM method with magnetic measurements had to be revisited several times because the dimensions of the available test samples—cut from already irradiated and mechanically tested specimens—changed repeatedly. The final measurement concept, therefore, relies on a combination of "absolute" and "relative" techniques, as the absolute approach alone proved unfeasible for the selected targets.

An additional advantage is that the HC-approved MAT method was chosen as the relative technique, offering exceptional sensitivity to subtle changes in magnetic properties. The MAT measurement results open further opportunities for monitoring material degradation, which may be highly relevant for upcoming Fusion projects.

An important advantage of the MAT configuration is that the response of the MAT probe consists of two components: the so-called linear part (Fig. 3b), originating from the air-coupled excitation and pick-up coils, and the non-linear part, arising from the magnetic behaviour of the inserted specimens. During reverse magnetisation, the linear time dependence of the excitation field—stemming from its constant rate of change—produces a constant offset in the signal, the sign of which depends on the magnetisation direction (Fig. 4a). This offset was determined through baseline analysis of the measured data (Fig. 3b) and found to be 2.237193×10^{-4} V for the HC-13e MAT probe. After subtracting this offset, the permeability curves can be integrated, allowing the corresponding B–H curve to be obtained.

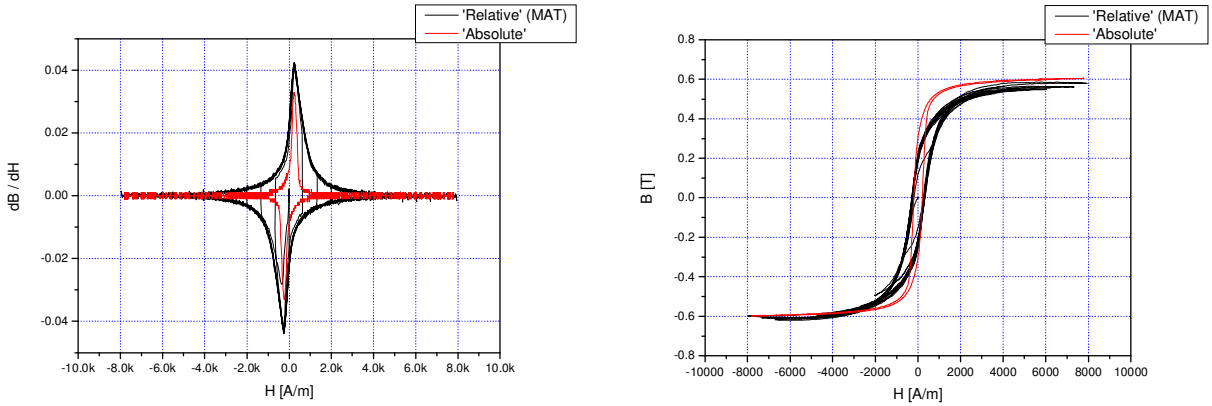


a) *b)* *c)*

Figure 6: Unscaled, pre-processed MAT results (i.e. resultant permeability loops) in the case of Nickel specimen a) Raw data; b) Offset-compensated raw data; c) Integrated offset-compensated raw data

The vertical (i.e., flux-density) scaling factor S_γ can be determined by fitting the magnetic saturation values obtained from the B–H curves (see Fig. 5c and Fig. 6c). This analysis yielded a value of S_γ = 9.549693.

However, a more reliable approach for determining the horizontal (i.e., excitation-field) scaling factor S_x of the MAT results is to align the permeability curves and compare the excitation-field values corresponding to the peak permeability (see Fig.7). This procedure produced a value of S_x = 2 450.2062.



a) *b)*

Figure 7: Comparison of the absolute measurement and the MAT results in the case of the nickel specimen a) comparison of permeability loops; b) comparison of the B–H curves

The remaining discrepancies between the absolute measurements and the MAT results can be attributed to the so-called demagnetisation factor (N). The magnetisation of the specimen generates an internal field that opposes the externally applied excitation, thereby reducing the effective internal magnetic field within the material. This relationship can be expressed as:

$$\mathbf{H}_{\text{internal}} = \mathbf{H}_{\text{applied}} - N\mathbf{M}$$

where $\mathbf{H}_{\text{internal}}$ is the resulting internal excitation field of the tested specimen, $\mathbf{H}_{\text{applied}}$ is the excitation field produced by the yoke, and $\mathbf{M}$ is the magnetisation of the specimen. The demagnetisation factor N can be determined by fitting the two corresponding magnetisation curves to one another.

MAT measurements were conducted on sectioned samples with dimensions of 10 × 5 × 1 mm, obtained from fractured test specimens irradiated at different temperatures. The resulting permeability curves are presented in Fig. 8. These initial measurement results do not indicate any significant shift in the excitation field at which the permeability reaches its maximum. This observation is consistent with the absence of significant changes in the chemical composition of the investigated materials.

However, variations observed in the maximum values of the permeability loops suggest the presence of magnetic coupling issues, most likely arising from imperfect mechanical contact or minor sample misalignment during measurement. Since the maximum relative magnetic permeability ($\mu_{r,max}$) and the coercive field (H_c [A/m]) are interrelated, such discrepancies warrant careful consideration. For most soft magnetic materials, the coercive field can be estimated from the magnetic exciting field corresponding to the maximum permeability, due to their reciprocal relationship—a correlation that has been well established in the literature. The underlying physical basis is that both magnetic properties are governed by the same mechanism, namely, the mobility of magnetic domain walls. Consequently, in the case of neutron-induced material degradation, a shift in the field position corresponding to the maximum permeability would also be expected.

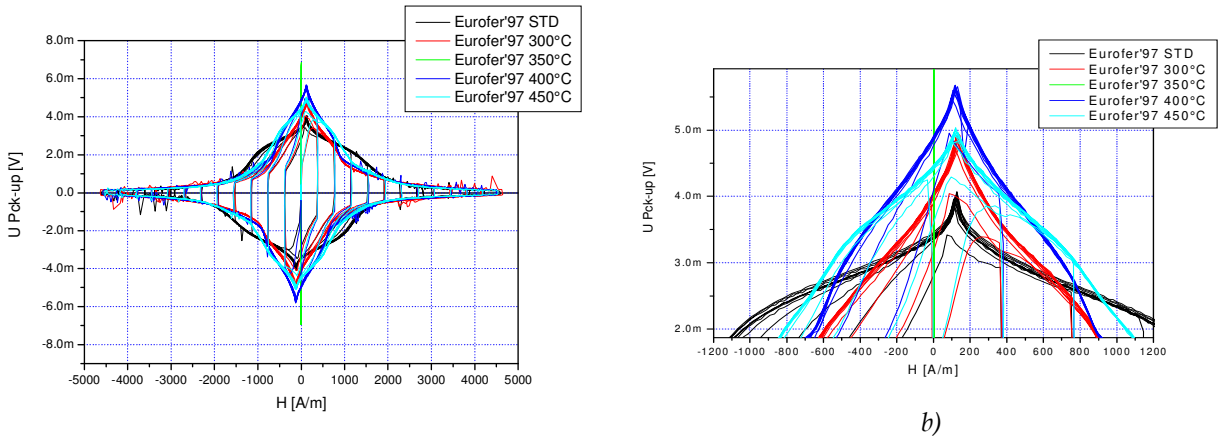


Figure 8: MAT results in the case of irradiated specimens
a) Comparison of resultant permeability loops; b) comparison of resultant permeability loops around their maximum

The newly developed HC-13e MAT probe has been demonstrated to be suitable for performing magnetic measurements on irradiated specimens in a hot-cell environment. It is capable of magnetically saturating EUROFER'97 test samples with dimensions of 10 × 5 × 1 mm and of acquiring permeability loops with an adequate signal-to-noise ratio. The first series of measurements on activated, irradiated samples has been successfully completed.

Remaining work

The work is planned to continue beyond the current project framework. The next phase will focus on reducing uncertainties associated with the magnetic coupling of the MAT probes and further refining the calibration of the MAT measurement system. Upon completion of these activities, the newly developed HC-13e probe, in combination with the MAT system, will be capable of determining the characteristic points of the B–H curve of irradiated materials with enhanced precision. This advancement will provide valuable input data for the design and optimisation of structural components intended for application in fusion reactors.

COMPARATIVE PETROLOGICAL, PETROPHYSICAL AND GEOCHEMICAL INVESTIGATIONS OF POLISHED STONE ARTEFACTS AND POTENTIAL SOURCE ROCKS FROM THE POINT OF PREHISTORIC RAW MATERIAL SELECTION STRATEGY

Zsolt Kasztovszky[1], Kata Furholt[2], Katalin Gméling[1], Annamária Kis[3], Zoltán Kovács[1], Attila Kreiter[4], Dóra Miklós[4], Bálint Péterdi[5], Tamás Sági[6,1], Ákos Török[3], Attila Virág[6]

1 – HUN-REN EK, 2 - Universität zu Kiel, 3 - BME Department of Engineering Geology and Geotechnics, 4 - HNM Archaeometry Laboratory, 5 - Supervisory Authority for Regulatory Affairs, 6 - ELTE Department of Petrology and Geochemistry

Objective

The main task in prehistoric stone tools research is provenance research, i.e. the identification of the sources of the raw materials of the objects. In the new project, we aim to find out which physical and fabric properties of rock types determine the quality and durability of prehistoric tools. It will provide archaeological insights into aspects of raw material selection, prehistoric community choices, socio-economic values and the know-how based on the rocks. Because of the similar geochemical properties of some rock types, the identification of source regions may be doubtful. The physical analysis of such rocks could provide a solution to this problem, which could be of great international interest. Applying statistical analysis to the measured data and to the shapes of the stone tools, we aim to model how the physico-chemical properties of the rocks predict the selection of raw materials and the way and duration of the use of the tools.

Methods

The applied analytical methods on archaeological objects and geological reference samples are field petrology, petrography based on macroscopic investigations, polarising microscopy and Scanning Electron Microscopy with Energy Dispersive X-Ray microanalysis (SEM-EDX) analyses in HUN-REN EK and in ELTE; Prompt-Gamma Activation Analysis (PGAA) and Neutron Activation Analysis (NAA) in HUN-REN EK on selected sub-samples.

Results

In the first project year, we had the following achievements: We reviewed the existing databases of previous polished stone tools research projects. Based on existing databases, we selected the archaeologically most relevant rock types (dolerite, contact metabasite, hornfels, basalt, metadolerite, 'white stone', andesite, limestone, sandstone, serpentinite) and archaeological collections for analytical studies.

First field trips were organised to collect reference raw materials:

1/1. Czechia (Hrubšice, Braszowice, Želešice, Velké Hamry, Jistebsko, Železný Brod): serpentinite, greenschist, amphibolite and contact metabasites; Poland (Szklary, Jordanów, Nasławice, Tapadla Pass): serpentinite, nephrite, metagabbro; Slovakia (Pernek-Pezinok region): greenschist, contact metabasite, metadolerite, metagabbro.

1/2. Slovakia (Central Slovakian Volcanic Field: Brehy, Putikov vŕšok): basalt, basanite.

1/3. Mecsek, Hungary: alkaline basalt, gabbro, microgabbro.

First geochemical studies were done to check the compositions of the freshly collected reference raw materials (PGAA, NAA, SEM EDX). First steps were made to design and implement a series of non-destructive mechanical test measurements on selected representative archaeological samples from the Carpathian Basin (based on previous archaeometry studies). Destructive and non-destructive petrophysical analyses of some geological samples were done from the first collecting campaign.

Remaining work

In the following project years, we will continue the research according to the original plan. This work is an integral part of the No. 132 HUN-REN project "Chemical and physical macrostructure and composition of materials".

Related publications

[1] V. Szilágyi, et al.: *'Whitestone' - A Specific Polished Stone Tool Raw Material in the Late Neolithic of Southern Hungary,* Heritage **8:(3),** 112 (2025) https://doi.org/10.3390/heritage8030112

[2] Kasztovszky Zs.: *Csiszolt kőeszköz és szerszámkő nyersanyagok nagyműszeres vizsgálata a Kárpát-medence és környezete őskori távolsági és regionális kereskedelmi hálózatainak feltérképezéséhez (Large-scale instrumental examination of polished stone tools and tool stone raw materials for mapping prehistoric long-distance and regional trade networks in the Carpathian Basin and its surroundings)* (NKFI K 131814). Magyar Régészeti és Művészettörténeti Társulat (Hungarian Archaeological and Art History Society): Tudományos régészeti és művészettörténeti kutatási projektek bemutatója (Presentation of scientific

archaeological and art historical research projects) VII/2. 17 February 2025, Magyar Nemzeti Múzeum (Hungarian National Museum), Budapest

[3] V. Szilágyi, Z. Kovács, P. Kónya: *Characterization of medium-temperature fired iron-free clays based on microtexture and mineralogical composition,* 15th Assembly of Petrology and Geochemistry, Nagybörzsöny – Banská Štiavnica, 2-4 October 2025

[4] V. Szilágyi, K. Furholt, Z. Kovács, Zs. Kasztovszky, A. Füzesi, P. Raczky, M. Biró, Zs. Farkas, T. Sági, S. Józsa, Gy. Szakmány: *Polished stone tool assemblage of Late Neolithic Öcsöd-Kováshalom site,* 15th Assembly of Petrology and Geochemistry, Nagybörzsöny – Banská Štiavnica, 2-4 October 2025

[5] V. Szilágyi, K. Furholt, Z. Kovács, Zs. Kasztovszky, A. Füzesi, P. Raczky, M. Biró, Zs. Farkas, T. Sági, S. Józsa, Gy. Szakmány: *Polished stone tool assemblage of Late Neolithic Öcsöd-Kováshalom site.* 15. Kőkor Kerekasztal (15. Stone Age Round Table), Eger, 5 December 2025

[6] Szilágyi, V., Furholt, K., Kovács, Z., Kasztovszky, Zs. Biró M., Farkas, Zs., Sági, T., Józsa, S., Szakmány, Gy.: *Csiszolt kőeszköz nyersanyag típusok Öcsöd-Kováshalom neolitikus lelőhely leletanyagából. (Polished stone tool raw material types from the finds of the Öcsöd-Kováshalom Neolithic site.),* MRMT Jubileumi előadónap (MRMT Anniversary Lecture Day) — Fókuszban Öcsöd-Kováshalom - bemutatkozik az Archeometriai Műhely szakosztály), — (Focus on Öcsöd-Kováshalom - the Archeometric Workshop department presents), Budapest, 9 December 2025

GRANUM REMODELLING DURING DROUGHT AND RECOVERY IN CTENANTHE SETOSA

Renáta Ünnep, Gergely Nagy[*], Richard Hembrom[**], Éva Sárvári[***] and Katalin Solymosi[**]

[*]Neutron Scattering Division, Oak Ridge National Laboratory, Oak Ridge, Tennessee, USA
[**]Department of Plant Anatomy, Institute of Biology, Faculty of Science, ELTE Eötvös Loránd University, Budapest, Hungary
[***]Department of Plant Physiology and Molecular Plant Biology, Institute of Biology, Faculty of Science, ELTE Eötvös Loránd University, Budapest, Hungary

Objective

Our goal was to understand how photosynthetic organisms adapt to drought stress, with special focus on the exceptional tolerance of *Ctenanthe setosa*. We investigated how this plant can maintain the structure and function of its photosynthetic membranes during prolonged periods without water. We also aimed to follow these ultrastructural changes in living plants in real time by using a non-invasive method during drought and rewatering. Our results may help future breeding of more drought-tolerant crops and support global food security.

Methods

We studied drought-induced structural changes in living *Ctenanthe setosa* plants by monitoring intact potted specimens during water withdrawal and subsequent rewatering. The main measurements were performed using Small-Angle Neutron Scattering (SANS), first at the Yellow Submarine instrument of the HUN-REN Centre for Energy Research in Budapest and later at the EQ-SANS instrument of the Spallation Neutron Source at the Oak Ridge National Laboratory. This non-invasive method allowed us to follow nanoscale changes in the photosynthetic membranes repeatedly on the same leaves without disturbing their natural water content. Plants were exposed to prolonged drought for up to 45 days, followed by rehydration, while structural changes were recorded at different time points. To validate and complement the neutron data, we also used transmission electron microscopy. Further physiological and biochemical measurements were also carried out at the Eötvös Loránd University using chlorophyll fluorescence analysis, 77 K fluorescence spectroscopy, pigment determination, gel electrophoresis of thylakoid membranes, and light microscopy. The combination of these methods provided both *in vivo* dynamic structural and functional information during stress and recovery.

Results

Drought stress induced only minor structural changes in the photosynthetic membranes of *Ctenanthe setosa*, demonstrating the high stability of the chloroplast system under prolonged water deficiency. *In vivo* SANS measurements showed that the granum Repeat Distance (RD) of the periodically organised stacked thylakoid membranes decreased only slightly during the drought period. Even after 40–45 days without watering, the reduction in RD was approximately 1 nm (from an initial RD of about 2 nm), indicating that the membrane system remained largely intact. The results suggest that *Ctenanthe setosa* can preserve the ultrastructure of its thylakoid membranes during extended drought.

One of the most important findings of the study was the rapid structural recovery detected after rewatering. SANS measurements revealed that the granum RD showed substantial recovery within 18 hours after rewatering. In contrast, physiological and biochemical recovery processes were considerably slower. Photosynthetic performance and pigment-related parameters required a longer recovery period, reaching near-normal levels only after approximately three weeks. Therefore, restoration of membrane ultrastructure preceded full functional recovery.

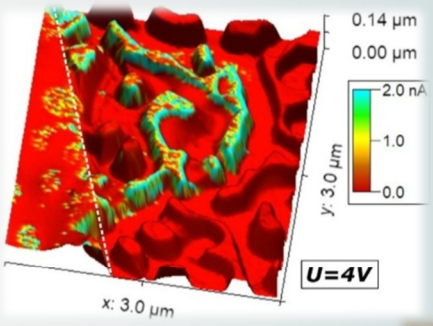
The non-destructive nature of SANS made it possible to repeatedly measure the same intact leaves throughout drought stress and recovery, which cannot be achieved by conventional invasive ultrastructural measurement techniques. This continuous monitoring provided unique time-resolved insight into membrane structural dynamics in vivo. Complementary microscopy supported the neutron results and showed only small anatomical changes, including reduced leaf thickness and chloroplast size under drought.

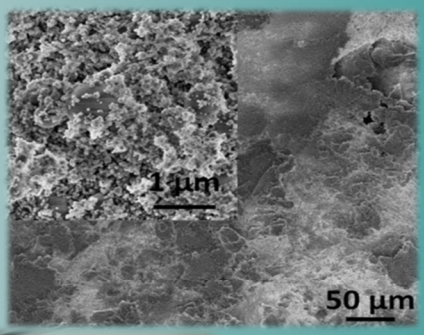
Remaining work

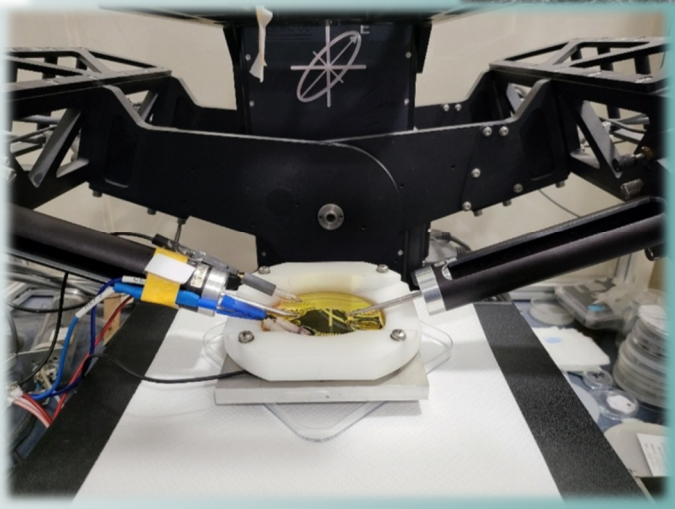
This project has been completed.

Related publication

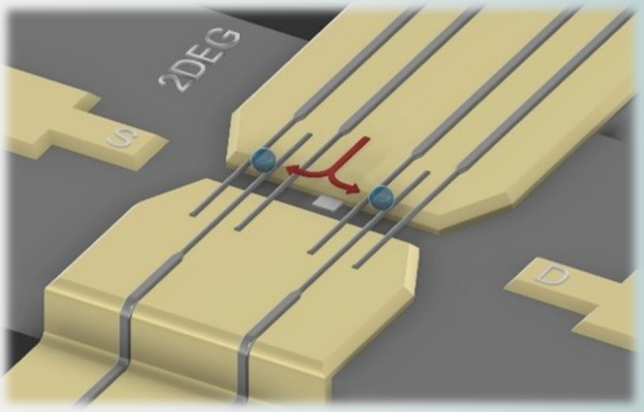
[1] R. Hembrom, R. Ünnep, É. Sárvári, G. Nagy, K. Solymosi: *Dynamic in vivo monitoring of granum structural changes of Ctenanthe setosa (Roscoe) Eichler during drought stress and subsequent recovery*. Physiol Plant. **177**, 1 (2025) https://doi.org/10.1111/ppl.14621

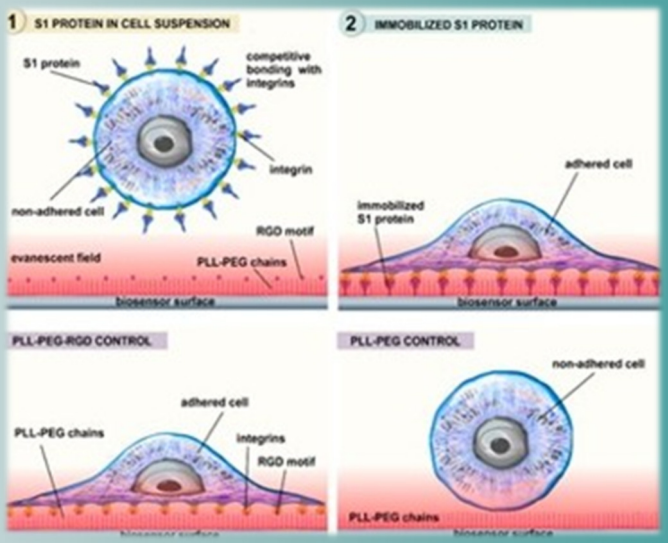


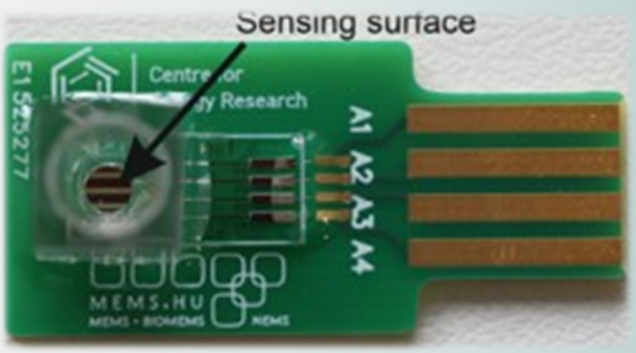




VI. RESEARCH AND DEVELOPMENT IN INSTITUTE OF TECHNICAL PHYSICS AND MATERIAL SCIENCES







IMPACT OF AMBIENT MOLECULAR CONTAMINATION ON SCANNING TUNNELLING MICROSCOPY MEASUREMENTS OF VAN DER WAALS MATERIALS

TKP2021-NKTA-05, Élvonal KKP 138144, Lendület LP2024-17, OTKA K 146156, EXCELLENCE 151372, 2022-1.2.5-TÉT-IPARI-KR-2022-00006

G. Kálvin, P. Vancsó, M. Szendrő, K. Kandrai, A. Pálinkás, L. Tapasztó, and P. Nemes-Incze

For more than a decade, the presence or absence of the phonon-induced gap in scanning tunnelling microscopy of graphene and graphite has remained an unresolved inconsistency in the literature. While some STM experiments reproducibly revealed a pronounced suppression of tunnelling conductance around the Fermi level, others, performed under nominally similar conditions, failed to detect this hallmark feature. Here, we identify and resolve the physical origin of this discrepancy by demonstrating that ambient molecular contamination [1] is the decisive factor governing the visibility of the phonon gap in STM measurements [2]. We show that exposure of graphite surfaces to ambient conditions leads to the formation of a self-assembled monolayer of normal alkanes, which profoundly modifies the tunnelling junction. The presence of this alkane overlayer manifests itself experimentally in several ways. Atomic-resolution STM images acquired on contaminated surfaces exhibit enhanced noise and reduced contrast compared to ultrahigh-vacuum-cleaved samples.

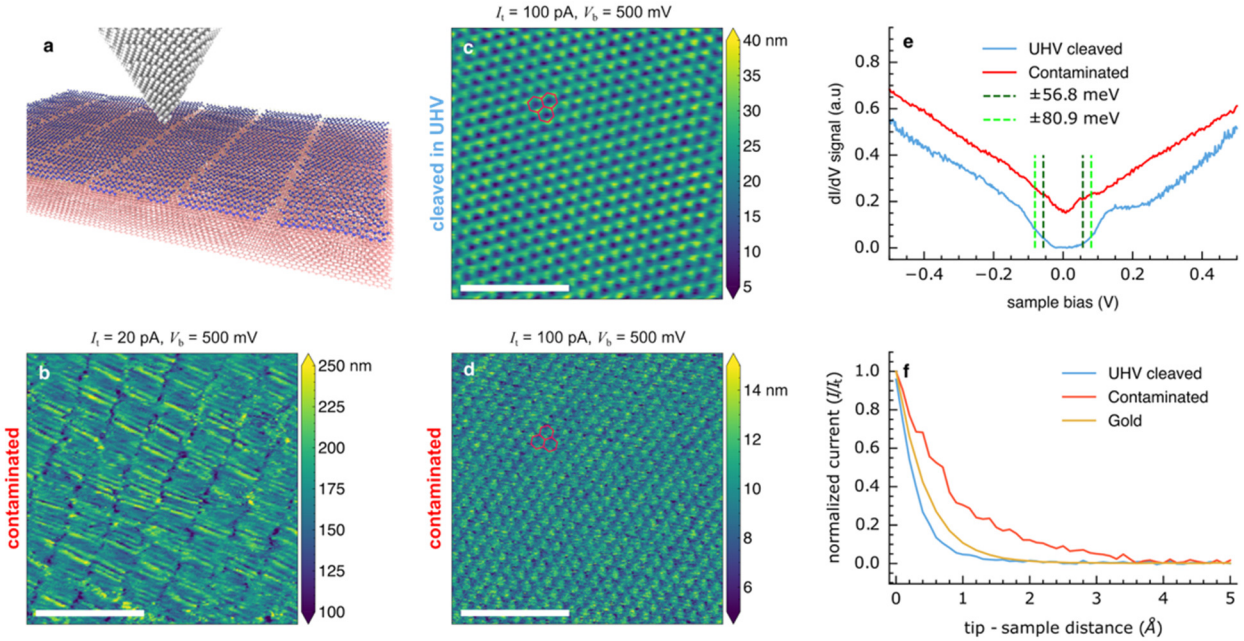


Figure 1: (a) Schematic image of the n-alkane self-assembled monolayer stemming from ambient air contamination. When measuring the surface by scanning tunnelling microscopy (STM), the tip can either scan above the layer or penetrate it. (b) STM image at the largest tip – sample separation showing the structure of the alkane overlayer. (c-d) Atomic resolution images of the contaminated surface (penetrating the alkane layer) show consistently larger current noise. (e) Comparison of the contaminated and clear graphite surface tunnelling conductance. The clean surface displays a clear phonon gap. (f) Examples of I(z) curves on clean, contaminated graphite and gold samples, by measuring the tunnelling current as the tip is retracted. The contaminated samples systematically show an anomalously low decay rate of the tunnelling current.

Current–distance I(z) curves reveal an anomalously slow decay of the tunnelling current, with decay constants reduced by factors of 1.5–5 relative to clean surfaces. Crucially, the same samples systematically lack the phonon-induced gap in their dI/dV spectra. These three observations - image noise, anomalous I(z) decay, and phonon-gap suppression - occur together and provide mutually consistent signatures of alkane contamination in the tunnelling junction [2] (see Figure 1).

We demonstrate that the underlying mechanism is the appearance of an additional current pathway mediated by the alkane molecules. Although normal alkanes are wide-gap insulators, their conductance in a nanoscale junction is comparable to typical STM tunnelling conductances. When the STM tip penetrates the molecular layer, one or more alkane chains can transiently bridge the tip and the graphite surface, forming a parallel transport channel analogous to a molecular break-junction configuration. As the tip is retracted, this molecular channel persists over several ångströms, producing a finite current even at tip-sample separations where pure vacuum tunnelling would have already vanished. This break-junction-like transport channel both enhances current fluctuations and introduces an additional elastic tunnelling contribution that fills in the phonon gap in the measured spectra.

Our first-principles calculations show that the presence of an alkane overlayer can modify the intrinsic decay of graphite electronic wave functions into the vacuum, reducing the decay constant relative to the clean surface. In principle, this altered decay could be detected experimentally as a change in κ. In practice, however, the measurement of the intrinsic wave-function decay is overwhelmed by the dominance of the molecular transport channel. The current measured in I(z) spectroscopy above contaminated surfaces is no longer governed solely by vacuum tunnelling, but is dominated by alkane-mediated conduction, masking the genuine electronic decay of the graphite surface states. As a result, the experimentally extracted decay constants do not reflect the true wave-function attenuation but rather the effective transport properties of a mixed tunnelling–molecular junction.

By establishing a direct and quantitative link between ambient alkane contamination, anomalous I(z) behaviour, and phonon-gap suppression, our results resolve a long-standing experimental ambiguity in STM studies of layered carbon systems.

Related publications

[1] A. Pálinkás, G. Kálvin, P. Vancsó, et al.: *The composition and structure of the ubiquitous hydrocarbon contamination on van der Waals materials*, Nat Commun **13,** 6770 (2022) https://doi.org/10.1038/s41467-022-34641-7

[2] G. Kalvin, P. Vancsó, M. Szendrő, K. Kandrai, A. Pálinkás, L. Tapasztó, P. Nemes-Incze: *Impact of ambient molecular contamination on scanning tunneling microscopy and spectroscopy of layered materials,* Physical Review B **113:(3),** 035428 (2026) https://doi.org/10.1103/f1vp-mlpw

STABILISATION OF ULTRA-SMALL MAGIC ANGLE GRAPHENE SUPERLATTICES BY MOLECULAR INTERCALATION

Élvonal KKP 138144, 2022-1.2.5-TÉT-IPARI-KR-2022-00006

G. Dobrik, P. Kun, M. Szendrő, P. Vancsó, P. Nemes-Incze, L. Tapasztó

The correlated electronic states emerging in Twisted Bilayer Graphene (TBG) at the first magic angle of 1.1° have been intensely investigated. This system offers particularly attractive features for studying strong correlations, since the electronic states are fully exposed and the charge carrier density can be electrostatically tuned, enabling rapid mapping of correlated phase diagrams.

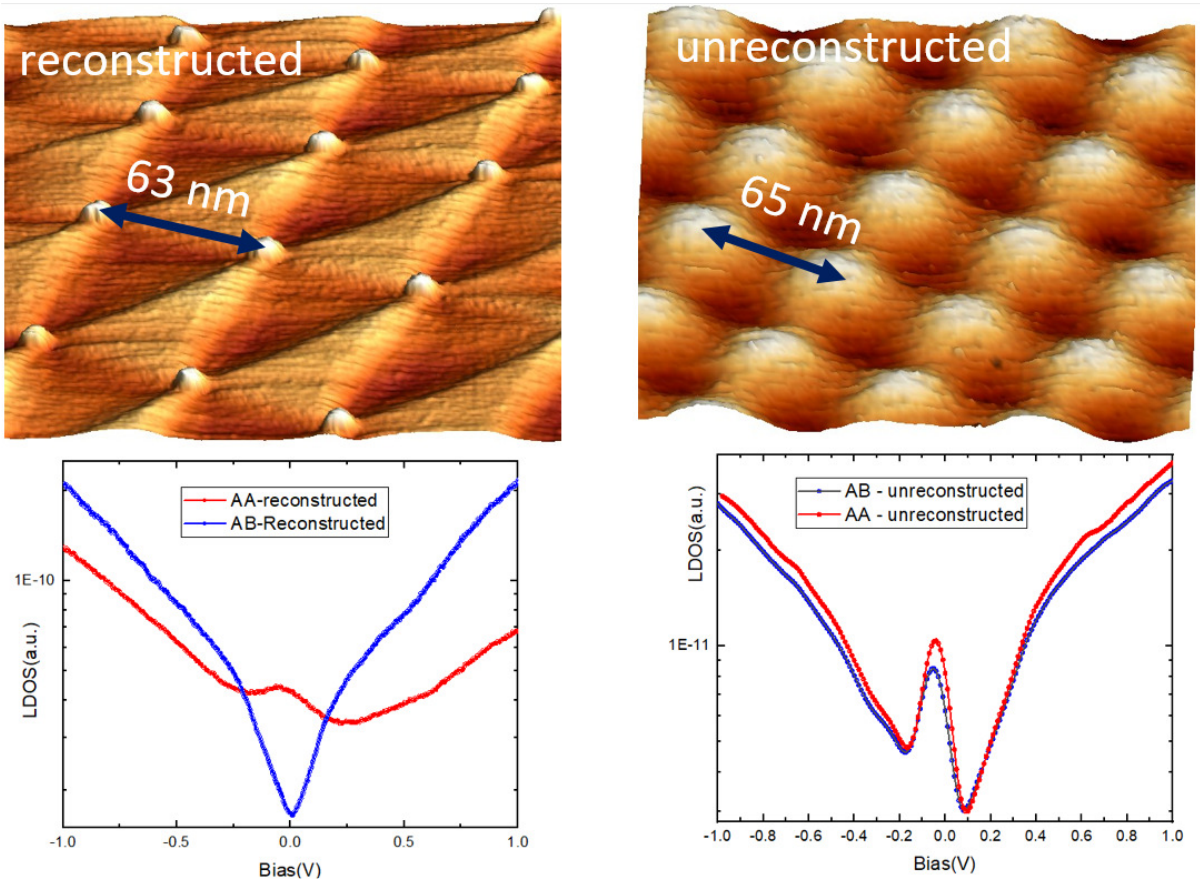


Figure 1: Topographic STM images of a) a reconstructed TBG superlattice of ~65 nm periodicity, corresponding to a twist angle of ~0.21º, fabricated by the conventional tear-and-stack method, and b) an unreconstructed giant (65 nm) TBG superlattice formed through the graphene auto-kirigami process. Tunnelling spectra recorded on the bright (AA) and dark (AB/BA) regions of the reconstructed (c), and unreconstructed (d) 0.21º MATBG superlattices, the latter displaying sharper (FWHM ~ 90 meV) LDOS peak near the Fermi level on both AA and AB/BA regions, while a less intense and much broader (FWHM ~ 180 meV) peak is observed only in the AA regions of the reconstructed superlattice.

The remarkable success of the Bistritzer–MacDonald continuum theory further predicts a hierarchy of smaller magic angles - near 0.5°, 0.4°, 0.24°, 0.21°, and beyond - which, however, have remained purely theoretical. Experimental studies revealed that moiré superlattices with twist angles below 1° become very fragile as the stacking configuration approaches the naturally favoured AB alignment (0° twist), where large regions can be driven into perfect registry by minimal local lattice distortions. These reconstructions substantially broaden the flat bands, suppressing the correlation physics characteristic of dispersionless states. Consequently, magic-angle superlattices of $\theta \leq 0.5°$ have long been considered too fragile - structurally and electronically - to be realised experimentally, despite the tantalising prospect that accessing smaller magic angles, with progressively stronger correlations, could unlock a series of novel quantum phases.

Marginally twisted intercalated bilayer graphene samples have been prepared employing the graphene auto-kirigami process, combined with the deposition of a highly ordered alkane molecular layer on top of graphene. STM images have been acquired under UHV conditions at room temperature, revealing a graphene superlattice with a large periodicity of about 65 nm, corresponding to a twist angle of about 0.21^0, closely matching the 5th predicted magic angle. In spite of the huge moiré unit cell (ultra-small twist angle), the intercalated superlattice displays extended bright (AA) regions at various bias voltages

(Figure 1.b). For comparison, the STM images of non-intercalated TBG samples with a similar (~ 0.21°) twist angle, fabricated by the conventional tear-and-stack method, display the widely reported, strongly reconstructed moiré superlattice, with point-like AA regions (bright dots in Figure 1.a). According to detailed simulations, the molecular spacer layer intercalated between the graphene sheets suppresses structural reconstructions while preserving sufficient interlayer tunnelling for flat-band formation, in excellent agreement with our measurements. Remarkably, intercalation also delocalizes the flat-band wavefunctions across the whole moiré superlattice. This effect can be attributed to the shallowing of the moiré potential by intercalation, as well as the presence of disorder, which remarkably promotes the delocalisation of the flat-band wave functions, as predicted theoretically.

A major practical limitation of fabricating intercalated MATBG with the above-discussed graphene auto-kirigami process is that the twist angle cannot be precisely controlled. Since the driving force of the auto-kirigami process is the van der Waals interaction, the twist angle is generally expected to be near 180° (0°), but the small deviations from 0 degree cannot be reliably controlled. Therefore, it is important to develop fabrication methods for intercalated graphene bilayers with more control over the twist angle, such as the widely used tear-and-stack method. The problem with the conventional tear-and-stack approach is that the forces exerted during the process are relatively high, squeezing the intercalant molecular layer into bubbles and reestablishing the conventional interlayer distance. By proceeding as gently as possible with this method, we were able to partially preserve the intercalated superlattices as shown in Figure 2.

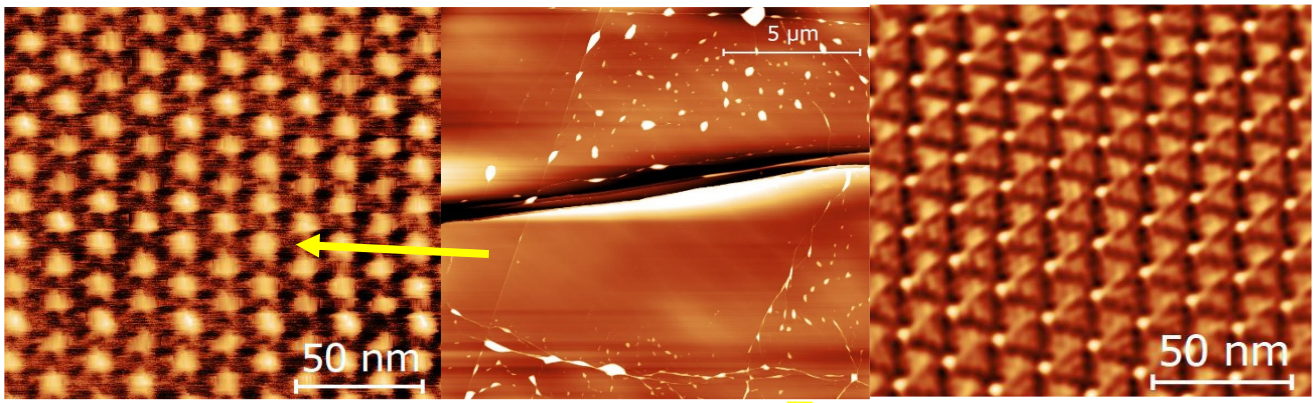


Figure 2: Centre panel shows the AFM topography of a 0.7° twisted bilayer graphene sample prepared by the tear-and-stack method with alkane intercalant layer, displaying a large (5x5 µm²) bubble-free area near the centre of the image, next to areas showing the presence of bubbles. Conductive AFM images of the areas with bubbles (right) display a reconstructed superlattice of 20 nm periodicity. By contrast, the bubble-free area preserving the alkane intercalant layer displays an unreconstructed 20 nm superlattice (left). We have also found that intercalated TBG superlattices are not only free of structural reconstructions but are also characterised by reduced twist-angle inhomogeneity, enabling the fabrication of uniform moiré superlattices on device scale, a critical step toward reproducible twistronic devices.

DIRECTIONAL REFLECTION ASYMMETRY IN HEXAGONAL AND RHOMBOHEDRAL GRAPHITE NANORIBBONS

TKP2021-NKTA-05, Élvonal KKP 138144, Lendület LP2024-17, OTKA K 146156, EXCELLENCE 151372, 2022-1.2.5-TÉT-IPARI-KR-2022-00006

K. Kandrai, A. Balogh (ELTE), G. Márk, D. Varga, Márton Szendrő, Z. Tajkov, K. Márity, P. Vancsó, L. Tapasztó, and P. Nemes-Incze

In a simple one-band medium, scattering from a defect obeys the principle of reciprocity: exchanging the source and detector yields the same response at the detector. However, if multiple bands are available, even with time-reversal symmetry and elastic scattering, this reciprocity can break, resulting in asymmetric reflection. Such non-reciprocal scattering has been demonstrated in photonic and phononic systems by introducing structural mirror asymmetry and employing mode-selective excitation. Here we demonstrate analogous behaviour in a condensed matter system of a Rhombohedral-Hexagonal Graphite (RG–HG) junction separated by a domain soliton (see Figure 1.a) in a scanning tunnelling microscopy experiment. In our experimental setup, purely intravalley elastic scattering from the domain soliton leads to reflection asymmetry. As shown in Figure 1. d-i, the local tunnelling conductance exhibits standing-wave modulation from intravalley scattering only within the hexagonal region, while the rhombohedral domains remain featureless, indicating absence of backscattering.

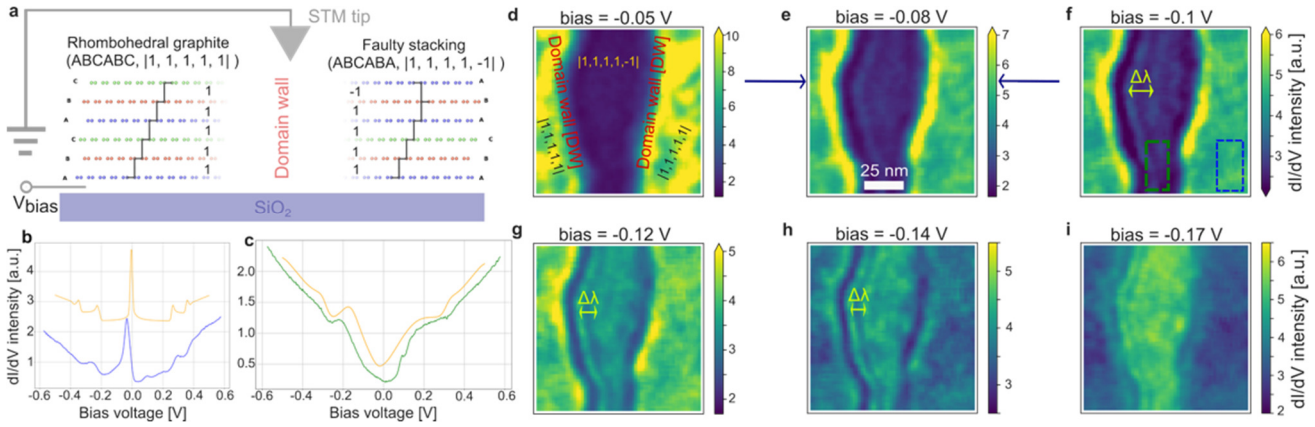


Figure 1: (a) Schematic illustration of the STM measurement on RG – hexagonal junctions. The hexagonal side of the sample is a 6-layer RG, with a hexagonal stacking fault at the top, denoted by the "-1" layer orientation of the top layer. (b, c) Measured and calculated LDOS of the RG and hexagonal side of the sample. The sample features hexagonal nanoribbon regions of a few 10 nm widths. One example is shown in panels (d - i), where we show the tunnelling conductance of the same area at various sample bias voltages. Ripples in the local tunnelling conductance can be observed in the hexagonal region bordered by two domain walls. The tunnelling conductance is a measure of the Local Density of States (LDOS) at the surface. The LDOS ripples shown by Δλ are only present in the middle hexagonal region.

Tight-binding calculations reproduce the intravalley interference patterns observed experimentally, supporting our interpretation (Figure 2.b). The observed reflection asymmetry originates from mode selection: the STM tip predominantly probes electronic states on the top surface, effectively isolating the top Dirac band in the hexagonal region and the top layer of the rhombohedral stack. Wave packet dynamics calculations confirm that this layer-specific probing, combined with the intrinsic layer polarisation of the wavefunctions, gives rise to strong anisotropic scattering. Within the energy window corresponding to the RG band gap, the wave packet simulations show that the scattering amplitude from ABC to ABA exceeds that in the reverse direction by up to a factor of five.

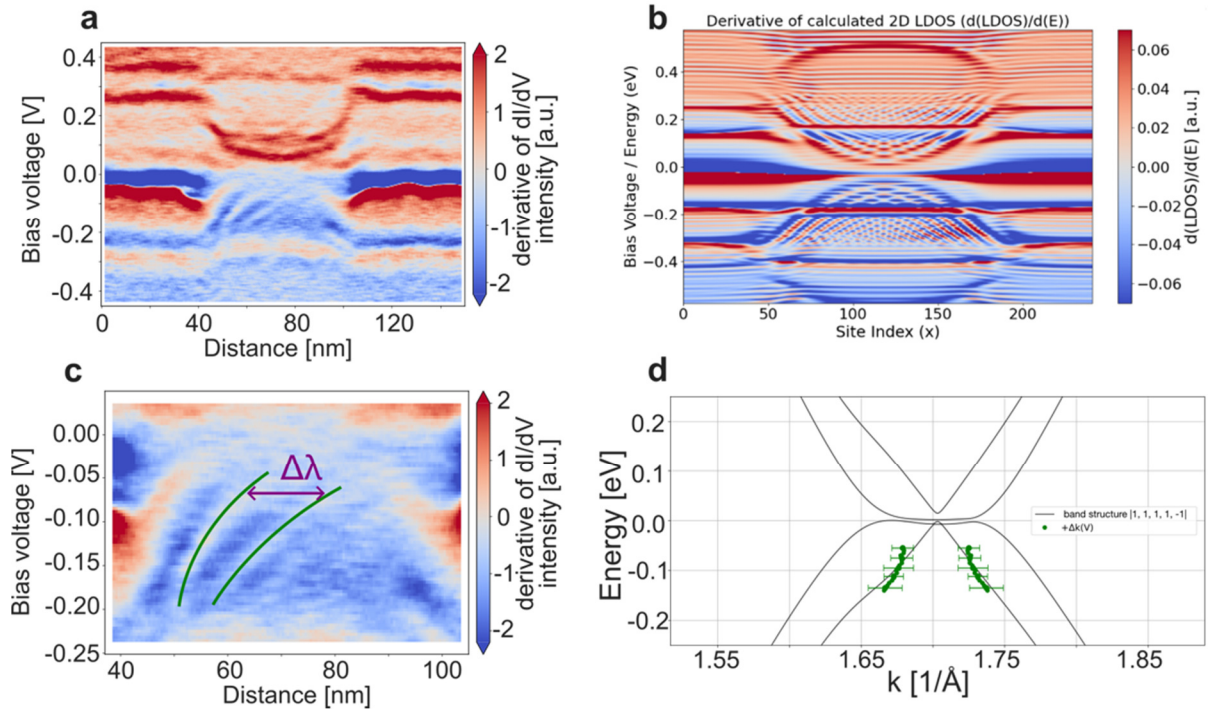


Figure 2: (a) dI/dV measurement across a RG – hexagonal – RG nanoribbon. The tunnelling conductance (dI/dV) is numerically differentiated along the bias voltage coordinate for better visibility of the intravalley scattering pattern. (b) Calculated LDOS of the top surface of the same nanoribbon geometry as in the measurement in (a). (c) Zoom into the dI/dV spectra in panel (b), highlighting the interference pattern arising in the hexagonal part of the sample. The scattering wavelength (Δλ) can be measured as the distance between peaks of the dI/dV signal across the sample surface. (d) From the bias voltage dependent Δλ values, we can obtain the scattering wave vector (Δk), which we overlay onto the surface Dirac band of the hexagonal |1, 1, 1, 1, -1| structure.

We demonstrated unidirectional scattering in RG – HG junctions, where the mode selection occurs due to the STM tip probing only the top surface of the material. Such tailored charge injection is in principle feasible with van der Waals material contacts, allowing for unidirectional electron wave steering capabilities for electron optics in a simple condensed matter system.

BIAS-FREE GENERATION OF SOLAR HYDROGEN AND HIGH-VALUE GLYCEROL OXIDATION PRODUCTS BY LOW-BANDGAP PEROVSKITE PHOTOELECTRODES

HORIZON-MSCA-2022-PF-01 101103762 SOLARHYVALUE, MTA NKM2025-4/2025, Élvonal KKP 138144

M. Daboczi, W.-J. Qiu, A. Koós, S. Keszei, L. Lutter, T. Ollár, J. S. Pap, C.-T. Lin, L. Tapasztó

Photoelectrochemical (PEC) water splitting by inexpensive photoelectrodes is a promising way of green hydrogen generation, which could become economically competitive if the reduction reaction of hydrogen evolution is coupled with the oxidation of biomass waste into high-value chemicals. Perovskite photoelectrodes have great potential in revolutionising this field; however, their application is currently limited by their instability in aqueous environments and the use of typically large amounts of expensive precious metal catalysts, such as Pt.

This year, we have grown molybdenum disulfide (MoS_2) on graphite sheets with thicknesses of 70 µm (G7) and 150 µm (G15) that are three orders of magnitude less expensive than the typically used Highly Oriented Pyrolytic Graphite (HOPG). Raman spectroscopy confirmed the presence of MoS_2 as well as its multilayer (> 5) structure (Figure 10). The G15/MoS_2 samples were applied as substrates for electrochemically depositing two atomic layers thick Pt (2L-Pt). These samples, despite their ultralow Pt loading, exhibited catalytic activity for the hydrogen evolution reaction in alkaline conditions comparable to that of commercial Pt/C deposited on G15 (Figure 1).

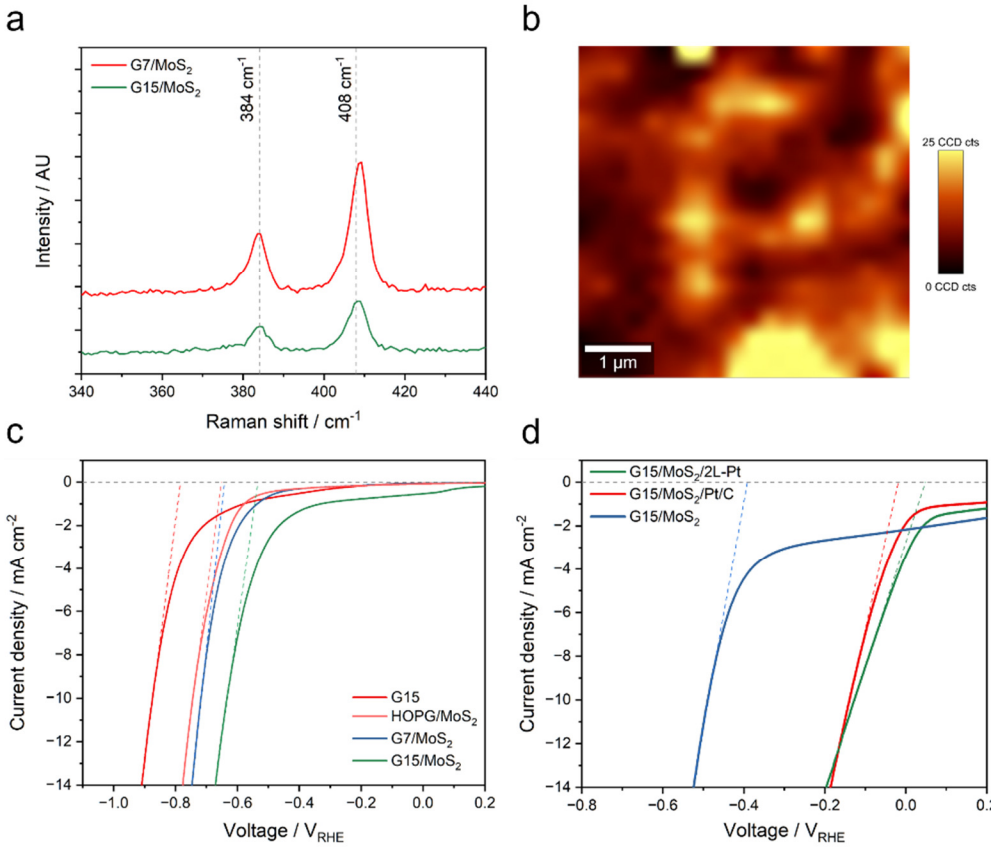


Figure 1: (a) Raman spectra of MoS_2 grown by Chemical Vapour Deposition (CVD) on G7 and G15 graphite layers. (b) Mapping of Raman peak intensity at 408 cm^{-1} for the G15/MoS_2 sample. (c) Current density–voltage scans of MoS_2 grown on different graphite substrates, recorded in an electrochemical cell in aqueous 0.5 M H_2SO_4 electrolyte. (d) Current density–voltage scans of G15/MoS_2 samples loaded with commercial Pt/C and an ultralow amount of electrodeposited Pt (2L-Pt), recorded in aqueous 1 M NaOH electrolyte.

The developed G15/MoS_2/2L-Pt catalytic sheet was integrated with a p–i–n type tin-lead perovskite photovoltaic device (bandgap of ~1.3 eV) by spraying a non-continuous adhesive layer at the back of the graphite sheet, followed by manual placement onto the top metal electrode of the solar cell to form an Ohmic contact. The photocathodes were prepared with different device designs, in which the active area was reduced to minimise losses due to low shunt resistance (Figure 2). The

shunt resistance (defined here as the resistance between the top and bottom contact layers) was observed more often to drop after applying the graphite sheet in devices with larger active areas, highlighting both the importance and challenge of forming a uniform, pinhole-free photoactive layer. The champion devices reached a stable photocurrent density of ~30 mA cm^{-2} under 1 sun illumination and a photocurrent onset potential as high as +0.8 V versus Reversible Hydrogen Electrode (VRHE) in a three-electrode Photoelectrochemical (PEC) setup.

The high fill factor and sufficient photovoltage of the photocathodes allowed for achieving a photocurrent density of ~30 mA cm^{-2} even without any external bias, in a two-electrode PEC setup (Figure 2). During this bias-free operation, solar hydrogen was generated at the surface of the photocathode, while glycerol was oxidised into high-value chemicals on the anode.

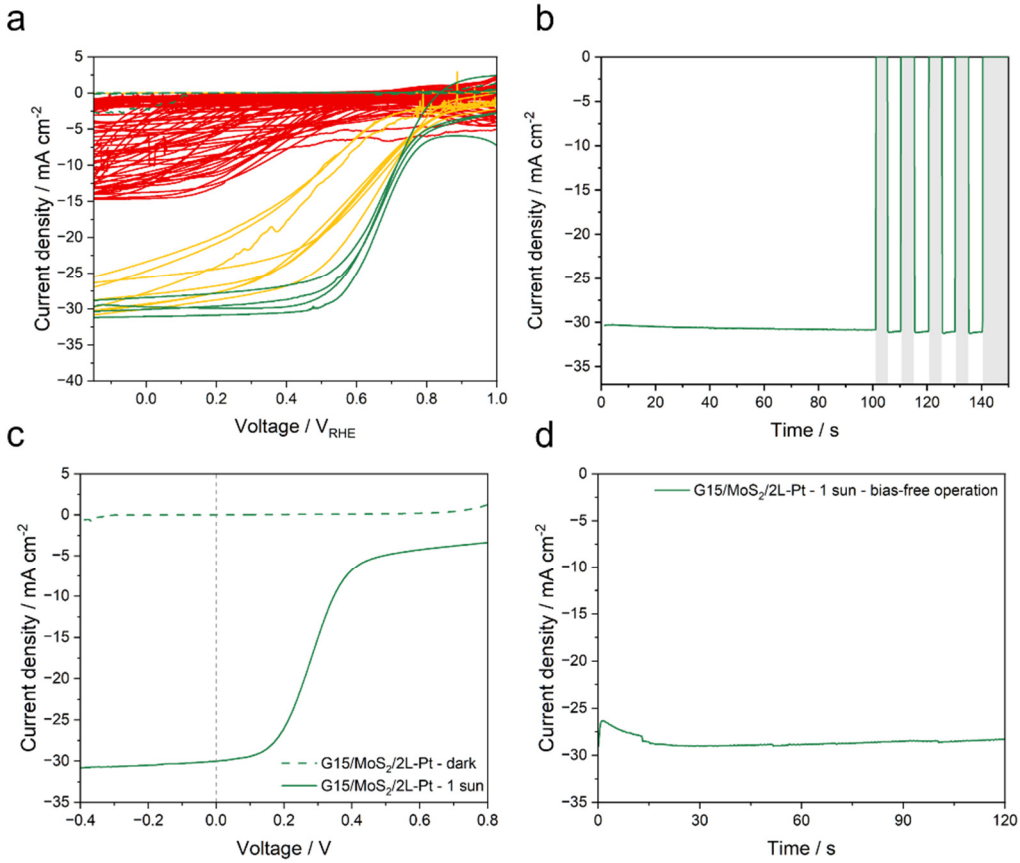


Figure 2: (a) Current density–voltage scans recorded in a three-electrode PEC setup for perovskite photocathodes with device design changing from larger (red) towards optimised, smaller active area (yellow and green). (b) Chronoamperometric measurement of a perovskite photocathode at 0 V_{RHE} applied. Shaded areas indicate switching off illumination. (c) Current density–voltage scans recorded in two-electrode PEC setup for a perovskite photocathode. (d) Bias-free operation of the perovskite photocathode for simultaneous hydrogen evolution and glycerol oxidation. All measurements were performed in the dark (dashed lines) or under 1 sun illumination (solid lines) in aqueous 2 M NaOH electrolyte containing 20 wt% glycerol.

Related publication

[1] A. Pálinkás, *et al.: Identification of graphite with perfect rhombohedral stacking by electronic Raman scattering*, Carbon **230**, 119608 (2024) https://doi.org/10.1016/j.carbon.2024.119608

STRAIN-INDUCED MODULATION OF THE LOCAL CONDUCTANCE IN MoS_2 LAYERS ON GOLD NANOPARTICLES

OTKA K 134258

M. Daboczi, W.-J. Qiu, A. Koos, S. Keszei, L. Lutter, T. Ollar, J. S. Pap, C.-T. Lin, L. Tapaszto

This study investigates the strain modulation of local conductance in MoS_2 layers induced by underlying Au NPs. By exfoliating MoS_2 onto thin gold films and subsequently annealing, we create strained mono- and multilayer MoS_2 structures. This process transforms the gold film into nanoparticles. To investigate the effect of strain on the local conductance of the MoS_2 monolayers, we performed Tunnelling Atomic Force Microscopy (TUNA) measurements. The topography of the study area is shown in Figure 1.a. Here, the larger part of the image shows gold nanostructures covered with monolayer MoS_2, except for the left edge of the image, which shows a few-layer MoS_2.

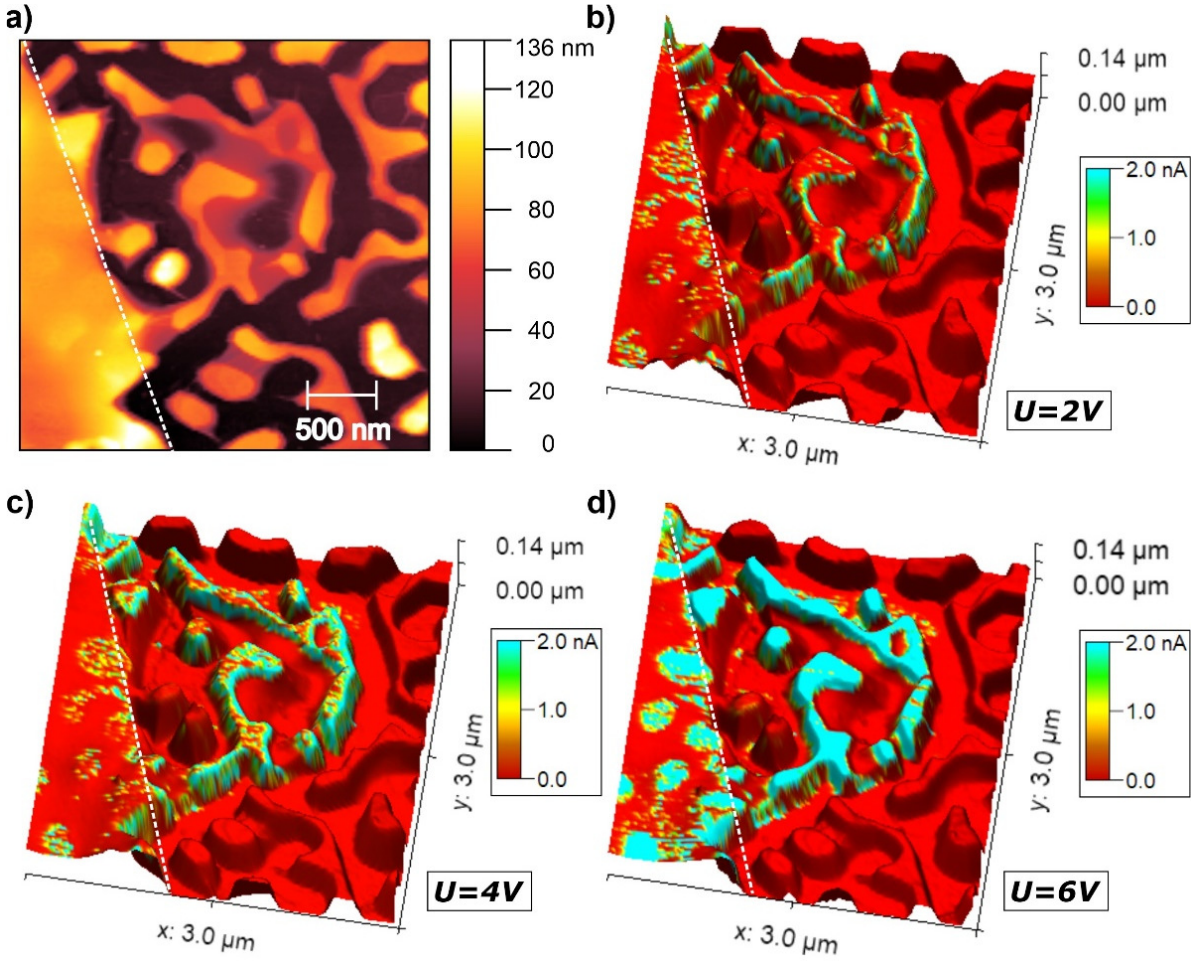


*Figure 1: (a) TUNA Atomic Force Microscopy (AFM) topography and (**b**)–(**d**) tunnelling current images of monolayer MoS_2 covering Au NPs. The current maps overlap with the topographic images. The dashed white line marks the few-layer/monolayer MoS_2 boundary. The tunnelling current maps were measured at bias voltages (U) of 2 V (b), 4 V (c) and 6 V (d).*

The few-layer/monolayer MoS_2 boundary is indicated by the dashed white line. Figures 1.b–d show composite images of the tunnelling current maps measured at different bias voltages (U), superimposed on the topographic image in Figure 1.a. Note that at U = 2 V (Figure 1), only some of the bent MoS_2 monolayer parts display nonzero conductance. Increasing the bias voltage to 4 V (Figure 1.c), a larger region becomes conductive, and this tunnelling conductance is further enhanced at U = 6 V (Figure 1.d). It is important to note that at these higher voltages, finite conductance is measured not only on the bent parts, but also on the MoS_2 parts which are directly supported by gold nanostructures. This indicates significant charge transfer from the Au NPs.

To exclude the electronic interaction with the gold, multilayer MoS_2 flakes were prepared on top of Au NPs. In this case, the TUNA measurements probe only the conductance of the topmost layer(s), which are not sensitive to the doping from the underlying Au NPs, showing a multilayer MoS_2 flake on top of Au NPs.

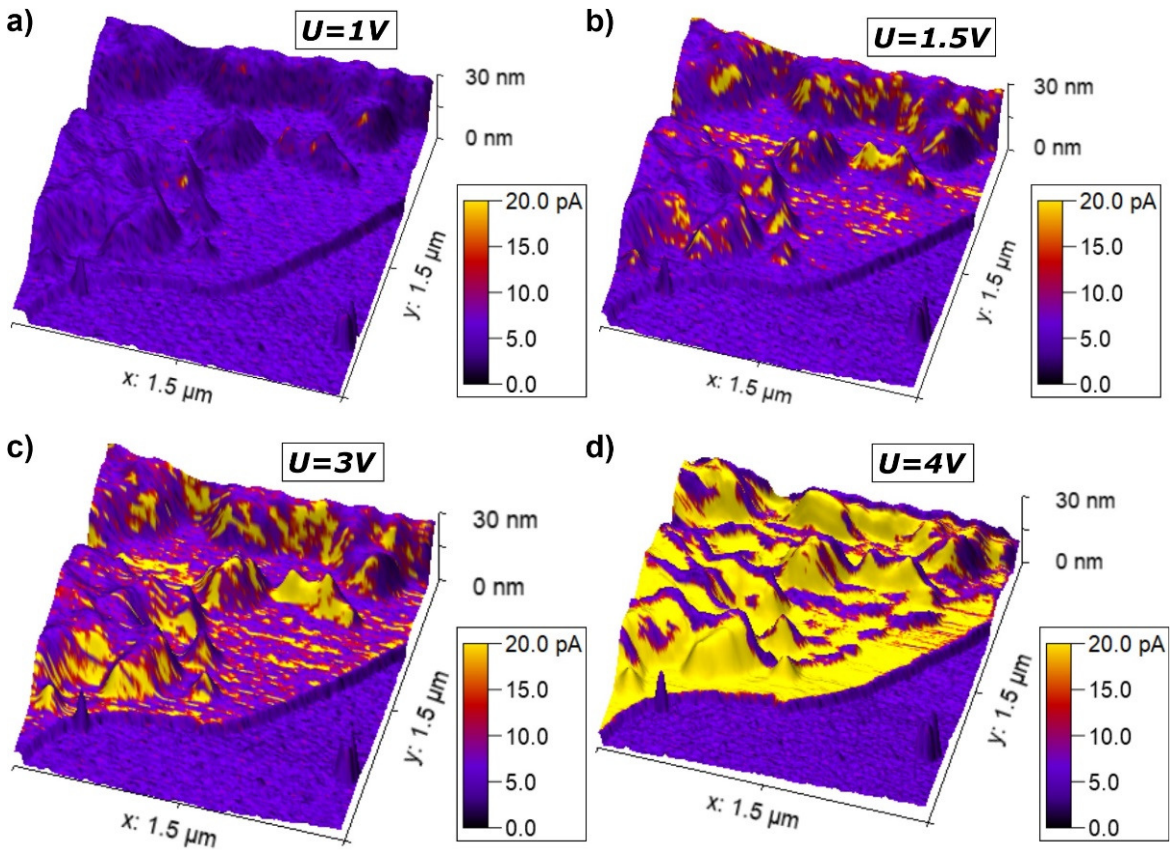


*Figure 2: TUNA AFM tunnelling current maps (overlapped with the topography) measured on a multilayer MoS_2, using bias voltages (U) of 1 V (**a**), 1.5 V (**b**), 3 V (**c**), and 4 V (**d**).*

The tunnelling current maps are superimposed on the topography, similarly to those in Figure 1.b–d. Using a bias voltage of U=1 V, nonzero conductance is detected only in a few specific points (Figure 2.a). Larger conducting regions are measured at U=1.5 V (Figure 2.b). These conducting domains further expand as the bias is increased to U=3 V (Figure 2.c), and at U=4 V the entire MoS_2 flake is conducting (Figure 2.d). The purple stripes observed in Figure 2.d are attributed to non-conducting hydrocarbon contamination trapped from the air. [1]

Related publication

[1] Z. Osváth, A. Pálinkás, Gy. Molnár, P. Kun, A.A. Koós: *Strain-induced modulation of the local conductance in MoS_2 layers on gold nanoparticles,* Surfaces and Interfaces **74,** 107725 (2025) https://doi.org/10.1016/j.surfin.2025.107725

BIOINSPIRED SEMICONDUCTOR NANOARCHITECTURES FOR ENVIRONMENTALLY FRIENDLY PHOTOCATALYSIS

OTKA PD 142985

K. Kertész, G. Piszter, G. Nagy, J. S. Pap, and L. P. Biró

Industrial pollutants in surface waters represent a growing environmental threat. An economical and environmentally sustainable strategy for their degradation is the utilisation of virtually unlimited solar energy. Building on our experience with biotemplated photocatalysts based on butterfly wing scale nanoarchitectures, we developed novel bioinspired nanocomposites from non-toxic semiconductor materials with a scalable preparation method which makes them suitable for future industrial implementation.

Sample preparation began with an ethanol solution of zinc nitrate hexahydrate ($Zn(NO_3)_2 \cdot 6H_2O$), which was drop-cast onto a heated textured-glass substrate. Rapid solvent evaporation produced a sponge-like, porous zinc nitrate layer on the glass surface. The fully dried samples were then heat-treated in a tube furnace at 400 °C, resulting in complete structural transformation. X-Ray Diffraction (XRD) measurements confirmed the formation of ZnO with a wurtzite crystal structure, similar to ZnO thin films previously deposited on butterfly wing biotemplates by atomic layer deposition and known for their excellent photocatalytic activity.

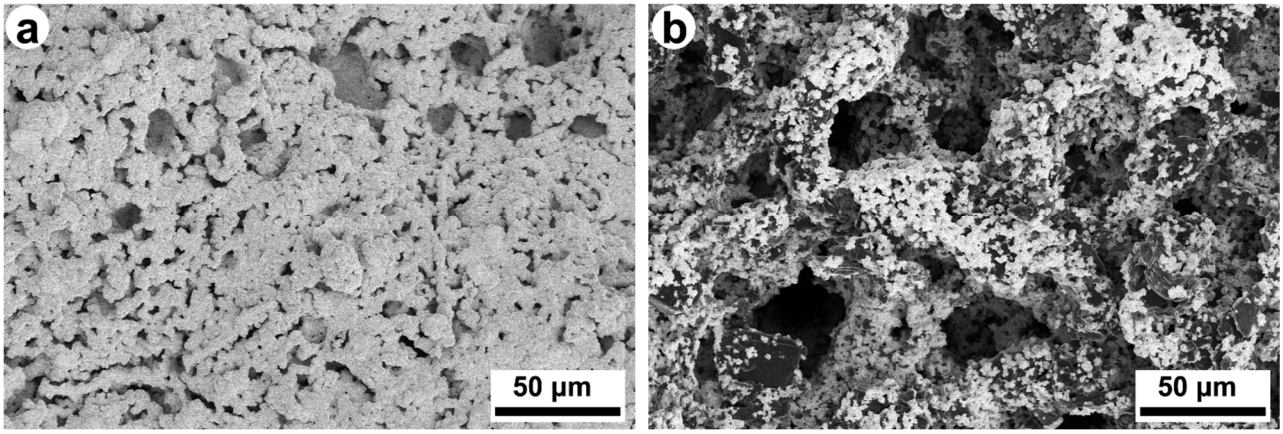


Figure 1: Scanning electron microscopy images of bioinspired ZnO nanostructures: (a) unmodified, pure ZnO; (b) ZnO-based sample doped with 10 wt% graphite nanoparticles.

A major advantage of this liquid-phase deposition method is its simplicity and suitability for coating large surface areas without the need for biological templates. The resulting structures, composed entirely of ZnO, exhibited a porous morphology resembling butterfly wing nanoarchitectures and a large catalytically active surface area. In addition, tuning the semiconductor band structure is straightforward, as dopants can be incorporated directly into the ZnO matrix by introducing them into the precursor solution or deposited onto its surface after annealing.

We investigated the optical and structural properties of the resulting bioinspired samples, as well as their photocatalytic performance, following the incorporation of various dopants (gold, graphite, MoS_2, and g-C_3N_4 nanoparticles). Figure 1 presents scanning electron microscope images of the unmodified, pure ZnO and graphite nanoparticle-doped samples. Their nanostructures were morphologically very similar; however, their catalytic performance was found to be significantly different.

The photocatalytic performance of the samples was evaluated by the degradation of an aqueous solution of methyl orange dye under two hours of visible light irradiation. The pure ZnO structures were doped with four types of nanoparticles in three different concentrations (5, 10, and 15 wt%), and three independent measurements were performed for each sample. The photocatalytic reaction rate was found to depend on both the material quality and the additive concentration (Figure 2).

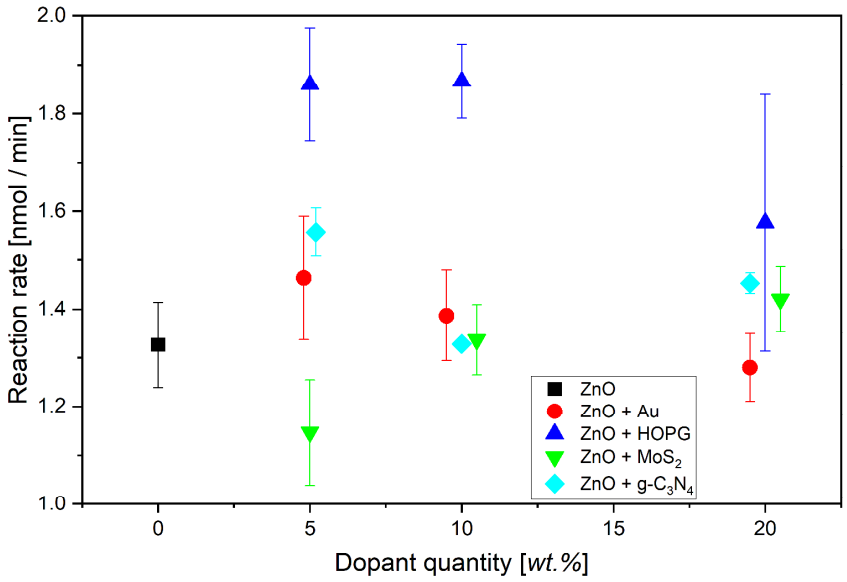


Figure 2: Photocatalytic performance of bioinspired ZnO nanostructures. The photodegradation rate of methyl orange dye was measured as a function of different additives and their concentrations.

Among the additives investigated, 10 wt% graphite nanoparticles proved to be the most effective in enhancing the photocatalytic reaction rate, closely followed by the 5 wt% sample. Their volumetric incorporation may increase dye adsorption at the surface of the nanocomposite and the absorption efficiency of the incident light, resulting in markedly improved photocatalytic performance compared to the undoped sample and those containing other additives.

The results above demonstrate that nanocomposites inspired by butterfly wing photonic nanoarchitectures have significant potential in photocatalytic water purification. Although these bioinspired structures do not exactly replicate biological nanoarchitectures, they retain their advantageous properties in a form suitable for both the intended applications and also industrial-scale production.

In summary, our experimental work has progressed through the years from the detailed investigation of the structural and optical properties of photonic nanoarchitectures in butterfly wings to their application in water purification as functional biotemplates of semiconductor thin films, ultimately leading to the fabrication of bioinspired artificial structures presented in this work.

Related publication

[1] A. Pálinkás, *et al.: Identification of graphite with perfect rhombohedral stacking by electronic Raman scattering*, Carbon **230**, 119608 (2024) https://doi.org/10.1016/j.carbon.2024.119608

VALIDITY OF YOUNG-DUPRÉ EQUATION FOR ADVANCING AND RECEDING SITUATIONS BY THE CAPILLARY BRIDGE PROBE METHOD

N. Nagy

The need for the determination of solid-liquid adhesion work is as old as Dupré's definition of the reversible work of adhesion. In addition to its scientific importance, this quantity is a critical factor affecting product quality and performance in many industrial fields. In general, it plays a crucial role in determining whether the liquid should completely cover a solid surface (e.g. coatings, paints, inks, lubricants, adhesives, pesticides) or, on the contrary, the liquid should not remain on the surface at all (liquid repellency, anti-icing, etc.).

Previously, a novel method was introduced to determine the value of adhesion work on flat surfaces directly, without the need for any model assumptions, and independently of uncertainties of contact angles. The method presented enables us to determine the adhesion work separately for both advancing and receding situations.

During a measurement cycle of a capillary bridge probe, the capillary force is measured as a function of the change in bridge length, which is a function of the vertical displacement of the cylinder.

This work is only spent on changing the interfacial areas if the gravitational force is negligible. During approach and retraction, both the area of the liquid-vapour interface (A) and that of the solid-liquid interface (B) change. Consequently, the energy balance can be written as

$$-\int \vec{F}d\vec{z} = \Delta A \cdot \gamma_{LV} + \Delta B \cdot (\gamma_{SL} - \gamma_{SV}) \qquad (1)$$

where $\vec{F}$ is the measured capillary force, $\vec{z}$ is the displacement of the cylinder, ΔA is the change of interfacial area between the liquid and vapour phase, and ΔB is the area change between the solid and the liquid, see Figure 1. (The values of ΔA and ΔB are also dependent on the start and end points of the interval (z-range), over which the integration is performed.)

After rearranging Equation (1), the difference term in the bracket can be expressed as:

$$(\gamma_{SL} - \gamma_{SV}) = -\frac{\int \vec{F}\, d\vec{z} + \Delta A \cdot \gamma_{LV}}{\Delta B}. \qquad (2)$$

One can substitute this experimentally otherwise unattainable term into the definition of adhesion work:

$$W_a \equiv \gamma_{LV} - (\gamma_{SL} - \gamma_{SV}) \qquad (3)$$

Furthermore, considering that the net force and the displacement have only a z-component, the vector notation can be omitted. This resulting formula gives the value of the solid-liquid adhesion work without the need of including any contact angle in the equation:

$$W_a = \gamma_{LV} + \frac{\int F\, dz + \Delta A \cdot \gamma_{LV}}{\Delta B}. \qquad (4)$$

Integration between the start and end points of approach and retraction gives the mechanical work done in the advancing and receding phases, respectively. The change of interfacial areas can be determined by simple image analysis in cylindrically symmetric case. Therefore, the solid-liquid adhesion work can be calculated according to Equation (4) for both the advancing and receding contact lines.

It is an interesting question what the relation is between the directly measured adhesion work values and the values calculated from the Young-Dupré equation. In other words: is the Young-Dupré equation valid separately for advancing and receding situations?

In Figure 1, the directly measured adhesion work values were plotted. The blue and red points represent the work of adhesion measured in the advancing and receding phase, respectively. The green points were measured in a readvancing situation. This readvancing effect can be observed in the case of perfect wetting: the receding contact line starts to advance again during the retraction of the cylinder. (The readvancing contact line already finds wetted surface in front of it; hence the measured contact angle is lower than in the receding situation, its value is typically ≤1°.) The corresponding vertical error bars show the standard deviation of the directly measured adhesion work values determined according to the above-described procedure. The adhesion work values were plotted as a function of contact angle, the values of which were measured during the same capillary bridge probe measurement and obtained by analytic evaluation as described previously. The horizontal error bars show their standard deviation.

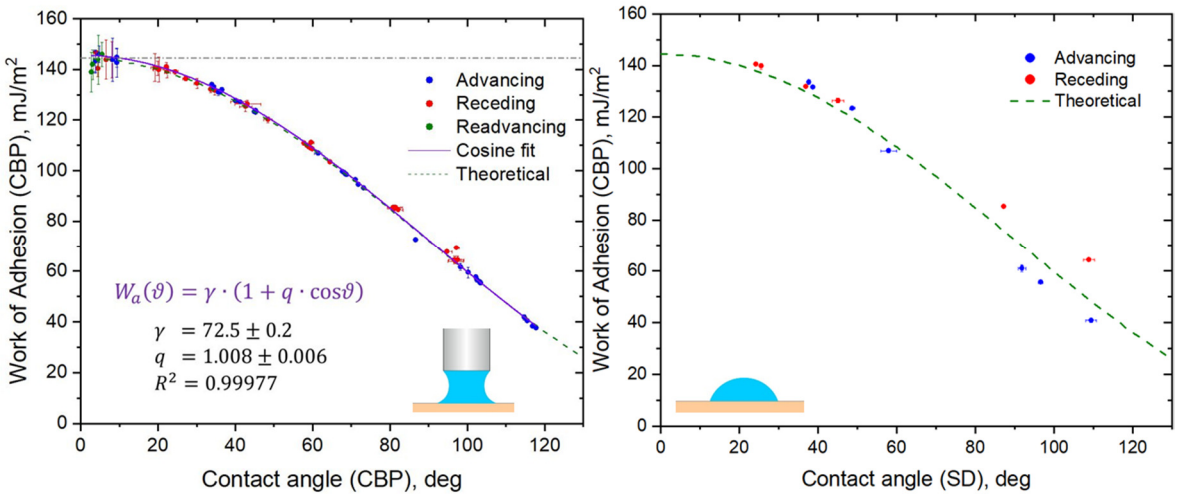


Figure 1: (left) Directly measured adhesion work values as a function of contact angles determined during the same Capillary Bridge Probe (CBP) measurement. The inset shows the result of the fit of a general cosine function to all measurement points. The fitted purple curve is in excellent agreement with the theoretical dashed green curve corresponding to the Young–Dupré equation. For this validation, metal, semiconductor, dielectric, and polymer surfaces were measured in clean, contaminated, acid-, and plasma-treated conditions using ultrapure water as test liquid. (right) Work of adhesion values measured by CBP as a function of water contact angles determined by the Sessile Drop (SD) method. The purple dashed line represents the theoretical prediction of the Young–Dupré equation.

In conclusion, accurately measured advancing and receding contact angles can be used to calculate the adhesion work for the two different situations. It is worth noting that the calculation of adhesion work from the Young–Dupré equation relies on the precise measurement of the contact angle. When, for instance, the directly measured adhesion work is plotted against the sessile drop contact angles, the correlation is of much lower quality (Figure 1 (right)). Furthermore, in accordance with the previous consequence, this novel direct method provides an additional advantage: if the receding contact angle is not a stationary definite value, an effective receding contact angle can be calculated from the measured adhesion work using the Young–Dupré equation. [1], [2], [3]

Related publications

[1] N. Nagy: *Determination of solid-liquid adhesion work on flat surfaces in a direct and absolute manner*, Scientific Reports **14,** 29991 (2024) https://doi.org/10.1038/s41598-024-81710-6

[2] N. Nagy: *Eljárás és berendezés folyadék-szilárd adhéziós munka meghatározására (Method and Apparatus for Determining Liquid-Solid Adhesion Work)*, Hungarian patent (231 506)

[3] N. Nagy: *Method and Apparatus for Determining Liquid-Solid Adhesion Work*, WIPO PCT patent application (WO2023094846)

A NOVEL, PHOTOASSISTED SYNTHETIC ROUTE TO TRANSFORM Cu_2O NANOOCTAHEDRA TO Cu_2S QUANTUM-DOT SUPERSTRUCTURES

OTKA FK 142148; TKP2021-NKTA-05

D. Kovács, G. Z. Radnóczi, Zs. E. Horváth, K. Frey, A. Sulyok, Z. Fogarassy, J. S. Pap, A. Deák, D. Zámbó

The family of copper sulphides includes numerous materials, which are relevant in mineralogy as well as in nanoscience and possess various stoichiometries (hence, they can be denoted as $Cu_{2-x}S$, where $0<x<1$). For well-defined nanocrystals or nanoparticle-based materials, the structure, composition and stoichiometry have a profound impact on the optical and electrochemical properties. The main challenge in synthesising copper chalcogenides is closely connected to the ability of natural oxidation and sulfidation of chalcophile metals such as Cu or Ag. This technically means that copper sulphides and oxides tend to oxidise and sulphidize at ambient conditions, respectively.

In recent years, we have developed a reliable strategy for the synthesis of Cu_2O nanooctahedra showing excellent morphological stability, tuneable optical and enhanced catalytic activity. However, even in optimised storage conditions (dark, 4°C, ethanol as solvent), the particles' composition and morphology slightly changed after 8 months of storage. We have shown that the particles undergo partial natural sulfidation which phenomenon can be linked to the presence of thiolated molecules and inorganic sulphur compounds in the atmosphere. This natural process motivated us to develop a novel strategy of the transformation of Cu_2O nanooctahedra to copper sulfide particles by using a small-chain thiolated alcohol (β-mercaptoethanol, BME) to initiate the oxide-sulphide transition wet-chemically. [1] The schematics in Figure 1 show the steps of the synthesis.

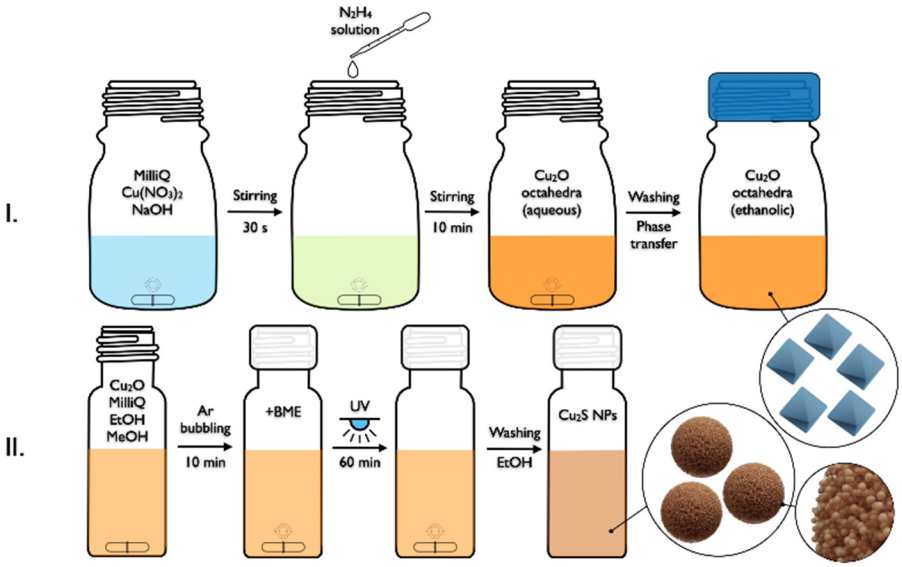


Figure 1: Schematics of the synthesis of Cu_2O nanooctahedra and their photoassisted chemical transformation to Cu_2S quantum-dot superstructures. [1]

The presence of mercaptoethanol itself does not generate well-defined copper sulphide species due to the oxidation and sulfidation occurring simultaneously under ambient conditions. This results in partially sulphidized particles and overoxidized (CuO) fibres in the solution. This oxidation pathway can be successfully eliminated by applying an inert atmosphere (Ar) and UV-light illumination, enabling the reliable synthesis of colloidally stable, spherical copper sulphide particles. The optical properties change stepwise upon increasing the amount of added BME, showing a shifting peak position from ca. 550 nm to 400 nm and a broadening (Figure 2.a). Interestingly, the TEM investigations reveal the presence of small (4-5 nm) quantum dots building up the larger copper sulphide particles. Moreover, the dots are separated by an amorphous organic thin layer. Elemental mapping confirmed that the ca. 250 nm in diameter spheres consist of Cu and S, and a low amount of O is present (Figure 2.b). However, this oxygen content cannot be further suppressed, which implies the existence of a stable copper sulphide phase and another oxygen-containing species.

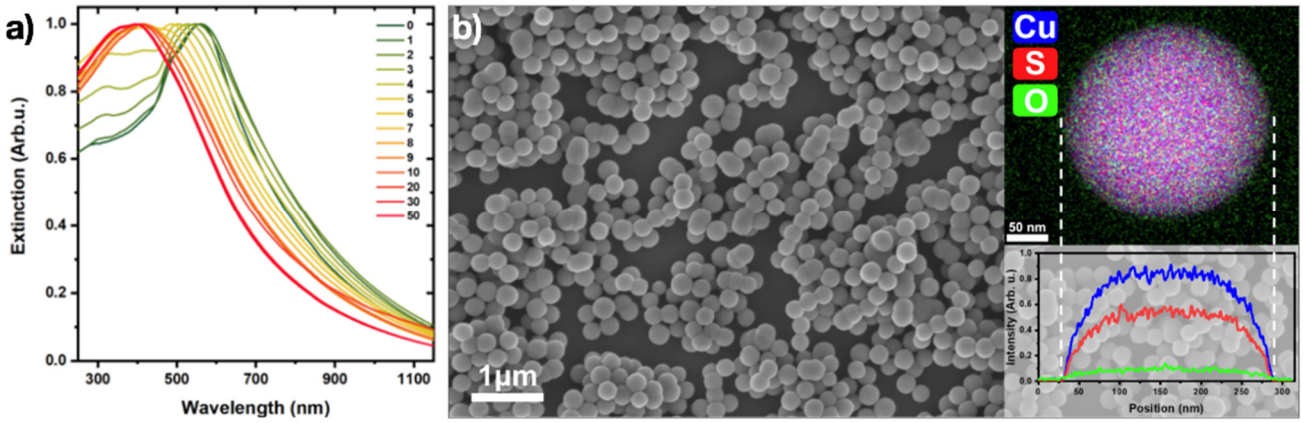


Figure 2: Evolution of the extinction spectrum upon increasing the concentration of BME (a). SEM image and TEM elemental map of the Cu_2S particles (b). [1]

By performing an advanced TEM sample preparation method and Selected Area Electron Diffraction (SAED), the precise stoichiometry and phase of the nanospheres could be identified (Figure 3.a-c). The sulfidized particles are superstructures consisting of small Cu_2S quantum dots, which are separated by a thin layer of organic thiol. Furthermore, these spherical particles can be decorated with small Au nanograins to achieve a semiconductor-metal multicomponent nanosystem, where the photogenerated carriers can be spatially separated. Macroscopic electrodes from the Cu_2S and Cu_2S/Au particles can be prepared on a conductive substrate, thus, the electrochemical properties of the model systems were also investigated. Open circuit potentiometry (Figure 3.d) revealed that all synthesised nanoparticle electrodes show p-type nature, and the presence of Au suggests an enhanced charge carrier separation. Under chopped light illumination, the electrodes generate cathodic current, which reaches the maximum value of 50 µAcm^{-2} for the Cu_2S@Au platform (Figure 3.e). After negative polarisation, the particles at the surface of the ITO remain morphologically stable (Figure 3.f), which suggests their potential use in (photo)electrochemical processes. [1]

Regarding the formation mechanism of the Cu_2S quantum-dot superstructures, the following pathway can be proposed (Figure 4): Reactive Sulphur Species (RSS) are formed from the organic thiol upon high-energy UV illumination, facilitating first the homolytic cleavage of the S-H bond or the disulfide (S-S) bond. These (most probably thiyl) radicals can interact with the surface Cu centres of the copper oxide nanoparticles, initiating a gradual anion (from O to S) in the sublattice. Simultaneously, UV light generates charge carriers in the Cu_2O itself, from which the electrons can reduce the surface-bound organocopper species to provide sulphur for the ion exchange reaction. This work sheds light on the complex formation mechanism, the optimal conditions and the optical, structural and electrochemical properties of novel Cu_2S superstructures prepared from a Cu_2O sacrificial template. [1].

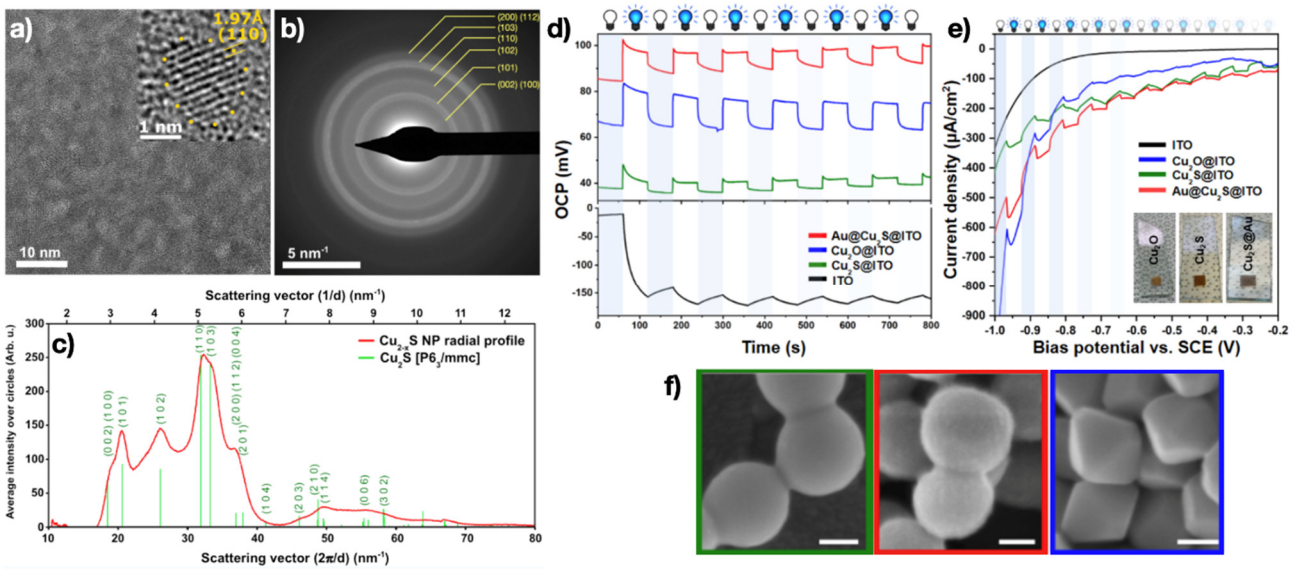


Figure 3: Phase identification (a-e) and electrochemical investigations (d-f) on the synthesised nanoparticles. [1]

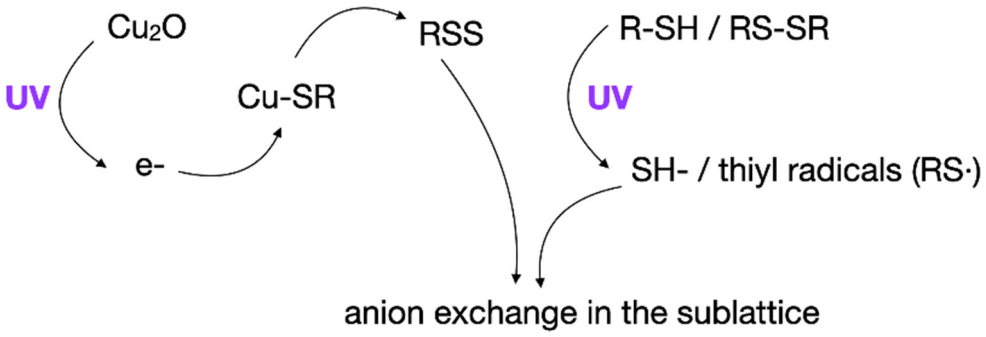


Figure 4: Proposed mechanism of the Cu_2O-Cu_2S photoassisted transformation process

Acknowledgement: D.K. acknowledges the support of Pro Progressio and the József Varga Foundation. Project no. TKP2021-NKTA-05 has been implemented with the support provided by the Ministry of Innovation and Technology of Hungary from the National Research, Development, and Innovation Fund (NKFIH), financed under the TKP2021 funding scheme. The work was financially supported by the NKFIH Fund of Hungary under the grant OTKA FK 142148.

The work has been selected as the „Paper of the month" by the Section of Chemical Sciences of the Hungarian Academy of Sciences in Sept. 2025: https://mta.hu/vii-osztaly-a-honap-publikacioja/2025-szeptemberi-kiemelt-publikaciok-114720.

Related publication

[1] D. Kovács, G.Z. Radnóczi, Z.E. Horváth, K. Frey, A. Sulyok, Z. Fogarassy, J.S. Pap, A. Deák, D. Zámbó: *Photoassisted Chemical Transformation of Cu_2O Nanooctahedra into Cu_2S Quantum-Dot Superstructures: Structural and Photoelectrochemical Properties,* ACS Mater. Au **5:(6),** 1018 (2025) https://doi.org/10.1021/acsmaterialsau.5c00106

SPATIAL MODULATION OF Cu_2O SHELL GROWTH ON GOLD NANOPRISMS

OTKA FK 142148, TKP2021-NKTA-05

Z. Ganieva, D. Kovács, Z. Osváth, D. Zámbó, and A. Deák

Environmentally friendly and earth-abundant metal oxide semiconductors are intensively studied for optoelectronic and catalytic applications, but they suffer from low charge carrier mobilities, which represent a major obstacle for their large-scale use. Nanoscale metal/metal-oxide nanoparticles might help in this regard, as at this scale recombination processes might be suppressed, and a more efficient separation of the charge carriers generated in the semiconductor domain could be achieved [1]. Another advantage in such hybrid systems might come from the possibility to harvest hot carriers from the metal. Theoretically, the hot carriers generated in the plasmonic metal nanoparticles have to overcome only the Schottky barrier formed at the metal/oxide semiconductor interface, hence charge injection into the semiconductor and contribute to the efficiency of optoelectronic processes at the semiconductor. In this regard, partial core/shell structures are especially appealing, as they allow simultaneous access to both the metal and semiconductor domains. Cu_2O is a p-type semiconductor with its optical band gap located in the visible wavelength range and has excellent compatibility with gold, allowing the wet-chemical growth of a Cu_2O shell around gold nanoprisms [2].

In this work, we used the controlled spatial modulation of the gold nanoprisms' surface energy to partially prevent Cu_2O deposition on gold nanoprisms [3]. The approach relies on the inhomogeneous accumulation of a thiol molecule (5-amino-2-mercaptobenzimidazole - AMBI) on the prisms' surface during a surface modification reaction before Cu_2O deposition. AMBI is known to effectively block the deposition of Cu_2O on gold nanoparticles, provided it is present at a sufficiently high packing density at the interface. Under appropriate conditions in terms of reaction temperature and AMBI concentration, submonolayer coverage of the prisms can be achieved, showing the presence of some high-density molecular patches (Figure 1). Already at concentrations that show patchy AMBI adsorption at the nanoprisms' flat faces (Figure 1.b), almost complete coverage of the side and tip regions can be anticipated due to the higher-energy binding sites in these regions, which can be exploited to reduce the Cu_2O deposition in these particle regions during the wet-chemical growth of the shell.

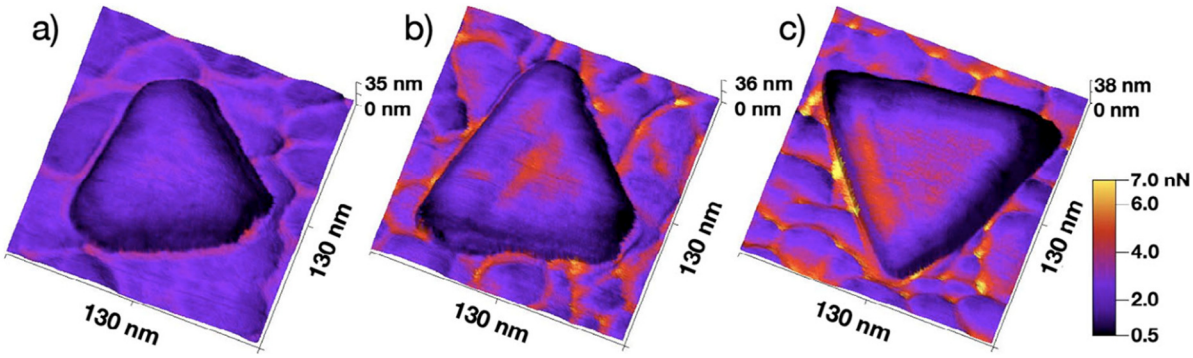


Figure 1: Scanning probe microscopy-derived topography of the indium tin oxide supported nanoprisms overlain with the adhesion force maps: no AMBI treatment a) and surface modification at 1 µm b), and 190.5 µm AMBI c). [3]

This was confirmed by investigating the evolution of the Cu_2O shell growth over the reaction time, quenching the process at different time instances and investigating the particle morphology ex-situ by transmission electron microscopy (Figure 2). If AMBI is absent, Cu_2O forms a neat shell around the gold nanoprisms in a shape-conform manner (top row). When the gold nanoprisms are pretreated with AMBI under optimised conditions, however, strong structural inhomogeneity of the shell develops. The number of nucleation sites is strongly reduced, which is especially clear in the early phase of the shell growth. It must be stressed that the few Cu_2O domains on the prism surface in the presence of AMBI in the beginning phase (15 s) agreed well with the scanning probe microscopy derived adhesion map pattern. Nevertheless, the observed Moiré pattern for these few dots indicates that the excellent compatibility between the gold and Cu_2O is preserved at the nucleation sites. At later growth stages, the initial Cu_2O domains grow larger and fuse together. It seems, however, that the combination of AMBI coverage and the surface curvature at the prism tips effectively prevents the growing and fusing Cu_2O domains from engulfing the prism tips, leaving them exposed even after the competition of the growth process.

The prepared structure ensures the simultaneous access of both the metal and semiconductor domains and hence can be of interest for optoelectronic and catalytic use. Additionally, the high optical near field at the prism tips that develops upon exciting localised plasmons at the prisms can also be utilised.

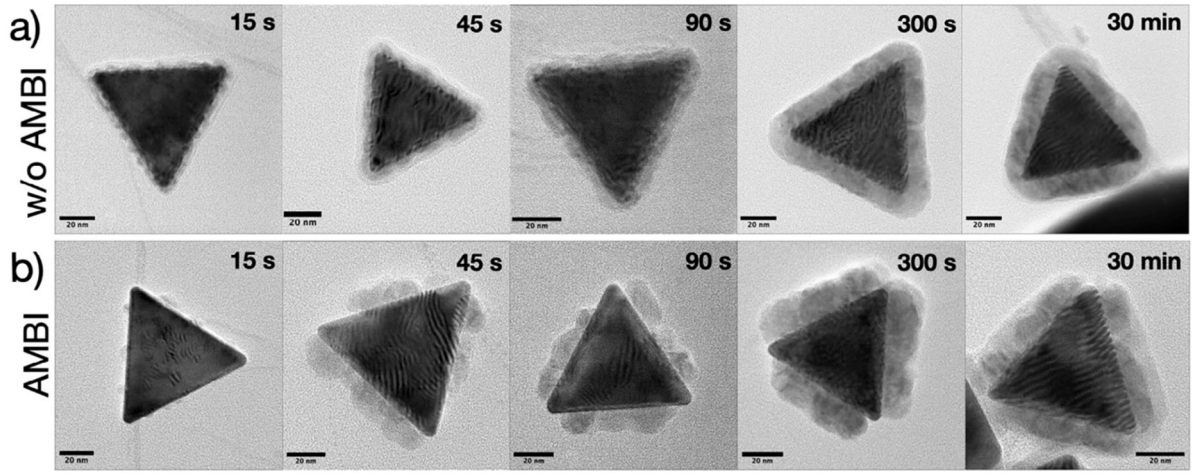


Figure 2: TEM images of the Cu_2O/Au nanoparticles prepared without (upper row) and in the presence of AMBI (lower row). [4]

Related publications

[1] D. Kovács, A. Deák, G.Z. Radnóczi, Z.E. Horváth, A. Sulyok, R. Schiller, O. Czömpöly, D. Zámbó: *Position of Gold Dictates the Photophysical and Photocatalytic Properties of Cu_2O in Cu_2O/Au Multicomponent Nanoparticles,* J. Mater. Chem. C **11:(26),** 8796–8807 (2023) https://doi.org/10.1039/d3tc01213a

[2] D. Zámbó, D. Kovács, A. Deák: *Optical and Structural Properties of Cuprous Oxide Shell Coated Gold Nanoprisms,* Part & Part Syst Charact 2400082, (2024) https://doi.org/10.1002/ppsc.202400082

[3] Z. Ganieva, D. Kovács, Z. Osváth, D. Zámbó, A. Deák: *Region-Selective Growth of Cu_2O Shell on Gold Nanoprisms.* Adv Materials Inter **12:(16),** e00512 (2025) https://doi.org/10.1002/admi.202500512

ELECTROCHEMICAL METHODS AND ELLIPSOMETRIC CHARACTERISATION OF GOLD NANOPARTICLE-BASED SENSORS

OTKA K 146181

M. K. Stift, A. Bonyár, Z. Lábadi, É. Tóth, H. Jankovics, F. Vonderviszt, P. Petrik

Heavy-metal ions in drinking water can lead to serious health risks even at low concentrations, and rapid, on-site monitoring remains a major challenge. We aimed to develop a portable electrochemical sensor concept that combines selective biomolecular recognition with fast and objective readout, while making sure that it can be used without skilled labour [1].

Our sensing interface is built from an electrochemically deposited gold nanoparticle (AuNP) layer formed on an Au-evaporated silicon substrate and a layer of genetically engineered flagellin filaments immobilised on the nanostructured surface. This approach is based on prior work at the Photonics Laboratory demonstrating that bioengineered flagellar nanotubes can be immobilised on gold surfaces and used to create selective sensing layers for Ni(II) detection [2], [3]. Figure 1 shows the Au-evaporated 15 x 15 mm silicon substrate before electrochemical treatment.

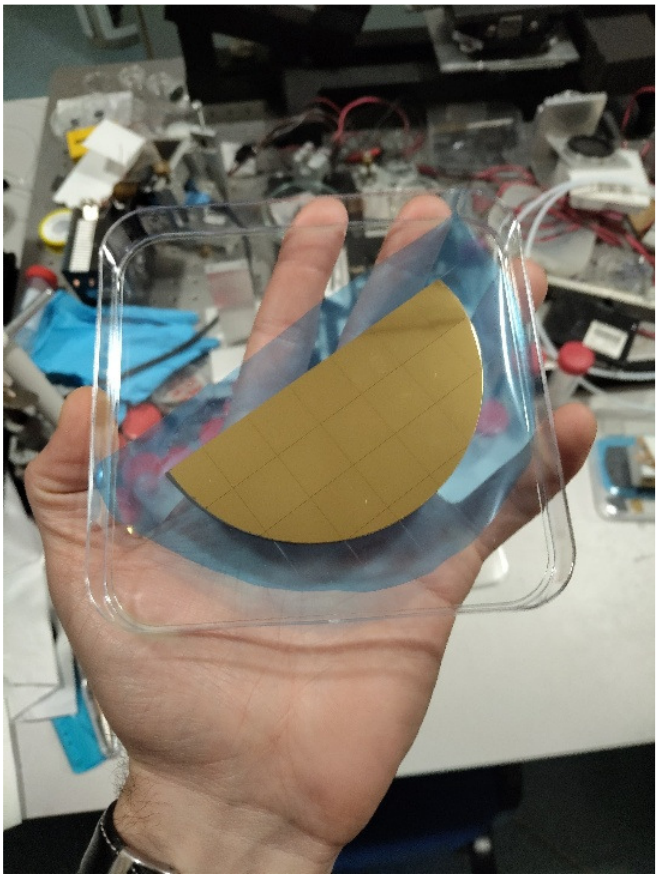


Figure 1: Au-evaporated silicon substrate (15 x 15 mm) before the electrochemical deposition treatments

AuNP growth and specific protein immobilisation were performed in a three-electrode electrochemical cell using different amperometry methods such as preparative cyclic voltammetry and chronoamperometry. Cyclic voltammetry provides a convenient way to track redox changes and characterise the response of the sensor through certain anodic and cathodic peaks [4], [5].

Throughout the deposition steps, in-situ spectroscopic ellipsometry was used as a non-invasive optical monitoring method to follow the changes on the surface during the electrochemical processes. So, to conclude, our approach was a combined electrochemical-optical workflow.

Figure 2 shows an SEM image after AuNP deposition and subsequent protein immobilisation. It illustrates an adequate nanostructured gold surface; together with electrochemical measurements in Ni(II)-containing solutions, the results support the feasibility of semi-quantitative Ni detection and motivate further selectivity studies with additional heavy-metal ions. [2]

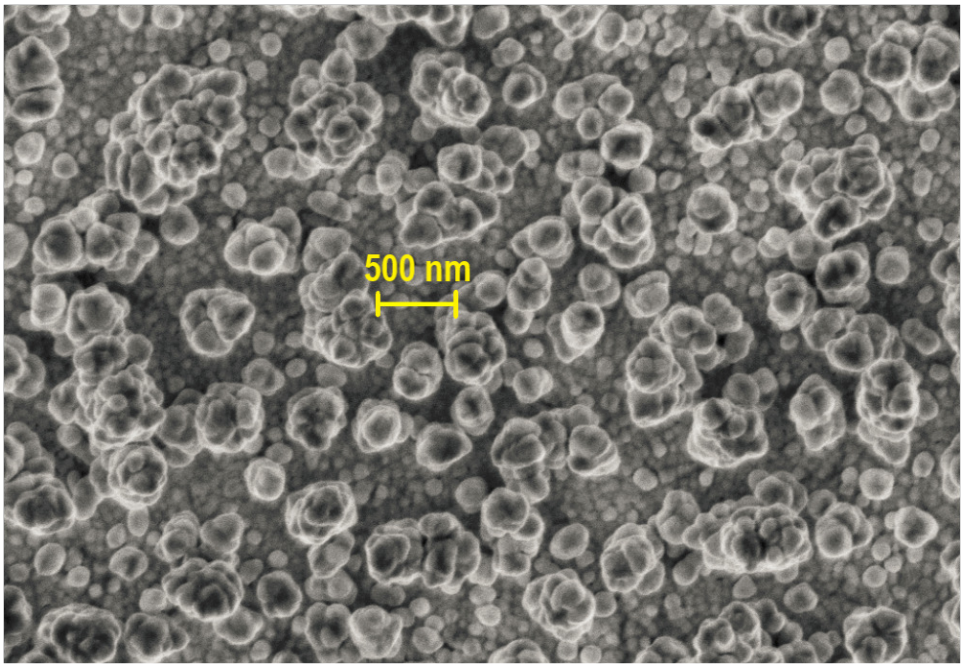


Figure 2: SEM image of the surface after electrochemical AuNP deposition and immobilisation of engineered protein filaments

Related publications

[1] M. S. Braga, R. F. V. V. Jaimes, W. Borysow, O. F. Gomes, and W. J. Salcedo: *Portable multispectral colorimeter for metallic ion detection and classification,* Sensors (Basel) **17:(8),** 1730 (2017) https://doi.org/10.3390/s17081730

[2] Z. Labadi et al.: *Sensing layer for Ni detection in water created by immobilization of bioengineered flagellar nanotubes on gold surfaces,* ACS Biomaterials Sci. Eng. **6:(7),** 3811 (2020) https://dx.doi.org/10.1021/acsbiomaterials.0c00280?ref=pdf

[3] S. Kurunczi et al.: *In situ ellipsometric study of surface immobilization of flagellar filaments,* Applied Surface Science **257:(1),** 319 (2010) https://doi.org/10.1016/j.apsusc.2010.06.095

[4] P. T. Kissinger and W. R. Heineman: *Cyclic voltammetry,* Journal of Chemical Education **60(9),** 702 (1983) https://doi.org/10.1021/ed060p702

[5] N. Elgrishi, K. J. Rountree, B. D. McCarthy, E. S. Rountree, T. T. Eisenhart, and J. L. Dempsey: *A practical beginner's guide to cyclic voltammetry,* Journal of Chemical Education **95:(2),** 97 (2018) https://doi.org/10.1021/acs.jchemed.7b00361

INVESTIGATION OF IN- AND OUT-DIFFUSION OF LI-IONS IN ELECTROCHROMIC TUNGSTEN-MOLYBDENUM COMBINATORIAL OXIDE FILMS BY SPECTROSCOPIC ELLIPSOMETRY

OTKA K 143216, OTKA K 146181

Z. Lábadi, P. Petrik and M. Fried

Reactive (Ar-O_2 plasma) magnetron sputtered WO_3-MoO_3 mixed-oxide electrochromic layers [2] were deposited onto a 4' [100] silicon wafer. The layer was composition graded (i.e. WO_3 content changed in the 0-100% range alongside the wafer diameter).

We determined and mapped the composition and optical parameters. Measurements were done in a liquid electrochemical cell using Spectroscopic Ellipsometry (SE). Electrochemical measurements were performed in 1 M lithium perchlorate ($LiClO_4$) / propylene carbonate electrolyte.

Different optical models, such as the Bruggeman Effective Medium Approximation (BEMA) or the 2-Tauc–Lorentz multiple oscillator model (2T–L), were used to obtain the thickness and composition maps of the sample. Scanning Electron Microscopy (SEM) with Energy-Dispersive X-ray Spectroscopy (EDS) was used to check the SE results. The performance of diverse optical models has been compared. We showed that in the case of molecular-level mixed layers, 2T–L is better than EMA. [1] Figure 1 shows the experimental arrangement for the combined SE and electrochemical measurement.

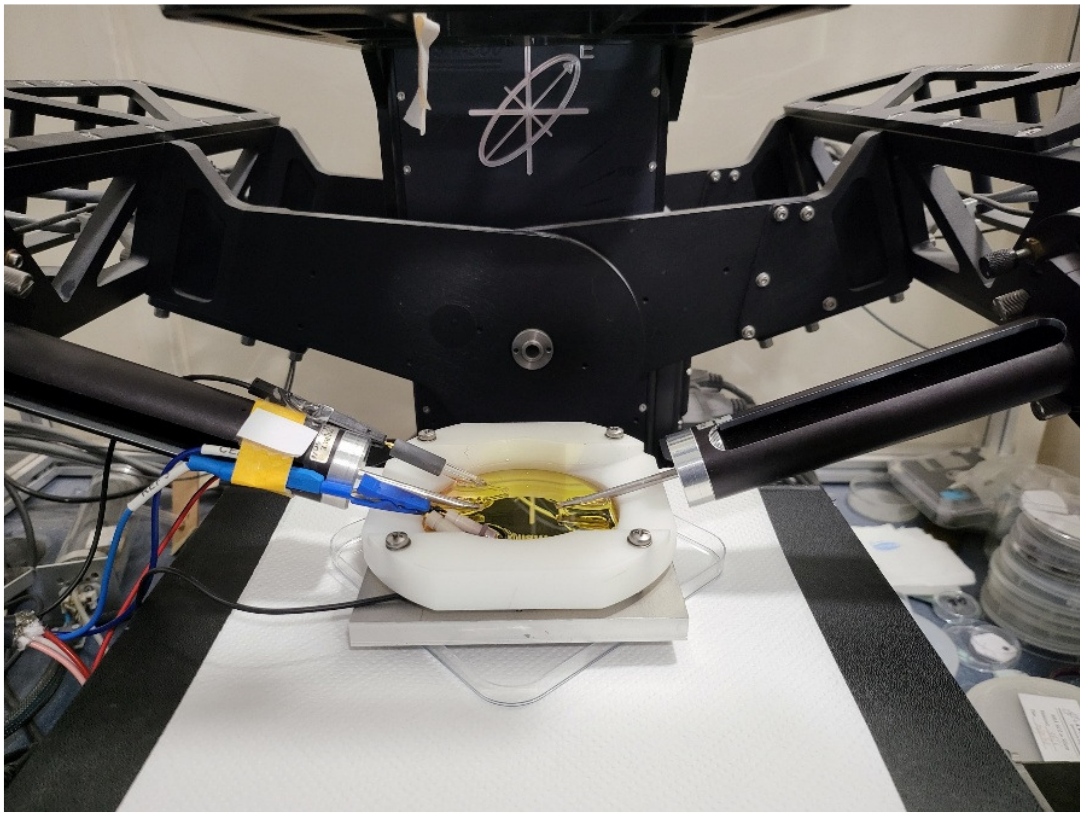


Figure 1: Experimental arrangement for in-situ SE measurements in the electrochemical liquid cell

Electrochromic Colouration Efficiency (CE) as a function of composition (Figure 2) was established on independent transparent samples [3] (Colouration Efficiency measures the amount of optical change per unit of charge injected into the material. Higher CE indicates more efficient use of energy and can lead to lower power consumption in devices.)

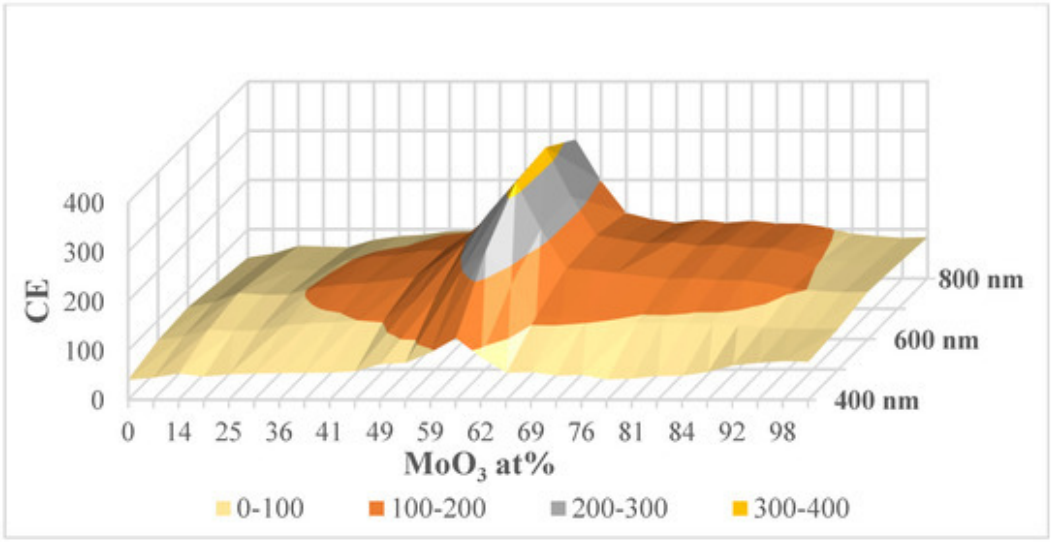


Figure 2: Calculated CE data as a function of MoO_3 fraction – 3D graphical representation

After determining the thickness and composition maps, the sample was forced through electrochemical reduction and oxidation cycles. Controlled current was applied through the cell, setting up reversible electrochemical cycles of colouration and bleaching [2]. SE measurements were recorded in the central position in situ, in real time, and full mapping was performed after the last colouration cycle. Ellipsometric spectra were evaluated using a multi-layer, multi-parameter optical model. Components of complex refractive indices were attributed to the in- and outdiffusion of Li into the oxide layer.

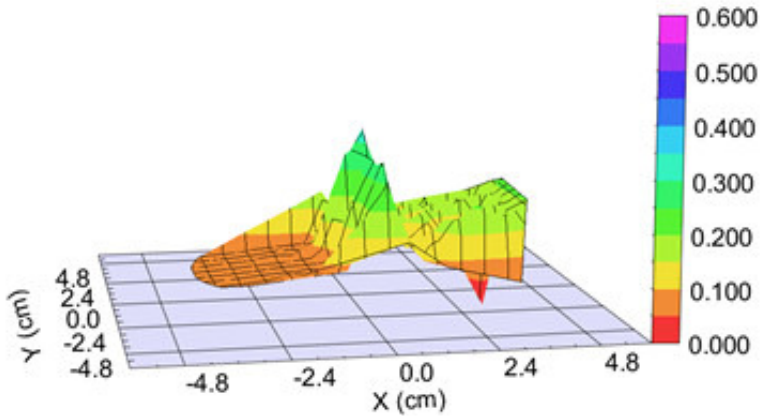


Figure 3: Amplitude of the k (extinction) parameter as a function of the position

The optical model (used for dry mapping after electrochromic experiment) consisted of the following layers: Air - Surface roughness - Cauchy disp. (mixed layer + Li) - intermixed – Gold substrate.

Figure 3 shows the measured k parameter map. The k Amplitude (extinction) parameter can be considered as a good indicator of CE. The maximum k value shows that the optimal composition is at 75 % MoO_3 – 25 % WO_3 composition. Changes in the k parameter in the top layer are proper indicators of the in- and out-diffusion of Li-atoms. Increasing Li concentration causes higher k values. The colouration process therefore can be in situ monitored by SE combined with an appropriate optical model.

Related publications

[1] M. Fried, R. Bogar, D. Takacs, Z. Labadi, Z. E. Horvath, Z. Zolnai: *Investigation of Combinatorial WO_3-MoO_3 Mixed Layers by Spectroscopic Ellipsometry using Different Optical Models,* Nanomaterials **12(14),** 2421 (2022) https://doi.org/10.3390/nano12142421

[2] Z. Labadi, D. Takacs, Z. Zolnai, P. Petrik, M. Fried: *Compositional Optimization of Sputtered WO_3/MoO_3 Films for High Coloration Efficiency,* Materials **17(5),** 1000 (2024) https://doi.org/10.3390/ma17051000

[3] S.P. Thompson: *Ye Magick Mirrour of Old Japan,* London, private edition (1893)

EFFECTS OF GLOBAL CURVATURE AND ILLUMINATION CONDITIONS ON MAGIC-MIRROR IMAGING

OTKA K 146181

F. Riesz

Magic mirrors (in Japanese, Makyoh) are bronze mirrors with a backside relief pattern, originating from ancient China and Japan. If a light beam falls on the mirror surface, an image is projected on a distant wall that resembles the back pattern as if the mirror was transparent [1]. These mirrors fascinated laymen and scholars alike for centuries, and since the 19th century, when Western scholars became aware of these mirrors, they have been actively studied. It was clarified that a nearly invisible surface relief is formed on the polished front face during manufacturing by mechanical means of the back relief. The image is then created by the local deflection of the reflected rays by this front relief; more precisely, the image intensity at a screen point is related to the local curvatures of the corresponding mirror surface element. The principle's fruitful modern application is 'Makyoh topography', used mostly for the visualisation of surface defects of semiconductor wafers.

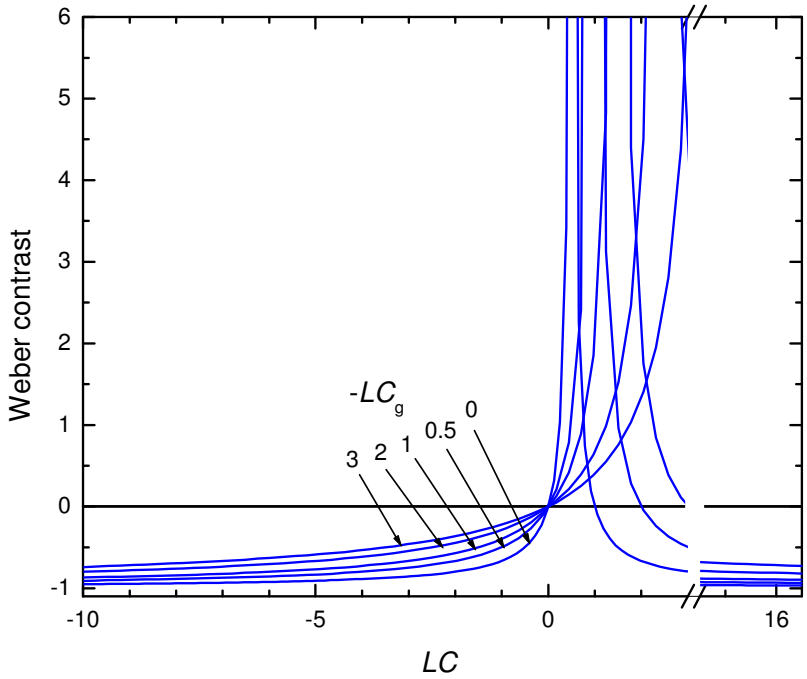


Figure 1: Dependence of the image contrast on local and global curvatures

Most ancient magic mirrors possess a global convexity, semiconductor wafers may also be curved or warped, thus, the effect of global curvature is worthy of attention. It has been shown earlier using a geometrical optical analysis [2] that a C_g global curvature (in addition to the trivial effects of image magnification and intensity reduction) can be considered by introducing an effective screen distance L_{eff} given as the reciprocal addition of the physical screen distance L and $-1/(2C_g)$. That is, a uniformly curved mirror with a surface relief behaves as a flat mirror with the surface relief "cascaded" with a curved mirror without a relief. The contrast relations can also be analysed using elemental models [3]. Even though the models are simple, there are several ways to visualise the results, each emphasising different aspects of the phenomenon. Figure 1 shows a possible way: one-dimensional curved surface elements are considered on a spherically curved mean surface, and the Weber contrast values of these elements are plotted against the curvature normalised with L for various global curvatures; that is, each point in a curve represents a given position of the mirror. The main conclusions are that the global convex curvature decreases contrast and decreases the sensitivity of the contrast to screen distance.

Original magic mirrors are meant to be illuminated by the Sun, that is, a collimated source. For modern demonstrations, exhibitions, as well as sometimes in semiconductor topography, the more convenient point source is used. This is optically equivalent to the introduction of a global convex curvature with radius twice the source distance (Figure 2). This leads to the appearance of the curvature effects outlined above even for a flat mirror: the reciprocal addition rule renders the sensitivity of the image pattern to screen distance reduced (a phenomenon often observed in magic mirrors), leading to an upper limit of the effective screen distance, thus, limited sensitivity in the topography application.

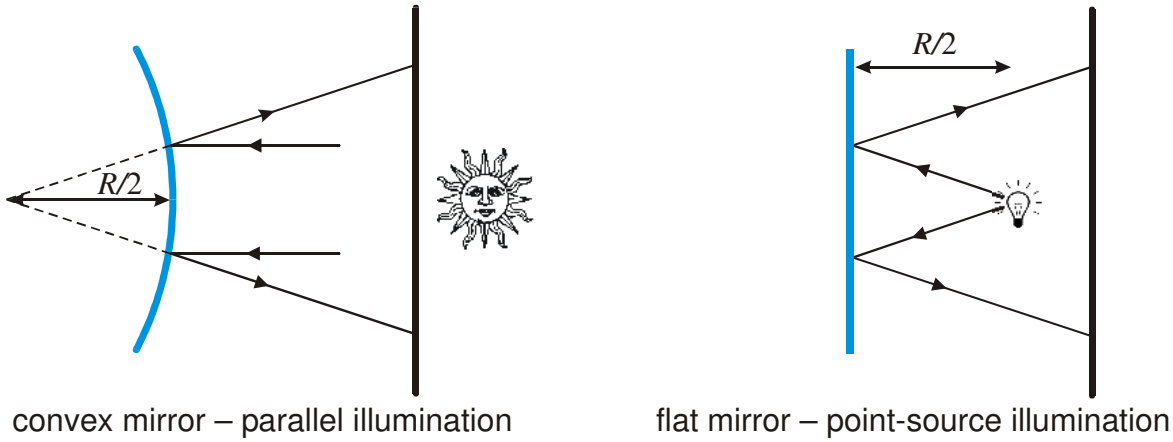


Figure 2: Optical equivalence of a globally convex mirror and a flat mirror with point-source illumination

Related publications

[1] S.P. Thompson: *Ye Magick Mirrour of Old Japan,* London, private edition (1893)

[2] F. Riesz: *The effects of the global surface curvature on Makyoh-topography imaging,* Photonics Letters of Poland **11:(4),** (2019) 4. https://doi.org/10.ol4302/plp.v11i1.862

[3] F. Riesz: *Curvature, illumination conditions and imaging properties in magic mirrors,* The 6th Makyoh Conversazione, 29-31 August 2025, Osaka, Abstracts, p. 25.

COMPOSITION-DEPENDENT STRUCTURAL AND OPTICAL PROPERTIES OF COMBINATORIALLY DEPOSITED, RF-SPUTTERED GALLIUM OXYNITRIDE LAYERS

TKP2021-NKTA-05

M. Gajdics, I. Cora, T. Kolonits, Gy. Sáfrán, E. Szilágyi, Zs. Zolnai and B. Pécz

Recently, Ga-based semiconductor thin films have gained increasing interest in the field of electronics and optoelectronics. GaN is commonly used in blue LEDs and in high-electron mobility transistors, while Ga_2O_3 can be utilised in rectifiers and solar-blind UV photodetectors. In comparison, gallium oxynitrides are in a less developed state. Nevertheless, gallium oxynitrides present promising optical and electronic properties for use in various electronic and optoelectronic applications. The possibility to tune these properties through the control of the elemental composition of Ga-O-N is an important aspect of these materials. Previous works only studied gallium oxynitrides with specific compositions, and the relationship between optical properties and elemental composition is still not fully explored.

In this work, we used a combinatorial method to deposit a gallium oxynitride film with a continuous composition gradient within the sample. This approach enabled us to map the optical and structural properties of the sample as a function of composition and accelerated the exploration of composition-property relationships. The combinatorial films were deposited using reactive Radio-Frequency (RF) sputtering where the nitrogen partial pressure was kept constant, while the oxygen flow rate (and hence the partial pressure) varied using a gas flow controller. The sputtering gas mixture also contained Ar, and different N_2/Ar partial pressure ratios were tested to cover as wide composition range as possible. The composition of the films was determined by Energy Dispersive X-ray Spectroscopy and Elastic Recoil Detection Analysis. The optical properties of the samples were investigated by Spectroscopic Ellipsometry both in reflection and in transmission mode. Structural characterisation was performed by X-ray Diffraction and Transmission Electron Microscopy.

As the oxygen flow rate decreased in the vacuum chamber, the oxygen content of the samples decreased, and simultaneously the refractive index increased. Refractive indices ranging from the index of Ga_2O_3 to the index of GaN were measured. The optical transmission of the film also changed as the oxygen content decreased, namely, the absorption edge shifted to higher wavelengths and the transmittance in the visible region decreased. The optical bandgap of the material decreased from that of Ga_2O_3 to that of GaN with decreasing oxygen flow rate. These results show that by controlling the deposition parameters, the elemental composition and the optical properties of the samples can be tuned. Combinatorial samples with different N_2/Ar partial pressure ratios were prepared, and the compositional variation, the refractive index and the optical bandgap are plotted in the ternary diagrams of Figure 1.a-b-c, respectively. From Figure 1.b-c, it is clear that the same refractive index/optical gap can occur for multiple different compositions (see dotted lines in Figure 1.b. To further characterise the relationship between these properties, it is useful to find a parameter that is invariant for the compositions with the same optical property. This parameter is determined to be S=(Ga-0.76O-0.24N)/(Ga+O+N), where Ga, O and N are the concentrations of the corresponding elements. If the refractive index data are plotted as a function of this S parameter (Figure 1.d), the curves corresponding to the different combinatorial samples shift relatively close together, indicating that the dependence of the refractive index on the composition of the sample can be reasonably described by this parameter. The only exceptions are at low and high values of the parameter, where a divergence of the curves can be seen.

The structural characterisation of the combinatorial films revealed that the layers are amorphous at high oxygen contents and, as the oxygen content decreases, the structure changes to polycrystalline. The crystalline phase was identified as the wurtzite-type phase of GaN. The growth pattern also changes with the oxygen flow rate, i.e. at first tiny nanocrystals were observed, and as the oxygen content further decreased, columnar grains started to appear. The change in the grain structure correlated well with the change in the oxygen concentration in the film.

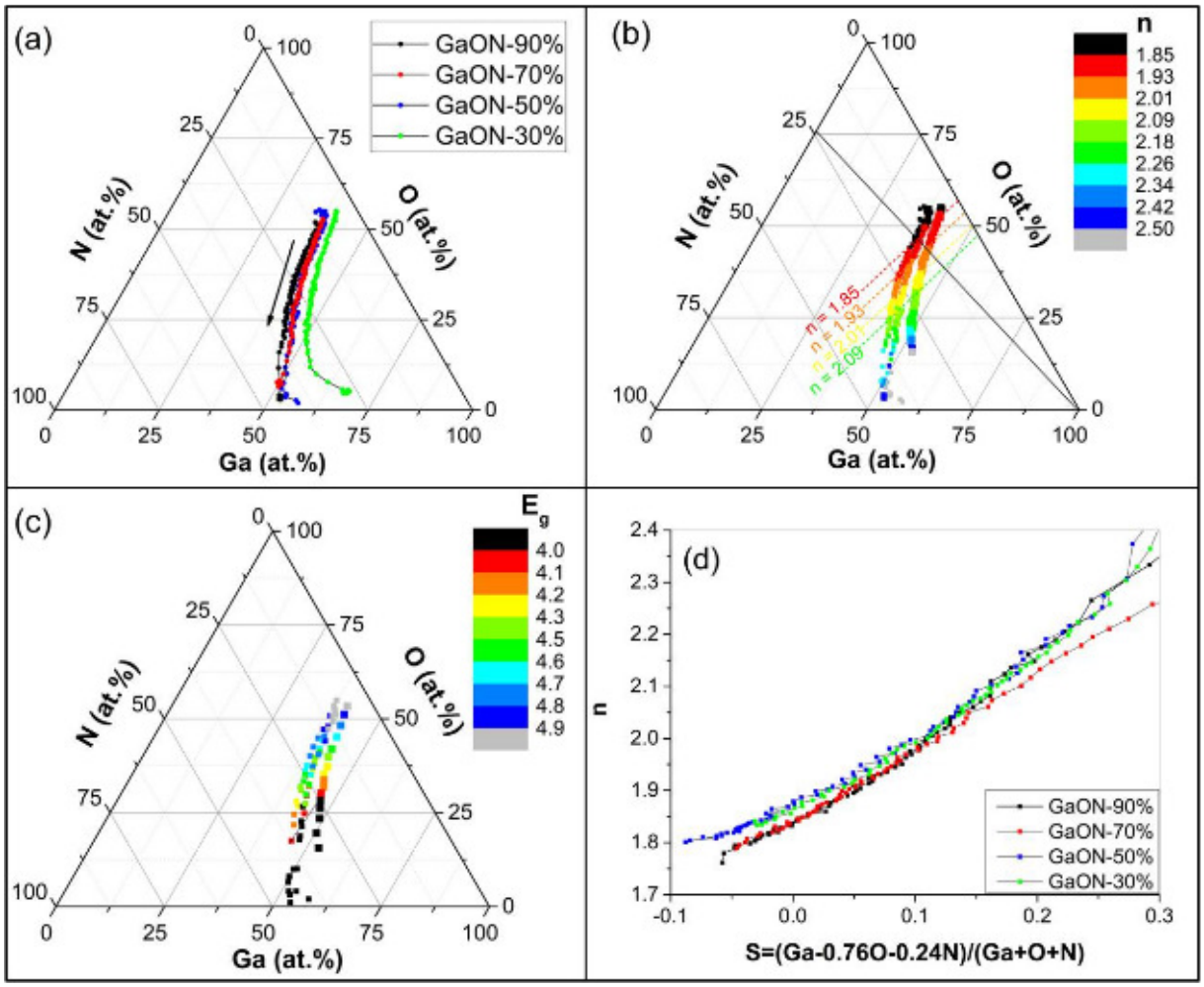


Figure 1: Ternary diagrams showing (a) the compositional variation, (b) refractive index (at 632.8 nm) and (c) optical gap of the four combinatorial samples with different N_2/Ar partial pressure ratios. The arrow in (a) represents decreasing oxygen flow rate during deposition, i.e. the direction from 0 mm to 20 mm. The dotted lines in (b) are the "iso refractive index" lines, while the black line is perpendicular to them. The (d) refractive index plotted as a function of the S parameter.

In conclusion, it was demonstrated that the optical and structural properties of the gallium oxynitride film can be tuned by controlling the composition, and the relationship between the refractive index and the composition was determined.

THE COMMON SUBLATTICE METHOD QUANTIFIES LOCAL DEFORMATIONS IN EPILAYERS

J. L. Lábár, I. Cora, B. Pécz, Alexander Azarov (University of Oslo) and Andrej Kuznetsov (University of Oslo)

Measurement of strain in epitaxial layers frequently faces the problem of localising "perfectly" unstrained regions to use as a reference for the whole structure. Here, we present a method developed for deducing such references in the unstrained substrate (with one crystal structure) to determine the local lattice deformations in the layer (with another crystal structure). The method works if there is a common sublattice in the layer and the substrate, so that the deviations from it may be used to interrelate the experimentally recorded data. Such a sublattice always exists in an epitaxial layer on a substrate system. The precision of the method is ~0.5% in strain values.

The Common Sublattice Method (CSM) is based on the measurement of electron diffraction patterns from thin lamellae using a Transmission Electron Microscope (TEM) operated in microprobe scanning mode (μP-STEM). It is based on the output of a four-dimensional (4D) Electron Diffraction (ED) dataset processed by the 4D-ED method.

The common sublattice is defined in reciprocal space. Let δ_1 and δ_2 be two predefined small numbers, while $\underline{\mathbf{a}}_1^*$ and $\underline{\mathbf{b}}_1^*$ are the base vectors of lattice$_1$ and $\underline{\mathbf{a}}_2^*$ and $\underline{\mathbf{b}}_2^*$ the base vectors of lattice$_2$. If there exists a pair of reciprocal vectors $\underline{\mathbf{a}}^*$ and $\underline{\mathbf{b}}^*$ that all the reciprocal vectors ($\mathbf{g}_1$) of lattice$_1$ in the 2D observed reciprocal space plane (i.e. the diffraction pattern measured from the given zone axis orientation) are close to $n_1\cdot\underline{\mathbf{a}}^* + m_1\cdot\underline{\mathbf{b}}^*$ (i.e. $|n_1\cdot\underline{\mathbf{a}}^*+m_1\cdot\underline{\mathbf{b}}^*-\mathbf{g}_1|<\delta_1$) and $n_2\cdot\underline{\mathbf{a}}^* + m_2\cdot\underline{\mathbf{b}}^*$ is close to all the reciprocal vectors ($\mathbf{g}_2$) of lattice$_2$ (i.e. $|n_2\cdot\underline{\mathbf{a}}^*+m_2\cdot\underline{\mathbf{b}}^*-\mathbf{g}_2|<\delta_2$) than linear combinations of $\underline{\mathbf{a}}^*$ and $\underline{\mathbf{b}}^*$ with integer multipliers define the common sublattice. Small deviations (δ_1 and δ_2) are treated by separate lattice fitting to each pattern irrespective of the fact that the small deviation was caused by changes in the lengths of the base vectors or in the angle between them or both. The d-values are always measured from the fitted lattice.

Relative lattice distortion (strain) is determined from the d-values in the layer (d_l) and the reference area (d_{ref}).

$$\boldsymbol{\varepsilon} = \frac{\boldsymbol{d_l} - \boldsymbol{d_{ref}}}{\boldsymbol{d_{ref}}} = \frac{\boldsymbol{g_{ref}} - \boldsymbol{g_l}}{\boldsymbol{g_l}}$$

where $g=1/d$ in accordance with convention in electron diffraction.

Our CSM method extends strain measurements in epitaxial layers from the simple case of a cubic layer on a cubic substrate to the general case of a substrate with one crystal structure and a layer on it from another crystal structure. In our method, we calibrate the system by measuring an unstrained reference in the substrate, and the strain in the layer is given relative to the unstrained lattice of the layer based on an interrelation of the two structures. The benefit of the new method over the GPA method is that the new method is insensitive to either variations in the local thickness of the sample or minor variations of bending of the lamella or experimental parameters like camera length and convergence angle. Another huge advantage is that a much larger area can be measured in the TEM as compared to High Resolution Transmission Electron Microscopy (HRTEM)-based methods like GPA. The proof-of-concept is obtained using samples of cubic γ-Ga_2O_3 layers on a monoclinic β-Ga_2O_3 substrate. Our measurements reveal anisotropic lateral strain resulting from the anisotropic lateral mismatch between the cubic γ-Ga_2O_3 layer and the monoclinic β-Ga_2O_3 substrate. The layer was created by Ni-ion irradiation of the monoclinic substrate. Two TEM lamellae were cut from each of the differently heat-treated samples. An as-implanted sample from both [110] and [100] orientations and samples heat-treated at 300°C and 700°C, respectively, from [110] orientations of the γ-phase. Figure 1 shows the measured local lattice deformations together with the changes in crystal structure (Model). Strain is obtained by subtracting the model from the measured lattice deformation as shown in Figure 1.

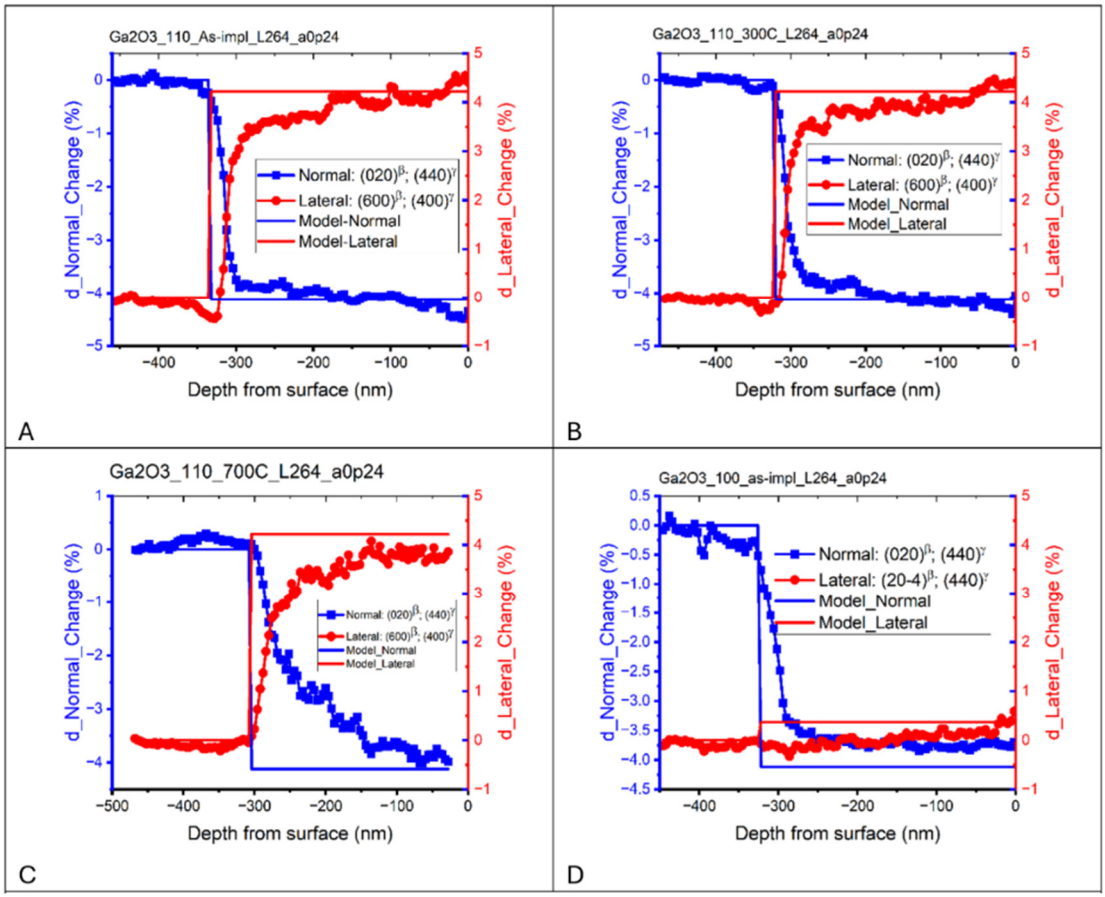


Figure 1: Depth distribution of measured changes in d-values together with changes in d-values of the model. Blue=Normal component. Red=Lateral component. (α=0.24 mrad and L=264 mm). (a) as-impl [110]$^{\gamma}$; (b) 300C [110]$^{\gamma}$; (c) 700C [110]$^{\gamma}$; (d) as-impl [001]$^{\gamma}$. Deviations of the measured values (symbols) from the model (lines) indicate the presence of strain. Notice that the orientations are orthogonal in (a) and (d).

In Figure 2 (as-implanted sample in [110]$^{\gamma}$ orientation), black squares show averaged in-plane (lateral) and out-of-plane (normal) strain components across the layer, including the substrate β-Ga_2O_3 and the transformed γ-Ga_2O_3 layer. Three main parts of the strain curves can be differentiated, which we discuss in detail: 1) the β→γ transformation front, 2) a ca. 35 nm wide range after the transformation front (interface region), where the slope of the strain curves is high, 3) range up to the top of the layer (far from the interface region) where the slope of the strain curves is low. The implantation depth, where the strain curve shows sharp jump/step is measured to be 320 nm (+-10). At the transformation front the top of the β substrate probably shows a little bit of compression strain, while γ shows 3.75 % out-of-plane tensile strain and -4 % in-plane compression strain. After the β/γ transformation front within ca. 35 nm, most of the strain is relaxed and reaches +0.4 the % in normal direction (tensile strain, measurement sets) is shown to provide trend-lines in the individual regions. If we disregard the observed trend in either the substrate region or in the far from interface region and interpret any variation of data as if it were statistical scattering of data, we obtain a conservative overestimation of standard deviation (precision).

Annealing of the sample at 300°C only caused slight changes in the strain curve. The most striking difference compared to the non-annealed sample is the depth of the γ Ga_2O_3 layer, which is ca. 10 nm less, i.e. the thickness of the γ layer has been decreased to ~310 nm. This indicates that (back)transformation from γ→β has started at the interface front. Meanwhile, the compression strain measured at the top of the β substrate in the as-implanted sample disappeared/relaxed. Parallel to this, the compression in-plane and tensile out-of-plane strain seem to slightly increase, but the change is within the error of the measurement. After the transformation front with ca. 35 nm, the slope of the curve is very similar to the strain curves measured from the as-implanted sample. Energy dispersive x-ray spectrum (EDS) depth distributions showed the same Ni distribution in all three samples.

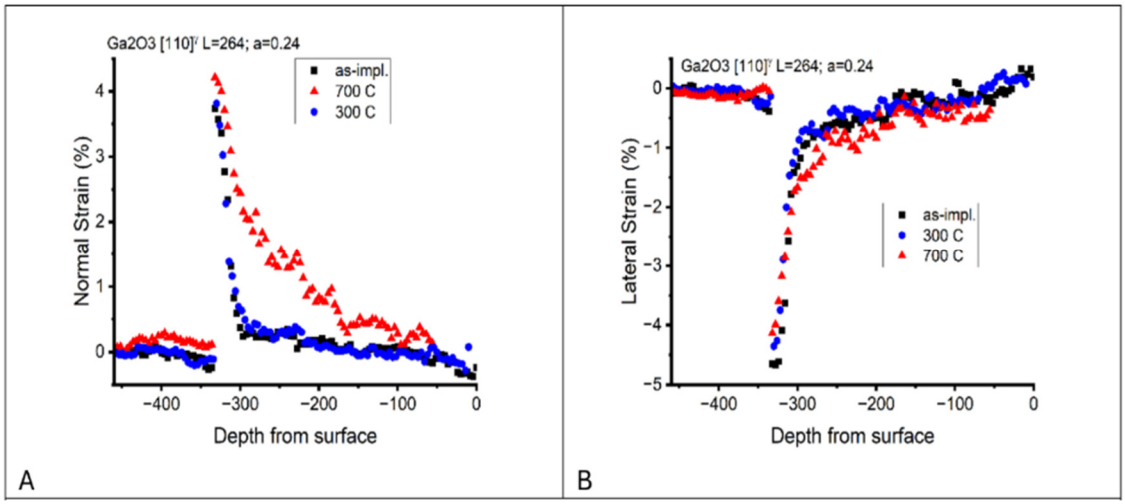


Figure 2: Variation of depth distribution of strain in samples with different heat treatments. (α=0.24 mrad and L=264 mm. Beam direction=sample orientation $[110]^{\gamma}$). Black square=as implanted. Blue circle=heat treated at 300 C. Red triangle=heat treated at 700 C. (a) Normal strain (in direction of $(020)^{\beta}//(440)^{\gamma}$). (b) Lateral strain (in the direction of $(600)^{\beta}//(400)^{\gamma}$). Three spatial sections are identified: Substrate region (from -460 nm to -328 nm), interface region (from -324 nm to -292 nm) and far from interface (close to surface) region (from -288 nm to 0 nm). Strain is close to zero at the substrate region, as expected. A steep change is observed in the interface region. Strain curves for the as-impl and the 300 C samples coincide within the statistical scatter, while the 700 C sample shows a much slower variation of strain in the far from interface region.

Annealing of the sample at 700°C caused more significant changes. At this annealing temperature γ transforms back to β not only at the interface but inside the γ layer as well, as we documented in individual ED patterns. Therefore, the slope of the strain curve after the transformation front shows more tensile out-of-plane and compressive in-plane strain components with slower decrease toward the surface caused by the coexistence of both polymorphs. This also implies the increasing relative amount of β closer to the interface. The maximal measured strain values of the layer at the interface are +4 % tensile out-of-plane strain and -4 % compression in-plane strain. As a continuation of the tendency/trend the transformation front γ→β shifts toward into the layer, which results in a decreased thickness (304 nm+-10 nm) of the layer containing γ phase.

The common sublattice method deduces references in the unstrained substrate (with one crystal structure) to determine the local lattice deformations in the layer (of another crystal structure). The method works if there is a common sublattice in the layer and the substrate (what is fulfilled in all epitaxial configurations), so that the deviations from it may be used to interrelate the experimentally recorded data. The new method overcomes several severe limitations of the geometrical phase analysis method, e.g. of having a limited field of view and requirements to resolve the lattice image, which may be challenged by the camera size for large areas to examine. Furthermore, our method is insensitive to lamella thickness variations. Measurements on lamellae cut from orthogonal crystal orientations revealed non-isotropic lateral strain in Ga_2O_3 layers. The reliability was further proven by collecting data with different camera length, convergence angle conditions, and variable lamellae thicknesses. The consistency of the results shows the usefulness of the method. [1]

Related publication

[1] Lábár et al.; *Local deformations quantified with the common sublattice method,* Nanoscale **18(4),** 2264 (2026) https://doi.org/10.1039/d5nr03934g

EVALUATION METHODS FOR XPS DEPTH PROFILING: A REVIEW

A.S. Rácz, M. Menyhárd

X-ray Photoelectron Spectroscopy (XPS) is a widespread method in modern materials science to study widely varied functional materials (metals, polymers, semiconductors). In most of these applications, there is a need for detailed knowledge of the surface and surface close chemistry. XPS, with its excellent chemical sensitivity, can directly be applied to the analysis of the surface layer in the range of some nms. It is known that its depth resolution is poor because of its relatively high information depth (5-10 nm). Several methods have been developed to solve this problem. An additional problem arises when thicker regions are to be analysed. In this case, it should be combined with various depth profiling techniques, which introduce alterations like mixing, preferential sputtering, roughening, etc. In this case, one should consider both problems: high information depth and altered sample during the evaluation of the measured spectra. In this review, we present the advantages and disadvantages of the techniques available for tackling these issues, focusing mainly on ion etching techniques, monoatomic and cluster argon sputtering, available. We also discuss modern methods like high-energy XPS (HAXPES) and femtosecond Laser Ablation (fs-LA). Evaluation problems are discussed through case studies aiming to provide a guide for choosing between the different methods, highlighting pitfalls and proposing solutions. The different XPS depth profiling methods are summarised in Table 1. [1]

Table 1: Tips for XPS-based analyses for various types of samples

Substance	Method	Advantage	Disadvantage
organics, polymers	GCIB	preserve of chemical bonds	morphology development
thin layers up to 10 nm	No sputter removal ARXPS Tougaard method	preserve of chemical bonds, band structure etc.	thickness limitation, special evaluation methods
buried interfaces	Sputter removal of cover layer until the altered layer reaches the interface: XPS HAXPES	preserve of chemical bonds, band structure etc.	HAXPES: X-ray sensitivity, complex experimental setup, issues with sensitivity factors
layers thicker than 10 nm	monoatomic argon	high sputtering rate, well developed evaluation techniques	argon implantation, preferential sputtering, morphology development, chemical bond alteration
layers thicker than 10 nm containing inorganic compounds	Monoatomic ion + GCIB	might optimize the damage reasonable sputtering rate	complex experiment no sufficient understanding of GCIB effects
sensitive inorganics	GCIB	preserve of chemical bonds	low sputtering rate preferential sputtering, morphology development
thick inorganics	fs laser ablation	preserve of chemical bond high sputtering rate	new technique, little experiences, not for thin layers

Related publication

[1] AS Racz, M. Menyhard: *Evaluation methods for XPS depth profiling; A review,* Appl. Surf. Sci. Advances **30,** 100872 (2025) IF=8.7, D1 https://doi.org/10.1016/j.apsadv.2025.100872

EFFECT OF NON-SPHERICAL SHAPE OF DRY POWDER AEROSOL DRUGS ON THEIR AIRWAY DEPOSITION DISTRIBUTION

T. Kolonits, Sz. Kugler (EKBI), P. Füri (EKBI), A. Nagy (Wigner FKI), Á. Farkas (EKBI)

During the research, 5 commercially available aerosol drugs were investigated in aspect that in which part of the airways, and in what size and shape distribution do they deposit. These drugs are currently used in the therapy of Chronic Obstructive Pulmonary Disease (COPD) and/or asthma as short- or long-acting bronchodilators and anti-inflammatory cortico-steroids. The commercial names of the drugs are: Bretaris® Genuair®, Buventol® Easyhaler®, Trelegy® Ellipta®, Ultibro® Breezhaler® and Symbicort® Turbuhaler®.

The lung was emulated with a so-called cascade impactor, to which the inhalers were connected with 3D-printed adapters. A scanning electron microscope was used to quantify the size and shape ("non-sphericity") of the particles. The latter is important because in medical R&D flow simulations, drug particles are considered spherical. Comparing our measurement data with numerical models, we found that although the particles visibly deviate from the spherical shape, neglecting the irregular shape does not lead to a major distortion of the simulation results. There is one exception: in the case of one drug (Trelegy® Ellipta®), we have observed small, elongated fibres. These fibres already showed significantly different behaviour than spherical particles, which is manifested in a significant increase in their deposition in the terminal bronchioles, immediately before the respiratory bronchioles [1].

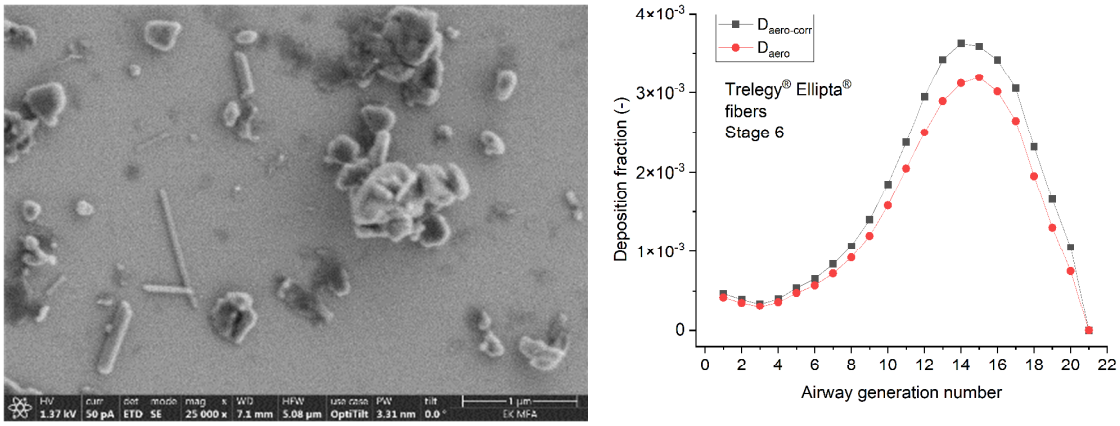


Figure 1: Left: quasi-spherical and fibre-like particles found in Trelegy® Ellipta® Right: bronchial deposition fractions of the fibres with and without considering the diameter correction with the shape factor.

Related publication

[1] T. Kolonits, Sz. Kugler, A. Nagy, P. Füri, R. Ambrus, S. Kheirandish, A. Horváth, Á. Farkas: *Effect of non-spherical shape of dry powder aerosol drugs on their airway deposition distribution,* International Journal of Pharmaceutics **671,** 125209 (2025) https://doi.org/10.1016/j.ijpharm.2025.125209

MICROCOMBINATORIAL PREPARATION AND CHARACTERISATION OF MULTICOMPONENT THIN FILMS

OTKA K 143216

Gy. Sáfrán, M. Serényi, D. Olasz, E. Dódony, T. Kolonits, I. Cora, V. Kovácsné Kis, N. Szász, A. Jakab, A. Kovács, P. Petrik, M. Fried, Zs. Zolnai

The mid-term performance of our project was rated excellent by the OTKA Committee in 2024. In 2025, we continued and further developed the single-sample-based microcombinatorial method that had been elaborated for a comprehensive investigation of the composition-dependent properties of binary and ternary thin films. The results have led to several scientific publications [1] - [7].

1. Development of a simplified combinatorial thin film growth and characterisation technique

With the participation of Gergő Dobrik, Noémi Szász, Peter Petrik and Levente Illés, we are developing a simplified combinatorial thin film deposition and characterisation technique that enables the efficient combinatorial preparation and investigation of 3–4 component thin film systems. A patent application based on this technical solution is planned for submission in 2026.

2. Microcombinatorics combined with variable pulsed gas inlet (GPC)

By combining microcombinatorics with variable pulsed gas inlet (GPC) using new Bronkhorst mass flow controllers, cathode poisoning during reactive sputtering can be avoided, thereby eliminating abrupt changes in the sputtering regime and in film properties.

This method was applied to the combinatorial growth of RF-sputtered ternary thin film systems, namely various (Si–Ga–Al) -oxynitrides, and to the investigation of their optical and structural properties, in collaboration with researchers Miklós Serényi and Marcell Gajdics, and PhD student Dániel Olasz.

3. Cooperative Doctoral Program (KDP) – PhD work of Dániel Olasz

Within the framework of the Cooperative Doctoral Program (KDP) associated with the OTKA project, PhD student Dániel Olasz is conducting research entitled "Composition-dependent structural and mechanical properties of binary thin films" in collaboration with university supervisor N. Q. Chinh (ELTE).

The student prepared Al–Cu, Y–Ti–O and Al–O–N thin films with compositions varying over the entire concentration range. Transmission electron microscopy (TEM), ellipsometry, and nanoindentation measurements were performed to characterise their structural, morphological, and material properties, i.e. hardness, deformation mechanisms, optical refractive index, amorphous and crystalline phases and their composition.

The publication on the Al–Cu system appeared in January 2026. The first version of the PhD dissertation has been completed, and the defence is planned for 2026.

4. PhD work of Erzsébet Dodony – Me-silicide thin films

Also methodologically connected to the present OTKA project is the PhD work of Erzsébet Dodony entitled "Formation of Me-silicide thin films." The candidate has completed her PhD dissertation and successfully passed the internal (pre-defence) examination. The thesis has been officially submitted to the ELTE Doctoral School of Physics, and the public defence is expected in 2026.

5. Application of microcombinatorial TEM in catalysis research – methane pyrolysis at the nanoscale

The principal investigators of the internal EK project entitled "Application of microcombinatorial TEM in catalysis research; methane pyrolysis at the nanoscale." are Anita Horváth, EKBI and György Sáfrán, MFA.

Combinatorial Mo–Ni nanocrystalline bimetallic catalysts with composition varying continuously within a single sample were investigated by TEM and EDS to determine their composition, structural, and morphological properties. This method enables efficient optimisation of bimetallic catalyst composition to maximise catalytic activity and lifetime.

We demonstrated that at high temperatures (600–900 °C), the Au TEM grid is unstable; Au diffusion occurs, and the presence of gold has a degrading effect on methane decomposition catalysis. A peer-reviewed publication has resulted from this work.

6. Development and optimisation of gold nanocrystal biosensors

In collaboration with the Photonics Laboratory led by Péter Petrik, we contributed to the development of gold nanocrystal biosensors based on the influence of plasmonic effects evoked by various applied molecules. The particle morphology and

size distribution were combinatorially optimised by preparing and annealing graded-thickness thin films, followed by TEM and ellipsometric characterisation and testing with water ethanol and RAMAN MBA reporter molecules

7. Ellipsometric phase mapping of combinatorial thin film systems

Together with the Photonics Laboratory led by Péter Petrik, we worked on a patentable method and technical solution for comprehensive composition- and temperature-dependent ellipsometric characterisation and phase mapping of two-component combinatorial thin film systems. The related patent application is under preparation. Submission is expected in 2026.

Related publications

[1] A. Horváth et al.: *Dramatic interference of Au TEM grid with model and supported MoNi/MgO catalysts during high temperature reduction and methane decomposition,* Materials Today Nano **32,** 100690 (2025) IF: 8.2 https://doi.org/10.1016/j.mtnano.2025.100690

[2] E. Dodony et al.: *Structural variability of gamma Ni-silicides,* Journal of Alloys and Compounds **1036,** 181554 (2025) IF: 6.3 https://doi.org/10.1016/j.jallcom.2025.181554

[3] M. Gajdics et al.: *A Study of HiPIMS Process Characteristics in SiO_2 Deposition,* Coatings **15(9),** 1023 (2025) IF: 2.8 https://doi.org/10.3390/coatings15091023

[4] M. Gajdics et al.: *Assistance to Determine the Stability State of a Reactive Sputtering Process Based on the Analytical Solution of the Classical Berg Model,* Coatings **15,** 499 (2025) IF: 2.8 https://doi.org/10.3390/coatings15050499

[5] N. Q. Chinh et al.: *Indentation size effects and its relevance to ultrafine-grained materials,* Materials Science and Engineering **A 923,** 147733 (2025) IF: 7.0 https://doi.org/10.1016/j.msea.2024.147733

[6] D. Mukherjee et al.: *Optimized sensing on gold nanoparticles created by graded-layer magnetron sputtering and annealing,* Sensors and Actuators B: Chemical **425,** 136875 (2025) IF: 7.7 https://doi.org/10.1016/j.snb.2024.136875

[7] D. Olasz et al.: *Comprehensive characterisation of the Al–Cu binary thin film system: Correlation between composition, microstructure and mechanical properties,* Journal of Alloys and Compounds **1051,** 186114 (2026) https://doi.org/10.1016/j.jallcom.2026.186114

COMBINATORIALLY OPTIMISED SENSORICS OF SPUTTERED GRADIENT GOLD NANOPARTICLE LAYERS

OTKA K 143216, KDP-2021 scholarship

D. Mukherjee, K. Kertész, Zs. Zolnai, Z. Kovács, A. Deák, A. Pálinkás, Z. Osváth, D. Olasz, A. Romanenko, M. Fried, S. Burger, Gy. Sáfrán, P. Petrik

Within our institution, within the framework of cooperation between two laboratories (Thin Film Physics and Photonics), Au nanoparticles with gradually changing properties were produced on fused silicon dioxide using DC magnetron sputtering and annealing in order to find the range in the sample that provides the best response, i.e., to optimise the plasmonic sensing of molecules. The combinatorial gradient approach [1] resulted in a linear change in the effective thickness of the deposited Au on the substrate.

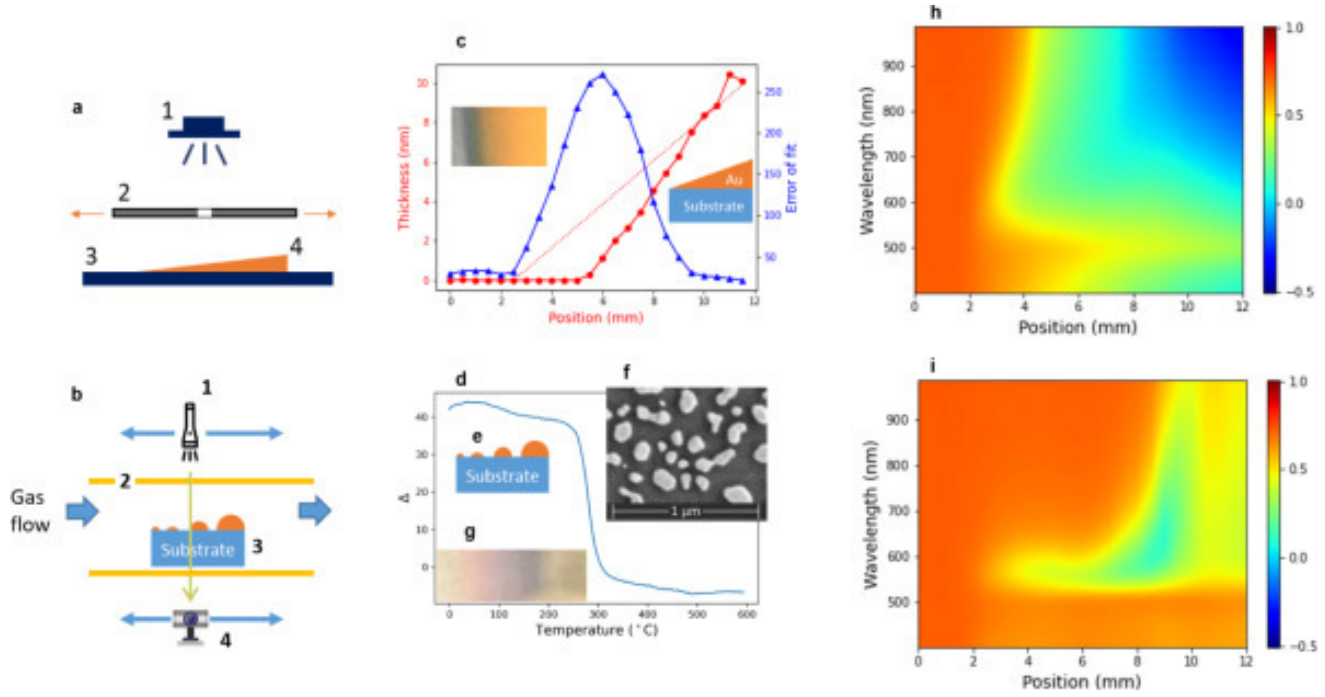


Figure 1: (a) Set-up for micro-combinatorial deposition (1) magnetron sputtering source, (2) moving slit, (3) substrate, and (4) graded-thickness gold layer. (b) Optical transmission cell with (1) light source, (2) glass chamber, (3) substrate with annealed nanoparticles and (4) spectrometer. (c) Thickness vs. position (red circles), effective thickness (also called 'mass thickness' corresponding to the deposited amount of material (dotted line), and error of fit for the as-deposited graded Au sample 'B' measured by Spectroscopic Ellipsometry (SE). (d) Change of measured thickness by SE as a function of temperature during annealing at the position at 8 mm on sample 'B.' (e) Schematic, (f) scanning electron micrograph (at a position of 8 mm), and (g) optical image of the sample after annealing. (h) and (i) show m33 spectra on sample 'B' over the range of positions from 0 to 12 mm for the as-deposited and 300 °C annealed state, respectively.

Scanning optical spectroscopies [2] were used to characterise the optical and sensing properties for water, ethanol and Mercaptobenzoic Acid (MBA) reporter molecules, as a function of equivalent deposited thickness di. The best gas sensing positions along the sample were found for di values of 2–4 nm, explained by the high surface density of gold particles and the high ratio of covered area in this region. The covalently bonded Raman reporter MBA molecules can be detected most sensitively at the highest plasmon peak region of di ≈ 7 nm when using ellipsometry. However, the most sensitive region for the Raman measurement of the MBA molecules is at di ≈ 1.6 nm. The formation and sensing performance of the layers were modelled and explained using finite element calculations. We have shown that our combinatorial sputtering method for arbitrary thickness and composition profiles can accurately and quickly locate optimal sensing parameters [3]. It supports the discussion of theoretical and experimental considerations due to the large amount of data generated by quick optical scanning. The present results also show that our approach is suitable for the high-throughput testing of new materials and structures and for creating experimental databases for theoretical analysis and machine learning.

Acknowledgements

This publication was supported by the Cooperative Doctoral Programme of the Ministry of Innovation and Technology, KDP-2021, Doctoral Student Scholarship Programme, funded by the National Research, Development and Innovation Fund. The research was also supported by the OTKA grants 146181, K-143216, K-134258 and PD-146479.

Related publications

[1] G. Sáfrán: *"One-sample concept" micro-combinatory for high throughput TEM of binary films,* Ultramicroscopy **187,** 50 (2018) https://doi.org/10.1016/j.ultramic.2018.01.001

[2] B. Kalas G. Sáfrán M. Serényi M. Fried P. Petrik: *Scanning-resonance optical sensing based on a laterally graded plasmonic layer-optical properties of Ag_xAl_{1-x} in the range of x=0 to 1,* Appl. Surf. Sci. **606,** 154770 (2022) https://doi.org/10.1016/j.apsusc.2022.154770

[3] D. Mukherjee, K. Kertész, Zs. Zolnai, Z. Kovács, A. Deák, A. Pálinkás, Z. Osváth, D. Olasz, A. Romanenko, M. Fried, S. Burger, G. Sáfrán, P. Petrik: *Optimized sensing on gold nanoparticles created by graded-layer magnetron sputtering and annealing,* Sensors and Actuators: B. Chemical **425,** 136875 (2025) https://doi.org/10.1016/j.snb.2024.136875

DRAMATIC INTERACTION BETWEEN THE AU TEM GRID AND SAMPLE AS WELL AS SUPPORTED MONI/MGO CATALYSTS

Application of Micro-Combinatorial TEM in Catalysis Research (EK internal project)

A. Horváth, M. Németh, A. Beck, D. Olasz, M. Serényi, Gy. Sáfrán

The decomposition of methane in an inert atmosphere—also known as methane pyrolysis—produces CO_2-free "turquoise" hydrogen and solid carbon. The MgO-supported bimetallic molybdenum–nickel (MoNi) catalyst exhibits promising synergistic effects in this reaction. Our objective was to efficiently investigate how variations in the Mo/Ni ratio influence catalytic performance, with particular emphasis on carbon deposition. A novel micro-combinatorial TEM technique was successfully applied, in which magnetron sputtering was used to generate Mo–Ni nanoparticles with a continuous compositional gradient on a SiO_x-coated gold TEM grid, presumed to remain stable even at high temperatures [1]. Post-treatment of the model catalyst sample at 800 °C in diluted hydrogen resulted in uniform particles with varying compositions.

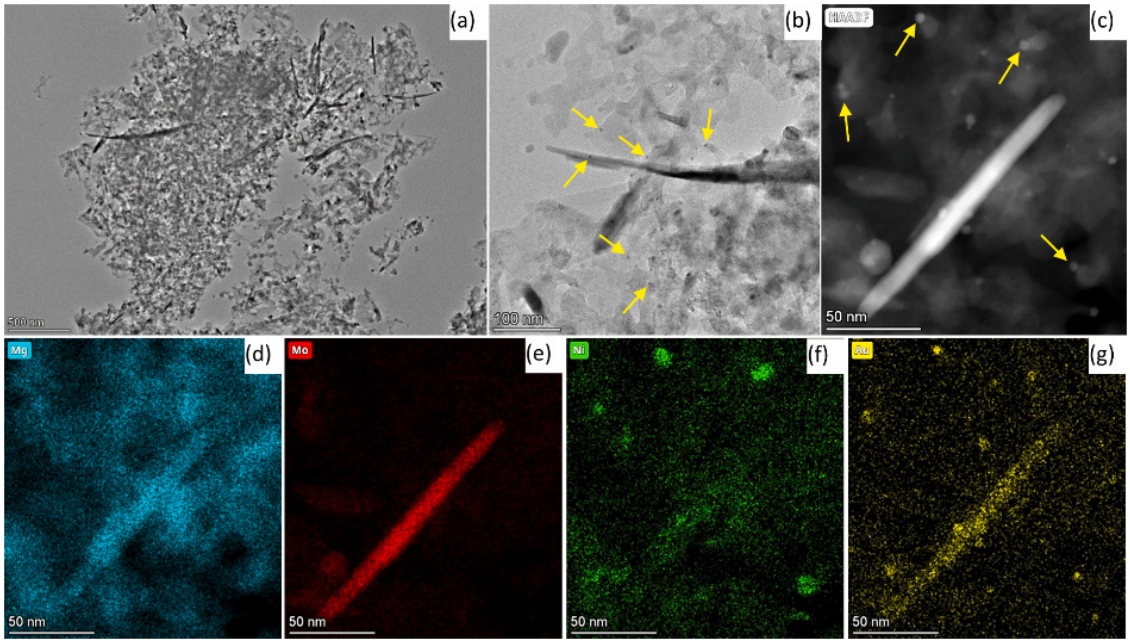


Figure 1: TEM micrographs of the supported MoNi/MgO powder catalyst deposited on a C/Au grid and subjected to reduction and reaction treatment at 800 °C: a) TEM overview image; b) high-magnification image, with dark-contrast Au particles indicated by arrows; c) selected area for further STEM–EDS analysis, Au particles marked by arrows; d) STEM–EDS Mg map; e) Mo map; f) Ni map; g) Au map of the same area.

However, methane treatment experiments revealed a significant limitation: at high temperatures, the gold and SiO_x components of the TEM grid interacted with the catalyst, leading to partial segregation and oxidation of Mo and Ni, thereby inhibiting carbon formation. A model MoNi sample sputtered onto an MgO-coated carbon membrane supported on a gold TEM grid exhibited similar gold-induced effects—mixed metal oxides formed, but no carbon. Interestingly, when a MoNi/MgO powder catalyst was placed onto the gold grid, no carbon formation occurred either. In contrast, in control experiments conducted without the gold grid—as expected—carbon nanotubes were formed. These results highlight the critical influence of the TEM grid material on catalytic behaviour and suggest that gold may actively suppress coke formation. This could be valuable in reactions where the inhibition of coking is desirable.

Related publication

[1] A. Horváth, M. Németh, A. Beck, D. Olasz, M. Serényi, Gy. Sáfrán: *Dramatic interference of Au TEM grid with model and supported MoNi/MgO catalysts during high temperature reduction and methane decomposition,* Materials Today Nano **32,** 100690 (2025) https://www.sciencedirect.com/science/article/pii/S258884202500121X

STRUCTURAL STUDY OF (001) RUTILE-TYPE GeO_2 SEMICONDUCTOR ON RUTILE (TiO_2)

MTA NKM2023-15/2023

I. Cora, B. Pécz (HUN-REN EK)
P. Mazzolini, M. Bosi, G. Cicconi, F. Mezzadri (IMEM CNR, Uni. of Parma)
A. Ugolotti, Leo Miglio (Uni. of Milano)

The ultra-wide bandgap semiconductor rutile germanium oxide (r-GeO_2, Eg ≈ 4.6 eV) is gaining momentum in the quest for novel materials for power electronics. In this work, we experimentally and theoretically investigate the physical mechanisms behind the nucleation and growth of epitaxial (001) r-GeO_2 on isostructural r-TiO_2 substrates via Metalorganic Vapour Phase Epitaxy (MOVPE) using isobutylgermane and O_2 precursors. In the identified deposition window, the thin film growth seems to be affected by partial GeO suboxide desorption, and we observe that the layers are always composed of r-GeO_2 islands embedded and/or surrounded by amorphous material. Ge/Ti interdiffusion at the epilayer-substrate interface is found at the base of each r-GeO_2 island; combining experimental analysis and multiscale theoretical simulations, we discuss how such a process is fundamental to achieve partial strain mitigation, allowing for the nucleation of epitaxial r-GeO_2 and suggest, in this regard, a limiting threshold to avoid the formation of amorphous material. Moreover, we shed light on the formation of different facets in r-GeO_2 at early stages of growth and after merging of islands. [1]

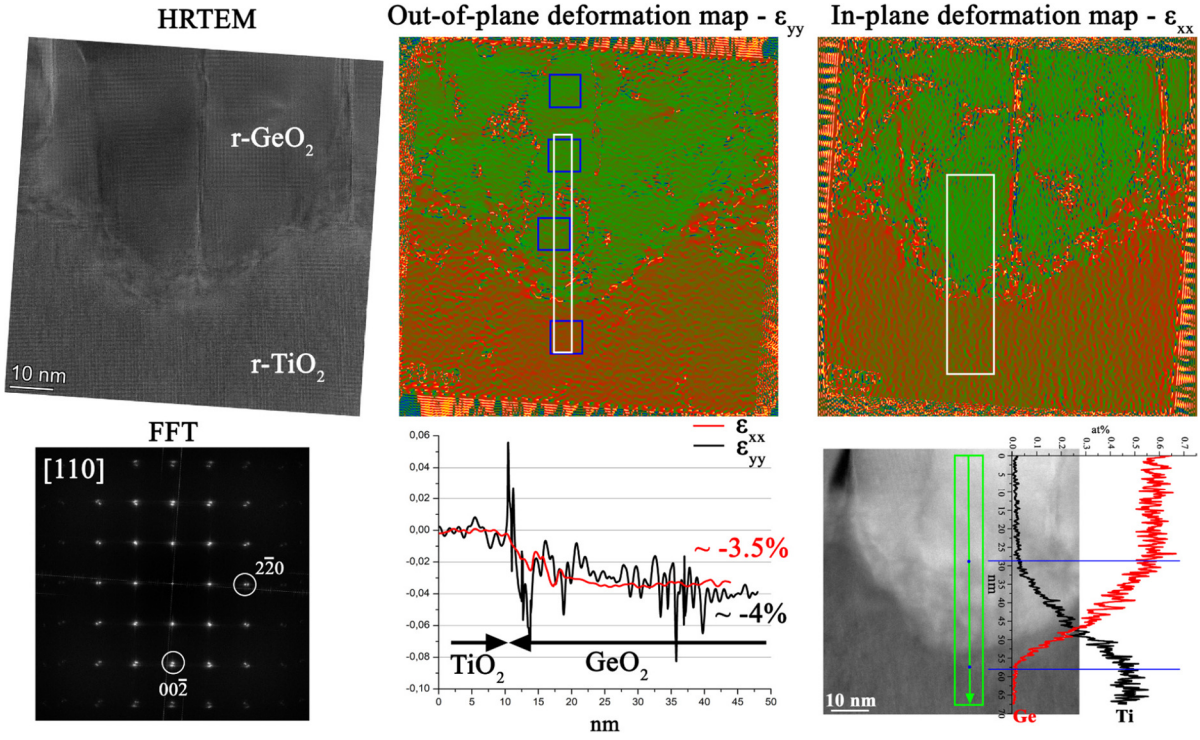


Figure 1: Geometric Phase Analysis (GPA) was performed from HRTEM images of the intermixing region, obtaining ε_{xx}, ε_{yy} deformation maps. The HRTEM image with the corresponding FFT, ε strain/deformation maps and integrated EDS line-profiles of Ti and Ge are shown on the HAADF image in [110] projection (sample #212). ε_{xx} and ε_{yy} strain/deformation maps were calculated using periodicities signed on the FFT. TiO_2 was selected as the reference. The integrated and averaged deformation values inside the white rectangles are presented below the maps. The average out-of-plane deformation values calculated inside the blue rectangles are the following; r-TiO_2: ε_{yy} =0.0004(50), and r-GeO_2: ε_{yy} =-0.027(14) in the mixing area at the interface, ε_{yy} =-0.040(7) and ε_{yy} =-0.040(7) above. ε_{xx} =-0.035(10) is more homogeneous in the root part of the r-GeO_2 crystal and above.

Related publication

[1] G. Cicconi, M. Bosi, F. Mezzadri, A. Ugolotti, I. Cora, L. Seravalli, H. Tornatzky, J. L¨ahnemann, M.R. Wagner, P. Bhatt, P.K. Thakur, T.-L. Lee, A. Regoutz, A. Baraldi, D. Bersani, L. Cademartiri, A. Parisini, B. Pecz, L. Miglio, R. Fornari, P. Mazzolini: *Nucleation and faceting in (001) r-GeO_2 heteroepitaxy on r-TiO_2 by metalorganic vapor phase epitaxy,* Applied Surface Science **725,** 165788 (2026) https://doi.org/10.1016/j.apsusc.2025.165788

EFFECT OF NITROGEN CONTENT ON MICROSTRUCTURE AND MECHANICAL PROPERTIES OF DC MAGNETRON SPUTTERED CRMNMOSIY(N) HIGH ENTROPY COATINGS

L. Vrána, T. Stasiak, M. Fekete, V. Buršíková, Zs. Czigány, K. Balázsi, P. Souček

This study investigates Cr-Mn-Mo-Si-Y-(N) high-entropy alloy and high-entropy nitride coatings, with a focus on their structural, compositional, and mechanical properties [1]. These coatings were developed using reactive DC magnetron sputtering in an Ar/N_2 atmosphere, combining strong and weak nitride-forming elements with significant differences in atomic radii. The nitrogen content in the coatings was found to saturate below 45 atomic per cent (at. %), stabilised by nitrogen vacancies. Bias applied during deposition did not influence the chemical composition or microstructure. Increasing the N_2 flow rate led to a reduction in the deposition rate due to target poisoning while also increasing the nitrogen content until saturation was reached. Microstructural analysis revealed that coatings deposited at room temperature formed an amorphous structure, while formation of nanocrystals occurred at a substrate temperature of 580 °C in coatings containing more than 40 at. % nitrogen. The coatings exhibited a distinctive structure with alternating Cr-Mo-rich and Si-Mn-rich nanolayers (Figure 1). These layers showed significant compositional variability, with Cr and Si demonstrating the greatest changes. Cr-Mo-rich layers contained FCC nanocrystallites, whereas Si-Mn-rich layers remained amorphous due to the weak nitride-forming properties of Mn and the lattice distortion introduced by Si and Y.

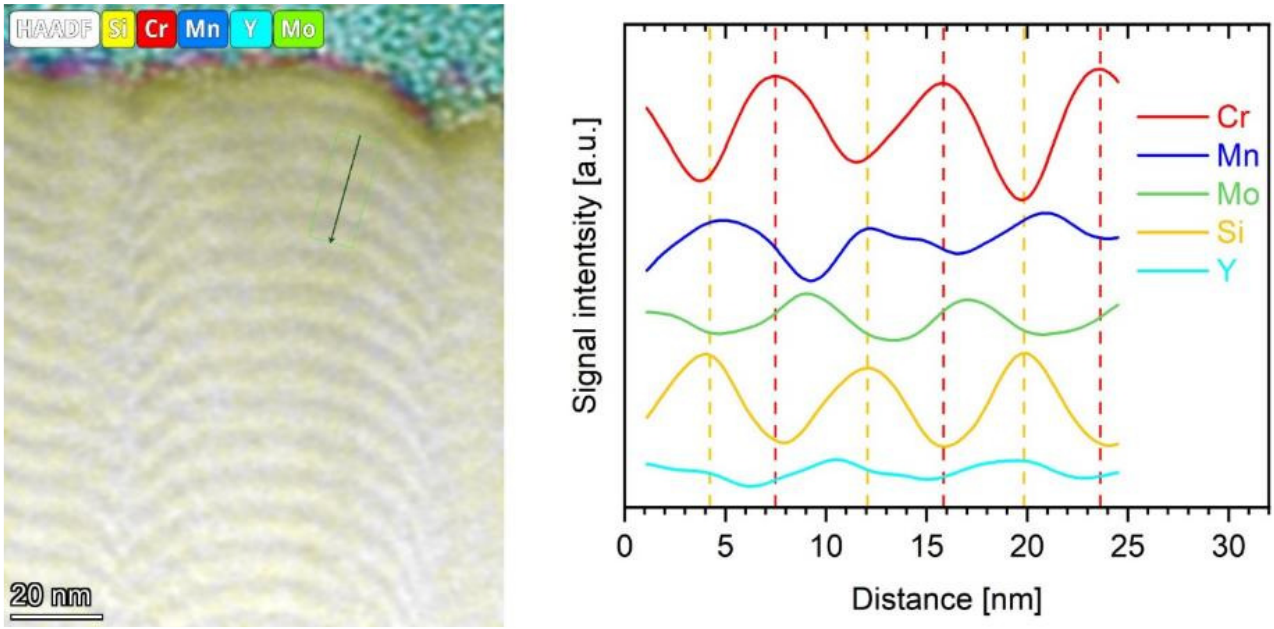


Figure 1: Line profile in the EDS elemental map indicating the concentration correlation of Cr with Mo and Si with Mn

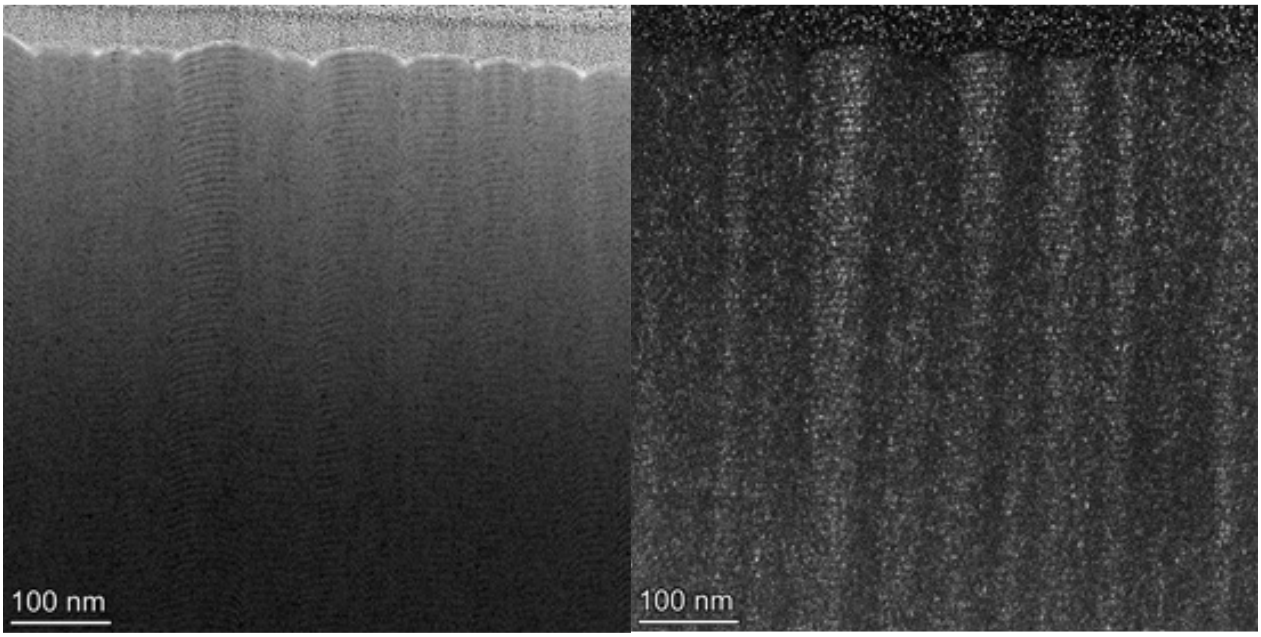


Figure 2: Bright and dark field images of the Cr-Mn-Mo-Si-Y-(N) high-entropy nitride coating deposited at 580 °C and 100 V bias. The bright contrast in the DF image indicates the location of the crystalline fcc phase.

The evidence for the alternation of amorphous and crystalline phases is the bright field (BF) and dark field (DF) image pairs: the crystalline layers are a bit darker in BF images, and these layers contain some distinct bright spots (crystallites) in DF images (Figure 2). High-resolution TEM images also confirmed this nanostructure. The mechanical properties of the coatings improved significantly with nitrogen incorporation and a substrate temperature of 580 °C. At these conditions, the coatings achieved a peak hardness of 15.5 GPa and a reduced modulus of 195.1 GPa. Elastic deformation parameters (H/E) and plastic deformation parameters (H^3/E^2) reached values of 0.09 and 0.12 GPa, respectively, indicating enhanced durability and resistance to mechanical deformation. The study also highlighted the influence of deposition geometry, substrate rotation, and elemental targets in forming the alternating nanolayer structure. The phase separation observed between Cr-Mo-rich and Si-Mn-rich layers suggests a potential chemical separation mechanism, warranting further investigation. Nitrogen incorporation and a substrate temperature of 580 °C emerged as key factors driving the improved structural and mechanical performance of the coatings. These findings provide valuable insights into the development of high-entropy nitride coatings, positioning them as promising candidates for advanced material applications.

Related publication

[1] L. Vrána, T. Stasiak, M. Fekete, V. Buršíková, Z. Czigány, K. Balázsi, P. Souček: *Effects of Nitrogen Content on Microstructure and Mechanical Properties of DC Magnetron Sputtered CrMnMoSiY(N) High Entropy Coatings*, Surface & Coatings Technology **497,** 131742 (2025) https://doi.org/10.1016/j.surfcoat.2025.131742

BIOMINERALISATION AT THE NANOSCALE

OTKA K 125100

V. Kovácsné Kis, Zs. Kovács (ELTE), M. Hegedűs (ELTE), N. Rózsa (Semmelweis University), É. Mlinkó (Semmelweis University), Z. Szekanecz (University of Debrecen), L. Illés, N. Szász, L. Vásárhelyi (University of Szeged), Á. Kukovecz (University of Szeged), H. Schwarcz (McMaster University), N. Nassif (CNRS LCMCP)

In 2025, we published two important papers in the field of Ca-phosphate biomineralization, both were preceded by a couple of years of research.

Bone apatite crystal structure [1]. While detailed multiscale models explain the complex hierarchical structure of bone, there has been an unresolved paradox between bone apatite nanomorphology dominated by large (010) facets and apatite hexagonal crystal structure. Crystal structure studies of bone apatite are difficult due to intimate structural intergrowth with the organic matrix and small crystal size (2-6 nm thickness along b and 30-40 nm width). Our high-resolution TEM (HRTEM) analysis (Figure 1) of isolated individual Mineral Platelets (MPs) shows that the MPs are polycrystalline, composed of crystallites whose **c**-axes are mostly co-aligned with a few degrees of misorientation, forming mesocrystalline assemblies. Based on Fast Fourier Transform analysis of HRTEM images of nanocrystals, we propose a monoclinic structure with a(mon)=a(hex), b(mon)=2a(hex), c(mon)=c(hex). The monoclinic model resolves the paradox and explains nanomorphology in terms of crystal structure. Moreover, it allows the development of non-equivalent (010) facets with different composition, polarity and atomic arrangement. As a consequence, the orientation of the (010) crystal surface relative to collagen becomes biologically significant, which was presumed in previous studies [2].

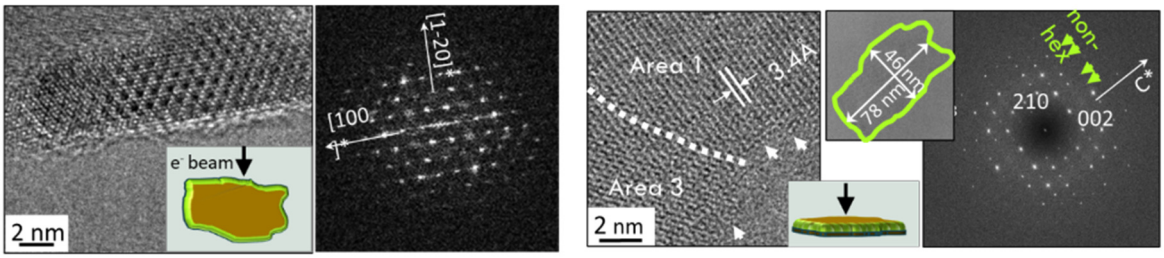


Figure 1: Edge view (left) and plane view (right) HRTEM of individual bone mineral platelets with their corresponding FFTs. Features deviating from hexagonal symmetry are indicated in the plane-view FFT.

Monoclinic crystal structure of bone apatite was verified inside bone tissue, using cryo-Ar milled thin sections as well. We also show that the same monoclinic structure appears in plate-like crystals of biomimetic apatite used successfully for bone regeneration [3].

Ribbon-like hypomineralization in human enamel [4]. Molar-Incisor Hypomineralization (MIH) is a developmental enamel disorder with up to 14 % prevalence, characterised by reduced mineral content, hypersensitivity, and post-eruptive enamel breakdown. As the causes of this disorder remain unclear to date, MIH, including the optimisation of treatment strategies, is an area of intensive investigation. We have reported a new form of hypomineralization with an uncommon appearance in dental practice for the first time. We have compared structural and chemical alterations in teeth exhibiting this Ribbon-Like Hypomineralization (RLH) to the characteristics of sound and MIH-affected teeth.

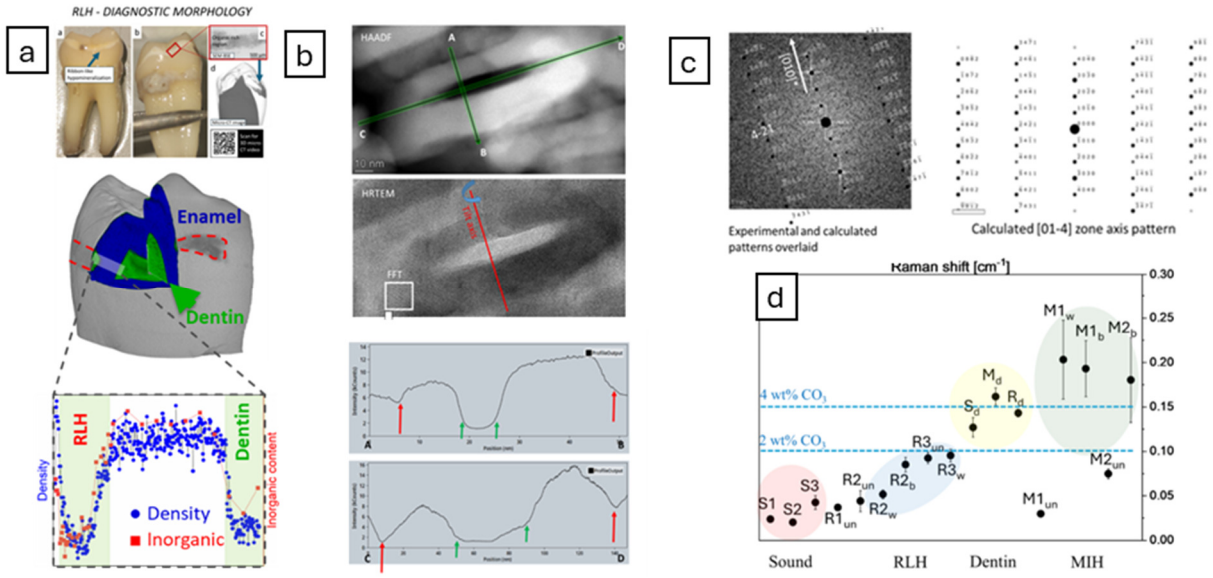


Figure 2: (a) Diagnostic appearance of RLH enamel and density change shown by micro-CT. b) HAADF and HRTEM of hollow nanocrystals characteristic of RLH enamel. (c) Simulated SAED shows that asymmetric contrast gradient around the core of the crystals, observed on HAADF, is due to a small tilt. (d) Raman spectral parameters of RLH enamel allow clear distinction from MIH enamel.

Microporosity, mineral density and characteristic 3D macroscopic shape of the RLH affected volumes were captured by micro-CT analysis. On the submicron-scale (Figure 2), nanoporosity, unusual nanocrystal morphologies and reduced size of apatite nanocrystals have been revealed. These RLH specific features are coupled with a particular chemical fingerprint in Raman spectroscopy, which allows its clear separation from MIH-affected and sound enamel. Based on these nanostructural features, we conclude different failure mechanisms in the biochemical control during crystallisation of the RLH and MIH enamel.

Acknowledgement: Funding of this study was provided by the National Research, Development and Innovation Fund Office, Hungary (grant number 125100, V.K.K.). Some aspects of hypomineralized enamel research were funded by ÚNKP-23-3 New National Excellence Program of the Ministry for Culture and Innovation of Hungary (M.H.).

Related publications

[1] V.K. Kis, H.P. Schwarcz, N. Nassif, Z. Szekanecz: *Bone mineral platelets are mesocrystals formed by monoclinic nanocrystals,* Communications Mater. **6,** 1–8. (2025) https://doi.org/10.1038/s43246-025-00890-4

[2] J. Tao, K.C. Battle, H. Pan, E.A. Salter, Y.C. Chien, A. Wierzbicki, J.J. De Yoreo: *Energetic basis for the molecular-scale organisation of bone,* PNAS **112(2),** 326–331 (2015) https://doi.org/10.1073/pnas.1404481112

[3] M. Robin, E. Mouloungui, G. Castillo Dali, Y. Wang, J-L. Saffar, G. Pavon-Djavid, T. Divoux, S. Manneville, L. Behr, D. Cardi, L. Choudat, M.M. Giraud-Guille, A. Meddahi-Pellé, F. Baudimont, M.L. Colombier, N. Nassif: *Mineralized collagen plywood contributes to bone autograft performance,* Nature **636,** 100 (2024) https://doi.org/10.1038/s41586-024-08208-z

[4] M. Hegedűs, Zs. Kovács, L. Vásárhelyi, Á. Kukovecz, L. Illés, N. Szász, É. Mlinkó, N.K. Rózsa, V.K. Kis: *Ribbon-like hypomineralization in human dental enamel,* Acta Biomaterialia **196,** 281 (2025) https://doi.org/10.1016/j.actbio.2025.02.064

PREPARATION AND INVESTIGATION OF BIOPOLYMER COMPOSITE MATERIALS CONTAINING CALCIUM PHOSPHATE DOPED WITH MG AND ZN COMPONENTS

OTKA FK 146141

M. Furkó

A novel method for producing porous biopolymer composite scaffolds doped with bioactive Mg- and Zn-containing calcium phosphate (mCaP) was developed.

Two polymers were used as matrices: a natural polymer, Cellulose Acetate (CA), and a synthetic polymer, polycaprolactone (PCL). The biomineralized calcium phosphate particles were synthesised via wet chemical precipitation, followed by the addition of organic biominerals, such as magnesium gluconate and zinc gluconate, to enhance the bioactivity of the pure CaP phase. The morphological and chemical characteristics of the two composite types were evaluated, as well as the impact of biomineralisation on the particle structure of pure CaP. The precipitated mCaP primarily consisted of nanocrystalline apatite, and the addition of organic trace elements significantly influenced morphology by reducing particle size. FE-SEM EDS confirmed the successful incorporation of mCaP particles into both the CA and PCL polymer matrices. Short-term immersion tests revealed slow degradation rates for both composites, with moderate and gradual ionic dissolution observed via ICP-OES measurements. The PCL-based composite exhibited minimal weight loss during immersion, decreasing by only 0.5%, while the CA-based composite showed an initial slight weight gain before gradually decreasing over time. The morphology of the composites is shown in Figure 1.

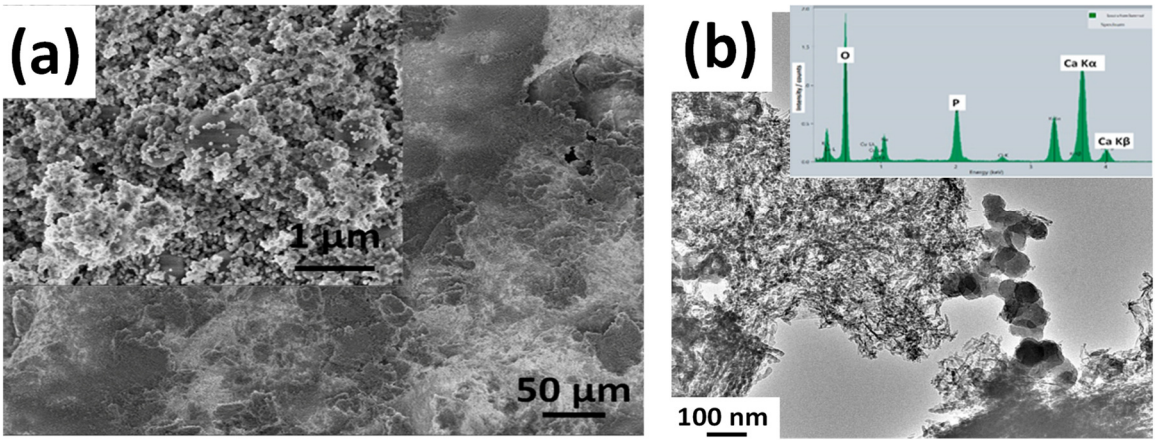


Figure 1: Scanning electron microscope image (a), low-magnification TEM image (b) and the corresponding EDS of PCL-mCaP composite

The changes in both morphology and weight of the composites were monitored over a short-term (two weeks) immersion period to assess the biodegradability of the composite samples and to gain insights into the morphological changes caused by the soaking procedure in general. In addition, we measured the concentrations of the dissolved calcium, magnesium, zinc, and phosphorus ions by ICP-OES at different time intervals. Figure 2 illustrates the morphology of CA-mCP and the PCL-mCP samples as prepared and after two weeks of immersion in saline solution.

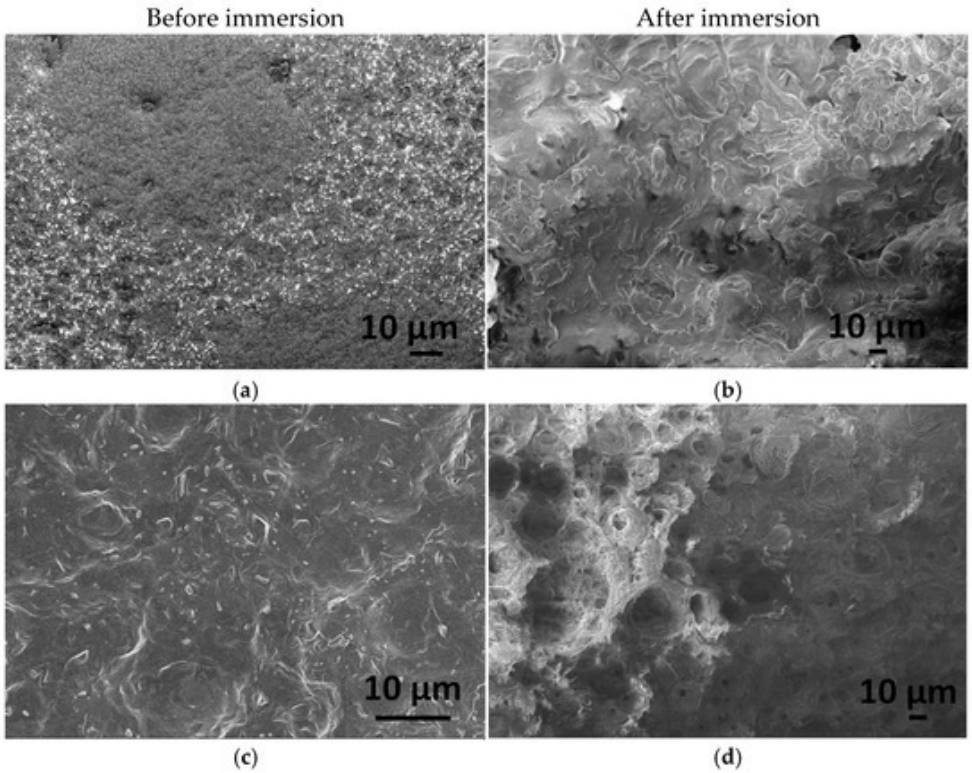


Figure 2: FE-SEM images of CA-mCP (a) and PCL-mCP (c) composites, as well as CA-mCP (b) and PCL-mCP (d) composites, after two weeks of immersion in saline solution

SYNTHESIS AND CHARACTERISATION OF HYDROXYAPATITE FROM EGGSHELLS

B. Almássy, K. Balázsi and Cs. Balázsi

The objective of the PhD research of Boglárka Almássy (Óbuda University) is to develop a novel and efficient synthesis route for hydroxyapatite (HAp) from eggshells. The work aims to systematically optimise all controllable synthesis parameters in order to replicate the structure and properties of natural bone, producing a highly biocompatible and bioactive material for bone tissue engineering applications.

The pure hydroxyapatite (HAp) was successfully produced by using eggshells as a calcium precursor. The calcined eggshells were reacted with diammonium hydrogen phosphate in a mechanochemical method using attritor milling. Half of the synthesised samples were subjected to a second calcination process. The structures of the samples were investigated by scanning electron microscopy, X-ray diffraction, and Fourier transform infrared spectroscopy. As-milled samples had pure, nanosized HAp particles, while the secondarily calcinated samples exhibited larger, well-defined, porous, closely resembling natural HAp structures. This sintered sample has high potential for bone tissue engineering applications due to its morphology and structure.

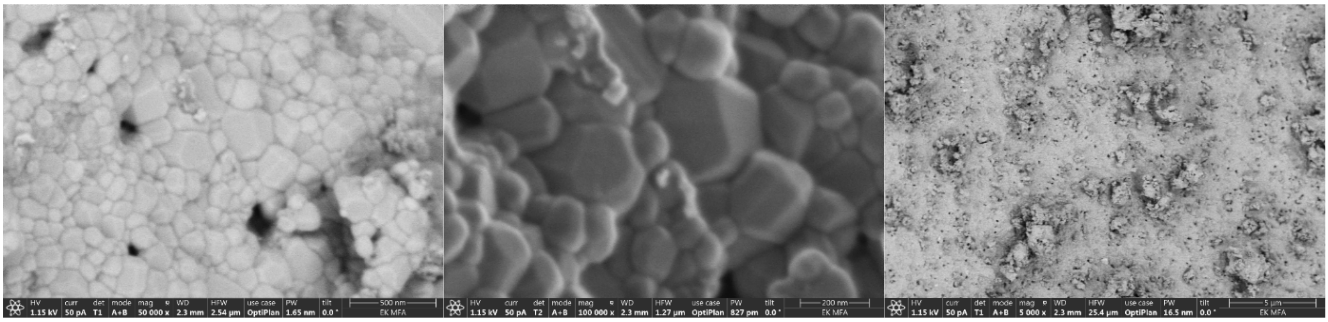


Figure 1: SEM micrographs of the HAp sample obtained at different magnifications. The high-magnification images reveal well-defined crystalline particles with faceted surfaces. Pores can be observed between the agglomerated particles, while the lower magnification image provides an overview of the porous architecture of the material. The presence of an interconnected pore network is important for bone-related applications. It can support tissue ingrowth and osseointegration.

HUNGARIAN CHIPS COMPETENCE CENTRE (HCHIP)

101217997 — HCHiP — DIGITAL-Chips-2024-SG-CCC-1, 2025-1.3.4-KDT_HCHIP-2025-00001

K. Balázsi, P. Fürjes, C. Balázsi, J. Volk

The Hungarian Chips Competence Centre (HCHiP) was established in line with the objectives of the European Chips Act to strengthen Hungary's role in the semiconductor ecosystem (Figure 1). The Centre is implemented in cooperation with three key domestic institutions – Bay Zoltán Applied Nonprofit Ltd., as the consortium leader, Budapest University of Technology and Economics and HUN-REN Centre for Energy Research as consortium members. The competence centre, which has been operating since March 2025, aims to make state-of-the-art technologies, educational opportunities and research infrastructure available to domestic companies, especially Small and Medium-sized Enterprises (SMEs). HCHiP provides access to design and manufacturing platforms, pilot production lines and European research networks through the network of chip competence centres (aCCCess - www.acccess.eu), while supporting technology transfer, innovation and professional training.

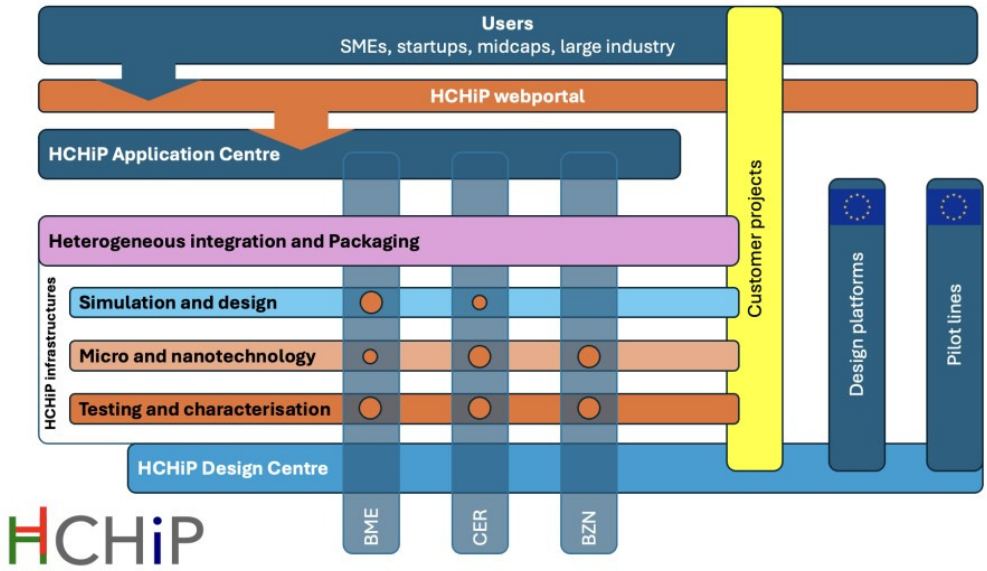


Figure 1: Structure of HCHiP competence centre (www.hchip.eu)

The main objective of WP4 led by HUN-REN EK is to create the technological framework that enables the connection of the infrastructures and their interoperability.

Define and create a fully interoperable connected infrastructure capable of extensively and efficiently supporting the pilot development of the users of the Chips Competence Centre.

Demonstrate the technological connectivity and interoperability within the Competence Centre through a selected development case study.

Identify the external technological gateways to industrial service providers and other EU CCs to reach EU compatibility.

The HUN-REN EK undertakes tasks in the fields of research, technological development, prototyping services and education, and leads the "Development of Infrastructure Interoperability" work package in the project. The main competencies of the research centre are micro- and nanotechnology solutions, chip packaging and integration techniques; thin films, complex material systems, ceramic substrates and their manufacturing technologies; and the development and application of state-of-the-art material testing techniques. The cleanroom infrastructure, featuring available micro- and nanomechanical technologies, is suitable for 3D machining of 4" diameter semiconductor/glass/polymer substrates, development and electro-mechanical integration of mechanical, chemical and biosensors, and optoelectronic devices. Our specialists are able to successfully support chip development and manufacturing processes in the modelling, design, prototyping and functional validation stages.

NEUTRON ABSORPTION IN THIN BORON CARBIDE LAYERS

OTKA K 143263, TKP2021-NVA-03

Z. Zolnai, Z. Kis (HUN-REN EK Nuclear Analysis and Radiography Department), N. Q. Khánh, Z. Kovács, G. Battistig

Boron-based neutron absorbers offer a promising alternative to their competitors, e.g. ^{6}Li-based ones. The benefits of using boron are as follows: (i) ca. four times higher capture cross-section of ^{10}B for thermal (cold) neutrons as compared to that of ^{6}Li. (ii) less kinetic energy of 2.79 MeV in the ^{10}B(n,α)^{7}Li neutron capture reaction is distributed on the reaction products as compared to the ^{6}Li(n,α)^{3}H neutron absorption process with a higher energy release of 4.78 MeV. Consequently, there are shorter stopping ranges of the reaction products in the neutron absorber and in the coupled scintillator layer for ^{10}B as compared to ^{6}Li. (iii) Such features enable reduced neutron absorber thickness and more confined light production volume for scintillation-type isotopically enriched ^{10}B-based neutron detector structures.

A favourable boron-containing neutron absorber material is boron carbide [1], with unique physical properties beneficial for a wide range of applications. The high melting point and thermal stability enable its use as a refractory material. It can also be applied as abrasive powder and coating, as well as in ballistic performance due to its low density and high hardness. Usually, the composition of boron carbide layers prepared by different technologies varies in the range B_4C – $B_{10}C$.

In nuclear science applications, a simple construction for neutron detection may be a thin boron carbide neutron absorber layer on top of an efficient scintillator substrate. In this case, 1.47-MeV α and 0.84-MeV Li^+ particles, emitted in the ^{10}B(n,α)^{7}Li reaction, induce ion-induced light emission, i.e., ionoluminescence (IL) in the scintillator. A promising scintillator material is e.g. Al_2O_3, with intense IL light emission and high radiation resistance [2]. The left panel in Figure 1 shows schematics of a $^{10}B_5C/Al_2O_3$ scintillation-based planar neutron detector structure.

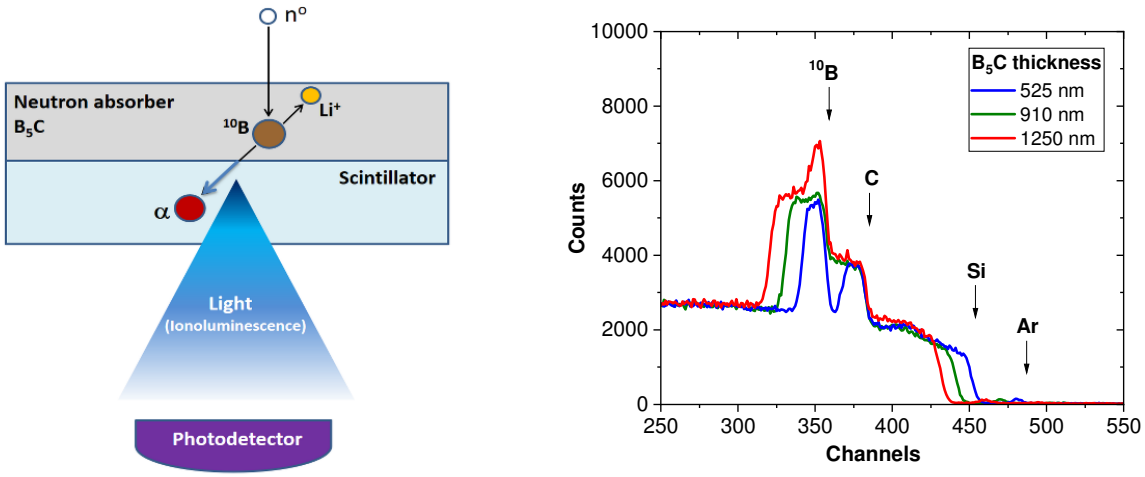


Figure 1: Left: Schematics of a scintillation-based planar neutron detector structure. Right: 1.6 MeV proton-EBS spectra of 10B5C layers with varying thickness deposited on Si substrate. Arrows represent spectral edge positions for different components.

In this case, geometrical optimisation based on well described energy conversion processes in the system results in effective neutron capture and detection. We deposited isotopically enriched $^{10}B_5C$ layers (boron-rich boron carbide) on Si substrates by pulsed DC-sputtering. The right panel in Figure 2 shows 1.6 MeV proton-EBS (Elastic BackScattering) spectra of our $^{10}B_5C$ layers with varying thickness deposited on Si. ^{10}B/C atomic ratios and boron carbide layer thicknesses were determined from the proton-EBS spectra with good accuracy.

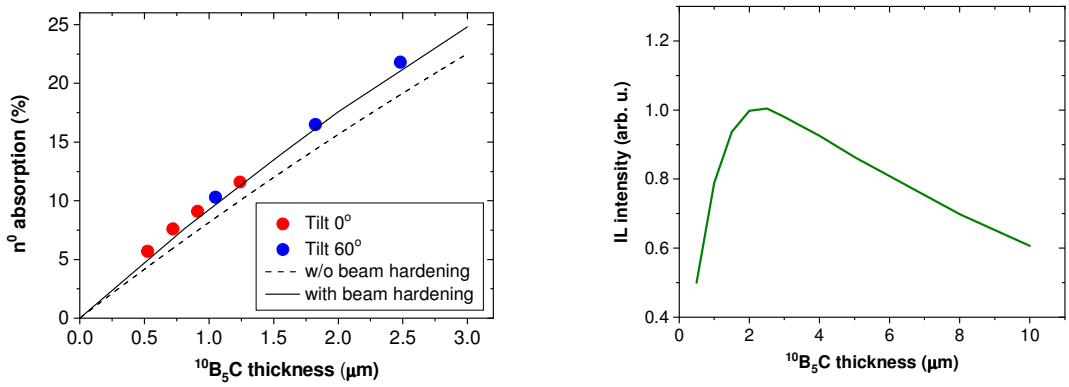


Figure 2: Left: Neutron absorption as a function of $^{10}B_5C$ layer thickness. Dots represent experimental data recorded at 0° and 60° sample tilt angle, while the solid (dotted) line shows calculated values with (without) taking into account beam hardening for neutrons. Right: Calculated normalised light (ionoluminescence, IL) yield of the scintillator vs. $^{10}B_5C$ layer thickness for a planar neutron detector structure shown in Figure 1.

Neutron absorption experiments on the $^{10}B_5C$ layers were performed with a poly-energetic cold neutron beam at the NORMA station of the Budapest Neutron Centre (BNC) [3-4]. The left panel in Figure 2 shows neutron absorption as a function of deposited $^{10}B_5C$ layer thickness. NORMA measurements were performed at two different sample tilt angles of 0° and 60° with respect to the neutron beam. There is good agreement between measured and calculated absorption values when the $^{10}B_5C$ layer-induced beam hardening (change of the neutron energy spectrum after crossing through an absorbent layer) for the poly-energetic neutron beam is taken into account, see the black solid line in Figure 2.

The right panel in Figure 20 shows the calculated normalised light yield (IL intensity) of the scintillator as a function of deposited $^{10}B_5C$ layer thickness, for a $^{10}B_5C/Al_2O_3$ planar neutron detector structure. The interplay between neutron absorption in the $^{10}B_5C$ layer and the IL emitted by the α and Li^+ ions due to their electronic stopping in Al_2O_3 results in a maximum IL yield for a $^{10}B_5C$ layer thickness of ca. 2.5 μm, see the green line in Figure 2.

Our experiments with thin $^{10}B_5C$ layers as neutron absorbers show that effective neutron capture and energy conversion into ionoluminescence light intensity can be achieved already at a small boron carbide layer thickness of 2.5 μm and a simple planar detector geometry.

Related publications

[1] https://bnc.hu/norma/

[2] Z. Baji, Z. Kovács, Z. Szabó, O. Hakkel, A. Sulyok, Z. Fogarassy, Z. Bérces, J. Volk: *Controlled nucleation of metal-sulfide layers via surface functionalization with sulfur species: Enhanced initial growth of GaS_x thin films,* Journal of Vacuum Science & Technology **A 44,** 032402 (2026) https://doi.org/10.1116/6.0005254

[3] G. Csaba and W. Porod: *Coupled oscillators for computing: A review and perspective,* Applied Physics Reviews **7(1),** 011302 (2020) https://doi.org/10.1063/1.5120412

[4] H. Liu, et al.: *Artificial Neuronal Devices Based on Emerging Materials: Neuronal Dynamics and Applications,* Advanced Materials **35,** 2205047 (2023) https://doi.org/10.1002/adma.202205047

CONTROLLED NUCLEATION OF METAL SULPHIDE LAYERS VIA SULPHUR-BASED SURFACE FUNCTIONALISATION: ENHANCED INITIAL GROWTH OF GaS_x THIN FILMS

OTKA FK 139075, 2024-1.2.2-ERA_NET-2025-00025, TKP2021-NKTA-05, Bolyai Scholarship

Zs. Baji, Z. Kovács, Z. Szabó, O. Hakkel, A. Sulyok, Zs. Fogarassy, Zs. Bérces, J. Volk

Atomic Layer Deposition (ALD) allows nanometre precision control of film thickness, chemical composition, and conformality. Transition metal chalcogenides and related sulphides have attracted considerable interest. One persistent problem with sulphide ALD is the poor nucleation on SiO_2. Untreated Si-oxide surfaces contain an insufficient number of OH sites, which leads to island formation and non-uniform early-stage growth. Additionally, sulphides adhere poorly to oxygen-terminated surfaces and tend to agglomerate.

This work demonstrates that surface chemistry critically determines sulphide ALD nucleation behaviour. Replacing surface -OH groups with sulphur-containing sites provides more chemically compatible nucleation sites for metal-sulphide ALD. GaS_x ALD serves as a model system to illustrate how surface chemistry governs nucleation, coalescence dynamics, and island morphology.

The GaS_x films were grown at 200 °C in a Picosun R 200 reactor using $Ga_2(NMe_2)_6$ (heated to 135 °C) and H_2S. The as-grown films were amorphous, smooth (RMS ~0.4 nm), and optically transparent. XPS confirmed uniform Ga:S ≈ 1:1 composition throughout the depth, with negligible oxidation. The optical band gap (~4 eV) is consistent with amorphous GaS_x.

The nucleation behaviour on different SiO_2 surfaces was examined, and it was found that an island-like growth occurs on native oxide, CVD and thermal oxide surfaces on Si. According to the XPS measurements, GaS layers grown on thermal oxide exhibited a 30% higher nucleation density than those on native oxide, and CVD oxide had a 90% higher surface coverage, suggesting that the chemical and structural characteristics of the oxide layer play a significant role.

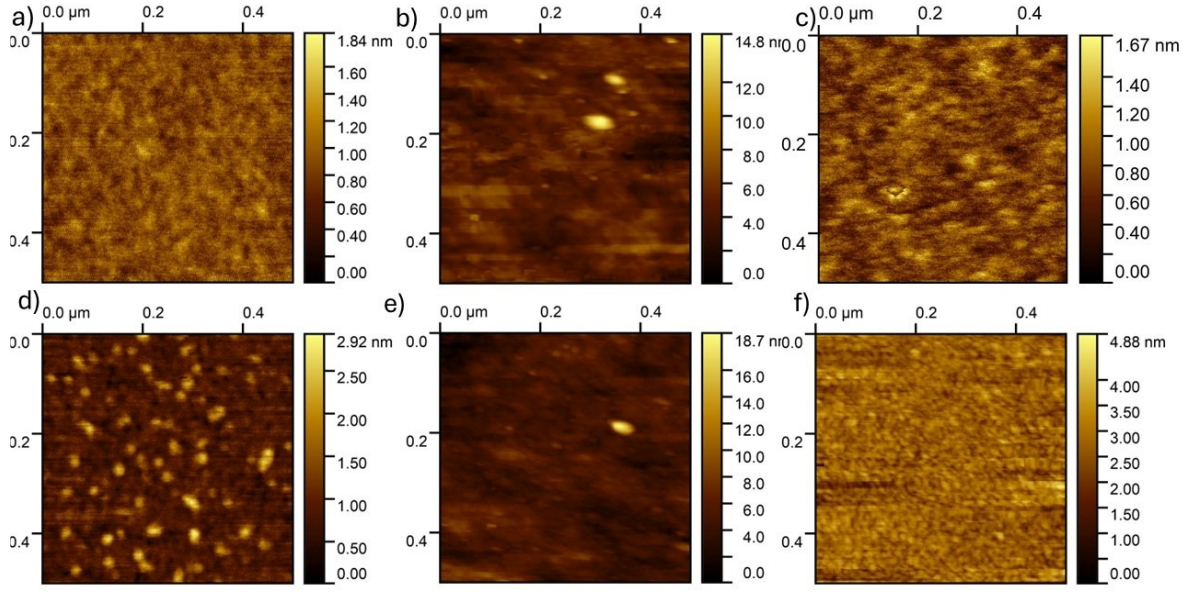


Figure 1: The surfaces of the different oxides: (a) native Si-oxide, (b) CVD oxide and (c) thermal oxide; and their morphologies after 15 deposition cycles: (d) deposition on native oxide, (e) deposition on CVD oxide, and (f) deposition on thermal oxide.

Nucleation of ALD layers is often enhanced by increasing the -OH coverage with a chemical pretreatment. This was attempted with a Piranha treatment, which enhanced the chemisorption of the gallium precursor, thus, these samples showed higher island densities and partial coalescence after only 5 cycles. However, agglomeration remained an issue: sulphides preferentially bond to themselves rather than to –OH, causing clustering and slow lateral growth, thus, hydroxylation improves nucleation quantity but not chemical compatibility.

The novelty of the present work lies in the approach of modifying the surface with sulphide-containing anchoring species. The applied three different surface functionalization approaches investigated in this study are shown in Figure 2.

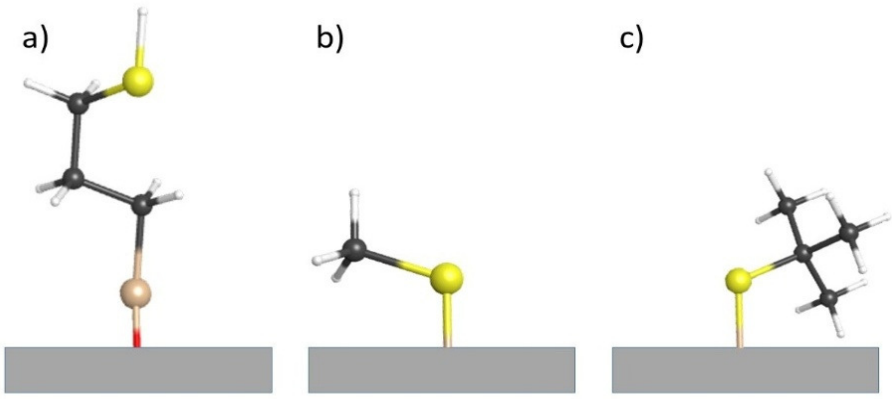


Figure 2: Schematic illustration of the three surface functionalisation approaches applied to silicon oxide substrates before GaS_x deposition: (a) silane-based thiolation using mercaptopropyl-trimethoxysilane, yielding an organic spacer layer terminated with –SH groups; (b) gas-phase treatment with DMDS (c) or DTBDS producing sulphur-containing surface species. The grey line represents the native Si-oxide surface covered by surface hydroxyl groups.

Mercaptopropyl-trimethoxysilane introduces surface $-(CH_2)_3-SH$ groups. While XPS confirmed successful thiol adsorption, AFM showed increased roughness and non-ideal morphology. The presence of an organic spacer layer introduced steric effects and heterogeneous surface energies. GaS_x coverage improved but did not reach the quality needed for uniform sulfide nucleation.

Gas-phase dialkyl disulfides treatments offer a cleaner and easier sulphur-functionalisation pathway. Dimethyl disulfide (DMDS) and di-tert-butyl disulfide (DTBDS) are sulphur-containing ALD precursors that can be in-situ used in the ALD reactor by pulsing them onto the substrate surface prior to deposition. DMDS dissociatively chemisorbs, yielding CH_3S- surface groups. This resulted in the highest nucleation density among single-step treatments, with a uniform and fine island distribution. XPS showed ~2.6× higher Ga content after 20 cycles, and a near-continuous coverage was measured with AFM after 15–20 cycles. DTBDS treatment yielded an improved nucleation relative to untreated Si but was less effective than DMDS due to steric hindrance from bulky tert-butyl groups, limiting the density of accessible sulphur sites.

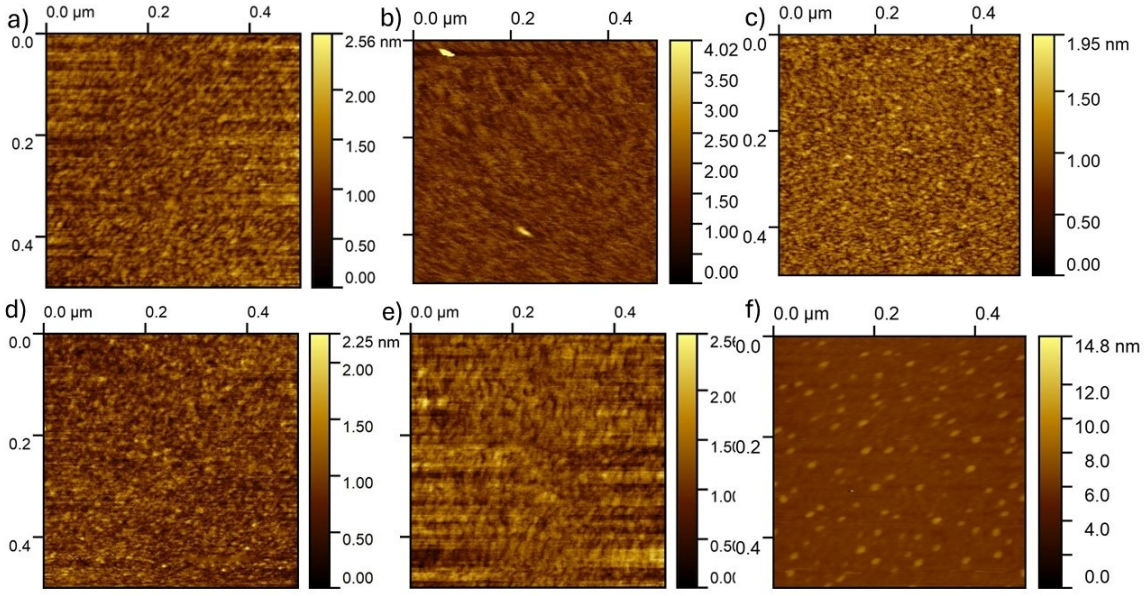


Figure 3: AFM micrographs of (a) 5 cycles of GaS_x on native oxide covered Si, (b) the same with piranha pretreatment, (c) DMDS pretreatment, (d) di-tert-butyl-disulfide pretreatment, (e) piranha+dmds pretreatment, and (f) thiolation with mercaptopropyl-trimethoxysilane

Our findings establish sulphur-based surface functionalisation as a powerful and general strategy to improve nucleation in sulphide ALD for GaS, VS_x, ZnS, and potentially TMDC systems. [1]

Related publication

[1] Z. Baji, Z. Kovács, Z. Szabó, O. Hakkel, A. Sulyok, Z. Fogarassy, Z. Bérces, J. Volk: *Controlled nucleation of metal-sulfide layers via surface functionalization with sulfur species: Enhanced initial growth of GaS_x thin films,* Journal of Vacuum Science & Technology **A 44,** 032402 (2026) https://doi.org/10.1116/6.0005254

ULTRAFAST OSCILLATORS MADE OF NANOSCALE VO_2 MEMRISTORS FOR NEUROMORPHIC ELECTRONICS

OTKA K 143282

Zs. Pollner (BME), T. N. Török (BME), L. Pósa, M. Csontos, S. W. Schmid (BME), H. Kim, A. Piqué, J. Volk, and A. Halbritter (BME)

Oscillatory neural networks (ONNs) have emerged as a promising solution to overcome the von Neumann bottleneck in data processing, which limits the speed and efficiency of traditional computing architectures. ONNs leverage the inherent oscillatory properties of volatile memristors to perform computations in a parallel and energy-efficient manner, offering a significant advantage over conventional systems [1]. In particular, the performance of ONNs is directly influenced by the frequency of oscillations; higher oscillation frequencies enable faster and more energy-efficient computations, thereby reducing the overall computing time and energy consumption. Vanadium dioxide (VO_2) memristors have garnered significant interest in the field of neuromorphic computing due to their unique property of undergoing an insulator-to-metal transition (IMT) near T = 67 °C [2], [3]. This characteristic enables them to function as dynamic memory elements with applications in ONNs [4].

A traditional VO_2 oscillator circuit (see Figure 1.a) consists of a serial resistor, the memristor and a parallel capacitance. The primary function of the series resistor in this circuit is to establish a voltage divider, thereby ensuring that when the memristor is in its high resistance state, it undergoes a high voltage, so an electronically induced insulator-to-metal transition happens. However, in its low resistance state, the memristor is subjected to a reduced voltage, which induces it to switch off immediately. The capacitance in the circuit is the main decisive factor of the oscillation frequency. One can measure the voltage drop on the memristor (Figure 1.c), blue trace) and the current passing through the memristor (Figure 1.c), black trace) and easily determine the frequency. Our goal was to design a circuit which can exceed the previously reported highest 10 MHz oscillation frequency [5]. With our simplified oscillator circuit (Figure 1.b), it is possible to reach ultra-fast 167 MHz oscillations as shown in Figure 1.d. In this circuit, we measure only the flowing current to reduce the measurement system impact on the circuit.

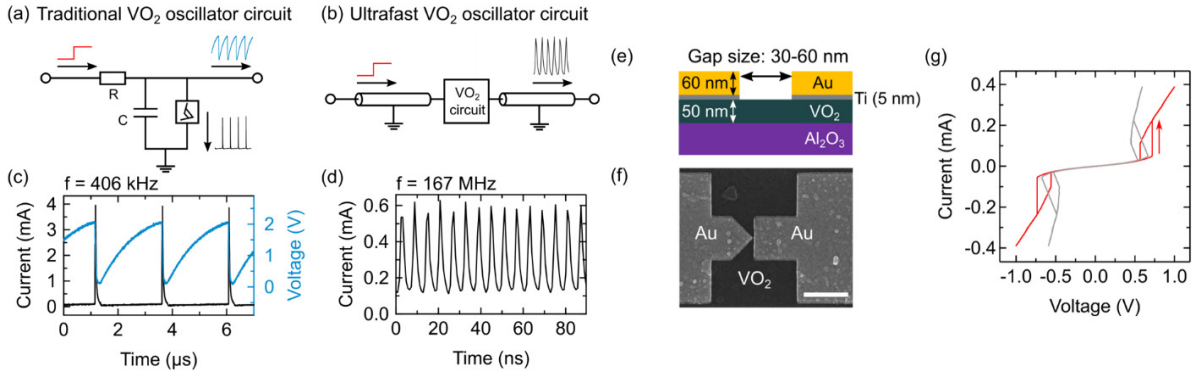


Figure 1: Device characteristics and comparison of high and low frequency oscillations. (a) Low frequency oscillator setup. (b) High frequency oscillation setup. (c) Low frequency oscillation waveforms showing the measured current (black) and voltage drop on the memristor (blue). (d) Measured current waveform of the highest frequency oscillation at 167 MHz. (e) Schematic of the memristor device highlighting the small device size. (f) Scanning electron micrograph of a representative VO_2 memristor, scale bar: 1 µm. (g) Low-frequency I(V) graph of a VO_2 device as a function of driving voltage (red) and as a function of the bias voltage measured on the memristor (grey).

This noteworthy frequency advancement was made possible by the creation of a simplified and optimised electrical circuit, coupled with the use of memristors featuring small active domain sizes of ~30 nm. The schematic vertical cross-section of our planar, ≈30 nm gap size devices is shown in Figure 1.e. For the high-frequency experiments, the use of a doped Si substrate would be disadvantageous due to the high stray capacitance towards the substrate, so a well-insulating Al_2O_3 substrate was applied. The 50 nm thick epitaxial VO_2 layer was deposited on the substrate by the pulsed laser deposition method according to [6]. The 60 nm thick gold top electrodes were patterned by standard electron beam lithography, also using a 5 nm Ti adhesive layer underneath.

A key feature of the structure is the asymmetric lateral geometry (Figure 1.f): a rectangular electrode on one side faces a V-shaped electrode on the other side. This geometry enables the production of ultrasmall (≈30 nm) gap sizes and the confinement of the active region in an ultranarrow, nanoscale spot [7]. This confined geometry is considered crucial for the ultrafast operation, as well as for achieving sufficiently low switching threshold voltages at room temperature [8]. The electrical switching is represented by the *I(V)* curves of our devices in Figure 1.g, where the red trace shows the measured current as a

function of the V_{drive} *drive voltage* applied to the VO_2 memristor and the R_S = 1050 Ω resistor in series, whereas the grey graph is the function of the $V_{bias}=V_{drive}-I\cdot R_S$ voltage drop on the memristor.

Figure 2.a depicts the circuit diagram of the ultrafast oscillator measurements. Note that at both ends, impedance matched output/input of the function generator/oscilloscope were used. The signals were transmitted via coaxial cables to a coplanar waveguide PCB, where an SMD resistor *R* was connected to the memristor. This sample holder has *C* < 2 fF capacitance, which does not affect the oscillations in the ~ 100 MHz regime. Compared to the traditional oscillator circuit (see Figure 1.a), the key difference is that capacitance is omitted from the circuit, and two factors can limit the oscillation speed in such circuits: (i) the finite times required for the operation of the memristor, the inner set/reset timescales of the device, and (ii) the *d* distance between the resistor and the memristor, which introduces a finite voltage build-up time in the circuit.

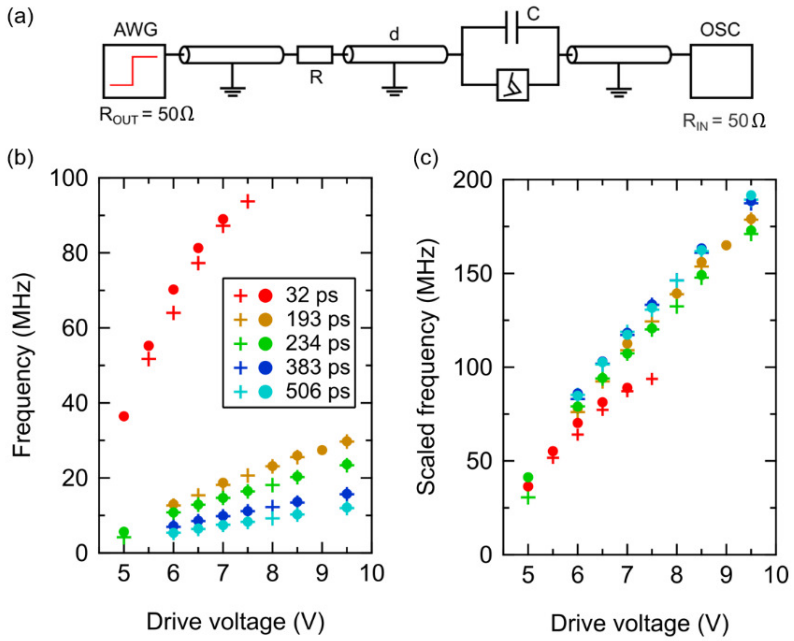


Figure 2: In-depth experimental results concerning distance limitation. (a) Circuit schematics used for achieving ultrafast oscillations and to study distance limitation. (b) Drive voltage and distance dependence of the achieved oscillation frequency. Different colours show different memristor-serial resistance cable lengths, as shown in the legend. (c) Cable length scaling of the oscillation frequency.

The distance *d* is in the ~mm regime in our case, corresponding to signal propagation times of tens of picoseconds. To understand how the frequency of ~100 MHz oscillators (~ns period time) is limited by delay times of tens of picoseconds, we need to incorporate signal propagation times while investigating our high-frequency circuit. First, for simplicity, and because of negligible parallel capacitance (C < 2 fF) of our memristor, we treat the memristor in its ON/OFF states as a simple resistive element. Its behaviour at high frequencies can be easily described by transmission and reflection originating from current continuity and Ohm's law. Those imply that on a resistor, part of the electrical signal is reflected and part of it is transmitted. So, as voltage is turned on, a wavepacket will come and get partially reflected from the serial resistor, and a part will be transmitted. The same process happens at the memristor. As time goes on, due to the reflections, voltage drops will build up on the memristor and the serial resistance. In the time → ∞ limiting case, the ratio of the voltages across the memristor and the resistor would be the same as the ratio of the voltage drops expected in the DC scenario.

To study the distance dependence of the oscillation frequency, we varied the distance d between the memristor and the resistor, and tuned the driving voltage amplitude to different values, as seen in Figure 2.b. We re-scaled the oscillation frequencies with the time delays according to the equation $\boldsymbol{f_{Scaled} = f_{LongDistance} \cdot (\Delta t_{LongDistance}/\Delta t_{ShortDistance})}$. In Figure 2.c the scaled frequencies are plotted with respect to the drive voltage which show great match with each other for the four longest distances (delay times). However, in the scenario of the minimal time delay of $\boldsymbol{t_{Delay} = 32\ ps}$ (red datapoints in Figure 2.c, the frequency deviates from the perfect scaling. This deviation is caused by the inner set/reset times of the memristor, which start to play a role in the investigated time domain.

In conclusion, we demonstrated a high-frequency VO_2 oscillator consisting of a serial resistor and a memristor only. Our planar antisymmetric geometry samples can reach 167 MHz and reproducibly reach the 100 MHz frequency regime. We conducted measurements varying the time delay between the resistor and memristor, which demonstrate that in the case of the shortest delay, the inner switching times of the device start to limit the oscillation frequency. Further details can be found in our recent work [9].

Related publications

[1] G. Csaba and W. Porod: *Coupled oscillators for computing: A review and perspective,* Applied Physics Reviews **7,** 011302 (2020) https://doi.org/10.1063/1.5120412

[2] H. Liu, et al.: *Artificial Neuronal Devices Based on Emerging Materials: Neuronal Dynamics and Applications,* Advanced Materials **35(37),** 2205047 (2023) https://doi.org/10.1002/adma.202205047

[3] E. Corti, et al.: *Scaled resistively-coupled VO_2 oscillators for neuromorphic computing,* Solid-State Electronics **168,** 107729 (2020) https://doi.org/10.1016/j.sse.2019.107729

[4] S. Kumar, et al.: *Dynamical memristors for higher-complexity neuromorphic computing,* Nature Reviews Materials **7(7),** 575 (2022) https://doi.org/10.1038/s41578-022-00434-z

[5] Md. Suruz Mian, et al.: *Self-oscillation up to 9 MHz based on voltage triggered switching in VO_2/TiN point contact junctions,* Journal of Applied Physics. **117(21),** 215305 (2015) https://doi.org/10.1063/1.4922122

[6] H. Kim, N. S. Bingham, N. A. Charipar, A. Piqué: *Strain effect in epitaxial VO_2 thin films grown on sapphire substrates using SnO_2 buffer layers,* AIP Advances 1 **7 (10):** 105116 (2017) https://doi.org/10.1063/1.5004125

[7] L. Pósa, P. Hornung, T. N. Török, S. W. Schmid, S. Arjmandabasi, G. Molnár, Z. Baji, G. Dražić, A. Halbritter, and J. Volk: *Interplay of Thermal and Electronic Effects in the Mott Transition of Nanosized VO_2 Phase Change Memory Devices,* ACS Applied Nano Materials **6 (11),** 9137 (2023) https://pubs.acs.org/doi/10.1021/acsanm.3c00150

[8] S. W. Schmid, et al.: *Picosecond Femtojoule Resistive Switching in Nanoscale VO_2 Memristors,* ACS Nano **18:33,** 21966 (2024) https://doi.org/10.1021/acsnano.4c03840

[9] Z. Pollner, T. N. Török, L. Pósa, M. Csontos, S. W. Schmid, Z. Balogh, A. Bükkfejes, H. Kim, A. Piqué, J. Leuthold, J. Volk, A. E. Halbritter: *VO_2 Oscillator Circuits Optimized for Ultrafast, 100 MHz-Range Operation,* Advanced Electronic Materials, in pre. No. e00433. ISSN 2199-160X (2025) https://doi.org/10.1002/aelm.202500433

PROGRESS TOWARD KITAEV TRANSMON GENERATION

HORIZON-EIC-2022-PATHFINDERCHALLENGES-01-06-101115315 (QuKIT)

M. Sütő[1], O. Kürtössy[1], B. Vasas[1], D. Kóti[1], Z. Kovács, and Sz. Csonka[1]
[1]In collaboration with the Department of Physics, BME, Budapest, Hungary
BME staff: M. Berke, Z. Scherübl, P. Makk

Quantum computing promises much faster calculations than today's computers, but building reliable quantum devices is still challenging because quantum bits (qubits) are very sensitive to their environment. In the QuKIT collaboration, we aim to develop a new type of robust qubit by combining a Kitaev chain with a transmon qubit (Figure 1.a). A Kitaev chain is a special superconducting structure that can protect quantum information from small disturbances, a property known as topological protection. In simple terms, this means the qubit becomes more resistant to noise and errors. The transmon qubit is a well-established platform that allows precise control and reliable readout of the qubit state. The device is based on an InAs/InGaAs heterostructure, covered by a superconducting aluminium film (Figure 1.b). Our work focuses on two goals: testing whether this aluminium layer can be used to build high-quality transmon qubits and fabricating and measuring a minimal Kitaev chain device.

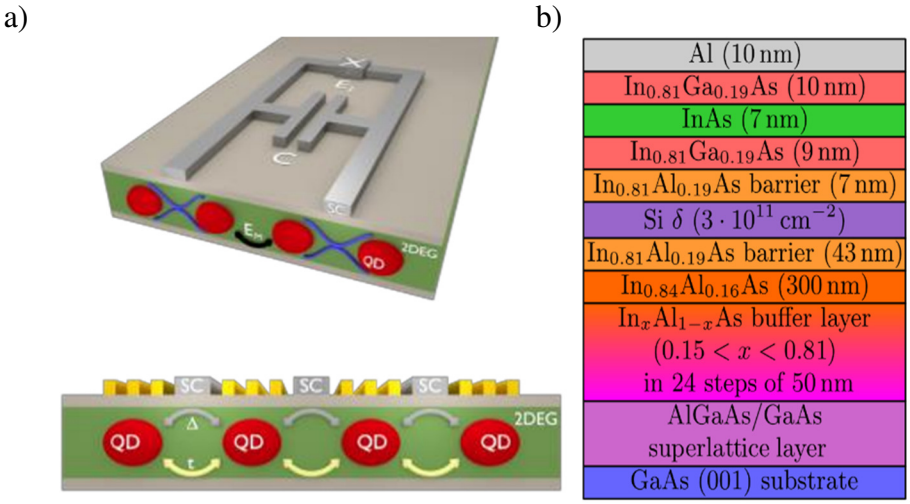


Figure 1: (a) Schematics of the novel Andreev qubit formed by coupling a traditional transmon to a minimal Kitaev chain (source: QUKIT Proposal Part B). (b) Our platform for the realisation of the Kitaev qubit: near-surface InAs 2DEG contacted by an epitaxial Al layer.

In earlier work [1], we investigated a Josephson junction based on a two-dimensional electron gas with epitaxial aluminium contacts, integrated into an rf SQUID inductively coupled to a superconducting microwave resonator. In this configuration, the junction behaves as a flux-tuneable inductance, allowing its properties to be extracted from shifts in the resonator frequency. The technique enables characterisation of the junction's supercurrent and average transmission, establishing a reliable platform for studying hybrid devices.

Building on this platform, we designed and fabricated a device consisting of two superconducting loops, each containing a Josephson junction and coupled to the same resonator, to explore the predicted hybridisation of Andreev bound states into an "Andreev molecule". The phase across each junction can be controlled independently using magnetic fields or on-chip control lines. The first generation of devices has been successfully fabricated and measured at millikelvin temperatures. The data already show nontrivial behaviour indicative of mutual coupling between the junctions. Ongoing measurements and analysis aim to quantify the strength and nature of this coupling.

To realise half of a minimal Kitaev chain, two quantum dots separated by a narrow superconducting segment are required (Figure 3.a). In this architecture, the superconducting channel serves as a source of Cooper pairs, which are subsequently split into the two quantum dots. As a first step toward this goal, we fabricated a gate-defined quantum dot device using multiple layers of electrodes. The first gate layer confines the two-dimensional electron gas (2DEG) into a quasi-one-dimensional channel, while a second layer of thin finger gates is used to define and control the quantum dots. Measurements on this device demonstrate the formation of single quantum dots, as evidenced by the observation of Coulomb diamonds in the transport measurements (Figure 3.b). However, the dots are not sufficiently stable for reliable operation. Based on these results, we are currently designing and fabricating a more stable double quantum dot device, in which the dots will be separated by a superconducting element to enable controlled Cooper-pair splitting and further progress toward the minimal Kitaev chain implementation.

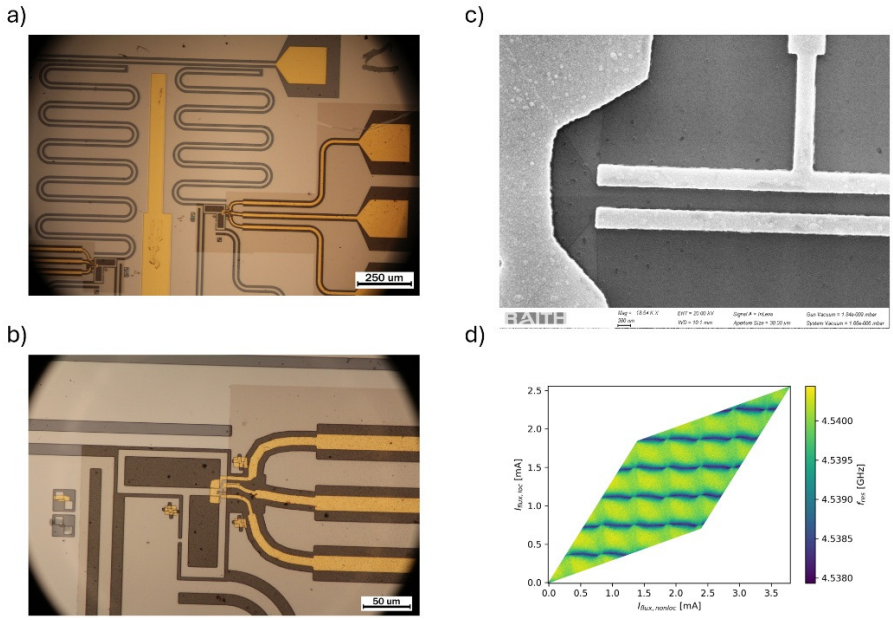


Figure 2: (a–b) Optical micrographs of a λ/4 coplanar waveguide resonator patterned from the epitaxial Al layer and the inductively coupled double-loop structure. (c) Scanning electron micrograph of the double Josephson junction device. Electrostatic gate electrodes are used to tune the charge carrier density in the junctions. (d) Resonance frequency of the resonator as a function of the magnetic flux applied to the two superconducting loops. The crossing of resonance-frequency dips indicates a nontrivial, mutually dependent response of the two loops.

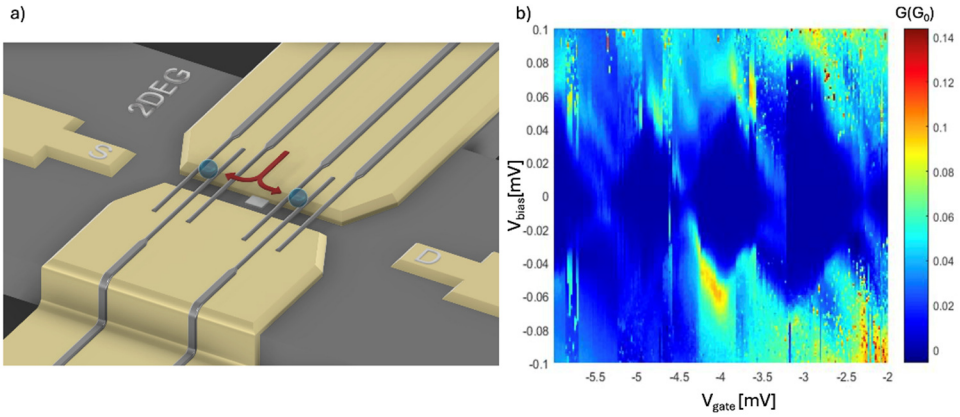


Figure 3: (a) Cooper-pair splitting device. The trapezoidal electrodes deplete the electrons in the 2DEG, forming a quasi-one-dimensional channel. Beneath this channel lies the end of the superconducting aluminium contact, which acts as the Cooper-pair source. Finger gates deposited on top define and control the quantum dots. (b) Single quantum dot measurement. Coulomb diamonds are visible in the transport data; however, the device exhibits instability during operation.

Related publication

[1] Z. Scherübl et al.: *Determination of the current-phase relation of an InAs 2DEG Josephson junction with a microwave resonator,* Phys. Rev. Research **7(2),** 023173 (2025) https://doi.org/10.1103/PhysRevResearch.7.023173

BIOMECHANICAL INVESTIGATION OF SOFT TISSUE TRANSECTION USING MEMS FORCE SENSING

J. M. Bozorádi, P. Révész, F. Braun, L. Illés, A. Nagy, J. Volk

Biomechanical characterisation of biological tissues is an increasingly important field at the intersection of medical and engineering sciences. Depending on the clinical relevance, investigations may focus on the elasticity, thickness, or mechanical response of various tissue types. However, in vivo characterisation remains challenging, particularly in the case of delicate anatomical structures.

In collaboration with the Department of Otorhinolaryngology at the University of Pécs, our work focused on the biomechanical investigation of the Chorda Tympani Nerve (CTN), which is frequently exposed during middle-ear surgery. Accidental injury of the nerve may lead to altered taste sensation and dry mouth, affecting a considerable fraction of patients after surgery. Despite its clinical importance, the force required to transect the CTN has not previously been quantified.

To address this challenge, we developed a compact handheld measurement tool based on a MEMS force sensor assembly (Figure 1). The system enables controlled in-situ force measurements on human cadaveric samples while reproducing realistic surgical conditions. The disposable sensor head consists of miniature, in-house developed 3D MEMS force sensors mounted on flexible printed circuit boards, while the handheld unit contains the readout electronics and wireless data acquisition system.

Following ethical approval at the University of Pécs, measurements were carried out on fresh human cadaveric samples. The developed platform enabled the successful recording of transection events and provided the first experimental estimates of the force range associated with CTN injury. Further details and comprehensive experimental results are provided in a manuscript currently under review for publication [1].

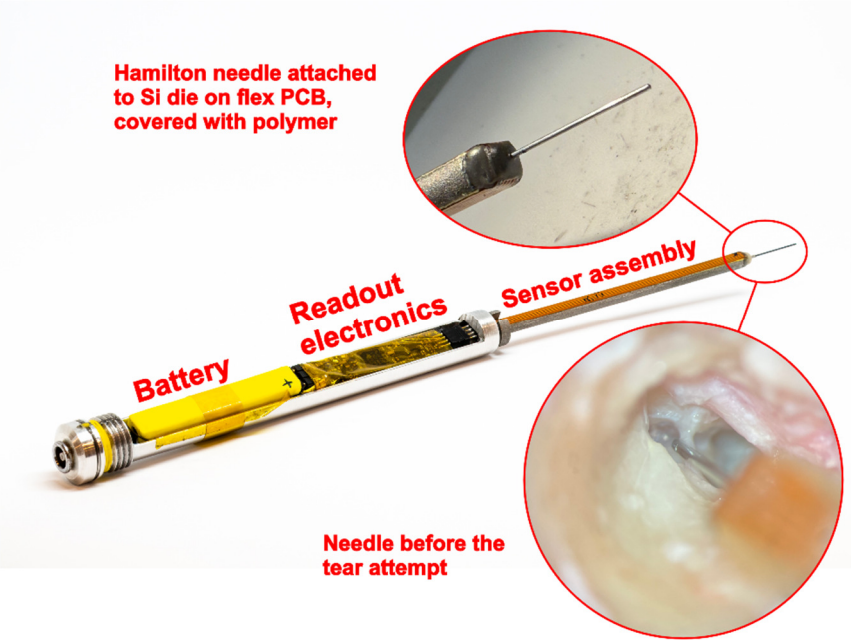


Figure 1: Handheld tissue tester with the sensor assembly before transection of the chorda tympani nerve.

Related publication

[1] P. Révész1, J.M. Bozorádi, D. Martini, J. Volk: *Estimate of the force required to transect the chorda tympani: A preliminary study using a novel measurement tool,* under review

WEARABLE GAS SENSORS FOR EMERGENCY AND EXTREME CONDITIONS

TKP2021-NVA-03

A. Király, K. Pankász, F. Braun, J. Bozorádi, Z. Szabó, F. Bíró, Cs. Dücső

Chemoresistive gas sensor chip-set for wearable devices

Continuous monitoring of the air in natural, built and industrial environments has become essential to identify the presence and source of toxic and hazardous gases originating dominantly from human activity and to take measures to eliminate pollution. Accurate measurements of gases, which are typically present in low concentrations, require expensive instruments, however, there is a high need for inexpensive small sensors that are primarily used for alarm purposes. This requirement can be met by measuring the various physical and chemical properties of the gases.

Two families of gas sensors are considered:

1. low-cost solid-state catalytic and chemoresistive sensors for demo applications
   target gases: H_2S, HCN, NH_3, Cl_2 or HCl (1-10-100ppm - TLV level or above)
2. moderate-cost optical sensor for more accurate concentration measurements
   target gases: CH_4, LPG, PB 1—5 %v/v (possibly CH_4 ~ 100 ppm)

The most widely investigated devices are solid-state conductivity sensors, which operate on the principle of chemisorption-controlled resistance change. As part of the project, we developed a universally applicable system consisting of a conductivity-type gas sensor chip based on measuring changes in the conductivity of thin layers of metal oxides with semiconductor properties, and a small portable device of evaluation electronics that supports low-power Bluetooth Low Energy (BLE) communication. Due to its low power consumption and size, the implemented system is suitable for wearing on clothing during emergency interventions or for mounting on drones to continuously measure gas concentrations and provide standard-compliant alarms.

The device is based on a 3.5x3.5mm² chip containing three microheaters and measuring electrodes on their top. The three independently operable elements provide the 50-400 °C temperature required for detection with a power of 2-26 mW each.

The critical component of conductive gas sensors is the sensor layer; its composition, 3D micro- or nanostructure, essentially determine the sensing characteristics. Therefore, the development of the sensing material requires a variety of synthesis processes and many qualification measurements. With our modified test system, we can test 3-3 elements of 5 chips at the same time.

For the demonstration, we prepared vanadium oxides with a nanofibrous structure using hydrothermal synthesis and deposited nanoscale particles of various precious metal catalysts onto their surfaces. We examined their gas detection properties for NH_3, H_2S, and NO in ranges around the maximum allowable workplace concentration (MAK or TLV) values. The series of measurements showed that, of the three gases, the gold-sensitised sensor operated at 250 °C provided good sensitivity and reproducible signals for H_2S in the range of 0.3 ppm-10 ppm with a response time (t90) of 5-15 s and an acceptable recovery time of a few minutes. The sensitivity of the system can be further improved by modifying the composition of the material system and its characteristic geometric dimensions. (Figure 1)

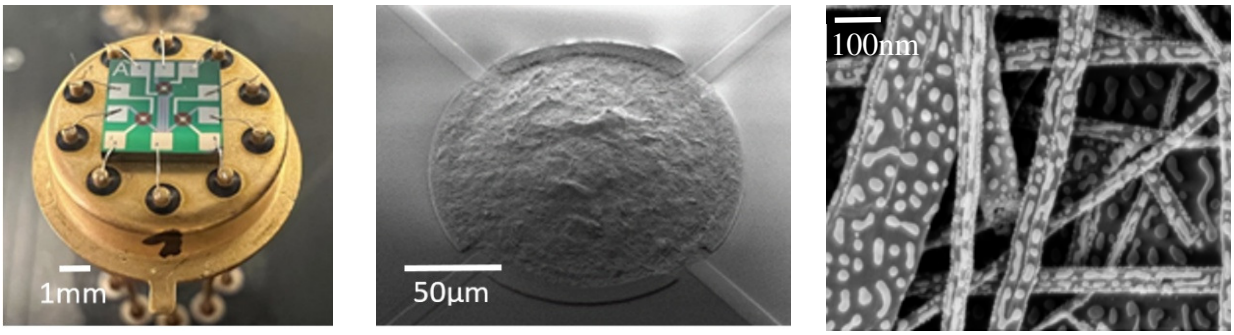


Figure 1: The chip containing the three sensor elements (left) and one of its heaters as covered with a nanofiber VO_x sensor layer (middle), and VO_x nanofibers sensitised with gold particles (right).

Another element of the development was the implementation of a portable instrument. The device was designed by focusing on low energy consumption, wireless data transmission, and on-site visual feedback. The electronics operates by 1.5 V supply voltage and are capable of reading a single sensor chip. The chip contains three independent sensor channels, each with individually controllable heating power. The system measures the conductivity of the sensor channels in the range between 1 kΩ and 10 MΩ. The average power consumption of the electronics is 5 mA. A conventional AA (pencil) battery has a nominal

capacity of approximately 2000 mAh, which allows for 8-20 hours of continuous operation, or even several days of operation with intermittent measurements.

The developed chip and BLE-based evaluation electronics, using appropriate sensor materials, offer an autonomous, small-sized, portable, and low-power solution for environmental monitoring, hazardous concentration detection, and even detection of multi-component gas mixtures. The ongoing activity focuses on the synthesis of nanostructured vanadium-oxide phases and investigation of their gas sensing properties.

Compact optical gas detector for portable applications

Gas sensors play an important role in environmental monitoring, healthcare applications and safety technology, not only in installed systems, but also in portable or drone-mounted forms. In addition to detectors that operate with chemoresistive or electrochemical transduction principles, optical gas detectors are becoming increasingly popular. These detectors use non-dispersive infrared (Non-Dispersive Infrared – NDIR) absorption to detect certain gas components in the middle infrared region (Middle Infrared Region – MIR) and, less frequently, in the near infrared region (Near Infrared Region – NIR). The term "non-dispersive" refers to the fact that the optical system does not contain a dispersive element, i.e., an optical grating or prism. Instead, an optical bandpass filter tuned to the optical absorption band of the target molecule in the infrared range and/or a monochromatic light source is used.

Although NDIR gas detectors have been used since the 1940s to reliably measure the concentration of certain gas components, the progress of microelectronics and the MEMS industry has made it possible to reduce the size of these devices and enable their rapid spread. With the use of increasingly complex integrated circuits (e.g., microcontrollers, front-end stages, etc.) and miniature light sources (LEDs, microheaters), a commercial NDIR gas detector can now be reduced to a volume of 3–4 cm^3. The minimum required electronics is placed on a circuit board with an area of approximately 2–3 cm^2, so the optical system still accounts for a significant part of the detector's volume.

To demonstrate one possible way of reducing the size, we have developed a 300 µm wide optical channel for the NDIR methane detector in this project, which was formed by photolithography in a thick SU8 polymer (Figure 2). The inner surface of the channel is coated with an optical reflective layer to reduce optical scattering and crosstalk. The transmitter side of the sensor consists of NIR/MIR LEDs and reference photodiodes placed in a common housing, while at the channel output (receiver side), a photodiode of the same type as the reference converts light pulses with a minimum frequency of 100 Hz and a width of 400 µs into electrical signals. In the presence of the target gas, the infrared LED light tuned to the absorption bands of the gas passes through the microchannel with an effective optical path length of 4.5 cm, with attenuation proportional to the concentration according to the Beer–Lambert's law of absorption. The microcontroller calculates the concentration of the target gas from the decrease in intensity detected on the receiver side, the absorption coefficient of the target gas, and the optical path length. The device is powered by a 3.7 V, 190 mAh lithium battery, which allows for approximately 8–9 hours of continuous operation. [1]

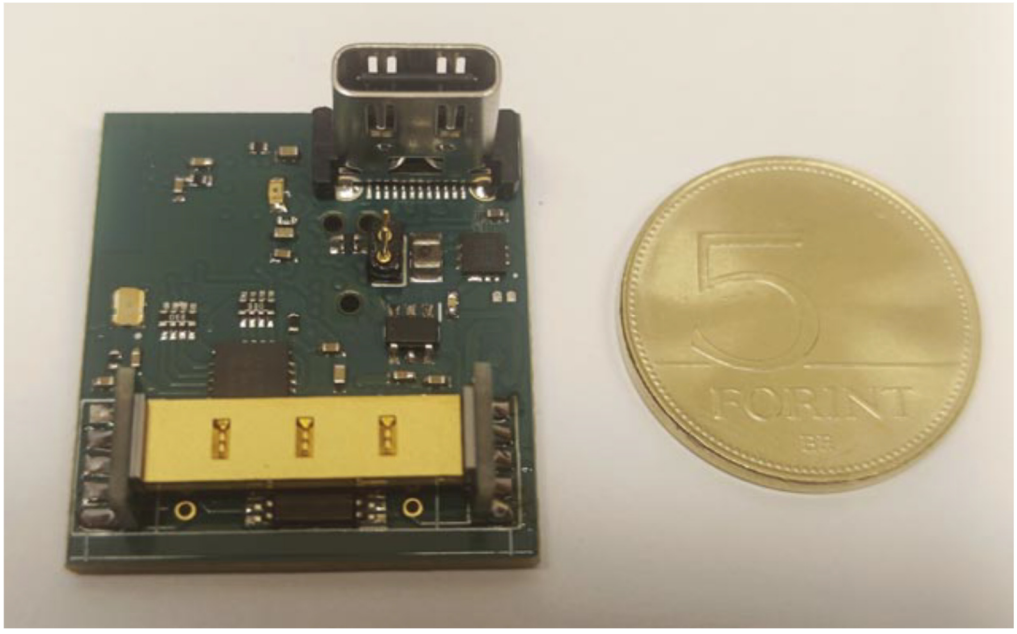


Figure 2: Prototype of an NDIR methane detector with an optical microchannel for portable applications. The gold surface optical channel covered with a gas-permeable reflector is visible on the lower half of the 25×25mm² circuit board.

Related publication

[1] Bíró F., Dücső Cs., Braun F., Neumann P.L., Király A., Bakos L., Mészáros A.B., Bozorádi J.M., Nguyen Quoc Khánh, Volk J.: *Vészhelyzetben és szélsőséges körülmények között alkalmazható környezetfigyelő szenzorok (Environmental monitoring sensors for use in emergencies and extreme conditions),* ELEKTROnet, 2025. dec. 05.

3D MEMS FORCE SENSOR FOR TISSUE RECOGNITION

H2020-ECSEL-2017-2-783132 "POSITION-II, 2018-2.1.6-NEMZ-ECSEL-2018-00001

J. M. Bozorádi, K. Gáspár, Zs. Bérces, G. Pap (Uzsoki Hospital), P. Fürjes

Laparoscopic devices have been widely used in the past decades during surgical procedures. Currently, they are the gold standard in minimally invasive surgery. Minimally invasive (possibly robotic) surgery (MIS) offers several advantages for the patients, although the lack of sensory feedback for the surgeon is also a barrier to its progress. Gathering immediate multi-parametric information about the physical and anatomic conditions of tissues is crucial for the operator to support tissue recognition and pathologic characterisation. Smart devices with integrated MEMS force sensors can provide such feedback and improve the safety of these interventions or help in on-site pathologic decisions.

At the Uzsoki Hospital in Budapest (Dr. Géza Pap), there is a growing interest in these sensors since they were already integrated in a laparoscope head in the previous INCITE project. Even with the existence of surgical robots, there's still a great need for handheld devices with the addition of a „smart element" embedded in them to help the work of the surgeon by providing information regarding tissue thickness, stiffness, composition and the effect of the surgeon's current action. Our first goal was to develop a novel device with integrated micromachined 3D force sensors to provide tactile information about the different organs and tissues touched. Our developed 3D piezoresistive force sensors were designed and manufactured using silicon micromachining technology and mechanically integrated in the appropriate biocompatible packaging and elastic coverage. Application-specific readout electronics were designed to solve the analogue-to-digital signal conversion, initialisation, noise filtering and communication with a LabVIEW data acquisition user interface.

In our joint project with Uzsoki Hospital in Budapest, our research group has been developing a 3D MEMS force sensor-based system for biomechanical characterisation of human gastrointestinal tissues. The long-term goal is to provide feedback during minimally invasive surgical procedures regarding tissue properties such as thickness and stiffness. Previous work focused on a tabletop measurement platform capable of implementing in vitro mechanical tissue characterisation by recording force-displacement characteristics of resected tissue samples and providing elastomeric and pathological data. Building on these results, the current period focused on redesigning the existing tabletop system into a more compact, instrument-integrated form.

As a first step, a "sensor cartridge" was designed, which is capable of housing the MEMS sensor and its flexible electronics. The cartridge is designed to be compatible with the standard laparoscopic devices, already used in clinical practice. A series of measurements were made as proof-of-concept on a resected stomach sample. In parallel, reference measurements were also made with the already existing tabletop system. While the tabletop system provides position-controlled force-displacement data, the cartridge currently yields force-time measurements due to the lack of direct position sensing. Despite this current limitation, the shape of the resulting force curve shows the same characteristic behaviour and stiffening effect of soft tissues under high compression observed in tabletop measurements (Figure 1). An important new finding of this experiment is that the maximum load applied on the tissue upon closing the laparoscopic stapler device might be significantly higher than previously expected, which may influence the decision-support information provided to surgeons. These results were presented at the EUROSENSORS XXXVII conference in Wroclaw. Our hope is that information regarding the patient's status before and after surgical procedures can be correlated with the tissue elasticity curves so an optimal stapler height can be determined by a neural network-based AI-supported data processing system in the future. [1]

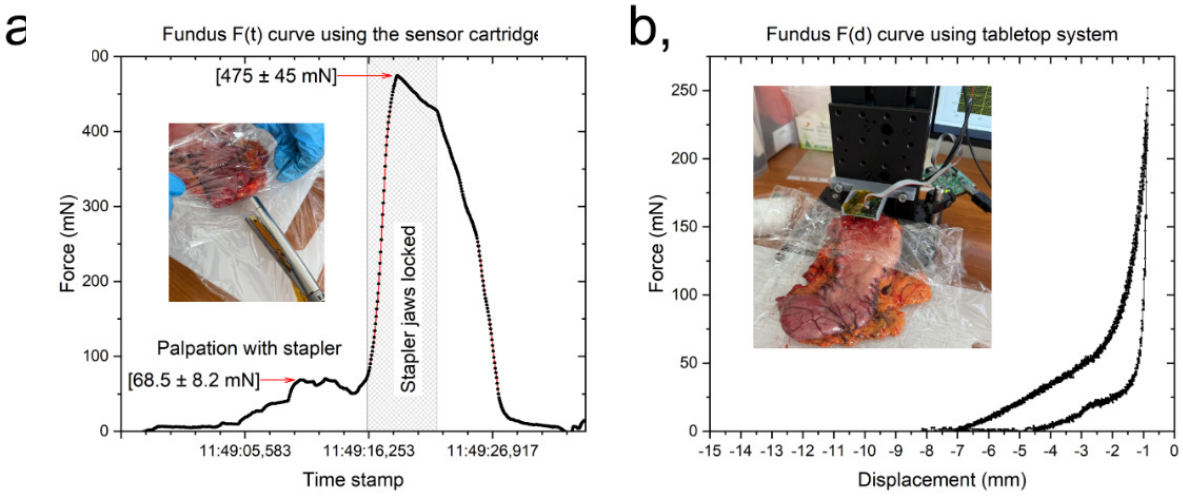


Figure 1: Force-time curve of a simulated laproscope jaws closed on a healthy stomach section (left). Force-displacement curve obtained with the tabletop measurement system (right). The compression of the same tissue section is similar to the time-dependent force measurement.

Related publication

[1] J.M. Bozorádi, Zs. Bérces, G. Papp, M. Berkes Maros, P. Fürjes: *Force measurement in Laparoscopic Stapler for Ex-Vivo Tissue Characterization,* Eurosensors 2025 Conference, Wroclaw, Poland, 2025 (poster) - AMA Proceedings of Eurosensors 2025 Confeghrence, https://doi.org/10.5162/EUROSENSORS2025/TP66

CHARACTERISATION OF MATERIALS FOR BIOMEMS APPLICATIONS

Moore4Medical, ECSEL Innovation Actions (IA), Call ECSEL-2019-1-IA

B. Beiler, Cs. Dücső, P. Fürjes

Nanoindentation Analysis of SU-8 Coated Wafers at Different Baking Phases

This study systematically characterises the mechanical behaviour of SU-8 thin coatings on silicon wafers through static and time-dependent nanoindentation at different baking stages in cooperation with Semilab Zrt. The results demonstrate a strong correlation between the degree of thermal curing and both the instantaneous and viscoelastic properties of the polymer. The post-bake process produces a marked increase in hardness and elastic modulus, while the creep and relaxation tests reveal a concurrent rise in the retarded modulus and viscosities of the Burgers model, indicating a substantial reduction in long-term viscoelastic flow. The mechanical behaviour of SU-8 is primarily governed by the extent of cross-linking rather than by strain rate or size effects. The increase in modulus and viscosity with baking temperature reflects the transition from a partially polymerised resist to a highly cross-linked, glassy network.

These findings underline the importance of optimised post-bake or hard-bake conditions to achieve mechanically stable SU-8 layers for MEMS and microfluidic applications. Furthermore, the nanoindentation-based evaluation of both instantaneous and creep responses provides a rapid and non-destructive method for monitoring polymerisation.

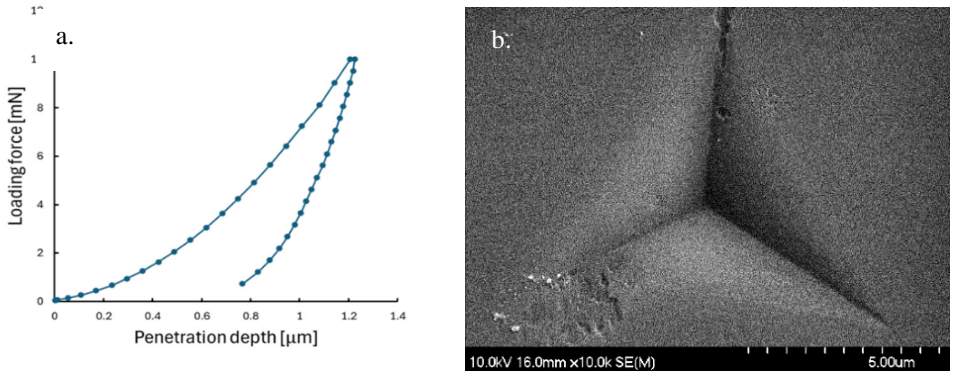


Figure 1: A representative force-displacement curve obtained from the nanoindentation measurement on the soft-baked SU-8 coated silicon wafer (a). SEM images of the SU-8 coated wafer surfaces show the indentation at a higher magnification, also showing the interfacial slipping (b).

Biocompatible coating of silicon integrated circuits

Silicon integrated circuits (ICs) are essential for the next-generation miniaturised active neural implantable devices, whether packaged in soft polymers for flexible bioelectronics or implanted as bare die for neural probes. In these applications, the integrated circuits are exposed to the corrosive body environment, raising reliability concerns, particularly for chronic use. In this study, the inherent hermeticity of bare die ICs was characterised, and the potential of polydimethylsiloxane (PDMS), a moisture-permeable elastomer was evaluated as a standalone encapsulation material. The one-year accelerated in vitro and in vivo analysis proved that the PDMS coating serves as an effective, long-term protective barrier for miniature neural implant ICs, maintaining both structural and electrical stability against bodily fluids, while uncoated areas suffer degradation. This study confirms that PDMS-covered regions prevent the failure typically seen in uncovered IC surfaces.

Results revealed stable electrical performance, indicating the unaffected operation of ICs even when directly exposed to physiological fluids. Despite this, material analysis revealed IC degradation in the bare regions. PDMS-coated regions, however, revealed limited degradation, making PDMS a suitable IC encapsulant for years-long implantation. Based on the new insights, guidelines are proposed that may enhance the longevity of implantable ICs, broadening their applications in the biomedical field.

Tailoring porous properties of polymer monoliths through the composition of the binary solvent mixture

Porous polymer monoliths with controlled porosity are critical materials for advanced separation technologies. Gamma-radiation initiated polymerization offers a straightforward and robust approach to their synthesis, employing a monomer mixture composed solely of monomers and solvents. Achieving precise control over the pore structure for a given monomer primarily depends on the careful selection of the porogenic solvent. This study presents a comprehensive investigation into how solvent composition affects both the structural characteristics and functional flow performance of diethylene glycol dimethacrylate (DEGDMA) monoliths prepared using binary solvent mixtures via gamma-radiation polymerisation. Three binary solvent systems—ethyl acetate/alcohols, acetonitrile/alcohols, and acetone/alcohols—were examined, with alcohol concentrations varying from 0 to 70 vol.% in a monomer solution containing 30 vol.% DEGDMA.

The addition of 20-30 vol.% of the good solvent (ethyl acetate, acetonitrile, acetone) to the poor solvent (alcohols) initially enhances pore formation, creating larger aggregated globules and increased pore sizes compared to the pure alcohol systems. While all three good solvents follow similar trends, they exhibit distinct characteristics: acetonitrile systems show the most pronounced surface area maxima (up to 60 m^2/g), acetone systems provide intermediate behaviour, and ethyl acetate systems demonstrate the most gradual transitions with sustained performance at higher concentrations. Among the alcohols, methanol consistently produces the highest flow rates and largest pore sizes, followed by ethanol and 2-propanol. This hierarchy reflects the different solubility parameters and their interaction with the DEGDMA monomer during polymerisation. Maximum flow-through performance is consistently achieved at 20-30 vol.% concentrations of the good solvent across all three systems, with peak flux values ranging from 0.17 to 0.38 mL/(min·mm^2). This optimal range represents a balance between maintaining macroporous structure and preserving pore connectivity. The complete loss of permeability at high good solvent concentrations (>30 vol.%) indicates the formation of microporous or bulk structures without interconnected pores. [1-3]

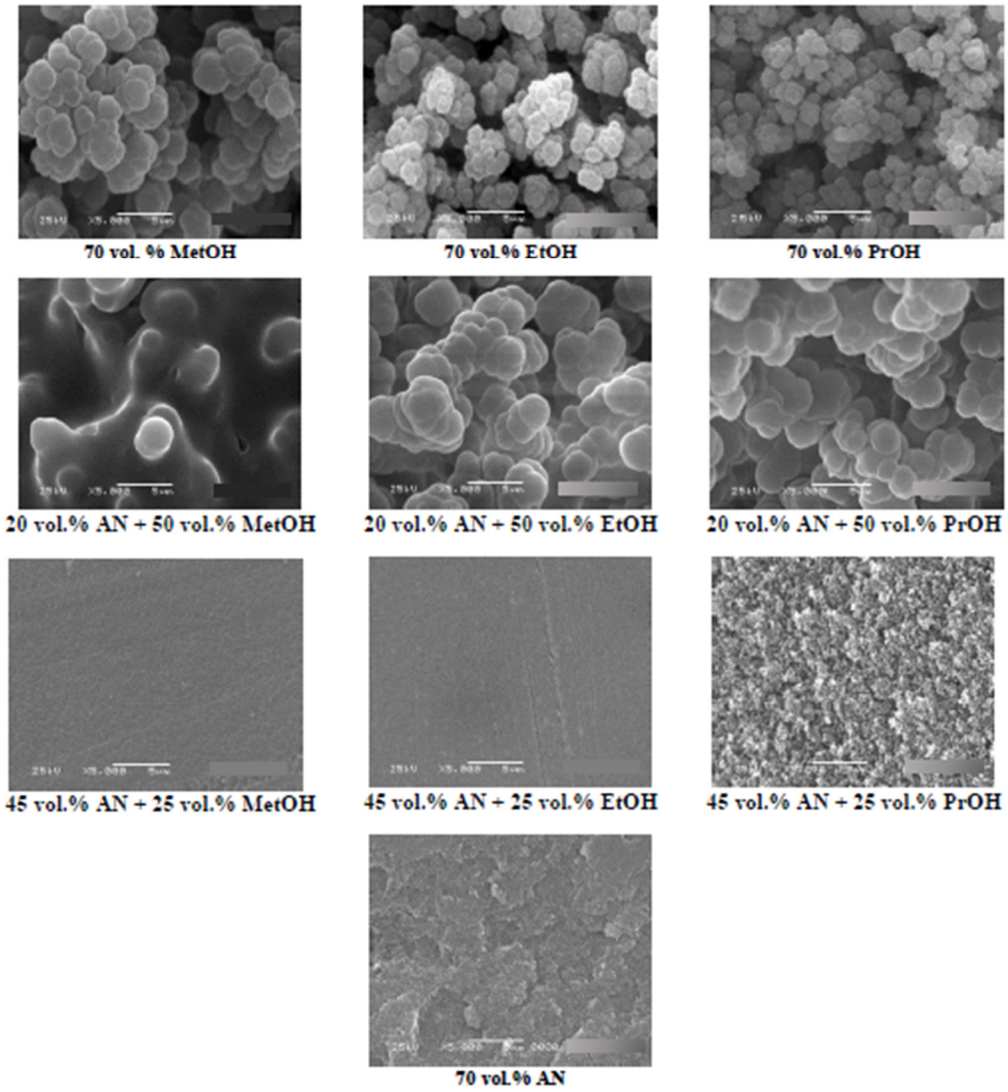


Figure 2: Morphology of DEGDMA monoliths prepared with different acetonitrile (ACN)/alcohol (MetOH, EtOH, PrOH) solvent ratios. The monomer mixture contained 30 vol.% DEGDMA and 70 vol.% of the solvent. The irradiation was performed with 30 kGy dose and 11 kGy/h dose rate.

Related publications

[1] T. Tarjányi, G. Gulyás, K. Bali, M. Sámi, R.A. Kiss, B. Beiler, P. Fürjes and T. Szabó: *Nanoindentation Analysis of SU-8 Coated Wafers at Different Baking Phases,* Polymers **17,** 3337 (2025) (IF 4.9 / Q1) https://doi.org/10.3390/polym17243337

[2] K. Nanbakhsh, A.S. Idil, C. Lamont, Cs. Dücső, Ö. Can Akgun, D. Horváth, K. Tóth, D. Meszéna, I. Ulbert, F. Mazza, T.G. Constandinou, W. Serdijn, A. Vanhoestenberghe, N. Donaldson & V. Giagka: On the longevity and inherent hermeticity of silicon-ICs: evaluation of bare-die and PDMS-coated ICs after accelerated aging and implantation studies, Nature Communications 16, 12 (2025) (IF: 15,7 / D1) https://doi.org/10.1038/s41467-024-55298-4

[3] B. Beiler, M. H. Mahmood, D. Bereczki, Á. Sáfrány, P. Fürjes, M. Veres: *Tailoring porous properties of polymer monoliths through the composition of the binary solvent mixture,* Reactive and Functional Polymers **220,** 106614 (2026) (IF: 5.1 / Q1) https://doi.org/10.1016/j.reactfunctpolym.2025.106614

MICROFLUIDIC METHODS FOR PARTICLE AND CELL MANIPULATION AND ANALYSIS

TKP2021-EGA-04

A. Bányai, M. Varga (77E Ltd.), L. Bató, Zs. Szomor, E. Leelőssyné Tóth, B. Beiler, M. Veres (HUN-REN Wigner), P. Fürjes

In the field of microfluidics, the development of medical diagnostic applications with the spread of Lab-on-a-chip (LOC) or miniaturised total analytical systems (μ-TAS), Point-of-Care (POC) diagnostic platforms, which can be used at the patient's bedside, ambulances or medical offices, has received great emphasis in recent decades. The use of Micro-Physiological Systems (MPS) or Organ-on-Chip (OoC) devices, the in-vitro study of cell populations or even individual cells in a controlled chemical environment, can be a significant step in the development of active pharmaceutical ingredients. Our goal is to develop application-specific devices that, by using integrated microfluidic and sensor systems, simultaneously solve the maintenance of artificial cell populations or even tissues, their treatment with chemical agents, and the real-time monitoring of their physiological behaviour. Our long-term goal is to develop microsystems that, due to their size, can accelerate the study of the effects of active pharmaceutical ingredients, which can be an important step forward the rapid screening of antibiotic resistance or the personal chemotherapeutic treatments.

Impedance study of localised cells in a microscopic chemical environment

In vitro testing of cell populations or individual cells in artificial systems that model their real environment is highly prospective from a biomedical and environmental point of view. Cell trapping and in-vitro analysis are powerful tools that enable the investigation of cell viability and proliferation in microfluidic structures. Impedance spectroscopy is a suitable method for studying various properties of cells and cell cultures, as it allows non-invasive and real-time measurements. By integrating microelectrodes, the microfluidic structure can be suitable for impedance-based cell analytical (ECIS and TEER) measurements. Our research aims to develop a fully electrical, non-invasive microfluidic measurement system that can be broadly applied in biological research. To achieve this, a microfluidic device (Figure 1) with integrated microelectrodes were developed to be capable of trapping cell populations or individual cells between the sensing electrodes. Using a dedicated Printed Circuit Board (PCB) designed for measurements and a channel-switching matrix integrated into the microscope, the optical and electrical responses of the system can be investigated simultaneously.

Impedance spectroscopy-based measurements were carried out using gold and platinum electrodes integrated into the microfluidic structures. The impedance spectra obtained with different electrode arrangements were investigated using both two- and four-electrode configurations. The four-electrode configuration increases measurement sensitivity and minimises contact impedance, enabling precise characterisation of the electrical properties of biological samples.

During functional testing of the device and the fabricated chips, the Electrochemical Impedance Spectroscopy (EIS) spectra of the microfluidic system filled with different media were examined, including phosphate-buffered saline, cell culture media relevant for later cellular applications (HepG2 or DMEM), and Yeast Peptone Dextrose (YPD) medium. For proof-of-concept validation of the system, yeast cells (*Saccharomyces cerevisiae*) were used, as their rapid division and ease of cultivation make them an ideal model system. The system enables the parallel acquisition of impedance spectra and optical measurements, which serve as an initial optical validation of the electrical measurements. This approach allows real-time, detailed characterisation of the effects of localised cells on their microenvironment individual electrodes.

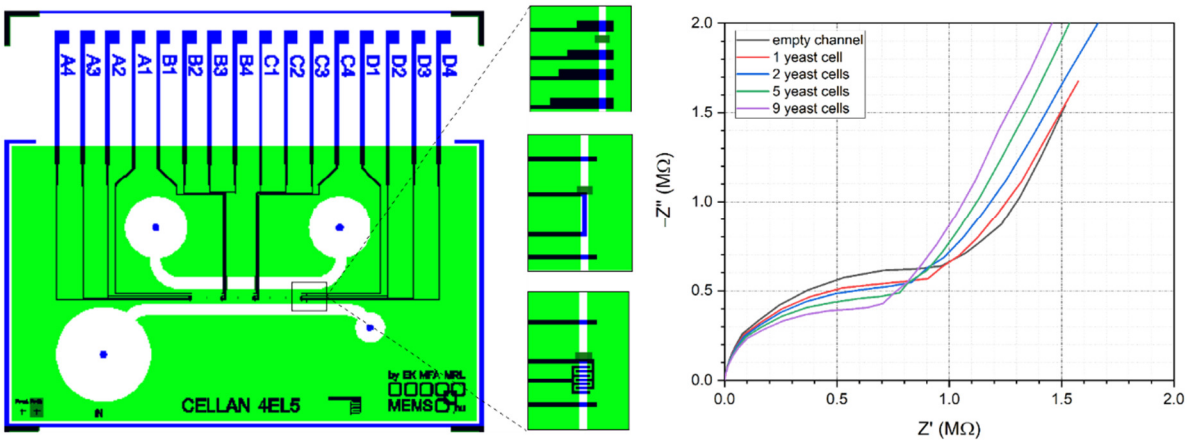


Figure 1: The layout of the microfluidically integrated EIS-based cell-analytical system (left) and Nyquist (right) plots of different numbers of trapped cells between

Electrochemical impedance tomography for morphological analysis of cell populations

EIS has numerous applications, including Electrical Impedance Tomography (EIT), whose most widespread macroscopic uses include body composition analysis and targeted medical diagnostic applications, such as tumour detection. However, a major limitation of this approach is that it provides only qualitative, macroscopic information about tissues and does not offer cell-level resolution.

Achieving cellular-level resolution through miniaturisation would significantly contribute to the in situ three-dimensional monitoring of cell culture growth, structural changes in 3D architectures, and the effects of therapeutic treatments. By combining microfluidic systems with EIS, it is possible to develop devices capable of detailed analysis of the spatially dependent properties of individual cells or cell populations, as well as high-resolution, real-time, and even three-dimensional structural investigations. Such developments represent an important step toward applications in drug testing, personalised medicine, and diagnostics. To realise such a system, our goal was to develop a device in which the placement of multiple parallel electrodes and their miniaturisation enables the localisation of cell distributions within a microfluidic channel, thereby paving the way for impedance tomography-based approaches. This strategy offers a new direction for overcoming the limitations of the technique and for moving toward quantitative evaluation.

In this work, the tomographic capabilities of the device and potential imaging approaches were investigated using microbeads. Two- and four-electrode measurements were taken of the bead distribution along the channel. During the experiments, the effect of microbeads on the EIS spectra was observed and correlated with the size of the beads relative to the channel height. The strongest correlation was achieved when the bead size was closest to the channel height. From the two measurement methods, the four-electrode one proved to be more accurate due to its more sensitive behaviour regarding the resistive part of the spectra, where the beads cause the most change.

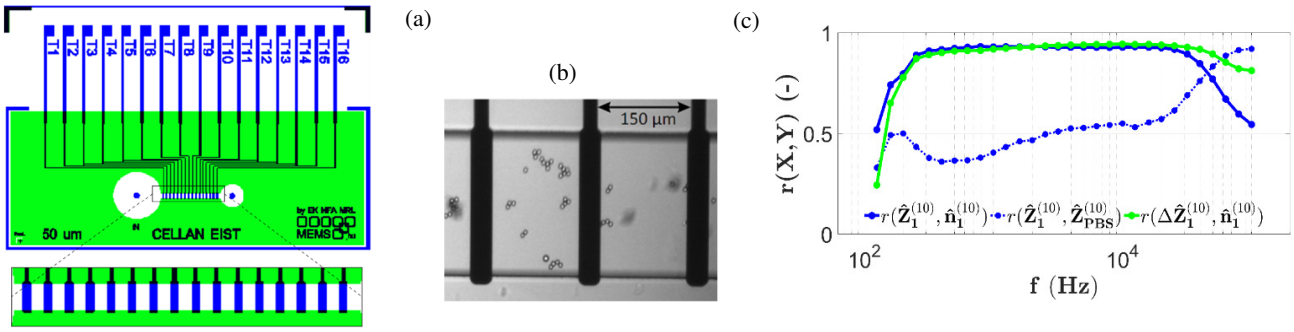


Figure 2: Microfluidic system designed for EIT measurement (a), bead distribution in the channel between two electrodes (b), and the correlation of the measurement with cell number in the case of 4-electrode configuration (c).

Investigation of flow and thermal processes in two-phase (digital) microfluidic systems

The capacity to construct intricate microfluidic architectures has empowered researchers to devise novel experimental formats for processing extremely small analytical volumes within short timeframes and with remarkable efficiency. These applications rely on generating small, separate droplets of the sample or reagent within a non-mixing carrier fluid, altering fluid behaviour. These artificial microscopic containers enable accelerated mixing of chemical primers, prevent contamination and non-specific molecular binding on channel walls, and support highly parallelised processes with the opportunity of single-cell or molecule analysis.

Our goal was to develop and investigate a digital microfluidic system capable of providing a stable and homogeneous chemical microenvironment for individual cells and biological samples, while supporting precise and reproducible chemical processes through targeted thermal treatment. Accordingly, our work focused on mixing phenomena and the analysis of temperature distributions within a complex microfluidic platform that enables controlled chemical and thermal treatment of individual cancer cells.

We designed and implemented two-phase flow systems, which are suitable for the reliable generation of micro-sized liquid droplets, even for the placement of cells in droplets. By appropriate modification of the microfluidic systems, we improved the reliability of the droplet generation process, and by trapping and analyzing the droplets, we investigated the course of flow (e.g. mixing) processes taking place in a closed microenvironment. We analyzed the droplet generation process, its dependence on material and hydrodynamic parameters, and the mixing phenomena taking place in closed microvolumes using 2D and 3D finite element models. Both theoretical and experimental analyses were performed to reveal the influence of various channel geometries and flow parameters, with a primary emphasis on enhancing mixing efficiency and subsequently establishing an appropriate thermal environment. The evolving temperature distribution was characterised using both single-phase and multiphase models, and our results demonstrated that, due to the low thermal conductivity of the oil phase, a highly localised and well-controllable temperature field develops within the droplets. Furthermore, Dean vortices generated in curved channel sections were shown to significantly enhance droplet homogenization, even in regions upstream of the thermal treatment zone. This work contributed to a deeper understanding of droplet-based microfluidic mixing and to the development of an integrated experimental–numerical methodology that lays the foundation for future biotechnological and Lab-on-a-Chip applications. To experimentally validate the numerical results, a specific two-phase microfluidic system was designed with integrated heating elements. [1-6]

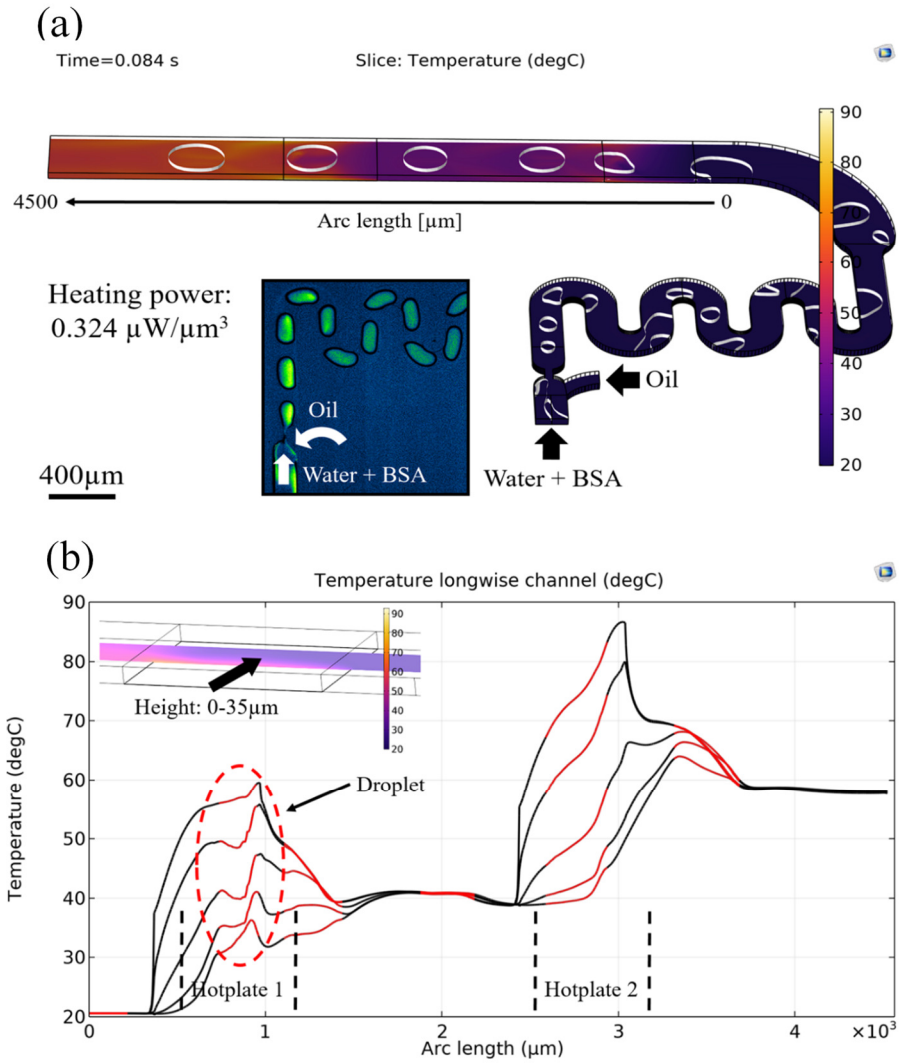


Figure 3: Simulated temperature distribution within the generated droplets (a). The longitudinal temperature distribution (b) presents the thermal isolation effect of the droplets.

Related publications

[1] L. Bató, J.M. Bozorádi, Z. Vizvári, P. Fürjes: *Real-Time Cell Viability Testing in Microfluidic System by EIS,* MPS 2025 World Summit, Brussels, Belgium, 2025 (poster)

[2] L. Bató, P. Fürjes, J.M. Bozorádi, V.Tadić, P. Odry, Z. Vizvári: *Sensitivity Analysis of Localized Electrochemical Impedance Spectroscopy Towards Tomography-on-a-Chip,* Sensors **25(20),** 6393 (2025) (IF 3.5/Q1) https://doi.org/10.3390/s25206393

[3] L. Bató, J.M. Bozorádi, Z. Vizvári, P. Fürjes: *Microfluidic System with Integrated Electrode Array for Impedance Tomography of Cell Cultures,* Symposium on Design, Test, Integration and Packaging of MEMS/MOEMS - DTIP 2025 Conference, Split, Croatia, 2025 (poster) (IEEE XPlore 11099198, https://doi.org/10.1109/DTIP66728.2025.11099198)

[4] Zs. Szomor, N. Gyimah, T. Pardy, P. Fürjes: *Three-dimensional finite element modelling of chemical environment in droplet-based microfluidic systems for drug therapy applications,* Physics of Fluids 37, 072045 (2025) (IF 4.3 / Q1) https://doi.org/10.1063/5.0275809

[5] Szomor Zs., Bereczki D., Fürjes P.: *Cseppek mikrofluidikai rendszerekben (Droplets in microfluidic systems),* Fizikai Szemle **853,** 410-415 (2025)

[6] Zs. Szomor, T. Pardy, P. Fürjes: *3D Modelling of Mass and Heat Transport in Multi-Phase Microfluidic Systems,* 31st International Workshop on Thermal Investigations of ICs and Systems – THERMINIC 2025 Conference, Naples, Italy, 2025 (poster) (IEEE XPlore 11216952, https://doi.org/10.1109/THERMINIC65879.2025.11216952)

SMALL-SCALE PRODUCTION AND DEVELOPMENT OF NEAR-INFRARED LEDS

HORIZON-KDT-JU-2023-1-IA-101140192 (UNLOOC), 2024-1.2.4-KDT-2024-00001, TKP2021-EGA-04

B. Beiler, J. M. Bozorádi, Cs. Dücső, P. Fürjes, Z. Szabó

Infrared spectroscopy is a very popular measurement technique, especially in the food industry, pharmaceutical industry and agriculture for the detection and measurement of organic materials. GaInAsP/InP is an ideal material system for the fabrication of double heterostructure devices as the emission wavelength is easily tunable between 950-1650 nm. As InP has a higher bandgap than the lattice-matched GaInAsP active layer, the absorption losses inside the device structure can be minimised. To tune the emission wavelength of the LED, the composition of the semiconductor light-emitting layer has to be properly set. Our high-quality single-peak LED chips (1220nm) have a stable market. Our business partners are SENOP Oy (Fi) and Anton Paar Ltd. (At).

Wide emission-spectrum NIR LEDs

Specific InGaAsP/InP layer structures were grown by Liquid Phase Epitaxy (LPE) to fabricate wide emission spectrum near-infrared LEDs. Multilayers structures resulting 4-wavelength emission were prepared in two consecutive LPE growth steps: by growing 2 InGaAsP photoluminescent layers, and other photo-luminescent and active layers in the second step. Preliminary results indicate that this layer configuration allows adequate control over the intensity of the longest-wavelength peak and the overall spectrum homogeneity. Samples were fabricated and characterised by optical transmittance measurements, by photo-luminescent measurements using various excitation sources in the NIR range, and by scanning electron microscopy to measure layer thicknesses and verify epitaxial crystal formation. Furthermore, ellipsometry measurements and optical modelling are underway to further understand and refine the device physics.

Various emission distributions (Figure 1) were measured on samples prepared by varying the thicknesses of the 3 photoluminescent layers in different layer order configurations. To achieve a homogeneous emission spectrum distribution, the measurement results are fed back into the planning process to refine the growth parameters. LED chips were characterised electrically and optically after dicing the wafer to 500x500 µm² LED chips. The shape of the emission spectra is quite stable, only slightly distorted with increasing current due to the saturation in the thinner layers. The total emitted optical power of the wide-spectrum LED compared to the emission of a standard single-wavelength LED indicates a relatively high internal photon conversion efficiency. [1]

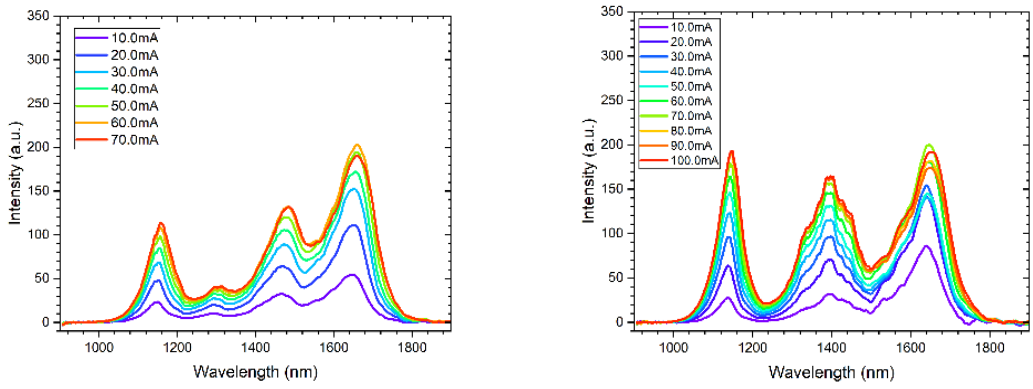


Figure 1: Emission spectrum of a 4-wavelength LEDs with different layer structures (layer order: 1650 nm, 1500 nm, 1300 nm & active 1170 nm) at forward current 10-100 mA.

Related publication

[1] Z. Szabó, B. Beiler, Zs. Baji: *Broadband InGaAsP/InP NIR LEDs based on multiple photon-recycling photoluminescent layers,* Journal of Crystal Growth **652,** 128045 (2025) https://doi.org/10.1016/j.jcrysgro.2024.128045 (IF 1.7 / Q2)

CELL CULTURE MEDIA ANALYSIS IN ORGAN-ON-CHIP APPLICATIONS

HORIZON-KDT-JU-2023-1-IA-101140192 (UNLOOC), 2024-1.2.4-KDT-2024-00001, TKP2021-EGA-04

D. Bereczki, K. Pankász, L. Bató, Zs. Szomor, A. Füredi, Z. Szabó, O. Bálint-Hakkel, P. Fürjes

Miniaturised pH sensor for cell culture media analysis

Accurate control and real-time monitoring of biological and chemical processes in microfluidic and Lab-on-a-Chip systems critically depend on the precise measurement of local environmental parameters, among which pH is of particular importance due to its fundamental influence on enzyme activity, cellular metabolism, cell viability, and the kinetics of biochemical reactions. This is especially critical in applications involving living cells, tissue cultures, and long-term incubation experiments. Motivated by these challenges, we developed an integrable pH sensor specifically tailored for lab-on-a-chip applications. Titanium dioxide (TiO_x)-based thin films were fabricated by Atomic Layer Deposition (ALD). ALD proved to be especially advantageous due to its ability to deliver excellent thickness control, conformality, and lateral homogeneity, even on complex or miniaturised substrates.

Electrochemical pH sensing was carried out using a PalmSens potentiostat in combination with a custom-developed Extended-Gate Field-Effect Transistor (EGFET)-based readout circuit. The EGFET configuration decouples the sensing membrane from the transistor itself, enabling flexible sensor integration while maintaining excellent electrical stability. Owing to the high input impedance and well-balanced measurement bridge of the custom readout electronics, even small potential variations induced by changes in proton concentration could be detected with high accuracy and low noise. This architecture is particularly well suited for low-power and portable sensing applications, which are increasingly important in point-of-care and on-chip diagnostic systems.

Experimental results demonstrated that TiO_x thin films deposited by ALD exhibited a pH sensitivity in the range of 52–58 mV/pH, approaching the theoretical Nernst limit of 59 mV/pH at 25 °C. This near-Nernstian response confirms the excellent electrochemical performance of the fabricated films and their suitability for high-precision pH sensing. In addition to sensitivity, the sensors showed good linearity, stability, and repeatability across multiple measurement cycles, further supporting their applicability. By combining advanced thin-film fabrication, detailed materials characterisation, and low-noise electrochemical readout, the developed sensing platform provides a robust foundation for real-time pH monitoring in Lab-on-a-Chip systems.

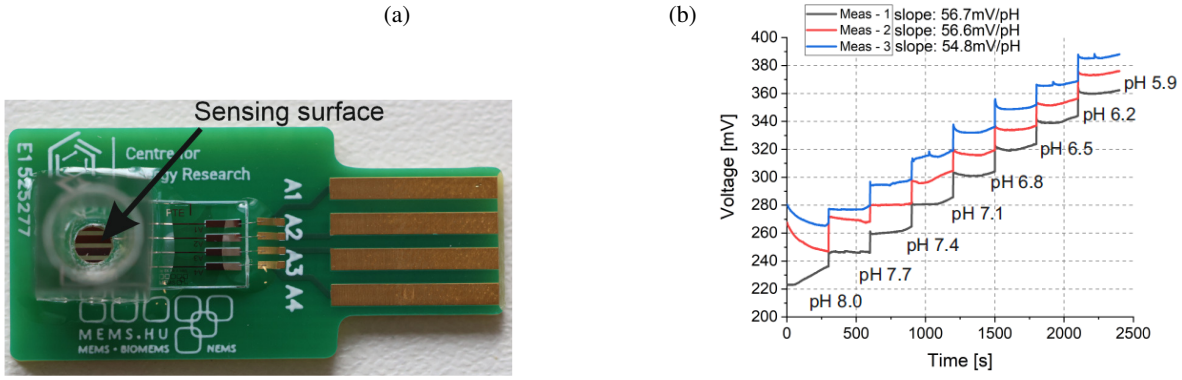


Figure 1: Perspective view of the electrochemical electrode platform highlighting the sensing surface where the functionalized TiO_x thin films are located (a) and the pH response of TiO_x layer deposited by ALD at 100 °C (b)

Therapeutic drug monitoring by fluorescent spectroscopy

Cancer claims almost 10 million lives annually, making it one of the major causes of death around the world. Chemotherapy is the most frequently used non-surgical method in clinical practice in cancer treatment to depress the growth, proliferation, or spreading of cancer cells. Detection of the anti-cancer drugs in patients' blood or standard cell culture media is the fundamental step forward in personalised treatments or in vitro drug tests in Organ-on-Chip devices.

Besides the gold standard mass spectrometry, optical spectroscopy must be considered as a potential analytical method, although there is no extensively accessible database of the spectral characteristics of the widely applied chemotherapeutic drug compounds. The inherent fluorescent properties of anti-leukemic drugs offer unique advantages for real-time therapeutic tracking and optimisation. In our work, we performed a systematic spectral mapping and parallel toxicity testing of several commercially available chemotherapeutic agents used in the treatment of leukaemia. Our goal was to identify fluorescent molecules by creating an accurate spectrum library. The optical spectral properties of 82 different active

pharmaceutical ingredients provided by Servier were investigated using a Tecan Spark Plate Reader. Accordingly, the absorption and emission spectra of these leukaemia-related compounds were screened, identifying 28 autofluorescent drugs suitable for fluorescence-based optical concentration monitoring. Excitation and emission parameters were evaluated across various solvents (DMSO, fetal bovine serum, and culture media), revealing solvent-dependent spectral changes, intensity variations and effects on detection limits.

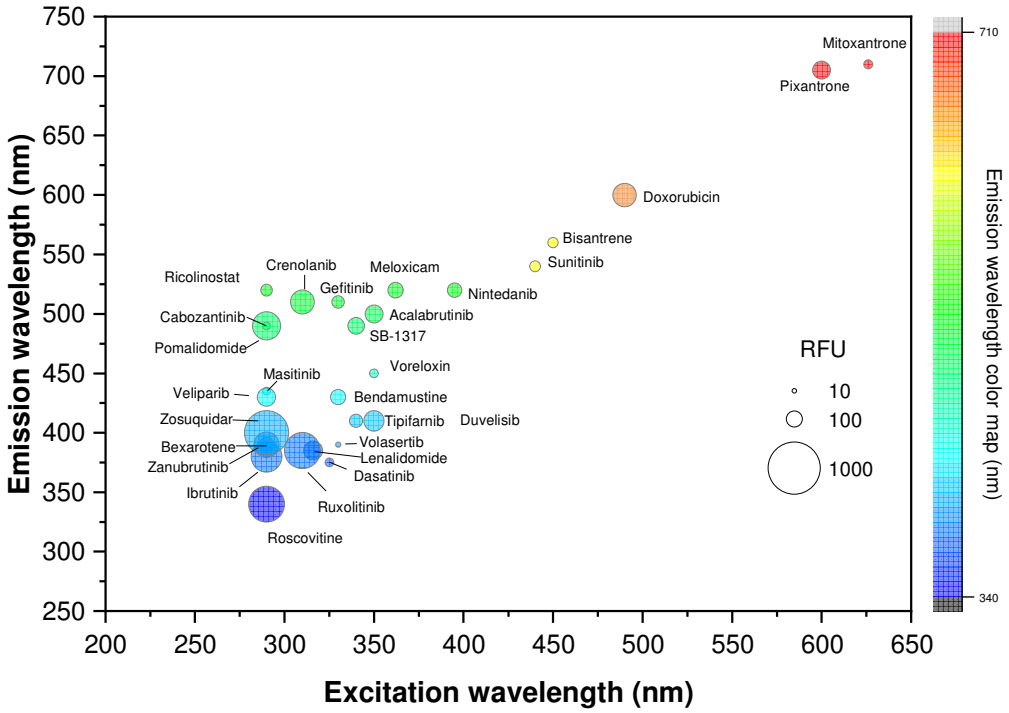


Figure 2: Spectral mapping of fluorescent U.S. Food and Drug Administration (FDA)-approved leukaemia drugs in DMSO. Excitation–emission properties are represented using wavelength-specific colour coding, and emission maxima are plotted with marker size proportional to relative detected fluorescence intensity.

Therapy-induced senescence in cancer cells

Therapy-Induced Senescence (TIS) is considered a permanent cell cycle arrest following DNA-damaging treatments; however, its irreversibility has recently been challenged. A. Füredi and his group demonstrated that escape from TIS is universal across breast cancer cells. Moreover, TIS provides a reversible drug resistance mechanism that ensures the survival of the population and could contribute to relapses. [1-4]

Our article "Therapy-induced senescence is a transient drug resistance mechanism in breast cancer" published in the journal Molecular Cancer, was selected as the article of the month by the International Cell Senescence Association.

Related publications

[1] Zs. Szomor, L. Bató, O. Hakkel, Cs. Dücső, Zs. Baji, A. Sulyok, E. Dodony, K. Balázsi, J.M. Bozorádi, Z. Szabó, P. Fürjes: *Characterisation of Titanium-Oxide Thin Films for Efficient pH Sensing in Low-Power Electrochemical Systems,* Sensors **25(19),** 6113 (2025) (IF 3.5 / Q1) https://doi.org/10.3390/s25196113

[2] E. Bajtai, Cs. Kiss, É. Bakos, T. Langó, A. Lovrics, É. Schád, V. Tisza, K. Hegedűs, P. Fürjes, Z. Szabó, G.E. Tusnády, G. Szakács, Á. Tantos, S. Spisák, J. Tóvári & A. Füredi: *Therapy-induced senescence is a transient drug resistance mechanism in breast cancer,* Molecular Cancer **24(1),** 128 (2025) (IF 33.9 / D1) https://doi.org/10.1186/s12943-025-02310-0

[3] A. Füredi, Sz. Tóth, K. Hegedüs, P.T. Szabó, A. Gaál, G. Barta, L.N. Naszályi, K. Kiss, K. Bölcskei, Z. Szeltner, E. Bajtai, B. Gombos, D. Kiss, M.T. Cserepes, A. Kiss, P. Pokreisz, L. Kenner, S. Högler, Cs. Magyar, J.D. Cowles, A. Csiszar, J. Tóvári, D. Szüts, Zs. Helyes, Z. Varga, G. Mező & G. Szakács: *Safe delivery of a highly toxic anthracycline derivative through liposomal nanoformulation achieves complete cancer regression,* Molecular Cancer **24:(1),** 269 (2025) (IF 33.9 / D1) https://doi.org/10.1186/s12943-025-02444-1

[4] D. Bereczki, I.L. Haffaressas, Z.Szabó, Sz. Tóth, A. Füredi, P. Fürjes: *Fluorescent properties of FDA-approved anti-leukemia drugs,* Biomedical Optics Express **17(2),** 963 (2026) (IF: 3.2 / Q1) https://doi.org/10.1364/BOE.580253

SOLID-STATE NANOPORES FOR EXTREMELY SENSITIVE NANOSENSORS

L. Illés, P. Fürjes, R. E. Gyurcsányi (BME NanoChemSens)

Nanoporous membranes are fundamental components of the transport modulation-based label-free electrochemical biosensors envisioned for highly sensitive molecule detection. The sensitivity and the specificity of these sensors are significantly affected by the pore geometry what has to be fitted to the size and conformation of the target molecules. Precise tailoring of nanopore geometries and alignment to target molecule conformation and size improves the signal-to-noise level of the identification method - in our case, impedance spectroscopy. This pore geometry engineering is essential for reliable and reproducible manufacturing of integrable solid-state nanopore arrays in molecular diagnostic devices.

Chemically functionalized single gold nanopores (GNPs) have been successfully developed and fabricated that act as ultra-miniaturised, solid-state ion channels for highly selective potentiometric sensing. A single nanopore was milled by Focused Ion Beam (FIB) milling in a double-layered membrane consisting of a low-stress non-stoichiometric silicon nitride (SiN_x) supporting layer, a Ti adhesion layer, and a gold layer enabling surface functionalization via chemisorption of functional thiol and disulfide derivatives. By modifying a 10 nm radius nanopore with a mixed self-assembled layer, they achieved silver ion (Ag^+) selectivity exceeding that of natural biological channels. This approach bypasses the traditional requirement for subnanometer pore size control and prevents the active component loss typically seen in conventional miniaturised ion-selective electrodes.

Dehydration governs ion selectivity in both natural ion channels and synthetic ion sieves, as ions must dehydrate to traverse subnanometer pores. Because lipophilic ions experience lower dehydration energy costs, an intrinsic lipophilic selectivity pattern known as the Hofmeister series arises. This Hofmeister selectivity is modulated in natural ion channels by electrostatic and coordinative interactions between ions and nanopore surfaces. In synthetic ion channels, surface hydrophobicity is also critical for ion selectivity; however, its exact role remains undetermined.

The contribution of hydrophobicity was elucidated by comparing structurally identical hydrophilic and hydrophobic cation-exchanger surface-modified gold nanopores. Zero-current potentiometry revealed that cation-exchanger nanopores do not discriminate among singly charged cations, except for a modest preference for H^+. The absence of Hofmeister selectivity was confirmed in both multipore membranes and single nanopores, ruling out ensemble nonidealities as an explanation. The lack of intrinsic Hofmeister selectivity may enable unique ion-sensing applications (e.g., total ion concentration measurements, ligand-tuned ion-selective sensors). [1] [2]

Our article “Single Solid-State Ion Channels as Potentiometric Nanosensors” published in the journal Advanced Functional Materials was selected as the publication of the month in October by the Department of Chemical Sciences of the Hungarian Academy of Sciences: https://mta.hu/vii-osztaly-a-honap-publikaciok/2025-oktoberi-kiemelt-publikaciok-114849

Related publications

[1] G. T. Solymosi, Gy. Jágerszki, L. Illés, P. Fürjes, R.E. Gyurcsányi: *Single Solid-State Ion Channels as Potentiometric Nanosensors,* Advanced Functional Materials **e19292,** 2025 (IF 19 / D1) https://doi.org/10.1002/adfm.202519292

[2] G. T. Solymosi, T. Kis, P. Fürjes, R.E. Gyurcsányi: *Absence of Hofmeister Selectivity in Hydrophobic Ion-Exchanger Nanopores,* Analytical Chemistry **97:(49),** 27289 (2025) (IF 6.7 / D1) https://doi.org/10.1021/acs.analchem.5c05239

KINETIC MONITORING OF MOLECULAR INTERACTIONS DURING SURFACTANT-DRIVEN SELF-PROPELLED DROPLET MOTION BY HIGH SPATIAL RESOLUTION WAVEGUIDE SENSING

Lendület LP2025-15/2025, OTKA ERC_HU 117755, TKP2021-EGA-04, OTKA KKP 129936, KDP Programs and Bolyai Scholarship

E. Farkas, K. D. Kovács, I. Székács, B. Péter, I. Lagzi, H. Kitahata (Chiba University, Japan), N. J. Suematsu (Meiji University, Japan), R. Horváth

Self-driven actions, like motion, are fundamental characteristics of life. Today, intense research focuses on the kinetics of droplet motion. Quantifying macroscopic motion and exploring the underlying mechanisms are crucial in self-structuring and self-healing materials, advancements in soft robotics, innovations in self-cleaning environmental processes, and progress within the pharmaceutical industry. Usually, the driving forces inducing macroscopic motion act at the molecular scale, making their real-time and high-resolution investigation challenging. Label-free surface-sensitive measurements with high lateral resolution could *in situ* measure both molecular-scale interactions and microscopic motion.

We employ surface-sensitive label-free sensors to investigate the kinetic changes in a self-assembled monolayer of the trimethyl(octadecyl)azanium chloride surfactant on a substrate surface during the self-propelled motion of nitrobenzene droplets. The adsorption–desorption of the surfactant at various concentrations, its removal due to the moving organic droplet, and rebuilding mechanisms at droplet-visited areas are all investigated with excellent time, spatial, and surface mass density resolution.

We discovered concentration-dependent velocity fluctuations, estimated the adsorbed amount of surfactant molecules, and revealed multilayer coverage at high concentrations. The desorption rate of surfactant (18.4 s^{-1}) during the microscopic motion of oil droplets was determined by *in situ* differentiating between droplet-visited and non-visited areas [1].

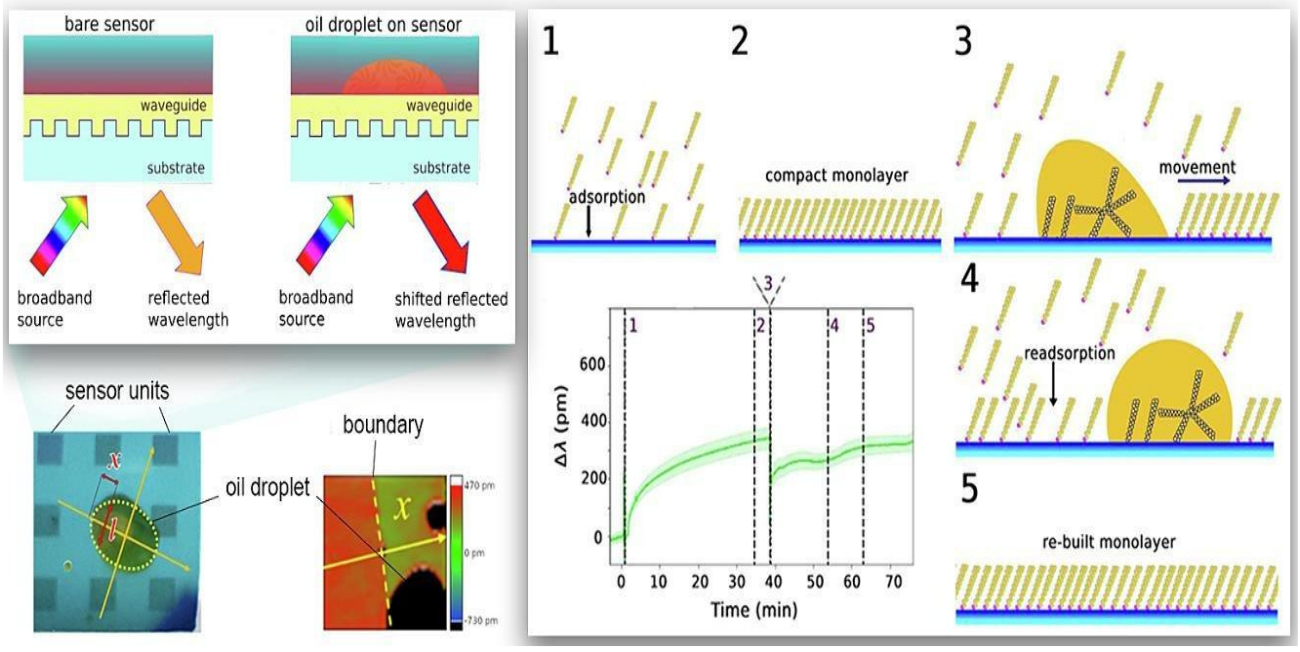


Figure 1: Schematic illustration of the measurement method

Related publication

[1] E. Farkas, K. D. Kovács, I. Székács, B. Peter, I. Lagzi, H. Kitahata, N. J. Suematsu, R. Horváth: *Kinetic monitoring of molecular interactions during surfactant-driven self-propelled droplet motion by high spatial resolution waveguide sensing,* Journal of Colloid and Interface Science **677,** (2025) https://doi.org/10.1016/j.jcis.2024.07.236

TEMPORAL PH WAVEFORMS GENERATED IN AN ENZYMATIC REACTION NETWORK IN BATCH AND CELL-SIZED MICROCOMPARTMENTS

Lendület LP2025-15/2025, OTKA ERC_HU 117755, TKP2021-EGA-04, OTKA KKP 129936

M. Itatani, G. Holló (University of Lausanne, Switzerland), P. Albanese (University of Siena, Italy), N. Valletti (University of Siena, Italy), S. Kurunczi, R. Horvath, F. Rossi (University of Siena, Siena, Italy), I. Lagzi (BME)

Investigating and designing reaction networks and their emergent phenomena are the backbone of systems chemistry. Designing chemical oscillators in homogeneous systems utilising enzymatic reactions is challenging due to the consumption of the substrates over one reaction cycle. Here, we show that an antagonistic enzymatic reaction network comprising urea-urease and ester-esterase reactions can generate temporal pH variations in a batch. We developed a coupled reaction kinetic model to elucidate the mechanism that accurately captures the experimentally observed pH variation over time. To demonstrate the remarkable potential of the enzymatic reaction network, we expanded on this discovery by generating front propagation and presenting several applications by coupling this enzymatic reaction network to fuel pH-dependent processes (gelation of pH-sensitive monomers and emulsion-vesicle transformation). By employing the coupling strategy of antagonistic enzymatic reactions, we engineered a single pH pulse in cell-sized microcompartments, which could contribute to developing synthetic cells with multiple functions [1].

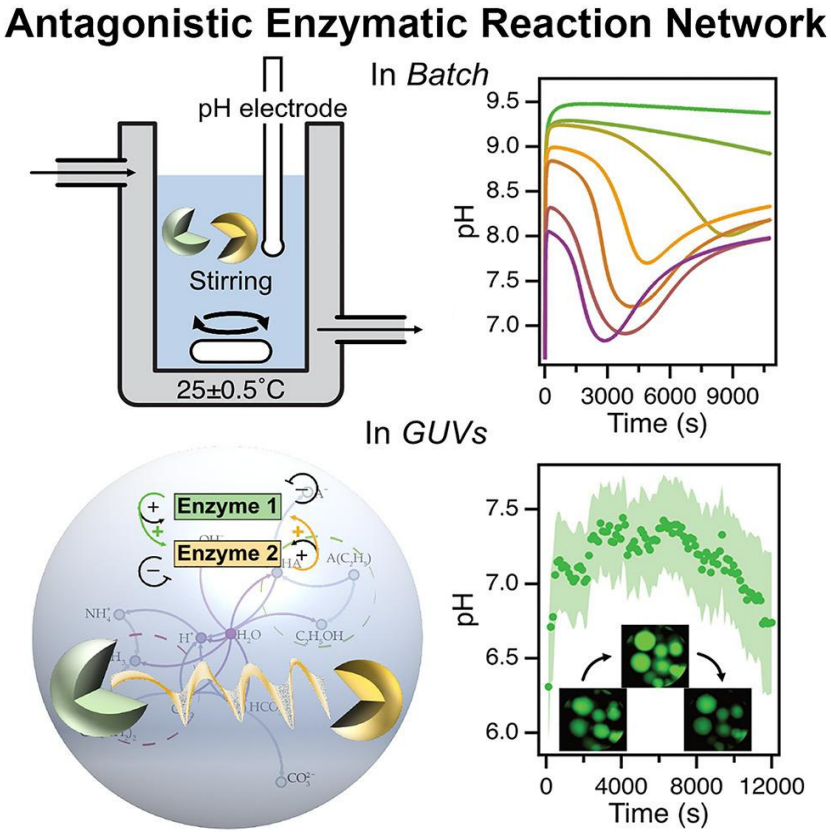


Figure 1: Schematic illustration of the antagonistic enzymatic reaction network

Related publication

[1] M. Itatani, G. Holló, P. Albanese, N. Valletti S. Kurunczi, R. Horvath, F. Rossi, I. Lagzi: *Temporal pH waveforms generated in an enzymatic reaction network in batch and cell-sized microcompartments,* Cell Reports Physical Science **6(1),** 102367 (2025) https://doi.org/10.1016/j.xcrp.2024.102367

ROBOTIC MANIPULATIONS OF SINGLE CELLS USING A LARGE-VOLUME PIEZOELECTRIC MICROPIPETTE WITH NANOLITRE PRECISION

Lendület LP2025-15/2025, OTKA ERC_HU 117755, TKP2021-EGA-04, OTKA KKP 129936

B. Kovács, Sz. Novák, I. Sallai, B. Magyaródi, I. Székács, D. Selmeczi (CellSorter), B. Szabó (CellSorter, ELTE), R. Horváth

Investigating the mechanism of adhesive interactions at the individual cell level holds significant importance. We used a computer-controlled piezoelectric micropipette (NanoPick) built onto an inverted microscope, offering subnanolitre precision liquid handling in the range of 0.1–600 nanolitres with a temporal resolution of 1 millisecond. In contrast to previous pipette-based cell manipulations, in our device, phase contrast and fluorescent imaging of the microscope were not limited by the micropipette. Moreover, this compact setup efficiently enabled single-cell detection, targeting, picking, and isolation without fluidic tubes and syringes. We investigated the integrin-mediated adhesion between an RGD (Arg-Gly-Asp) motif-displaying surface and the HeLa Fucci tumour cell line. Using a 70 µm inner diameter micropipette, we found that increasing the pipetting speed (voltage ramp rate applied on the piezoelectric head) improved the cell picking success rate to almost 100 %. However, the more strongly attached unmodified HeLa cells could not be picked up even at the highest flow rates. Compared to valve-controlled systems, NanoPick demonstrated higher efficiency and precision, particularly in handling THP-1 cells. Its rigid design minimised transient delays, allowing time-dependent flow profiles and enhanced detachment at lower flow rates. Our method allows adhesion measurements on hundreds of cells and offers precise control over fluid volume and timing, suitable for manipulating adherent cells or larger objects such as organoids, spheroids, oocytes, etc. [1].

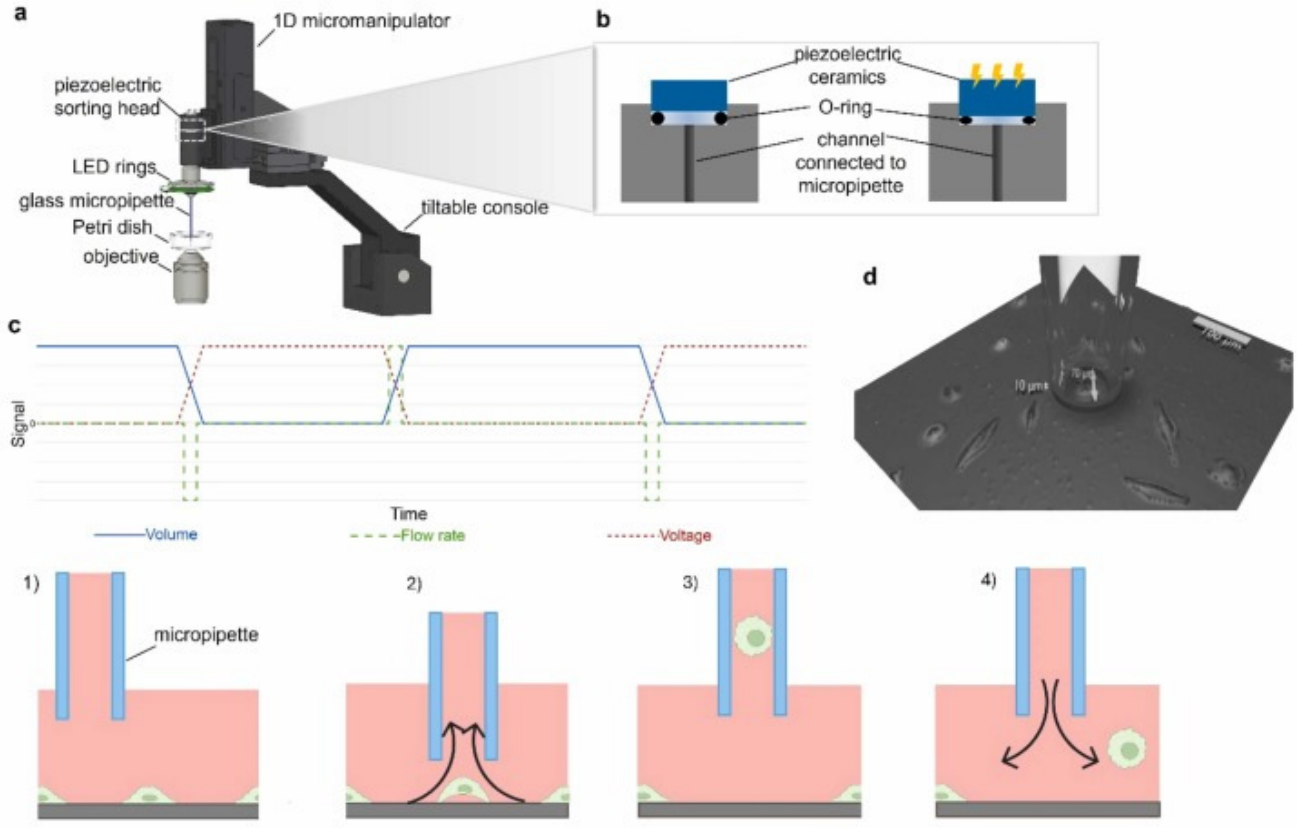


Figure 1: Configuration and working principle of the piezoelectric micropipette

Related publication

[1] B. Kovacs, Sz. Novak, I. Sallai, B. Magyarodi, I. Szekacs, D. Selmeczi, B. Szabo, R. Horvath: *Robotic manipulations of single cells using a large-volume piezoelectric micropipette with nanoliter precision,* Colloids and Surfaces B: Biointerfaces, **256(1),** 114972 (2025) https://doi.org/10.1016/j.colsurfb.2025.114972

KINETIC ANALYSIS OF SARS-COV-2 S1–INTEGRIN BINDING USING LIVE-CELL, LABEL-FREE OPTICAL BIOSENSING

Lendület LP2025-15/2025, OTKA ERC_HU 117755, TKP2021-EGA-04, OTKA KKP 129936 and KDP Programs, Bolyai Scholarship

N. Kanyó, K. Borbély, B. Péter, K. D. Kovács, A. Balogh, B. Magyaródi, S. Kurunczi, I. Székács, R. Horváth

The SARS-CoV-2 spike (S1) protein facilitates viral entry through binding to Angiotensin-Converting Enzyme 2 (ACE2), but it also contains an Arg–Gly–Asp (RGD) motif that may enable interactions with RGD-binding integrins on ACE2-negative cells. Here, we provide quantitative evidence for this alternative binding pathway using a live-cell, label-free Resonant Waveguide Grating (RWG) biosensor. RWG technology allowed us to monitor real-time adhesion kinetics of live cells to RGD-displaying substrates, as well as cell adhesion to S1-coated surfaces. To characterise the strength of the integrin–S1 interaction, we determined the dissociation constant using two complementary approaches. First, we performed a live-cell competitive binding assay on RGD-displaying surfaces, where varying concentrations of soluble S1 were added to cell suspensions. Second, we recorded the adhesion kinetics of cells on S1-coated surfaces and fitted the data using a kinetic model based on coupled ordinary differential equations. By comparing the results from both methods, we estimate that approximately 33% of the S1 molecules immobilised on the Nb_2O_5 biosensor surface are capable of initiating integrin-mediated adhesion. These findings support the existence of an alternative integrin-dependent entry route for SARS-CoV-2 and highlight the effectiveness of label-free RWG biosensing for quantitatively probing virus–host interactions under physiologically relevant conditions without the need of the isolation of the interaction partners from the cells [1].

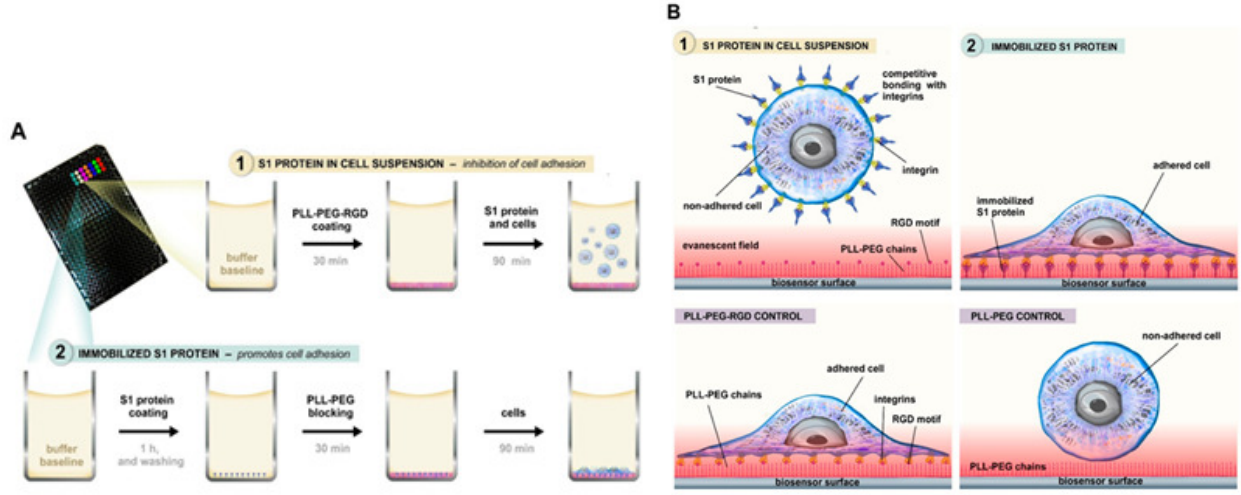


Figure 1: Experimental scheme and molecular mechanism of integrin-mediated adhesion assays. (A) Experimental workflow of the two biosensor assay setups: (1) inhibitory effect of soluble S1 protein in cell suspension and (2) adhesion to surface-immobilised S1 protein. (B) Schematic representation of molecular interactions during the assays.

Related publication

[1] N. Kanyo, K. Borbely, B. Peter, K. D. Kovacs, A. Balogh, B. Magyaródi, S. Kurunczi, I. Szekacs, R. Horvath: *Kinetic analysis of SARS-CoV-2 S1–integrin binding using live-cell, label-free optical biosensing,* Biosensors **15(8),** 534 (2025) https://doi.org/10.3390/bios15080534

IN SITU MONITORING OF CELL ADHESION KINETICS USING LABEL-FREE OPTICAL BIOSENSORS: EVALUATING ANTICANCER POTENTIAL AND SELECTIVITY OF NATURAL COMPOUNDS

Lendület LP2025-15/2025, OTKA ERC_HU 117755, TKP2021-EGA-04, OTKA KKP 129936, KDP Programs and Bolyai Scholarship

B. Péter, T. Ausbüttel (SE), N. Kanyó, P. Joó, K. Tóth, Z. Szittner, I. Székács, Sz. Bosze (ELTE), G. M. Kovács (ELTE), I. Boldizsár (ELTE, SE), R. Horváth

The limitations of conventional techniques hinder the identification of natural compounds with anticancer potential in terms of speed, throughput, sensitivity, and the capability of continuous monitoring of relevant biological effects. Novel label-free optical biosensors represent new opportunities in the discovery of drug candidates, eliminating these difficulties. Our study monitored the anti-adhesive effects of 11 isolated pure natural compounds (representing four different structural frameworks) and four crude extracts, obtained from plant and fungal sources. The Resonant Waveguide Grating (RWG) method (using an evanescent field-based label-free optical biosensor) and a combined miniaturised holographic microscope technique were applied to investigate the effects of pure compounds and crude extracts on cancerous (HeLa) and healthy (preosteoblast) model cells in real time. The adhesion kinetics on fibronectin-coated surfaces and the morphological parameters on polystyrene surfaces were studied using these model cells in the presence and absence of compounds and extracts. The introduced biosensor method also investigated their interaction with the fibronectin surface. This methodology enables continuous, high-sensitivity parallel measurements, facilitating the identification of natural compounds with anticancer potential while also providing insights into their mechanism of action. The interaction of the aryltetralin lignans deoxypodophyllotoxin and angeloyl podophyllotoxin with fibronectin was confirmed as a key mechanism behind their non-selective anti-adhesive effects. In contrast, the selective adhesion inhibitory effects of the neolignan balanophonin and the alkaloid vermelhotin against HeLa cells were unrelated to fibronectin interaction [1].

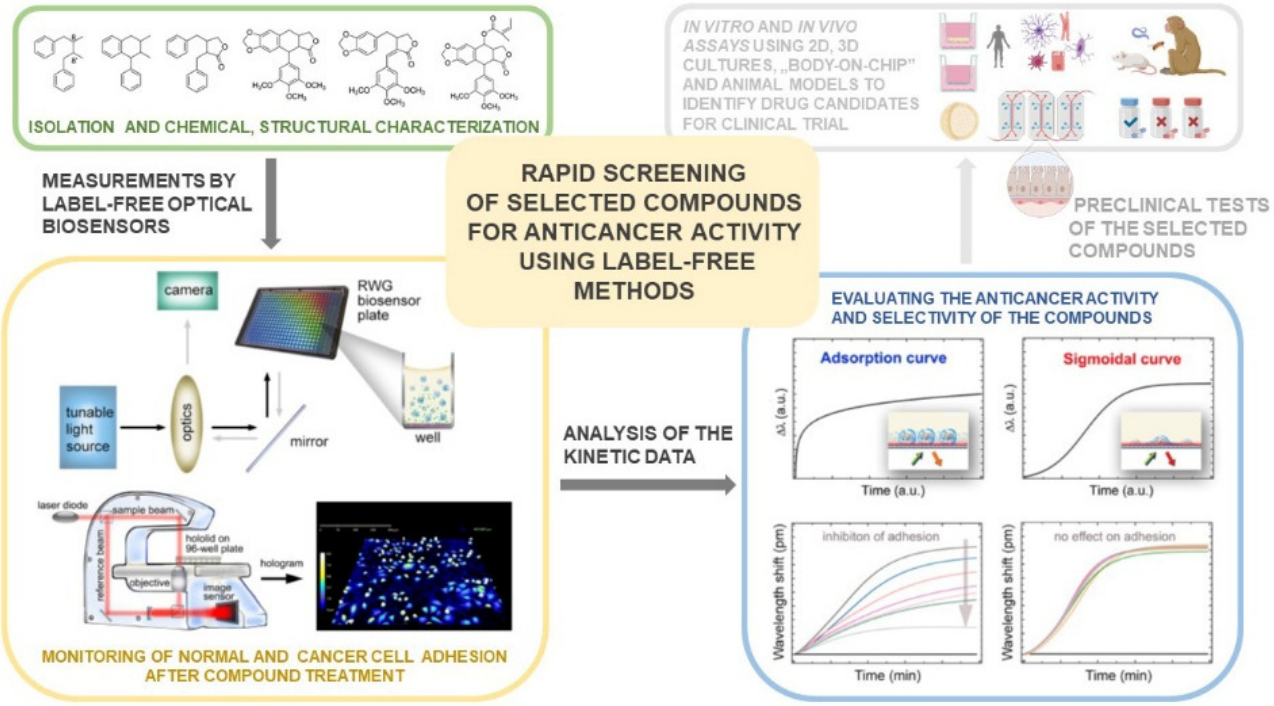


Figure 1: Schematic illustration of the measurement method

Related publication

[1] B. Péter, T. Ausbüttel, N. Kanyo, P. Joó, K. Tóth, Z. Szittner, I. Szekacs, Sz. Bosze, G. M. Kovács, I. Boldizsár, R. Horvath: *In situ monitoring of cell adhesion kinetics using label-free optical biosensors: Evaluating anticancer potential and selectivity of natural compounds,* View **7(2),** 20250061, 2025 https://doi.org/10.1002/VIW.20250061

INTER-ROLE RECIPROCITY IN EVOLUTIONARY TRUST GAME ON SQUARE LATTICES

OTKA K 142948

C. Wang, W. Zhang, X. Wang, and A. Szolnoki

Simulating bipartite games, such as the trust game, is not straightforward due to the lack of a natural way to distinguish roles in a single population. The square lattice topology can provide a simple yet elegant solution by alternating trustors and trustees. For even lattice sizes, it creates two disjoint diagonal sub-lattices for strategy learning, while game interactions can take place on the original lattice.

This setup ensures a minimal spatial structure that allows interactions across roles and learning within roles. By simulations on this setup, we detect an inter-role spatial reciprocity mechanism, through which trust can emerge. In particular, a moderate return ratio allows investing trustors and trustworthy trustees to form inter-role clusters and thus save trust. If the return is too high, it harms the survival of trustees; if too low, it harms trustors. The proposed simulation framework is also applicable to any bipartite game to uncover potential inter-role spatial mechanisms across various scenarios. [1]

This work was reviewed by The Science Archive: https://thesciencearchive.org/2508-06685v1/

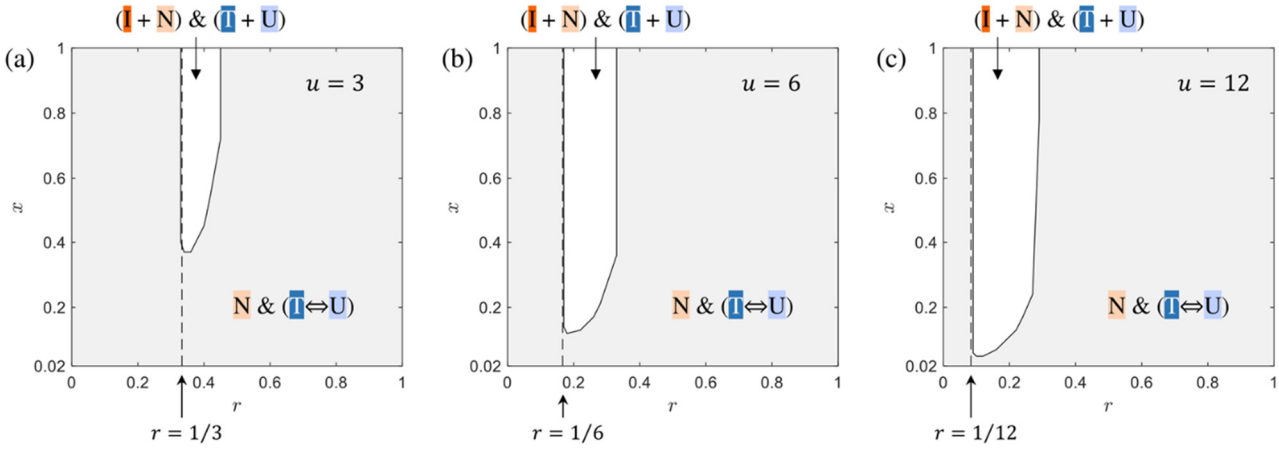


Figure 1: Phase diagrams of the system behaviour with respect to return ratio r and investment ratio x for different multiplication factors u = 3, 6, 12. Trust emerges in the (I + N)&(T + U) phase (white region) with large x and moderate r, where the four strategies of the two roles coexist. Trust cannot survive in the N&(T ⇔ U) phase (grey region), where trustors do not invest, and trustworthy and untrustworthy trustees are in neutral drift. The dashed line marks r = 1/u in each panel.

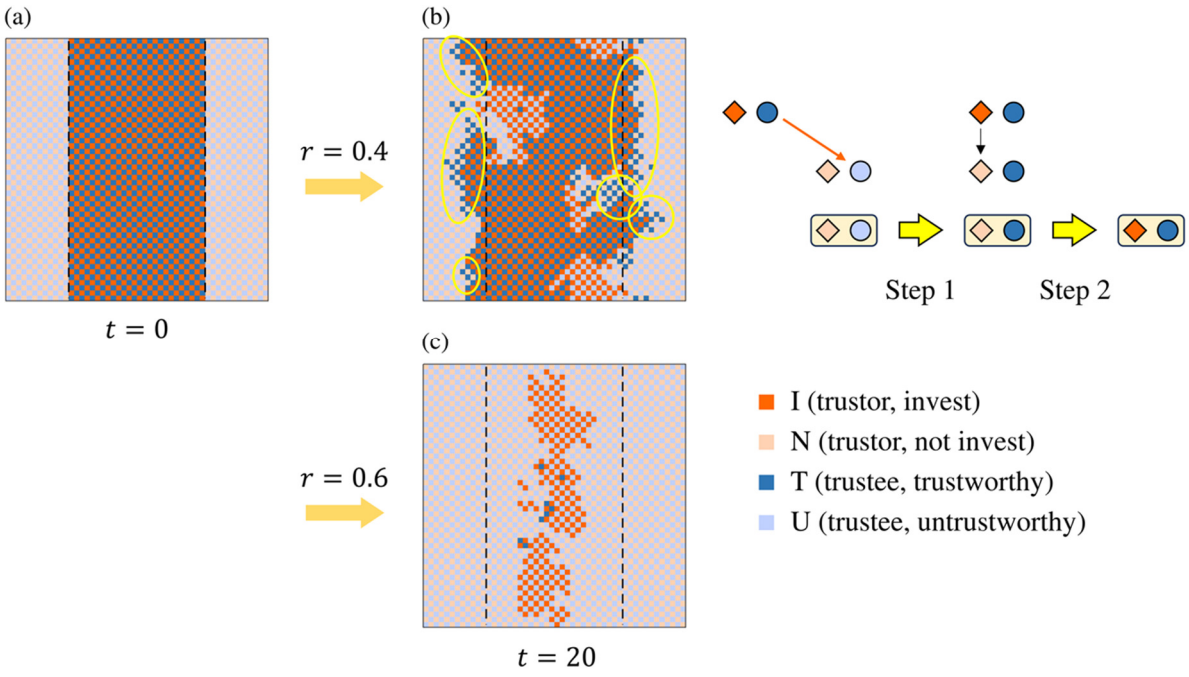


Figure 2: Inter-role spatial reciprocity in the two-step invasion I&T ⇒ I&U ⇒ N&U is key to trust emergence. (a) The initial preparation divides the lattice into two blocks, I&T and N&U, to better observe the two-step invasion. (b) At a moderate return ratio (r = 0.4), trustworthy trustees are supported by neighbouring investing trustors, thus invading untrustworthy trustees near non-investing trustors (Step 1, I&T ⇒ I&U, regions marked by yellow circles); near trustworthy trustees, an investing trustor has higher fitness and invades non-investing trustors (Step 2, I&U ⇒ N&U). (c) At a high return ratio (r = 0.6), trustworthy trustees have low fitness due to returning too much, thus unable to make the invasion in Step 1. Other parameters: u = 3, x = 1.

Related publication

[1] N. Xie, X. Bai, L. Wang, Y. Yılmaz, A. Szolnoki: *Emotion-driven switching game environments facilitates general cooperation,* Chaos Solitons & Fractals **202,** 117524 (2025) ISSN 0960-0779, https://doi.org/10.1016/j.chaos.2025.117524

QUANTITATIVE COMPARISON OF POWER GRID REINFORCEMENTS

B. Hartmann, G. Ódor, K. Benedek, I. Papp and M. T. Cirunay

This research presents a head-to-head evaluation of three grid reinforcement strategies for the Hungarian high-voltage power grid: (1) duplicating inter-community "bridge" links, (2) inserting bypasses around poorly synchronised nodes, and (3) fortifying edges identified as cascade-triggering vulnerabilities. Built from official operator data, our grid models avoid simplifications typical in prior work and show coupling distributions in close agreement with European and North American grids.

Our results show that community-based bridge duplication consistently outperforms both bypass additions and cascade-based reinforcements. It delivers the most robust increase in synchronisation, frequency stability, and cascade mitigation across all tested cases. In contrast, cascade-based reinforcement is stronger under low coupling conditions, while bypass strategies present superior frequency spread control in intermediate regimes. We also discuss how Braess' paradox is manifested in certain network configurations. As reinforcing specific lines decreases the grid's stability, there is a need for topology-aware planning. Our line-cut cascade simulations show fat-tailed cascade time distributions at intermediate coupling strengths, which is indicative of Griffiths-type scaling near a hybrid phase transition. Simultaneously, edge behaviours return to exponential at extremes of the evaluated range. To our knowledge, this is the first quantitative comparison combining oscillator models with conventional power system analysis tools, offering a rigorous bridge between theoretical and operational perspectives. [1]



Figure 1: Maps represent the first link cuts for different λ couplings for scenario #12. As we can see, several edges coincide at different values. The different number of cuts is due to the fact that for larger couplings, fewer lines are overloaded. These initial failures are typically concentrated around major power plants or large substations, surrounded by dangling ends.

Related publication

[1] B. Hartmann, G. Ódor, K. Benedek, I. Papp, M. Cirunay: *Quantitative comparison of power grid reinforcements*, Chaos Solitons & Fractals **200,** 117095 (2025) ISSN 0960-0779 https://doi.org/10.1016/j.chaos.2025.117095

SCALE-FREE BEHAVIOUR OF WEIGHT DISTRIBUTIONS OF CONNECTOMES

M. T. Cirunay, G. Ódor, I. Papp and G. Deco

To determine the precise link between anatomical structure and function, brain studies primarily concentrate on the anatomical wiring of the brain and its topological properties. In this work, we investigate the weighted degree and connection length distributions of the KKI-113 and KKI-18 human connectomes, the fruit fly, and the mouse retina. We find that the node strength (weighted degree) distribution behaviour differs depending on the considered scale. On the global scale, the distributions are found to follow power-law behaviour, with a roughly universal exponent close to 3. However, this behaviour breaks at the local scale as the node strength distributions of the KKI-18 follow a stretched exponential, and the fly and mouse retina follow the log-normal distribution, respectively, which are indicative of underlying random multiplicative processes and underpins nonlocality of learning in a brain close to the critical state. However, for the case of the KKI-113 and the H01 human) datasets, the local weighted degree distributions follow an exponentially truncated power law, which may hint at the fact that the critical learning mechanism may have manifested at the node level too. [1]

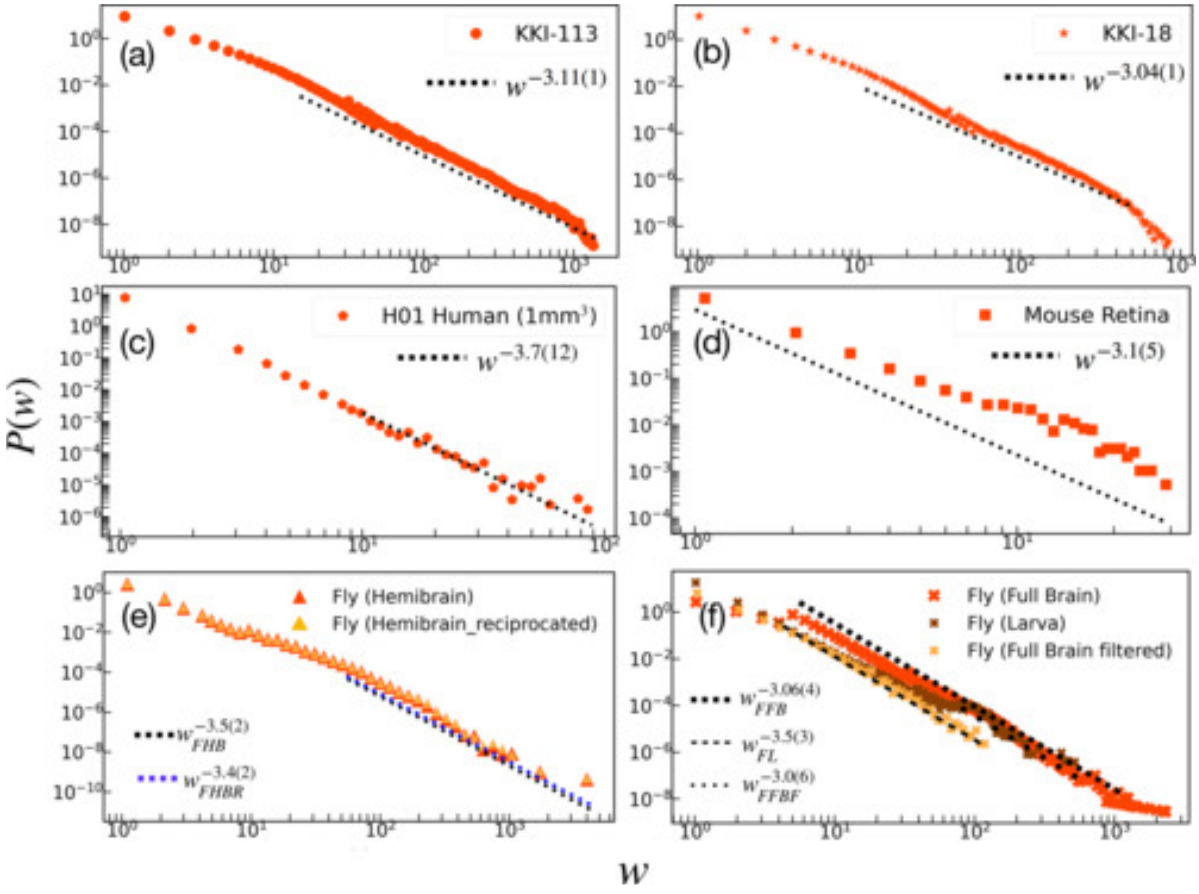


Figure 1: The weight distributions of (a) KKI-113, (b) KKI-18, (c) H01 human (1 mm³), (d) mouse retina, (e) fly (hemibrain), (f) fly (full brain, and its filtered version), and that of a larva all follow power-law behaviours on the global scale

Related publication

[1] M. Cirunay, G. Ódor, Géza I. Papp, G. Deco: *Scale-free behavior of weight distributions of connectomes,* Physical Review Research **7 (1),** 013134 (2025) ISSN 2643-1564 https://doi.org/10.1103/PhysRevResearch.7.013134

DERIVATION OF POTENTIAL FOR GROUP INTERACTIONS IN EVOLUTIONARY GAMES

Gy. Szabó and B. Király

In many-particle physical systems, potentials are used to describe the sum of pair interactions. A similar potential can be introduced for the investigation of evolutionary games where two-player games define the interactions. Now we have demonstrated the existence of a potential for two-strategy group interactions for which the players with identical strategies receive equal payoffs. This type of group interaction includes some extended versions of public goods and minority games that are widely used for the investigation of social dilemmas in human societies or ecological systems.

Some interesting consequences of group interactions are illustrated by a simple two-strategy model where the players are located at sites of a square lattice, and their income comes from five five-player games played with the nearest neighbours. In this model, the group interactions support curious formation of strategy arrangements in the ground state representing optimal choices for the players.

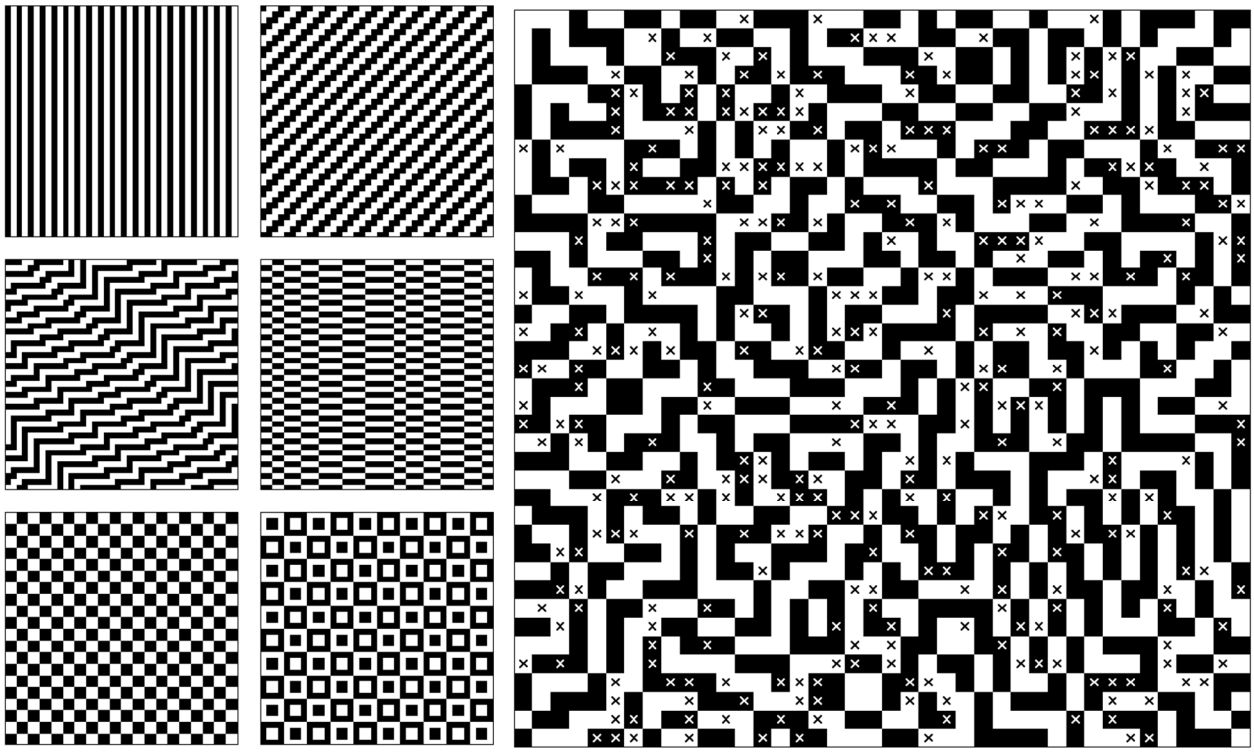


Figure 1: Optimal strategy distributions on square lattice

Six patterns (left side) show ordered or partially ordered spatial distributions of two (black and white) strategies that are found by theoretical analyses. In addition to these optimal spatial distributions, the Monte Carlo simulations have indicated the existence of many other disordered labyrinth-like patterns. One of these strategy distributions is shown on the right side with enlarged boxes. Here the small x-s denote players who can reverse their strategies without decreasing the optimal payoffs. This model illustrates combinations of features that were investigated separately via Ising-type models possessing ordered or disordered ground states and frustrations. [1]

Related publication

[1] Gy. Szabó and B. Király: *Derivation of potential for group interactions in evolutionary games,* Phys. Rev. E **112(6),** 064317 (2025) https://doi.org/10.1103/nhxn-6zqf

ABBREVIATIONS

2DEG	Two-dimensional Electron Gas
AC	Alternating Current
ACE2	Angiotensin-Converting Enzyme 2
ADI	Alternating Direction Implicit
AE	Acoustic Emission
AEKI	Institute for Atomic Energy Research (Hungarian acronym)
AFM	Atomic Force Microscopy
AIT	Air Ingress Test
AIV	Assembly, Integration and Verification
ALD	Atomic Layer Deposition
ALLEGRO	Experimental Helium Gas Cooled Fast Reactor Developed by the European V4G4
AMBI	5-amino-2-mercaptobenzimidazole
ASM	Analytic-Synthetic Method
ATF	Accident Tolerant Fuel, Alignment Test Facility
BC	Black Carbon
BCF	Boda Claystone Formation
BEMA	Bruggeman Effective Medium Approximation
BES	Beam Emission Spectroscopy
BF	Bright Field
BLE	Bluetooth Low Energy
BME	Budapest University of Technology and Economics, β-mercaptoethanol
BNC	Budapest Neutron Centre
BRR	Budapest Research Reactor
BWR	Boiling Water Reactor
CA	Cellulose Acetate
CAD	Computer Aided Design
CARC	Calculations for Atmospheric Release Criteria
CBP	Capillary Bridge Probe
CE	Colouration Efficiency
CEPROMAC	Combined Effect of Pre-treatment and Radiation on Mechanical Properties of Cladding Materials
CERES	Cooling Effectiveness on Reactor External Surface
CERIC	Central European Research Infrastructure Consortium
CH	Cultural Heritage
CHF	Critical Heat Flux
COD	Chemical Oxygen Demand
COP	Coefficient of Performance
COPD	Chronic Obstructive Pulmonary Disease
cps	counts per second
CS	Conceptual Shift
CSM	Common Sublattice Method
CTN	Chorda Tympani Nerve
CVD	Chemical Vapour Deposition
D3S	Distributed Space Weather Sensor System
DBA	Design Basis Accident
DBC	Design Basis Condition
DCT	Demo Central Team
DEGDMA	Diethylene Glycol Dimethacrylate
DEMO	DEMOnstration Power Plant
DF	Dark Field
DHR	Decay Heat Removal
DLR	German Aerospace Centre (German acronym)
DLS	Dynamic Light Scattering

DMDS	Dimethyl Disulfide
DMEM	Dulbecco's Modified Eagle Medium
DMS	Disruption Mitigation Systems
DMSO	Dimethyl Sulfoxide
DNB	Departure from Nucleate Boiling
DONES	DEMO Oriented NEutron Source
DPA	Displacement per Atom
DPBS	Dulbecco's Phosphate Buffered Saline
DSC	Design Safety Calculation, Differential Scanning Calorimetry
DSL	Design Service Lifetime
EAD	European Active Dosimeter
EC	Elemental Carbon
ECB	Ethanol-monochlorobenzene
ECSS	European Cooperation for Space Standardization
ED	Electron Diffraction
EDS, EDX	Energy Dispersive X-ray Spectroscopy
EDTA	Ethylenediaminetetraacetic acid
EGFET	Extended-Gate Field-Effect Transistor
EIA	Environmental Impact Assessment
EIS	Electrochemical Impedance Spectroscopy
EIT	Electrical Impedance Tomography
ELTE	Eötvös Loránd University, Budapest (Hungarian acronym)
EM	Engineering Model
EOL	Extended Operating License
EOT	Extended Operating Time
EPD	Electronic Personal Dosimeter
EPR	Emergency Preparedness and Response
ERO	Earth Return Orbiter
ESA	European Space Agency
ETM	EUROfusion TIMES Model
EU	European Union
EURATOM	European Atomic Energy Community
FAT	Factory Acceptance Tests
FbLSTM	Feature-based Long Short-Term Memory
FDA	Food and Drug Administration (USA)
FEA	Finite Element Analysis
FEM	Finite Element Method
FFT	Fast Fourier Transform
FIB	Focused Ion Beam
FIDES-II	OECD NEA Second Framework for Irradiation Experiments
FKKL	Laboratory (Department) of Surface Chemistry and Catalysis, EK (Hungarian acronym)
FOAK	First-Of-A-Kind
FPL	Fusion Plasma Physics Department (Laboratory), EK (Hungarian acronym)
fps	frames per second
FSAR	Final Safety Analysis Report
fs-LA	femtosecond Laser Ablation
FSR	Final Safety Report
FTIR	Fourier Transform Infrared Spectroscopy
FTL	Fusion Technology Department (Laboratory), EK (Hungarian acronym)
FWHM	Full Width at Half Maximum
GFR	Gas-cooled Fast Reactor
GIS	Geographical Information System
GM	Geiger-Müller
GNPs	Gold Nanoparticles (nanopores)
GPA	Geometrical Phase Analysis
GPC	Pulsed Gas Inlet

GPU	Graphics Processing Unit
GUI	Graphical User Interface
GTR	Ground Tyre Rubber
HALO	US Habitation and Logistics Outpost
HAp	Hydroxyapatite
HAXPES	High-Energy XPS
HC	High-Contamination
HCHiP	Hungarian Chips Competence Centre
HEPES-HBSS	4-(2-hydroxyethyl)-1-piperazineethanesulfonic acid) – Hank's Balanced Salt Solution
HERA RIA	High Burnup Experiment in Reactivity Initiated Accident
HLW	High-Level Waste
HOPG	Highly Oriented Pyrolytic Graphite
HPA	Heat Purchase Agreements
HRTEM	High Resolution Transmission Electron Microscopy
HTGR	High Temperature Gas-Cooled Reactors
HTTF	High-Temperature Test Facility
HUN-REN EK	HUN-REN Centre for Energy Research
HV	High Voltage
HVDC	High-Voltage Direct Current
IAEA	International Atomic Energy Agency
IC	Ion Chromatography
ICE	Instrument Calibration Enclosures
I&C	Instrumentation and Control
ICP-MS	Inductively Coupled Plasma Mass Spectrometry
ICP-OES	Inductively Coupled Plasma Optical Emission Spectrometry
IDA	Internal Dosimeter Array
IL	Ionoluminescence
ILW	
IoI	Intermediate-Level Waste
Institute of Isotopes	
IPWR	Integrated Pressurised Water Reactor
IR	Infrared
ISS	International Space Station
ITER	International Thermonuclear Experimental Reactor
JAXA	Japan Aerospace Exploration Agency
JEEPs	Joint Experimental Projects
JPL	Jet Propulsion Laboratory (NASA)
KIKO3DMG	Nodal Reactor Physics Calculation Code Developed in the EK
LBLOCA	Large-Break Loss-Of-Coolant Accident
LDH	Layered Double Hydroxide
LDOS	Local Density of States
LED	Light Emitting Diode
LET	Linear Energy Transfer
LLW	Low-Level Waste
LOC	Lab-on-a-chip
LOCA	Loss of Coolant Accident
LOC-HBu	Loss-of-Coolant High Burnup
LPE	Liquid Phase Epitaxy
LSPS	Large-Scale Pressure System
LSES	Large-Scale Engineering System
LTO	Long-Term Operation
LWR	Light Water Reactor
LW-SMR	Light-Water Small Modular Reactor
MALDI-TOF	Matrix-Assisted Laser Desorption/Ionisation Time-Of-Flight
MAPE	Mean Absolute Percentage Error
MAT	Magnetic Adaptive Testing

MBA	Mercaptobenzoic Acid
MC	Monte Carlo
MCDM	Multi-Criteria Decision Making
MCM	Monte Carlo Method
MCNP	Monte Carlo N-Particle
MCP	Minimum Controllable Power
MEMS	Microelectromechanical System
MFA	Institute of Technical Physics and Materials Science (Hungarian acronym)
MFC	Mass Flow Controller
MHTGR	Modular High Temperature Gas-cooled Reactor
MIH	Molar-Incisor Hypomineralization
MIR	Middle Infrared Region
MIS	Minimally Invasive Surgery
MOVPE	Metalorganic Vapour Phase Epitaxy
MPs	Mineral Platelets
MPS	Micro-Physiological Systems
MRR	Manufacturing Readiness Review
MSR	Mars Sample Return
MUCNE	Matrix-UCeNdEu
M&S	Modelling and Simulation
MVM	Hungarian Power Companies (Hungarian acronym)
NAA	Neutron Activation Analysis
NAL	EK Nuclear Analytical and Radiographic Laboratory (Hungarian acronym)
NASA	National Aeronautics and Space Administration, USA
NBL	Nuclear Safety Department (EK, AEKI)
NDE	Non-Destructive Evaluation
NDIR	Non-Dispersive Infrared
NIR	Near InfraRed
NKFIH	Hungarian National Research, Development, and Innovation Office (Hungarian acronym)
NMR	Nuclear Magnetic Resonance
NPs	Nanoparticles
NPP	Nuclear Power Plant
NRAs	National Nuclear Regulatory Authorities
NUBIKI	Nuclear Safety Research Institute (Hungarian acronym)
OAH	Hungarian Atomic Energy Authority (Hungarian acronym)
OC	Organic Carbon
ODS	Oxide Dispersion-Strengthened
OECD NEA	Organisation for Economic Co-operation and Development Nuclear Energy Agency
OL	Operating License
OM	Optical Microscopy
ONMD	Optical Nanomotion Detection
OoC	Organ-on-Chip
OPC	Optical Particle Counter
ORC	Organic Rankine Cycle
OSU	Oregon State University
OTKA	Hungarian Scientific Research Fund (Hungarian Acronym)
Paks NPP	Paks Nuclear Power Plant
PCB	Printed Circuit Board
PCL	Polycaprolactone
PCMI	Pellet-Cladding Mechanical Interaction
PDMS	Polydimethylsiloxane
PDR	Preliminary Design Review
PDS	Passive Dosimetry System
PEC	Photoelectrochemical
PFM	Proto-Flight Model

PGAA	Prompt-Gamma neutron Activation Analysis
PHMs	Precious Heavy Metals
PID	Proportional Integrator Differentiator
PIE	Post-Irradiation Examinations
PLC	Programmable Logic Controller
PM	Particulate Matter
POC	Point-of-Care
PPA	Power Purchase Agreements
PS	Polystyrene
PSI	Paul Scherrer Institute
PTS	Pressurised Thermal Shock
PV	Photovoltaic
PWR	Pressurised Water Reactor
R&D	Research & Development
RAFM	Reduced Activation Ferritic Martensitic
RD	Repeat Distance
REEs	Rare Earth Elements
RF	Radio Frequency
RGD	Arg–Gly–Asp
RG-HG	Rhombohedral-hexagonal Graphite
RIA	Reactivity-Initiated Accident
RLH	Ribbon-Like Hypomineralization
RMC	Reverse Monte Carlo
RME	Remote Maintenance Equipment
RMS	Root Mean Square
RPV	Reactor Pressure Vessel
RSS	Reactive Sulphur Species
RWG	Resonant Waveguide Grating
RWM	Radioactive Waste Management
SAED	Selected Area Electron Diffraction
SANS	Small Angle Neutron Scattering
SD	Sessile Drop
SDS	Space Dosimetry System
SE	Spectroscopic Ellipsometry
SEFOR	South-west Experimental Fast Oxide Reactor
SEM	Scanning Electron Microscopy
SEM-EDX	Scanning Electron Microscopy with Energy Dispersive X-Ray microanalysis
SFR	Sodium-cooled Fast Reactors
SICs	Structural Integrity Computations/Calculations
SIMTONIA	SIMulator Tools for Nuclear Industrial Applications
SMEs	Small and Medium-sized Enterprises
SMPS	Scanning Mobility Particle Sizer
SMR	Small Modular Reactor
SPI	Shattered Pellet Injection
SP	Scattering Production
SPW	Synthetic Porewater
SSNTD	Solid State Nuclear Track Detector
STEM	Scanning Transmission Electron Microscope
STEM-EDX	Scanning TEM - Energy Dispersive X-ray Spectroscopy
STM	Scanning Tunnelling Microscopy
SURET	SUbchannel REactor Thermohydraulics
TAL	Technically Allowable Lifetime
TAR	Test Acceptance Review
TBG	Twisted Bilayer Graphene
TCA	Total Carbon Analyser
TCS	Turbine Control System
TEM	Transmission Electron Microscopy

TEN-T	Trans-European Transport Network
TES	Thermal Energy Storage
TÉT	Bilateral Research Program (Hungarian acronym)
TIS	Therapy-Induced Senescence
TL	Thermoluminescent
TLD	Thermoluminescent Dosimeter/Detector
TLV	Threshold Limit Value
TOC	Total Organic Carbon
TPR	Temperature Programmed Reduction
TRASS	Time Reversal As Self-Supervision

IMPRINT

Editor and Lector

László Redler

Publisher

Ákos Horváth
Balázs Madas
Béla Pécz
HUN-REN Centre for Energy Research
H-1121, Budapest, Konkoly Thege M. út 29-33.
Hungary

Design

Zsófia Zsarnay

Picture credits

HUN-REN Centre for Energy Research

Accessibility

http://www.ek.hun-ren.hu/

Contact

HUN-REN Centre for Energy Research
Location: *KFKI Campus, Budapest Konkoly-Thege Miklós street 29-33., H-1121 Hungary*
Phone: *(+36 1) 395 91 59*
E-mail adresses: info@ek.hun-ren.hu



HUN REN

Centre for Energy Research

KFKI Campus, Konkoly-Thege Miklós út 29-33.
Budapest H-1121, Hungary
Phone: +36 1 395 9159
www.ek.hun-ren.hu